The Optical Microscopy of Colloidal Suspensions

Mark Stuart Elliot

Doctor of Philosophy

The University of Edinburgh

1999

"Get thee glass eyes . . . to see the things thou dost not."

KING LEAR, IV vi

Abstract

The colloidal state has long been of interest to physicists, both in its own right and as a model for atomic systems. In particular, colloidal suspensions with low size-polydispersity have been widely used as model hard spheres. Optical microscopy can resolve detail at the larger end of the colloidal length scale, and to image suspensions at an individual particle level of resolution would allow the investigation of local behaviour in a way denied to the established techniques of light-scattering. To achieve high-contrast single-particle resolution in dense suspensions that are thick enough to show behaviour the same as would be expected in the bulk is not a trivial exercise, however. This work builds on established advanced techniques of the light microscopy of phase objects, to develop an effective method of achieving this aim, addressing issues of imaging technique, suspension mounting and the interpretation of image data. The usefulness of this newly developed experimental protocol is demonstrated by, amongst other results, a detailed study of the structure of the colloidal crystals found in hard-sphere suspensions and an investigation of the nucleation of such crystals from the metastable colloidal fluid.

Declaration

I, Mark Stuart Elliot, do hereby declare that I alone composed this thesis and that this work is my own.

Witness my hand, this thirtieth day of July, one thousand nine hundred and ninety-nine

Acknowledgements

I am grateful to many people for their advice, encouragement or other help in bringing this thesis to completion. Without their combined contributions, this work would have been impossible. Though they are too many to all be named, my gratitude to every one is nonetheless heartfelt.

There are three, though, whose influence deserves personal recognition.

Paul Anning bears the responsibility for setting me on this path: his teaching was what persuaded me that, of all my school subjects, physics was the one to pursue further. This persuasion has been amply vindicated and I am most grateful to its progenitor.

Having turned to teaching this subject myself, it was Nick Lord's example and encouragement in maintaining a research interest that was instrumental in my taking up the opening that has lead to this work. Je vous remercie bien, Monsieur!

However, it has been Wilson Poon's inspiration, wisdom and friendship that have done most to keep my feet on the path that Paul Anning first showed me and along which Nick Lord walked with me for a short while. While I would claim responsibility for the erratic nature of this walk over the last seventeen years, that I have reached this point in a time considerably less than by pure chance is due in a large measure to Wilson. *'Ευχαριστέω σοι, ἀιῶνας μου κερδαίνων*!

Μόνῳ σοφῷ θεῷ ...

Contents

Abstract v

Declaration vii

Acknowledgements ix

1 Introduction 1

1.1 The colloidal state of matter 2

1.1.1 The colloidal state defined 2

1.1.2 Examples of colloidal dispersions 2

1.1.3 The stabilization of colloids 3

1.2 The appeal of colloids to physicists 4

1.2.1 Colloids as model atoms 5

1.3 Results from light scattering 6

1.4 The potential of optical microscopy 7

I Principles of Colloid Microscopy 11

2 Resolving Colloidal Length Scales 15

2.1 Generic features of observation systems 15

2.1.1 The observation process 15

2.1.2 Direction and notation conventions 16

2.1.3 Magnification 17

2.1.4 Aberration-free imaging 17
2.1.5 The microscopical observation system 18
2.2 Resolution-limiting factors 19
2.2.1 Detector segmentation 19
2.2.2 Imaging system aperture 20
2.2.3 Illumination degree of coherence 26
2.3 Practical bright field microscopy 28
2.3.1 The infinite tube-length compound microscope 29
2.3.2 Magnification 31
2.3.3 Conjugate planes 34
2.3.4 Köhler illumination 38
2.3.5 Oil immersion technique 38

3 Enhancing Colloidal Contrast 41
3.1 The problem of colloidal contrast 41
3.1.1 Definition of contrast 41
3.1.2 Colloids as phase objects 41
3.1.3 Bright-field micrographs of colloids 42
3.2 Phase contrast microscopy 44
3.2.1 Zernike's principle 44
3.2.2 Fourier representation 44
3.2.3 Phasor representation 46
3.2.4 Setting up phase contrast microscopy 50
3.2.5 Phase contrast images of colloids 51
3.3 Normarski DIC microscopy 54
3.3.1 The principle of differential interference contrast 54
3.3.2 The DIC microscope 55
3.3.3 Phasor representation 58
3.3.4 Normarski's modifications 61
3.3.5 Normarski DIC images of colloids 62

3.4 Digital image processing 69
3.4.1 Look-up table operations 69
3.4.2 Multiple-image arithmetic 72
3.4.3 Multipixel operations 75
3.4.4 Frequency space operations 79

4 The Microscopy of Thick Suspensions 83
4.1 Achieving bulk conditions under the microscope 83
4.1.1 Suspension requirements and optical limitations 84
4.1.2 A method for mounting thick colloidal suspensions 87
4.2 Acquiring three-dimensional information 89
4.2.1 The determination of depth of field 90
4.2.2 The control of image position 92
4.3 Displaying three-dimensional information 96
4.3.1 Montages of selected images 96
4.3.2 Longitudinal sections through stacks 96
4.3.3 Constructed views of entire stacks 98

II Applications of Colloid Microscopy 103

5 Colloidal Hard Sphere Suspensions 105
5.1 The ideal hard sphere system 105
5.1.1 Monodisperse hard spheres 105
5.1.2 Hard sphere phase behaviour 106
5.2 Real nearly-hard sphere colloids 108
5.2.1 Limitations of assemblies of colloidal spheres 108
5.2.2 Evidence for nearly-hard sphere behaviour in colloids . . . 109
5.2.3 The preparation of suspensions 110

6 The Structure of the Hard Sphere Solid 115
6.1 Background 116

6.1.1 Predicted structure and crystallographic scheme 116
6.1.2 Results from earlier work 118
6.2 Interpretation of single micrographs 119
6.2.1 Experimental details 120
6.2.2 Computer model 121
6.2.3 Hexagonal patterns 122
6.2.4 Zig-zag patterns 123
6.2.5 Disjointed-line patterns 129
6.2.6 Square patterns 132
6.2.7 Other patterns 136
6.3 Constructed views of an image stack 142
6.3.1 Experimental and analytical details 142
6.3.2 Views obtained by rotations about the y-axis. 144
6.3.3 Views obtained by rotations about the x-axis. 148

7 The Kinetics of Hard Sphere Nucleation 153
7.1 Experimental details 154
7.2 "Standard" suspensions 155
7.2.1 $\phi = 0.525$ 155
7.2.2 $\phi = 0.490$ 159
7.2.3 $\phi = 0.502$ 163
7.3 Suspensions with a better density match 166
7.3.1 $\phi = 0.489$ 167
7.3.2 $\phi = 0.510$ 168
7.3.3 $\phi = 0.50$ 172

8 Additional Interesting Observations 177
8.1 Sedimentation profiles 177
8.2 A particle recognition scheme 181
8.3 Measurements from time-average series 183

9 Conclusions **187**

A Derivations **191**

A.1 The Airy pattern – the bright field P.S.F. 191

A.2 Phase contrast image intensity 196

B List of Symbols and Abbreviations **199**

B.1 Symbols 199

B.2 Abbreviations 204

List of Figures **205**

List of Tables **208**

Bibliography **209**

Chapter 1

Introduction

Ever since the work of Thomas Graham [1861] on liquid diffusion first identified them as a separate class of materials, colloids have been the subject of physicists' interest. Although early experiments involved direct observation, over much of this century the favoured experimental approach has been light scattering, the optical equivalent of the highly successful X-ray techniques developed by the Braggs and others. While this approach has mirrored, and built upon, many of the successes of X-ray techniques, it also shares their disadvantages. However, the typical length scales in colloidal systems which make light scattering techniques possible also open up the possibility of direct imaging of structures in real space, *i.e.* microscopy. My contention is that optical microscopy of colloidal suspensions, undertaken with care, is a technique that is very fruitful in yielding results that other, already well-established techniques can do so only poorly, or not at all. This thesis is both an account of what "undertaken with care" means in colloid microscopy, building on standard microscopy with my own methods, and a "harvest festival" of colloid physics – the firstfruits of those methods.

1.1 The colloidal state of matter

While Graham [1861] originally distinguished colloids as being "solutions" which were unable to diffuse through a membrane, an understanding of the microscopic reasons for this behaviour enables a more prescriptive definition to be made.

1.1.1 The colloidal state defined

Colloids are a complex state of matter, but all consist of at least one of each of the following:

- a continuous phase (the dispersion medium);
- a particulate (or disperse) phase.

Various ranges of sizes of the particles (often – sometimes confusingly – referred to as "colloids") are suggested, but the important limits are that:

- The particles are large enough to have a definable size and shape – this will also satisfy the need for the particles to be larger than the molecules of the medium to a degree which allows the medium to be treated as a simple continuum.
- The particles are small enough for Brownian motion to be vigorous enough to keep them dispersed.

These requirements limit the particles to the size range of roughly 10 nm to 1μm [Pieranski, 1983; Tabor, 1991]. This range is intermediate between the microscopic length scale of molecules and atoms and the macroscopic one of objects resolvable by the naked eye and, for this reason, the colloidal length scale is often described as being mesoscopic.

1.1.2 Examples of colloidal dispersions

Many possibilities exist for colloidal systems and they are widespread in everyday life; some examples are given in table 1.1.

dispersion medium	disperse phase		
	solid	liquid	gas
liquid	colloidal suspensions: blood, ink, toothpaste	emulsions: margarine, milk	liquid foams: shaving foam, whipped cream
gas	solid aerosols: smoke	liquid aerosols: tobacco smoke, fog	–

Table 1.1: Examples of Colloids

In what follows only the case of solid particles dispersed in a liquid medium, *i.e.* colloidal suspensions, shall be considered.

1.1.3 The stabilization of colloids

A fundamental issue in colloid science is maintaining the stability of the dispersion. Where the particulate phase shows an affinity for the medium, the colloid is described as lyophilic ('liquid-loving') and is intrinsically relatively stable. In this case little is required beyond matching the densities of the phases and keeping the size of the particles small to mitigate the effects of gravity. On the other hand, the van der Waals attractions between particles in a lyophobic ('liquid-hating') colloid tend to cause aggregation, as the potential energy associated with the attractive forces typically exceeds the thermal energy of the particles by several orders of magnitude, once the particles have approached within distances of a few tens of nanometres [Tabor, 1991].

The van der Waals attraction, F_{vdW} between two identical spheres of radius R_p a distance $s_\asymp$ from touching has been shown [Hamaker, 1937] to be given by

$$F_{vdW} = -\frac{A_H R_p}{12 s_\asymp^2}, \tag{1.1}$$

where A_H is the Hamaker constant. As one might expect, the Hamaker constant

is related to the polarizabilities of the medium and particles, and hence their relative permittivities ϵ_m and ϵ_p respectively [Russel *et al.*, 1989, page 147]:

$$A_H \propto \left(\frac{\epsilon_p - \epsilon_m}{\epsilon_p + \epsilon_m}\right)^2 \tag{1.2}$$

Hence the van der Waals force will always be negative. However, the dielectric behaviour of the medium will mitigate this attraction, while closely matching the refractive indices ($n = \sqrt{\epsilon}$) of the particles and the medium will reduce the attractions between particles to negligible values.

To overcome residual attractions, two approaches are possible:

Charge stabilization relies on particles repelling one another due to like surface charges. This can be achieved with naturally neutral particles by adding salt to the liquid phase, of which one species of ion will preferentially adsorb onto the surface of the particles. In the absence of thermal motion, these charges would be balanced out by the counterions, whereas real temperatures mean that the counterion "blanket" will be diffuse. Particles whose counterion blankets overlap will experience a repulsive force, inhibiting aggregation.

Steric, or entropic, stabilization is achieved by attaching long chain polymers to the surface of the particles, with the decrease in entropy caused by "squashing" the polymers when two particles approach consequently causing a very steep and short ranged repulsion.

1.2 The appeal of colloids to physicists

Colloidal suspensions have been a fertile field of study for physicists, both in their own right and as tools for illuminating wider issues of interest.

The physics developed by workers such as von Smoluchowski [1903, 1918] on the movements of charged colloidal particles, Hamaker [1937] on the interparticle potential and culminating in the detailed theory of the stability of colloids

presented by Derjaguin and Landau [1941] and Verwey and Overbeek [1948] has been of seminal importance.

The classic example of the extrinsic usefulness of colloid physics is the way that the experiments performed by Perrin [1908] and the theories of Einstein [1905, 1906] and Langevin [1908] were able finally to confirm the molecular nature of matter.

1.2.1 Colloids as model atoms

Colloids can do more than just point to molecules and atoms, however: they can also be used to model atoms. Moreover, the number of particles in a colloidal model system can be many orders of magnitude larger than that possible in computer models and hence colloidal models can be much closer statistically to atomic systems.

With the liquid behaving as a continuum, it is possible [Pusey, 1991] to express the interaction between particles by an effective pair potential, so that the suspension has thermodynamic properties formally the same as an atomic system with the same pair potential (but where particles move ballistically between collisions with one another).

The advantages of colloids as model systems are manifold and stem from their size. Directly, this means that these model atoms are large enough to probe with visible light. Indirectly, as thermal velocities scale inversely with the cube of the particle size, it means that the time-scale of particle rearrangements is of the order of seconds to months, allowing the kinetics to be followed in detail. Furthermore, the forces between sterically stabilized colloids are so weak that structures can be easily shear-melted and the slow, optically resolvable, relaxation to equilibrium can be readily followed.

1.3 Results from light scattering

Owing possibly to their background in the X-ray methods of condensed matter physics of many of those involved in colloid physics, it has been the equivalent reciprocal space techniques of light scattering that have been most widely employed, to great effect.

Powder light diffraction (*q.v., e.g.,* Pusey [1991]) has yielded details of the structure of hard sphere colloidal crystals, in microgravity [Zhu *et al.*, 1997] as well as under conventional conditions [Pusey *et al.*, 1989; Liu *et al.*, 1993]; this technique has also been used to study the superlattices formed by binary mixtures of hard spheres [Bartlett *et al.*, 1992; Pusey *et al.*, 1994].

The colloidal crystallization process has also been studied by following the time evolution of Bragg peaks, for hard spheres by Harland *et al.* [1995]; He *et al.* [1996]; Harland and van Megen [1997] and for charged ones by Würth *et al.* [1995]. The effect of the size distribution of the particles on crystallization and the glass transition has been measured [Henderson *et al.*, 1996]. In combination with direct observation, static light scattering has been used by van Megen and Underwood [1993] to study the hard sphere glass transition and by Poon *et al.* [1995] to study the phase behaviour of colloid-polymer mixtures.

Using a technique first presented by Cummins *et al.* [1964] and expanded upon by Clark *et al.* [1970], Brown *et al.* [1975] showed how the dynamical properties of colloidal suspensions could be extracted using photon correlation spectroscopy (also known as dynamic light scattering). As well as the early foundational work [Pusey, 1975], this technique has been used to measure particle sizes very precisely [Pusey and van Megen, 1984], to identify the kinetic glass transition [van Megen and Underwood, 1994] and to relate structural relaxations to low-shear viscosity [Segrè *et al.*, 1995a]. To allow the application of dynamic light scattering to turbid suspensions where the single scattering assumption does not hold, a two colour method has also been developed [Segrè *et al.*, 1995b].

Reciprocal space methods such as these, while being very powerful, have a

number of inherent disadvantages: first, due to the generic phase problem, inverting diffraction patterns to determine structure is not without ambiguities (Bartlett *et al.* [1992] and Pusey *et al.* [1994] used electron microscopy of dried suspensions to confirm their findings); secondly, the spatial and temporal averaging inherent in these methods makes them unsuitable for studying the formation, structure and evolution of local defects such as vacancies and grain boundaries. The very earliest stages of nucleation are also inaccessible, because short-lived transient structures, probably containing only a small number of particles, are involved. For these purposes, the method of choice is real-space real-time imaging, which, while unfeasible for atoms, is readily achievable for colloids.

1.4 The potential of optical microscopy

In recent years, physicists have begun to exploit real-space techniques again, in particular digital video microscopy.

The standard configuration of a suspension enclosed between a microscope slide and a cover slip leads to a quasi-two-dimensional system. Using fluorescent tracker particles, Schaertl and Sillescu [1993] studied the dynamics of hard colloidal spheres in a narrow gap. Such "thin" suspensions can, however, allow for the sharp imaging of ordinary (non-fluorescent) particles, even in close configurations. Bongers and Versmold [1996] have studied the dynamics of single particles close to a glass wall in this way, while Dinsmore *et al.* [1997] have reported on the fluid-solid transition at a wall in binary mixtures of hard spheres. Both the measurement of the effective pair-potential between particles in a confined space [Carbajal-Tinoco *et al.*, 1996] and the investigation of their structural phase transitions [Marcus and Rice, 1996, 1997] have been reported recently.

To have suspensions thicker than a few particle diameters leads to difficulties with imaging, especially when the particle number density is large. Crocker and Grier [1996] have, however, managed to measure the hydrodynamic coupling between two isolated spheres (see also Crocker [1997]) while Grier and Murray

[1994] have studied heterogeneous crystallization in low-density charge-stabilized colloids.

For dense, thick suspensions some means of optical sectioning is required, in order to filter out out-of-focus information. The best optical sectioning is achieved by confocal microscopy and the imaging of individual particles in concentrated colloidal dispersions has been clearly demonstrated [van Blaaderen, 1993; Verhaegh and van Blaaderen, 1994]. This method has been used to image the real space structure of a colloidal hard sphere glass [van Blaaderen and Wiltzius, 1995] and to measure stacking disorder in colloidal hard sphere crystals [Verhaegh *et al.*, 1995]. Aside from expense, confocal microscopy has the disadvantage that individual images are acquired by scanning, so that bright images require either very intense illumination or exposure times which limit the suitability of the system for studying kinetics.

It is possible, however, to obtain good optical sectioning using a research-grade standard optical microscope and to obtain images that yield information about the three-dimensional structure of dense colloidal suspensions [Elliot *et al.*, 1997]. While care needs to be taken with the selection of contrast enhancing techniques and the interpretation of images, this approach holds out the prospect of being a relatively straightforward way of tracking the movements and configurations of small numbers of particles within a larger suspension, complementing the established scattering techniques which characterize larger samples so well.

The following chapters aim to realize some of the vast potential of optical microscopy, as applied to colloidal suspensions. Chapters 2 to 4 examine microscopy, reviewing the basics of imaging techniques and presenting the techniques and practices that I have developed, all with the end of achieving the best possible data from colloidal suspensions. Chapters 5 to 7 demonstrate the application of microscopy to a particular colloidal system, hard-sphere suspensions. Chapter 5 presents details of methods of preparing suitable suspensions. Chapter 6 examines the interpretation of images with reference to predicted structures and crystal-

lography. Chapter 7 is concerned with results from microscopical observations of the hard sphere disorder-order transition. Chapter 8 presents several further avenues of research by means of optical microscopy that hold out prospects of good colloid physics. On the basis of the evidence given in those chapters, my case is that careful optical microscopy is an extremely useful tool for the colloid physicist.

Part I

Principles of Colloid Microscopy

While the size of colloidal particles allows for the possibility of optical imaging, the exercise is not a trivial one. In studying colloidal suspensions, three main challenges are presented to those who would image individual particles:

- Typical length scales are of the order of the wavelength of the illumination, so that we are always working near the limit of **resolution**.
- Particles and medium are both highly transparent, with closely matched refractive indices, so that **contrast** is a problem.
- The desire to study bulk behaviour requires the imaging of a genuinely three-dimensional suspension, so that **object thickness** is an issue.

In this part I examine how these three challenges can be met, with each challenge being addressed in its own chapter. The earlier sections are largely a review of fundamental principles and well established microscopical techniques, presented with the aim of providing a self-contained exposition for the colloid physicist. As the chapters proceed, however, building upon these foundations, I present my own techniques and practices, specially developed for the full three-dimensional imaging of individual particles in thick colloidal suspensions. So, the part as a whole should provide a free-standing introduction to, and handbook of, colloidal microscopy for the physicist.

Chapter 2

Resolving Colloidal Length Scales

The fundamental problem with looking at small objects is the resolution of fine detail. In this chapter, we will first consider features of the process that constitutes "looking at" small objects; then we will turn to three factors that limit the resolving power of a given observation system: detector segmentation, imaging system aperture and illumination coherence; finally, the practicalities of the device designed to resolve small objects – the microscope – shall be set out in detail.

2.1 Generic features of observation systems

2.1.1 The observation process

The observation process involves using an optical system to form an image O' of an illuminated – or self-luminous – object O on a suitable detector. Any imaging system will, in principle, work "in reverse" *i.e* O is an image of O', as well as *vice versa*. Any pair of points, planes, distances which are images of one another are said to be **conjugate**.

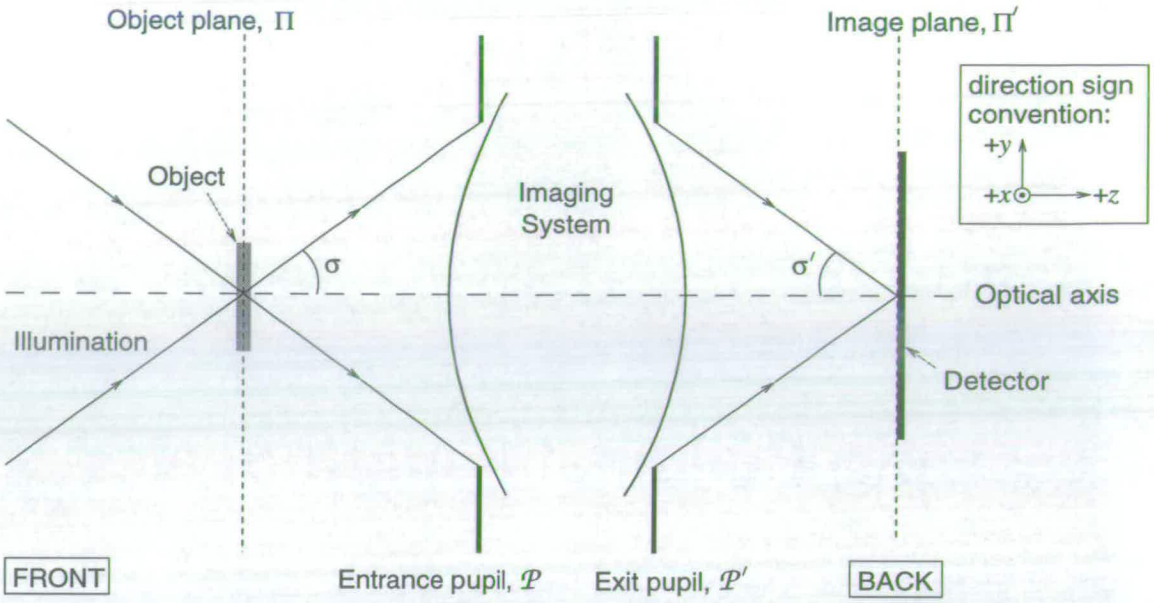

Figure 2.1: The generic observation system: At the front is a source of illumination; behind this is the object; next, an optical system which images the object in front of it; finally, at the back, is the image, recorded by a detector. The pupils of the imaging system limit the cone of light from the object which can be used to form the image.

2.1.2 Direction and notation conventions

A number of conventions are useful in describing the observation process. The fundamental one is that the source of the illumination is called the **front** of the process, and the final image the **back**, so that the various components are described as being **behind** or **in front of** one another, as appropriate. Positive directions are: from front to back along the optical axis (z), upwards from the optical axis (y) and to the right as seen when upright looking along the optical axis towards the back (x), as shown in figure 2.1.

My conventions for notation are given in table 2.1. Note that all planes are perpendicular to the optical axis, which passes through the coordinate origin of each of them. For polar coordinates r and θ, the positive directions are away from the optical axis and anticlockwise as viewed from the back of the system.

In the ... plane	Object O	Entrance Pupil $\mathcal{P}$	Exit Pupil $\mathcal{P}'$	Image O′
Symbol for Plane	Π	$\Pi_{\mathcal{P}}$	$\Pi'_{\mathcal{P}}$	Π'
Coordinate Variables	$x, y; r, \theta$	$x_{\mathcal{P}}, y_{\mathcal{P}}; r_{\mathcal{P}}, \theta_{\mathcal{P}}$	$x'_{\mathcal{P}}, y'_{\mathcal{P}}; r'_{\mathcal{P}}, \theta'_{\mathcal{P}}$	$x', y'; r', \theta'$
Maximum Extent	$X, Y; R$	$X_{\mathcal{P}}, Y_{\mathcal{P}}; R_{\mathcal{P}}$	$X'_{\mathcal{P}}, Y'_{\mathcal{P}}; R'_{\mathcal{P}}$	$X', Y'; R'$
Transmittance Function	τ	$\tau_{\mathcal{P}}$	$\tau'_{\mathcal{P}}$	τ'
Light Amplitude Distribution	u	$u_{\mathcal{P}}$	$u'_{\mathcal{P}}$	u'
Light Intensity Distribution	I	$I_{\mathcal{P}}$	$I'_{\mathcal{P}}$	I'

Table 2.1: Notation conventions

2.1.3 Magnification

The ratio of the height of an observation system's image y'_{O} to that of the object causing it y_{O}, taking the signs of the heights into account, defines the **transverse magnification** $\mathcal{M}$ of the system:

$$\mathcal{M} = \frac{y'_{\mathrm{O}}}{y_{\mathrm{O}}}. \tag{2.1}$$

When considering the details of an observation system, other measures of magnification can be necessary; these are dealt with in §2.3.2.

2.1.4 Aberration-free imaging

The ideal imaging system is one that is "aberration-free". Such a system is illustrated in figure 2.2 and is defined by:

> An imaging system that has as its output for a point object a spherical wavefront converging on that point's geometrical image is aberration-free.

In geometrical optics, only the axial position of the object is important, meaning, in the notation given above, that (1) all points on Π have their images on Π' and (2) the magnification $\mathcal{M}$ of the system is constant over Π'. In 1873, Abbe (and

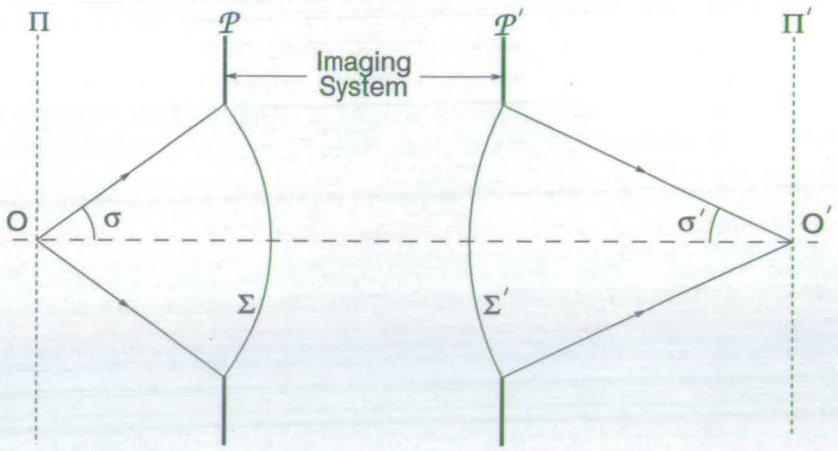

Figure 2.2: The meaning of an aberration-free imaging system: a spherical wavefront Σ at the entrance pupil $\mathcal{P}$, centred on the object O, leads to a spherical wavefront Σ' at the exit pupil $\mathcal{P}'$, centred on the (geometrical) image O′.

simultaneously, von Helmholtz) showed, by considering refraction at a spherical interface, that this means that an aberration-free imaging system obeys the condition

$$\boxed{\frac{n \sin \sigma}{n' \sin \sigma'} = \mathcal{M} = \text{constant}} \tag{2.2}$$

which is known as **Abbe's sine condition**. The best modern microscope optics are close to being aberration-free and equation 2.2 is an important relation.

2.1.5 The microscopical observation system

In microscopy, the illumination is provided by the substage assembly, with possibly an external light source. The imaging system is the combination of the part of the microscope from objective to ocular and the observer's eye, or camera. The detector is then the retina of the eye, or film/CCD microchip of the camera.

It is sometimes useful to divide a compound imaging system into sections and to treat each one as an independent imaging system, with one section's image being the next's object.

2.2 Resolution-limiting factors

However simple or complex an observation system, the basic factors limiting resolution are the same. These are: the spacing of the individual light-sensitive elements of the detector, the aperture/pupil size of the imaging system, and the degree of coherence of the illumination.

2.2.1 Detector segmentation

All image recording devices do so by being divided up into an array of detectors, each of which records the average light level in its own area.

In the human eye*, the retina consists of $\mathcal{O}(10^8)$ rods and cones arrayed over an area of $\mathcal{O}(10^3)$ mm^2. At the fovea – the most sensitive area on the retina – the cones are spaced as closely as 0.0015 mm apart, so, other considerations apart, the retina being about 24 mm from the pupil, the angular resolution of the eye cannot exceed about 6×10^{-5} radians. This corresponds to about $\frac{1}{25000}^{\text{th}}$ of the field of view.

In photographic film, the emulsion consists of silver halide grains of size $\mathcal{O}(10^{-3})$ mm, but plates or film can be $\mathcal{O}(10^2)$ mm across, so that the resolution may correspond to $\frac{1}{100000}^{\text{th}}$ of the field of view.

On the other hand, the charge-coupled devices used in video cameras consist typically of a rectangular array of 800×500 pixels over an area of, say, $9\,\text{mm} \times 7\,\text{mm}$, giving a spacing of $\mathcal{O}(10^{-2})$ mm and a resolution corresponding to only $\frac{1}{500}^{\text{th}}$ of the field of view, or so.

For faithful image recording we must therefore ensure that:

> The magnification of the imaging system must be such that the finest detail of the image is larger than the spacing of the elements of the detector.

*For further details, see *e.g.* Inoué [1997], Chapter 4, pages 163-187

2.2.2 Imaging system aperture

The wave nature of light means that diffraction by the finite aperture of an imaging system will limit its resolution.

Pupils and apertures

The physical dimensions of the imaging system mean that only a limited cone of light will be able to pass through it and take part in forming the image (see Figure 2.2). The angle of the cone accepted by the system, 2σ, is known as the **object-side angular aperture** of the system, whereas the angle of the cone that forms the image, $2\sigma'$, is the **image-side angular aperture**.

In colloid microscopy, the objects are suspended in a medium with refractive index $n_m > 1$, normally with a glass cover which has $n_{cs} \approx n_m$. Refraction will occur at the interface between the glass and the space in front of the imaging system (refractive index n), so the light in the cone of angle 2σ entering the objective will have come from a cone of a different angle leaving the object plane. If the space between the objective and the glass cover is just filled with air, $n = 1$ and the angle at the object will be smaller than 2σ. Changing n by using an immersion fluid will reduce this effect[†], so taking n (and n', of the space behind the imaging system) into account is important in considering the ability of the imaging system to capture light from the object. We therefore define the object-side and image-side **numerical apertures**, by respectively

$$\mathcal{A} = n \sin\sigma \qquad \text{and} \qquad \mathcal{A}' = n' \sin\sigma'. \tag{2.3}$$

Apertures are limited by the finite width of some component in the imaging system, but it is not generally necessary to identify its actual dimensions and position. This is because those components of the imaging system in front of the limiting component will form an image of its transverse limits, known as the **entrance pupil** of the system ($\mathcal{P}$); similarly, those components behind it will

[†]This is examined further in §2.3.2, under "Oil immersion technique"

form an image called the **exit pupil** of the system ($\mathcal{P}'$). When considering the effect on imaging, it is sufficient to consider either one of these images instead of the restricting object itself.

The amplitude transmittance functions $\tau_{\mathcal{P}}$ and $\tau'_{\mathcal{P}}$ are known as the entrance and exit **pupil functions**. Typically, pupils are circular, with a well defined edge and are centred on the optical axis so we can use

$$\tau'_{\mathcal{P}} = \mathrm{circ}\left(\frac{r'_{\mathcal{P}}}{R'_{\mathcal{P}}}\right) \tag{2.4}$$

etc., the function $\mathrm{circ}\left(\frac{r}{R}\right)$ being defined by

$$\mathrm{circ}\left(\frac{r}{R}\right) = \begin{cases} 1 & : \quad r \leq R \\ 0 & : \quad r > R \end{cases} . \tag{2.5}$$

The exit pupil of a well-adjusted microscope can be seen as a bright disc a centimetre or so above the eyepiece (technically, the "ocular back surface"), if the eye is moved back far enough to allow it to focus on this plane. This disc is the narrowest extent of the image-forming rays behind the microscope, so:

> To observe the object, without straining the eye or reducing the field of view, the pupil of the eye needs to be at the exit pupil of the microscope.

The distance between the exit pupil and the ocular is called the **eye relief** and is given on the side of most oculars.

When using a camera to record the image, it is important to have the exit pupil of the photo-ocular coincident with the entrance pupil of the camera. This should be set up when the photo-ocular and camera are fitted to the microscope, but may need to be checked – especially if the camera field of view appears restricted.

Point spread functions and diffraction-limited optics

The aperture of an imaging system will limit the brightness of the image, but it will also lead to diffraction effects. This means that, even if the system were

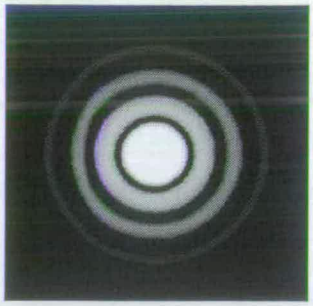

Figure 2.3: (a) The Airy pattern: the image of a point object in an aberration-free imaging system with circularly symmetric pupils. The central bright disc, known as the Airy disc, contains 84% of the luminous energy at the image plane and is often taken as the effective extent of the "point" image (the outer rings have been enhanced in the diagram for clarity).

aberration-free, a point object would not result in a point image, but instead a diffraction pattern, known as the **point spread function** (PSF). For this reason an aberration-free system is described as being diffraction-limited.

The full PSF extends over three dimensions, centred upon the geometrical image point; in this section we will just consider the two-dimensional cross-section of this at the image plane. For a diffraction-limited system with circularly symmetric pupils, this PSF is the **Airy pattern**, shown in figure 2.3.

Scalar diffraction and Fourier optics

To determine the intensity distribution in the Airy pattern (as plotted in figure 2.4), we need to consider the diffraction of light by the imaging system. To do this we will use the theories of Fourier optics, which was largely formulated by P.M. Duffieux [1946], building on foundations laid by Abbe [1873] and Lord Rayleigh [1896]. Here I present the key principles; for more detail, see the English translation of Duffieux's work [1983] or the classic operational treatment by Goodman [1996].

According to Rayleigh, we can associate all diffraction effects with the propagation of light between the exit pupil and the image, and treat the rest of the

system geometrically.

So, knowing that a point object will generate a spherical wavefront at the exit pupil of an aberration-free imaging system, all we need to do to find the point-spread function of such a system is to determine how a spherical wavefront of lateral extent determined by the exit pupil function will propagate from the exit pupil to the image plane.

In principle, what we do is to apply the Huygens-Fresnel construction, taking account of the phase variations across the exit pupil due to the fact that the wavefront is not parallel to $\Pi'_{\mathcal{P}}$.

This approach is valid if we can treat the light as scalar wave, which is the case if the radius of the exit pupil $R'_{\mathcal{P}}$ and the distance z' between the exit pupil and the image plane are both large compared to the wavelength of the light in that region. Under these conditions, approximating the spherical wavelets by parabolic surfaces also holds good – in other words, we have the **Fresnel diffraction** conditions.

What we find by doing this (see Appendix A.1) is that:

> The aberration-free image of a point object O is a scaled real-space Fourier transform of the pupil function $\tau'_{\mathcal{P}}$, centred on the geometrical image O′.

With a circular exit pupil with a sharp edge, we have $\tau'_{\mathcal{P}} = \mathrm{circ}(r'_{\mathcal{P}}/R'_{\mathcal{P}})$. Now, the Fourier transform of a circ function is a first order Bessel function of the first kind, J_1, which we can normalize to $\mathrm{jinc}(m) = 2\frac{J_1(m)}{m}$. Applying the necessary coordinate scaling, the light amplitude distribution in the image plane can therefore be given by

$$u'(r') \propto \mathrm{jinc}\left(\frac{2\pi R'_{\mathcal{P}} r'}{\lambda' z'}\right). \tag{2.6}$$

Intensity, $I' = u'u'^*$, so the Airy pattern is given by

$$I'(r') \propto \mathrm{jinc}^2\left(\frac{2\pi R'_{\mathcal{P}} r'}{\lambda' z'}\right). \tag{2.7}$$

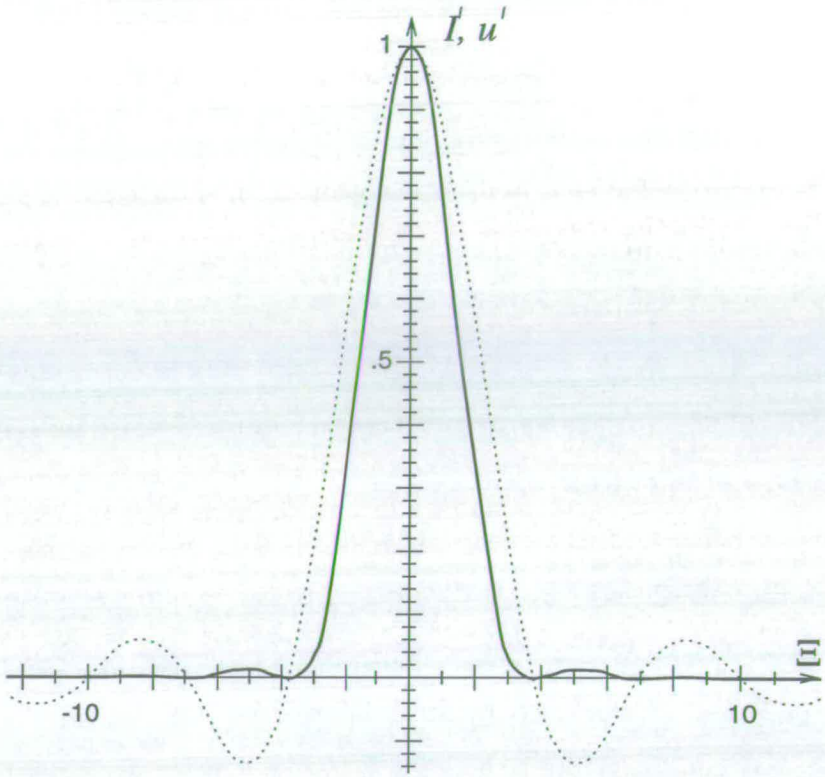

Figure 2.4: Light distribution in the Airy pattern, normalized to unity at the central maximum and with radial distance in Airy optical units Ξ. Solid line: intensity I'; dotted line: amplitude u'.

Figure 2.4 shows both the amplitude and intensity distributions plotted in terms of the Airy optical unit $\Xi = \frac{2\pi R'_{\mathcal{P}} r'}{\lambda' z'}$. Under the Fresnel approximations made, $z' \gg R'_{\mathcal{P}}$ so $\frac{R'_{\mathcal{P}}}{z'} = \tan\sigma' \approx \sin\sigma' = \frac{\mathcal{A}'}{n'}$. Using $\lambda' n' = \lambda_0$ and the Abbe sine condition (equation 2.2) allows us to write the more practically useful expression

$$\Xi = \frac{2\pi \mathcal{A}}{\lambda_0 \mathcal{M}}\, r'. \tag{2.8}$$

The minima of $\mathrm{jinc}^2(\Xi)$ correspond to the black rings in figure 2.3. The positions of the first six minima are given in table 2.2, along with the values and positions of the bright maxima in between. The central lobe contains 84% of the total luminous energy of the whole pattern. This region is called the **Airy disc** and we can consider it to be the limit of useful object information, with outer rings merely reducing the contrast of the image by brightening the background;

Minima ($I' = 0$)	Maxima	
Ξ	I'	Ξ
$3.831705970 = 1.219669891\pi$	1	0
$7.015586670 = 2.233130594\pi$	$1.749786278 \times 10^{-2}$	5.135622302
$10.17346814 = 3.238315485\pi$	$4.157996385 \times 10^{-3}$	8.417244140
$13.32369194 = 4.241062864\pi$	$1.600637668 \times 10^{-3}$	11.61984117
$16.47063005 = 5.242764375\pi$	$7.794453558 \times 10^{-4}$	14.79595178
$19.61585851 = 6.243921688\pi$	$4.370255517 \times 10^{-4}$	17.95981950

Table 2.2: The first twelve extrema of the Airy pattern

its radius,

$$r'_{\text{Airy}} \approx 0.610 \frac{\lambda_0 \mathcal{M}}{\mathcal{A}}, \tag{2.9}$$

therefore gives a useful measure of the size of the point spread function.

Real "point" objects

An ideal point object will always be coherently illuminated and this fact, implicit in Huygens-Fresnel construction, is used in the derivation of the Airy pattern. However, a point object is an idealized concept and even the smallest real objects will have finite size. An object may be treated as a point, however, if it is (1) illuminated coherently and (2) its radius is no greater than r_{Airy} which is the geometrical image in the object space of r'_{Airy} and is given by

$$r_{\text{Airy}} \approx 0.610 \frac{\lambda_0}{\mathcal{A}}. \tag{2.10}$$

In microscopy, with an oil-immersion objective, we can achieve $\mathcal{A} = 1.4$, so, as $\lambda_0 < 750$ nm, $r_{\text{Airy}} < 325$ nm, *i.e.*, larger colloidal particles are just about able to act as extended objects.

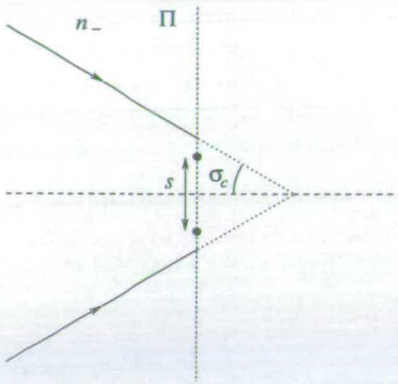

Figure 2.5: The illumination of two point objects

2.2.3 Illumination degree of coherence

The image of an extended object will consist of the superimposed images of individual points on the object. How these images superimpose depends on their mutual coherence, which will be determined by the degree of coherence of their illumination.

Mutual coherence between two point objects

The degree of coherence of the illumination of two points separated by a distance s across the object plane Π is given by

$$\xi_2 = \mathrm{jinc}\left(\frac{2\pi}{\lambda_0} s\, n_-\, \sin\sigma_C\right) \tag{2.11}$$

where the illumination is a uniform circular cone of angle $2\sigma_C$ and the refractive index in front of the object is n_- (see figure 2.5). In the microscope this angle is controlled by the condenser, which has numerical aperture $\mathcal{A}_C = n_- \sin\sigma_C$.

For $\xi_2 = 1$ the two points are coherently illuminated. This can only be achieved if the illumination is a beam parallel to the optical axis. However, close to coherent illumination can be achieved for small values of σ_C; generally, $\xi_2 = 0.88$ is taken as the lower limit of coherence. At this value $\frac{2\pi}{\lambda_0} s\, n_-\, \sin\sigma_C = 1$, *i.e.*, $\mathcal{A}_C = \frac{\lambda_0}{2\pi s}$. For a typical range $0.2 \leq \mathcal{A}_C \leq 0.9$, with $\lambda_0 = 550$ nm, we get 438 nm $\geq s \geq$ 97 nm, so separate colloidal particles of diameter $2R_p \geq 438$ nm

will not be coherently illuminated, even if the condenser diaphragm is closed to its minimum.

Although $\xi_2 = 0$ corresponds to incoherent illumination of the two points, the practical upper limit is taken at $\xi_2 = 0.18$. This has $\frac{2\pi}{\lambda_0} s\, n_- \sin\sigma_C = \pi$, *i.e.*, $\mathcal{A}_C = \frac{\lambda_0}{2s}$. Using the same values for $\mathcal{A}_C$ and λ_0 as before, we get 1380 nm $\geq s \geq$ 306 nm, so separate colloidal particles of diameter $2R_p \geq 306$ nm can be illuminated incoherently if the condenser diaphragm is opened sufficiently.

For $0.18 < \xi_2 < 0.88$, the illumination of the two points is referred to as being partially coherent.

The image of a two-point object

If the coordinates of the two points are (x_1, y_1) and (x_2, y_2), so that we have $s = \sqrt{(x_1 - x_2)^2 + (y_1 - y_2)^2}$, their geometrical images will be at $(\mathcal{M}x_1, \mathcal{M}y_1)$ and $(\mathcal{M}x_2, \mathcal{M}y_2)$ in Π'.

Leaving aside the identical constant prefactors, the image intensity

$$I' = \mathrm{jinc}^2(\Xi_1) + \mathrm{jinc}^2(\Xi_2) + 2\xi_2\, \mathrm{jinc}(\Xi_1)\, \mathrm{jinc}(\Xi_2), \tag{2.12}$$

where

$$\Xi_j = \frac{2\pi\mathcal{A}}{\lambda_0 \mathcal{M}} \sqrt{(x' - \mathcal{M}x_j)^2 + (y' - \mathcal{M}y_j)^2}, \qquad j \in \{1, 2\}. \tag{2.13}$$

For $\xi_2 = 1$,

$$I'_{\mathsf{coh}} = (\mathrm{jinc}(\Xi_1) + \mathrm{jinc}(\Xi_2))^2, \tag{2.14}$$

i.e., with coherent illumination, the image is obtained by summing the amplitudes.

On the other hand, for $\xi_2 = 0$,

$$I'_{\mathsf{incoh}} = \mathrm{jinc}^2(\Xi_1) + \mathrm{jinc}^2(\Xi_2) \tag{2.15}$$

i.e., with incoherent illumination, the image is obtained by summing the intensities.

Resolution limits

If two incoherently illuminated points are separated by $s = r_{\text{Airy}}$, the centre of the Airy pattern of each will coincide with the first dark ring of the other, giving an image with two bright peaks with a local intensity minimum midway between them. Summing intensities, the intensity at the mid-point will be $2\,\text{jinc}^2(\frac{3.83}{2}) = 73.5\%$ of the intensity at either of the peaks. Such a minimum is usually detectable and the condition $s = r_{\text{Airy}}$, called the **Rayleigh criterion**, is taken as the limit of resolution of two incoherently illuminated points. Using the Rayleigh criterion, we can therefore write the incoherent resolution limit ϱ_{incoh} as

$$\varrho_{\text{incoh}} = 0.610\frac{\lambda_0}{\mathcal{A}}. \tag{2.16}$$

For optical microscopy, with $\mathcal{A} = 1.4$, $\lambda_0 = 550$ nm, we get $\varrho_{\text{incoh}} = 240$ nm.

If the illumination of two points separated by s is coherent, amplitudes need to be summed and, to achieve a minimum of 73.5% of the peak intensity, we need to solve $[2\,\text{jinc}(\frac{\pi\mathcal{A}s}{\lambda_0})]^2 = 0.735[1 + \text{jinc}(\frac{2\pi\mathcal{A}s}{\lambda_0})]^2$. This value of s gives the coherent resolution limit of two points ϱ_{coh}. Solving the above equation gives us

$$\varrho_{\text{coh}} = 0.819\frac{\lambda_0}{\mathcal{A}}. \tag{2.17}$$

So resolution is not as good when the illumination is coherent; for $\mathcal{A} = 1.4$, $\lambda_0 = 550$ nm, we get $\varrho_{\text{incoh}} = 322$ nm.

Partially coherent illumination will give a resolution limit $\varrho_{\text{incoh}} < \varrho_{\text{pcoh}} < \varrho_{\text{coh}}$.

2.3 Practical bright field microscopy

The simplest way of increasing resolution is to bring the object closer to the eye, but there is a limit to how close an object can be and still be in focus. With a typical shortest distance of focus for the eye of 100 mm and a pupil diameter of 3 mm, the numerical aperture of the eye is about 0.015, so $\varrho_{\text{incoh}} \approx 0.02$ mm. To resolve detail smaller than this, we need an imaging system with a larger numerical aperture; the microscope is just such a system.

The microscopical system described in this section leads to standard **bright field** images, so called because the light-absorbing objects such a system is designed for appear dark on a bright field or background.

The simplest microscope is the magnifying glass or loupe. In order to resolve detail on the colloidal length scale without excessive aberrations over a reasonable field of view, however, a **compound microscope** – one that involves more than one imaging component – is required. For reasons to be described below, most modern research grade microscopes are designed with "infinite tube-length".

2.3.1 The infinite tube-length compound microscope

Figure 2.6 shows an "infinite tube-length compound microscope". The left-hand diagram shows the microscope set up for human observation, whereas the right-hand one shows it set up for image recording by camera (photographic film may replace the CCD microchip without changing the rest of the set-up). It should be noted that each of the lenses of the microscope will be a combination of several lenses in actual fact.

"Infinite tube-length" refers to the fact that the intermediate image formed by the objective is at infinity, because the object is at the front focal plane of the objective. This image is not shown on the diagram, but one can see that two rays from one object point are parallel behind the objective. Such an objective is often referred to as "infinity-corrected".

A traditional compound microscope uses an **objective** to form a real magnified inverted intermediate image at the front focal plane of the **ocular**, which in turn forms a further-magnified, still inverted, final image at infinity. Having the image at infinity means that the eye of the observer can be relaxed when focusing on the final image. With a camera, the intermediate image is in front of the photo-ocular front focal plane, so that a real final image is formed at the recording device.

With this two-lens system, maintaining the correct distance between the lenses

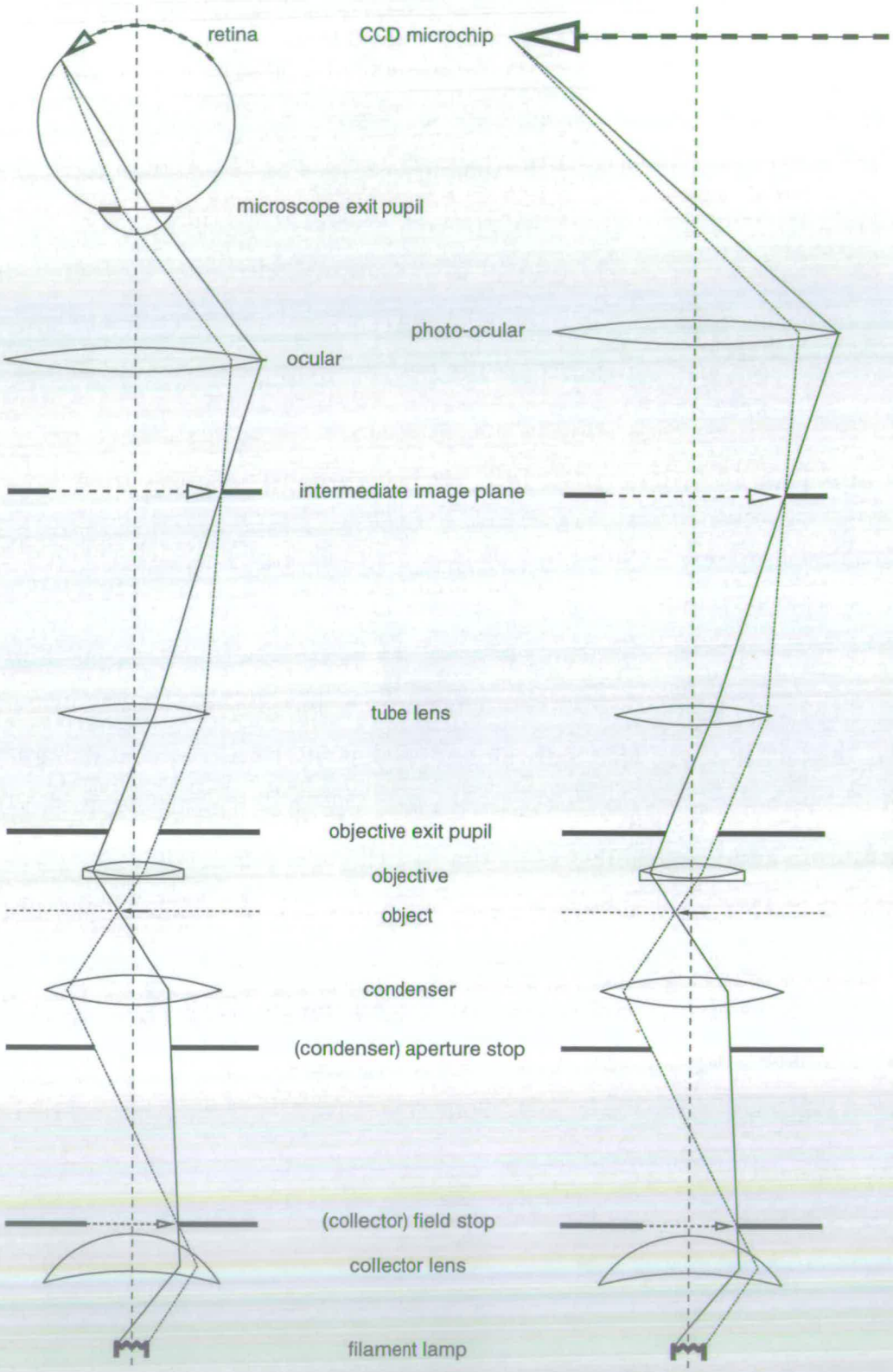

Figure 2.6: The infinite tube-length compound microscope.

– the tube length – is critical. Using an objective which forms an image at infinity and adding a **tube lens** behind it, to form a real intermediate image at the latter's back focal plane, chosen to coincide with the ocular front focal plane, means that the exact axial position of the objective becomes relatively unimportant and focusing can be achieved by moving the objective alone.

Imaging techniques other than the standard bright field described above rely on additional optical components placed behind the objective. With a finite tube-length microscope, the wavefronts behind the objective are curved, so such additional components require further compensating optics. Infinity corrected objectives have an obvious advantage in this respect and, mainly for this reason, most research grade microscopes are of infinite tube-length.

It is sometimes useful to consider the objective and tube lens to act together as a compound objective. Alternatively, the tube lens and ocular combine to make a telescope which looks at the objective's distant image.

2.3.2 Magnification

Three measures of magnification need to be considered when determining the overall magnification of the infinite tube-length compound microscope: transverse magnification, visual magnification and tube lens factor.

Transverse magnification $\mathcal{M} = \frac{\text{image size}}{\text{object size}}$, so this measure can only be used for real images. In terms of the symbols used in figure 2.7

$$\mathcal{M} = \frac{y_o}{y'_o} = -\frac{p'f}{pf'} = -\frac{q'}{f'} = -\frac{f}{q}. \tag{2.18}$$

Visual magnification M is used for virtual images and compares the angular size of the image with the angular size of the object viewed unaided (see figure 2.8). Unaided observation is taken to occur with the object at the "distance of distinct vision", *i.e.* the "working distance" of the eye w_{eye}, taken as -250 mm. The sign of w_{eye} indicates that it is measured from the eye backwards towards

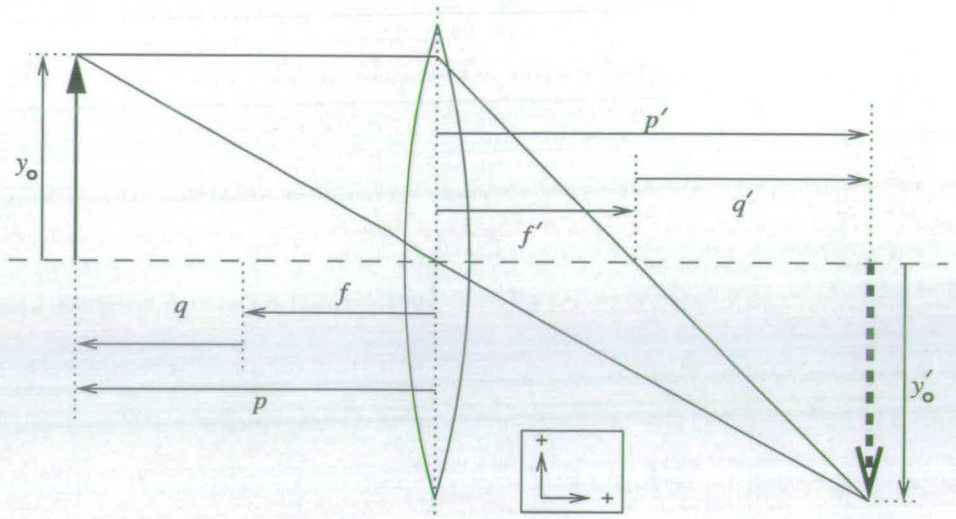

Figure 2.7: Transverse magnification: the inset shows the sign convention for directions.

the object. Using the notation of figure 2.8, we have

$$\mathsf{M} = \frac{\tan\omega'}{\tan\omega} = \frac{y'_o w_{\mathsf{eye}}}{(p_e - a')y_o} = -\frac{w_{\mathsf{eye}}(f' - p')}{f'(p_e - p')}. \tag{2.19}$$

With the image at infinity, as is the case for microscopy,

$$\mathsf{M}_\infty = \lim_{a'\to\infty} \mathsf{M} = -\frac{w_{\mathsf{eye}}}{f'}. \tag{2.20}$$

Tube lens factor: The tube lens has a virtual object and a real image. Its "magnification" is measured in terms of a "tube lens factor"

$$\mathcal{Q} = -\frac{f'_{\mathsf{TL}}}{w_{\mathsf{eye}}}, \tag{2.21}$$

where f'_{TL} is the back focal length of the tube lens.

Microscope magnification is given simply by the product of the objective and ocular magnifications and the tube lens factor. For human observation, the microscope magnification will be visual, whereas with a camera recording a real image, the microscope magnification will be transverse:

$$\mathsf{M}_\mu = \mathsf{M}_{\mathsf{Ob}}\,\mathcal{Q}\,\mathsf{M}_{\mathsf{Oc}} \qquad \text{or} \qquad \mathcal{M}_\mu = \mathsf{M}_{\mathsf{Ob}}\,\mathcal{Q}\,\mathcal{M}_{\mathsf{PO}}, \tag{2.22}$$

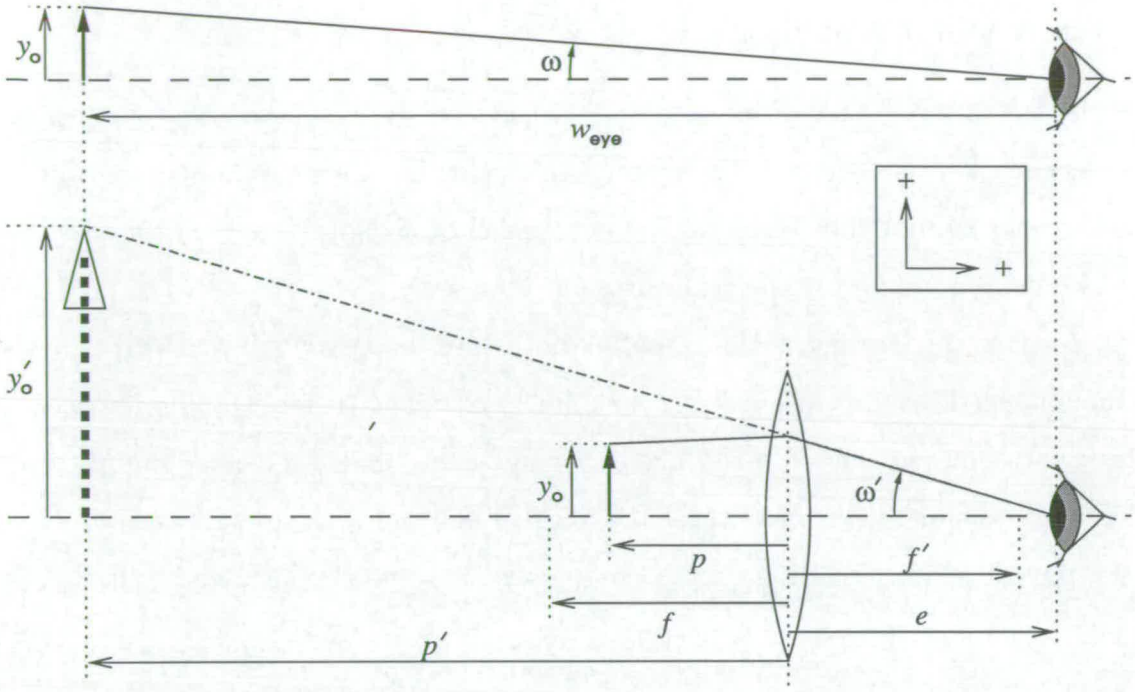

Figure 2.8: Visual magnification: the upper diagram shows conventional unaided vision; the lower diagram compares this with the case of a magnified virtual image.

where the subscripts μ, Ob, Oc and PO refer to the microscope, objective, ocular and photo-ocular respectively.

As mentioned previously, the overall magnification of a system needs to be such that the finest detail on the image is larger than the spacing of the elements of the light detector. The smallest detail resolvable on the image will be given by $\mathsf{M}_\mu\, \varrho$ or $\mathcal{M}_\mu\, \varrho$, as appropriate. There is no advantage to be gained by having the magnification such that more than a few elements of the detector correspond to the resolution limit of the image; any further magnification beyond this is called **empty magnification**. Practically speaking, I have found a useful range to be

$$5 < \frac{\mathcal{M}_\mu\, \varrho}{\Delta x_{\mathsf{pix}}} < 10, \tag{2.23}$$

where Δx_{pix} is the pixel spacing.

Calibration of digital images

A digital image is an array of pixels, which can be displayed at any desired magnification. One cannot, therefore, give a value for the magnification of digital image *per se*, but must refer to the **scaling** $\mathcal{S}$ of a digital image – that is, the distance represented by the pixel spacing.

Ideally, this scaling is the same for both dimensions of the pixel array. Although equal magnification along all azimuths is axiomatic for a good microscope, a small difference between the pixel spacings Δx_{pix} and Δy_{pix} is common, even for the best microchips. We therefore need to determine $\mathcal{S}_y$ as well as $\mathcal{S}_x$.

We can readily see that

$$\mathcal{S}_x = \frac{1}{\mathcal{M}_\mu \Delta x_{\text{pix}}} \quad \text{and} \quad \mathcal{S}_y = \frac{1}{\mathcal{M}_\mu \Delta y_{\text{pix}}}, \tag{2.24}$$

but a precision better than a few per cent (due largely to the measurement of the microchip dimensions) is hard to achieve by this method. This is not very satisfactory, especially as $\mathcal{S}_x$ and $\mathcal{S}_y$ usually only differ to this degree.

A more precise measure of scaling can be obtained by calibrating directly against a graticule (this also eliminates the need to assume that $\mathcal{M}_\mu^x = \mathcal{M}_\mu^y$). Given that the image of a section of graticule can extend over several hundred pixels, a precision of 0.5% is easily obtainable from this approach.

For a linear graticule, two images should be recorded, one for the graticule aligned along each of the directions of the pixel array. One can then determine directly from the recording how many pixels represent a known distance. This process should be carried out for all combinations of magnification and camera used.

2.3.3 Conjugate planes

Examination of figure 2.6 reveals a number of planes that are all conjugate with one another: the plane of the collector field stop, the object plane, the intermediate image plane and the final image plane. An additional plane, containing the

virtual image formed by the objective exists at infinity behind the microscope. This set of planes is called the **imaging or field set of optical planes** because any lateral restriction at one of these planes will alter the field of view of the microscope image. The collector field stop is an adjustable iris (often just called the "field iris") and this is how the field of view is controlled. The general rule is:

> Open the field iris sufficiently to illuminate only the area of the object that is under observation.

If the field iris is set too wide, stray reflections inside the microscope will reduce the contrast of the images.

The field set is not the only set of conjugate planes, however; another set is shown in figure 2.9: the plane of the illumination source and all the planes with its images – the plane of the condenser aperture stop, the objective exit-pupil plane and the exit pupil of the microscope. An additional plane, containing the virtual image of the lamp formed by the condenser exists at infinity in front of the microscope. These are called the **illumination or aperture set of optical planes** because any lateral restriction at one of these planes will alter the aperture of the illumination. The condenser aperture stop is an adjustable iris (often just called the "aperture iris") and this is how the aperture of the illumination is controlled. Closing the aperture iris will decrease the angle of the cone of light illuminating the object. As some light is scattered by the object, the cone of light containing image information is of a larger angle than this, so the general rule is:

> Open the aperture iris so that the condenser numerical aperture $\mathcal{A}_C$ is approximately 70% of the objective numerical aperture $\mathcal{A}$.

This should reduce stray reflections in most conditions. To increase the degree of coherence of the illumination, it may be necessary to close the aperture iris further than this.

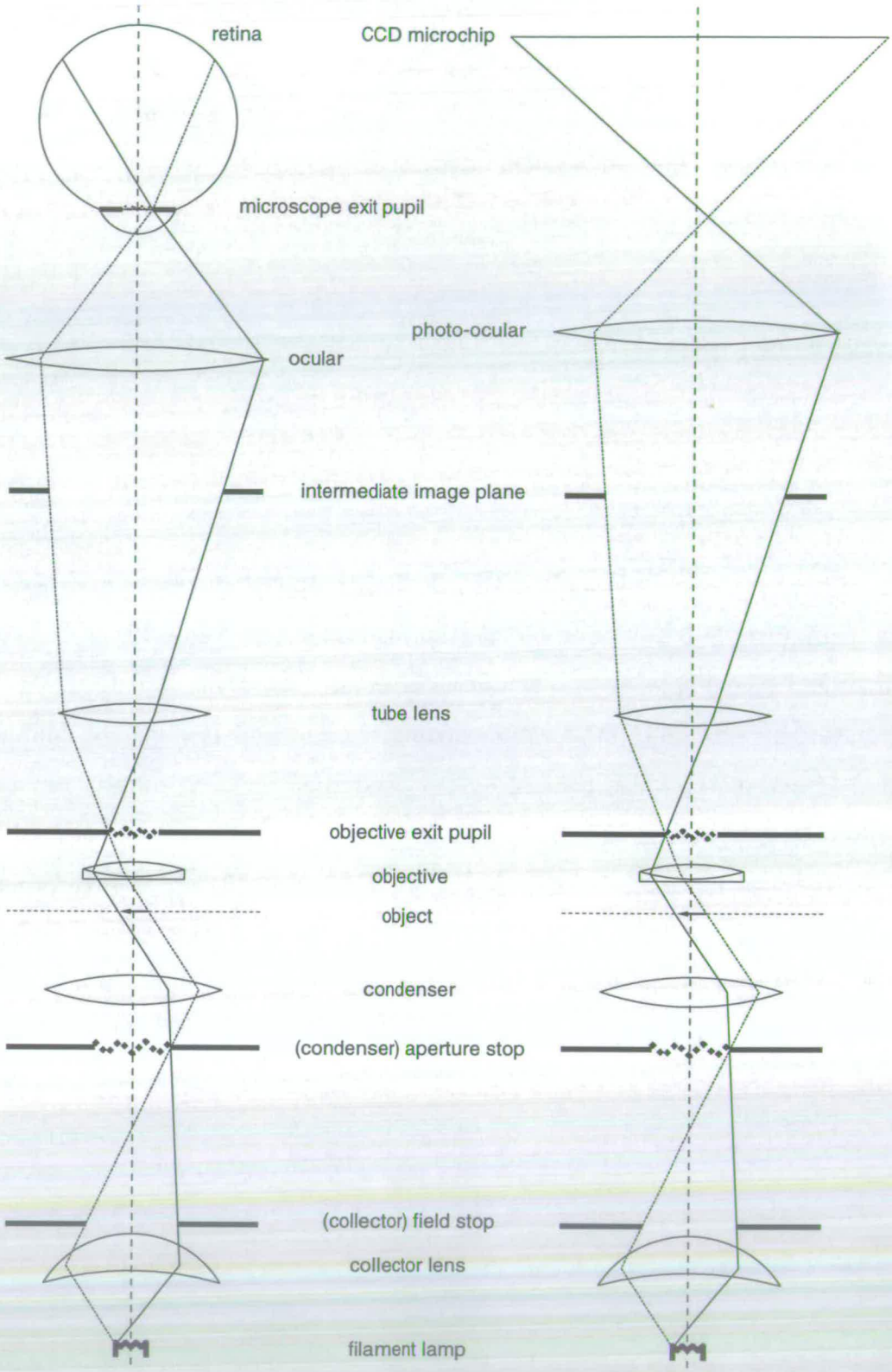

Figure 2.9: Illumination of the infinite tube-length compound microscope.

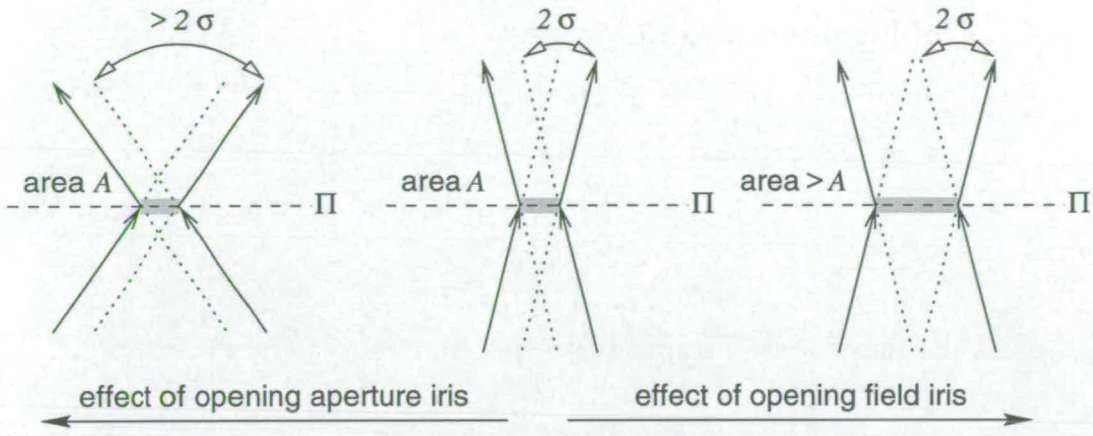

Figure 2.10: Controlling angular aperture and area of illumination.

Figure 2.10 shows the effect at the object plane Π of the two irises on the two sets of planes. The arrows show the outer edges of the frustrated cone of light illuminating the object and the frustrated cone of unscattered light leaving the object due to the continuation of the illuminating rays. Opening the **aperture** iris increases the **angle** 2σ of the cones, whereas opening the **field** iris increases the **area** A at the meeting point of the two frustra, *i.e.* the area of object illuminated – the field of view.

An important relationship exists between the two sets of planes as shown in figures 2.6 and 2.9:

> The light distributions in the field set of conjugate planes are the scaled Fourier transforms of those in the illumination set of conjugate planes, and *vice versa.*

This can be seen by the fact that rays crossing in one set of planes pass through opposite edges of the other set: light from a single point in one set passes through all points in the other set. This means that frequency-space operations can be performed on the images in one set by means of appropriate filters in the other set.

2.3.4 Köhler illumination

The requirements for microscope illumination are that:

1. The area of object illuminated is no larger than causes a minimum of stray light or glare.

2. The illumination is of controllable uniform intensity across the object.

3. The aperture of the illumination is adjustable according to objective and imaging requirements.

These requirements are best met by the system of illumination first proposed by August Köhler (see Haselmann [1983]), which has a condenser and illuminator in front of the object, in the arrangement depicted in figures 2.6 and 2.9. The essential details are that the collector field stop is imaged at the object plane, that the lamp is imaged at the condenser front focal plane, and that the condenser front focal plane is coincident with the condenser aperture stop. This system enables illumination to be uniform, despite a non-uniform filament, as the condenser will image the filament at an infinite distance in front of the object.

When setting up these conditions, it should be noted that removing the ocular and looking down the microscope tube reveals the aperture set of planes. Often a small telescope is fitted in place of the ocular to magnify the view of the aperture planes; alternatively, some microscopes have a Bertrand lens fitted to the tube which can be swung into place without having to remove the ocular.

The procedure for setting up Köhler illumination is given in table 2.3. For good image quality, Köhler illumination is essential and it behoves the microscopist to make this procedure one of habit.

2.3.5 Oil immersion technique

The presence of an air gap between an object and the objective places an upper limit on the numerical aperture of the imaging system and reduces the brightness

1. Use the substage focus to move the condenser close to the object plane.
2. Adjust the voltage to the lamp so that brightness is in mid-range.
3. Focus on the object plane; adjust brightness if necessary.
4. Close the field iris enough to obstruct part of the field of view
5. Use the substage focus to form a sharp image of the field iris; if necessary, use the condenser centring controls to centralize the image.
6. Open the field iris so that only slightly more than the area of interest of the object is illuminated; often this means just outside the field of view.
7. Viewing the objective exit pupil, adjust the position of the filament so that a sharp centralized image is formed.
8. Adjust the size of the aperture iris to give the desired $\mathcal{A}_C$ (for incoherent illumination this is usually set so that its image is slightly smaller than the objective exit pupil); if necessary, centralize, by adjusting the aperture iris mounting screws.

Table 2.3: Setting up Köhler illumination

of the image. Objectives designed to have this gap filled with a liquid of higher refractive index allow both these limits to be ameliorated.

The half-angle of acceptance of light by the objective σ can only be 90° if the object is in direct contact with the objective front lens. The presence of a cover slip on the object, amongst other practical considerations, limits σ to about 72° [Pluta, 1988, §2.3.5], and hence $\mathcal{A}$ to no more than 0.95. With cover slip glass of refractive index $n_{cs} = 1.515$, refraction at the cover slip-air interface means that the half-angle of the cone of light leaving the object cannot exceed 39° (see figure

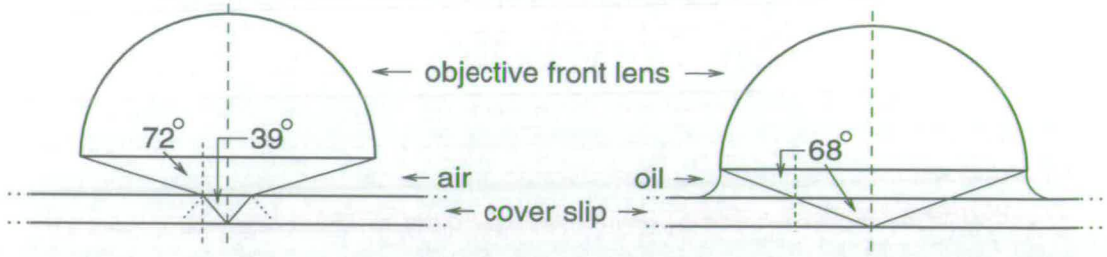

Figure 2.11: The effect on illumination of using an oil-immersion objective.

2.11). The critical angle for this interface being 41°, a significant proportion of the energy in the light cone will be reflected back into the cover slip.

If immersion oil of refractive index $n_{io} = 1.515$ is used between the objective and cover slip, σ can be about 68° [Pluta, 1988], which is similar to before, but the larger refractive index means that $\mathcal{A}$ can be 1.4. No refraction occurs at the cover slip-oil interface, so a cone of half-angle of 68° leaving the object will be accepted by the objective and no light energy will be lost by reflection.

A similar technique can be applied in front of the object, so that the condenser top lens is immersed and the aperture of the illumination $\mathcal{A}_C$ can be increased. This means that incoherent illumination can be achieved for smaller separations. A system where the refractive indices of the objective front lens, immersion oil, cover slip, object mounting medium, microscope slide and condenser back lens are the same and both the condenser and objective are immersed is described as a **homogeneous immersion** system; such a system maximizes the light capturing power of the microscope.

* * *

With oil-immersion bright field microscopy, as described above, resolving detail at colloidal length scales is just about attainable. However, the stability requirement that colloidal particles and their medium have similar refractive indices results in highly transparent suspensions, which give very low contrast images. The next chapter deals with more advanced imaging techniques, which make it possible to achieve clear images of transparent objects.

Chapter 3

Enhancing Colloidal Contrast

Colloidal suspensions, having closely matched refractive indices of particles and medium in order to reduce van der Waals attractions, produce very low contrast images under bright-field methods. This chapter, after demonstrating this problem, explains the microscopical techniques of phase contrast and Normarski differential contrast, before turning to the digital techniques of processing recorded images.

3.1 The problem of colloidal contrast

3.1.1 Definition of contrast

Contrast is usually defined in terms of intensities:

$$C'(x', y') = \frac{I'_0 - I'(x', y')}{I'_0}, \tag{3.1}$$

where I'_0 is the intensity of the background (*i.e.* the intensity when $\tau(x, y) = 1$). Positive contrast will therefore mean an image darker than the background.

3.1.2 Colloids as phase objects

Highly transparent objects, such as many colloidal suspensions, which cause only phase changes in the light passing through them are known as **phase objects**;

objects which cause attenuation only are known as **amplitude objects.**

In many applications, staining is used to give phase objects amplitude contrast, but few colloidal suspensions lend themselves easily to this approach. Furthermore, suspensions which are to be studied for their bulk behaviour cannot be stained, as this will obscure the interior. In imaging colloidal suspensions, therefore, techniques of turning phase shifts into intensity differences must generally be used.

3.1.3 Bright-field micrographs of colloids

Bright-field microscopy is unsuitable for unstained phase objects, because moderately out-of-focus images have greater contrast than in-focus images, which ideally have no contrast at all, as is demonstrated by figure 3.1. This has the consequence that digitally enhancing the contrast (see § 3.4 for examples of techniques) of images of planes within the body of a suspension will, in fact, cause more confusion:

> The strength of the contrast of slightly defocused images will completely obscure the object plane.

The series of 15 images at the top of figure 3.1 are of a single colloidal sphere at varying degrees of defocus. These images have had their contrast digitally enhanced, emphasizing the confusion caused: contrast is seen to be

- strong and negative for moderate positive defocus (upwards for an upright microscope) – images 1-7,
- close to zero in focus – image 8, and
- strong but reversed, to positive for negative defocus (downwards) – images 9-15.

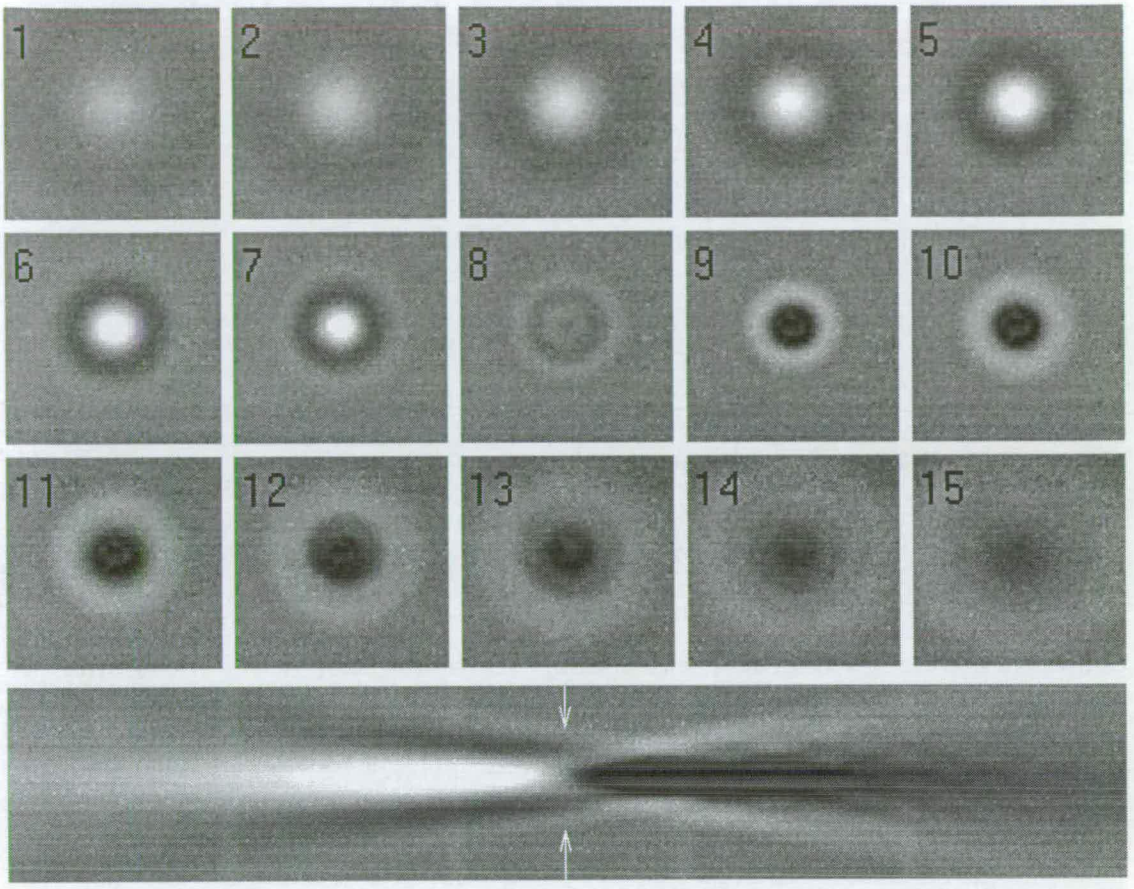

Figure 3.1: Bright-field images ($\mathcal{A} = 1.25$) of a single PMMA sphere, radius $R_p = 536 \pm 7$ nm, refractive index $n_p = 1.49$, in decalin, $n_m = 1.47$. The top 15 images (field of view 4.5 μm $\times$ 4.5 μm) form a series at varying degrees of defocus: 1.0 μm of forward axial (focusing) movement separate successive images, with 8 being in focus. The bottom image is a composite of 1 pixel-wide slices across the centre of 361 images like the above series, but with each separated by 0.05 μm; this gives a quasi-side-on view and makes the contrast reversal clear: image 8 of the upper series is at the line indicated by the arrows.

While naïf contrast *increasing* – as employed in figure 3.1 – does not work with bright-field images of phase objects, converting phase differences into contrast variations is possible. Two techniques suited to colloidal microscopy are phase contrast and differential interference contrast. These both involve optical operations at the objective exit pupil, so, in the next two sections, the imaging system shall be considered to be the objective alone.

3.2 Phase contrast microscopy

The phenomenon of phase contrast was discovered by Frits Zernike, who applied it to the testing of telescope mirrors [Zernike, 1934], before turning to microscopy [Zernike, 1935, 1942a,b]. His discovery won him the 1953 Nobel Prize for Physics, and his address at the award ceremony [Zernike, 1964] is a good overview of the principles and practice of this technique.

3.2.1 Zernike's principle

For a very weak amplitude/weak phase object only small perturbations to the illuminating wavefront occur and we can consider the light behind the object to consist of a **direct wave**, which is the unperturbed version of the wavefront, and a much weaker **diffracted wave**, which consists of all the perturbations. All the object information is contained in the diffracted wave, but interference between the two waves at the image results in the object information being swamped in bright-field microscopy.

> Phase contrast works by introducing a phase shift ψ to the direct wave, and attenuating it to a (real) fraction Υ, at a point where the two waves can be spatially separated, before they reach the image.

This phase shift and attenuation has the effect of turning small phase differences into large amplitude (or intensity) differences.

We can represent this technique quantitatively in a number of ways: a phasor representation is perhaps easier to visualize, whereas a Fourier representation emphasizes ties in more closely with diffraction theory.

3.2.2 Fourier representation

In phase microscopy $\psi = \pm\frac{\pi}{2}$ is usual; for mathematical transparency, we will consider just this case here, leaving more general phase shifts to the phasor treat-

ment below, where they can be more easily apprehended. For simplicity, we will also take all magnifications to be unity, so that the Fourier transforms between field and illumination planes will not require scaling.

For a phase object, the transmission function is of the form

$$\tau(x,y) = e^{\imath\varphi(x,y)}, \tag{3.2}$$

where φ is the phase shift caused by the object.

For a weak phase object, we can make the first order approximation

$$\tau(x,y) \simeq 1 + \imath\varphi(x,y). \tag{3.3}$$

Letting $u_-(x,y)$ and $I_- = u_-\, u_-^*$ be the amplitude and intensity distributions just in front of the object, we get

$$u(x,y) \simeq u_-(x,y) + \imath\varphi(x,y)u_-(x,y), \tag{3.4}$$

just behind the object. So, in words, the transmitted light can be considered as an unperturbed part and a phase shifted part, the first and second terms on the right-hand side of 3.4 corresponding to the direct and diffracted waves respectively.

At the objective exit pupil, $u'_p = \mathcal{F}\{u\}$, giving

$$u'_p \simeq \mathcal{F}\{u_-\} + \mathcal{F}\{\imath\varphi u_-\}. \tag{3.5}$$

Note that the linearity of Fourier transforms means that the direct and diffracted parts remain separate.

For coherent Köhler illumination, $u_- = \mathcal{F}\{\tau_{\mathsf{AS}}\}$, where "AS" refers to the (condenser) aperture stop. Fourier transforming twice just inverts the original function, so the first term on the right-hand side of equation 3.5 is just the image of the aperture stop, as expected.

Coherent illumination requires τ_{AS} to be non-zero over a very limited spatial extent, so its image at the objective exit pupil will also occupy only a small proportion of the area of the pupil. By placing a phase plate in the pupil, which

introduces a phase shift ψ and an attenuation Υ at the image of the aperture stop, we can achieve our desired manipulation of the direct wave.

A phase shift of $\pm\frac{\pi}{2}$ corresponds to multiplication by $\pm\imath$, so, applying this to the direct beam term, we get

$$u'_{\mathcal{P}} \simeq \pm\imath\Upsilon\tau_{\mathsf{AS}} + \mathcal{F}\{\imath\varphi u_-\}. \tag{3.6}$$

Fourier transforming again, to get the image, we have

$$u' \simeq \mp\imath\Upsilon u_- - \imath\varphi u_- = \mp\imath u_-(\Upsilon \pm \varphi) \tag{3.7}$$

and

$$I' \simeq I_-(\Upsilon \pm \varphi)^2. \tag{3.8}$$

With small φ, we can ignore terms quadratic in it, so

$$I' \simeq I_-(\Upsilon^2 \pm 2\varphi\Upsilon). \tag{3.9}$$

Finally, the background intensity I'_0 is given by the attenuated intensity of the direct wave $\Upsilon^2 I_-$, so we arrive at an expression for contrast,

$$C'(x', y') = \mp\frac{2}{\Upsilon}\varphi(x', y'). \tag{3.10}$$

Thus we have contrast proportional to phase differences due to the object; in other words, we have **phase contrast**. The inversion in the sign of the contrast compared to ψ reflects the more general result (see equation 3.20), that

- If φ and ψ have the same sign, we get negative phase contrast.
- If φ and ψ have opposite signs, we get positive phase contrast.

3.2.3 Phasor representation

Under this scheme, we treat the direct and diffracted waves as vectors rotating anticlockwise about their origin at an angular frequency given by $2\pi/\lambda_0$. These rotating vectors are what we mean by phasors.

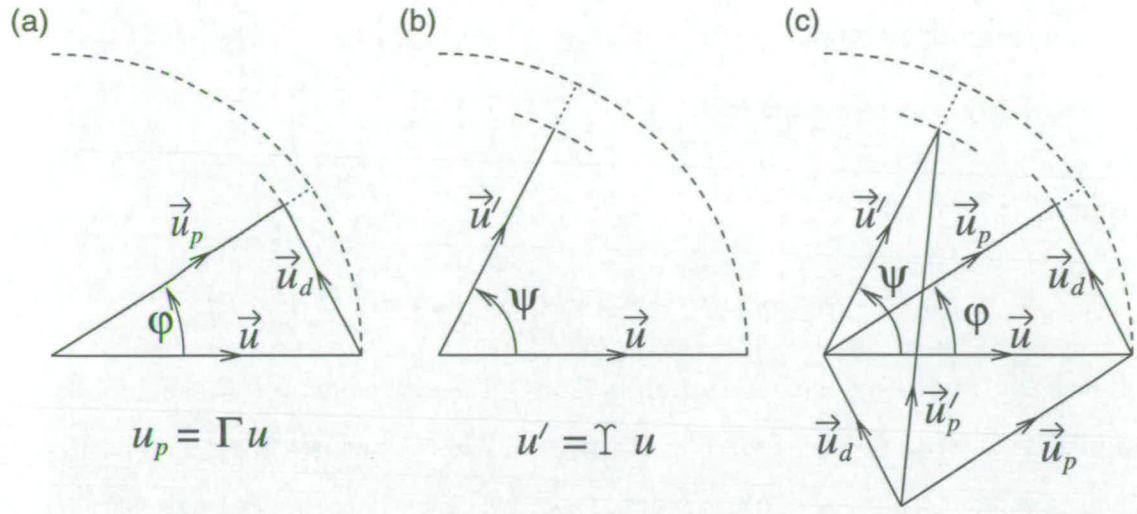

Figure 3.2: Phasor representation of phase contrast: (a) shows the perturbed wave $\vec{u}_p$, attenuated by Γ and phase shifted by φ by the object, as the resultant of the unperturbed direct wave $\vec{u}$ and the diffracted wave $\vec{u}_d$; (b) shows the effect on the direct wave $\vec{u}$ of attenuating by Υ and phase shifting by ψ; (c) shows the resultant wave $\vec{u}'_p$, as the sum of the diffracted wave $\vec{u}_d$ and the altered direct wave $\vec{u}'$.

Here we will consider the general case of an object that attenuates the amplitude of its illumination to a fraction Γ, as well as adding a phase shift φ. If we $\vec{u}$, $\vec{u}_d$, and $\vec{u}_p$ for the direct, diffracted and resultant waves, so that $\vec{u}_p = \vec{u} + \vec{u}_d$ we have

$$\vec{u}_p = \Gamma\, e^{\imath\varphi}\, \vec{u}. \tag{3.11}$$

This is represented in figure 3.2(a).

If we introduce a phase shift ψ to the direct wave and attenuate it to a fraction Υ (as before), then, using $\vec{u}'$ to represent the altered direct wave, we have

$$\vec{u}' = \Upsilon\, e^{\imath\psi}\, \vec{u}. \tag{3.12}$$

This is represented in figure 3.2(b).

The resultant wave will now be given by $\vec{u}'_p = \vec{u}' + \vec{u}_d$, with the image intensity $I' = |\vec{u}'_p|^2$. Figure 3.2(c) shows the whole scheme. By means of trigonometry*,

*see Appendix A.2

we can use this diagram to get

$$I' = I_- \left(1 + \Upsilon^2 + \Gamma^2 + 2\Upsilon\Gamma\cos(\psi - \varphi) - 2\Upsilon\cos\psi - 2\Gamma\cos\varphi\right). \tag{3.13}$$

Now $I'_0 = \Upsilon^2 I_-$, so

$$C' = \frac{2}{\Upsilon^2}\left(\Upsilon\cos\psi + \Gamma\cos\varphi - \Upsilon\Gamma\cos(\psi - \varphi) - \frac{1}{2}\left(1 + \Gamma^2\right)\right). \tag{3.14}$$

Phase contrast was developed for objects with Γ nearly constant; for such objects, and a given phase plate, *i.e.*, Υ and ψ are constants, we have contrast as a linear function of a combination of $\sin\varphi$ and $\cos\varphi$, which we can see if we write equation 3.14 as

$$C' = \left[\frac{2\cos\psi}{\Upsilon} - \frac{1+\Gamma^2}{\Upsilon^2}\right] + \left[\frac{2\Gamma\left(1 - \Upsilon\cos\psi\right)}{\Upsilon^2}\right]\cos\varphi - \left[\frac{2\Gamma\sin\psi}{\Upsilon}\right]\sin\varphi. \tag{3.15}$$

For objects with $\Gamma \approx 1$, such as many colloidal suspensions, this reduces to

$$C' = \frac{2}{\Upsilon^2}\left(\Upsilon\cos\psi - 1\right)\left(1 - \cos\varphi\right) - \frac{2}{\Upsilon}\sin\psi\sin\varphi. \tag{3.16}$$

From this, we can see that contrast, being zero at $\varphi = 0$ and of opposite sign on either side of this, will go to zero and reverse in sign again at $\frac{1-\cos\varphi}{\sin\varphi} = \frac{\Upsilon\sin\psi}{\Upsilon\cos\psi - 1}$. The region between these successive zeroes of contrast is known as the **region of unreversed contrast**. For an image to be unambiguous, one needs to ensure that contrast does not reverse more than once in a single image (or set of images, if several are to be compared); however, for no object information to be lost, it is better to ensure that contrast goes to zero only for $\varphi = 0$, *i.e.* to remain in the region of unreversed contrast.

A typical phase plate will have $\psi = \pm\frac{\pi}{2}$ and $0.3 \lesssim \Upsilon \lesssim 0.5$. For $\psi = \pm\frac{\pi}{2}$, equation 3.16 further reduces to

$$C' = \frac{2}{\Upsilon^2}\left(\cos\varphi - 1\right) \mp \frac{2}{\Upsilon}\sin\varphi. \tag{3.17}$$

This gives zeroes of contrast at

$$\varphi = 0 \text{ and } \mp 2\arctan\Upsilon \quad \text{when} \quad \psi = \pm\frac{\pi}{2}. \tag{3.18}$$

So, contrast will be positive for $-2\arctan\Upsilon < \varphi < 0$ and negative for the rest of the 2π domain of φ, if $\psi = +\frac{\pi}{2}$, but positive for $0 < \varphi < 2\arctan\Upsilon$ and negative otherwise, if $\psi = -\frac{\pi}{2}$.

The maximum positive and negative contrast values, C'_{+max} and C'_{-max}, will occur at the midpoints of their respective domains $\varphi = \mp\arctan\Upsilon$ and $\varphi = \mp(\pi - \arctan\Upsilon)$. These contrast values are given by

$$C'_{+max} = \frac{2}{1+\sqrt{1+\Upsilon^2}} \quad \text{and} \quad C'_{-max} = \frac{2}{1-\sqrt{1+\Upsilon^2}}. \tag{3.19}$$

For fairly weak phase objects, with $|\varphi| < \frac{\pi}{2}$, the region of unreversed positive contrast is the one containing the accessible maximum contrast.

It may be readily seen from the expression for C'_{+max} and the value of φ at that maximum that the smaller the value of Υ, the better the maximum contrast and the smaller the value of φ to achieve it. Obviously, the smaller φ is, the smaller Υ needs to be, if we are to get the best contrast conditions (given that $\Gamma \approx 1$). What also follows is that Υ should not be too small, if contrast is to remain unreversed.

This may be understood by considering that the amplitude of the diffracted beam is small, when $\Gamma \approx 1$, so a small value of Υ will bring the amplitude of the direct beam down to a value comparable with that of the diffracted beam, making for more efficient interference.

In the case of weak phase objects, where φ is small, equation 3.16 further reduces to

$$C' = -\frac{2}{\Upsilon}\varphi \sin\psi. \tag{3.20}$$

So we have the case that phase contrast is negative if φ and ψ have the same sign, but positive if φ and ψ have opposite signs, as mentioned earlier, in connection with equation 3.10 ($C' = \mp\frac{2}{\Upsilon}\varphi$), which is what equation 3.20 finally reduces to for $\psi = \pm\frac{\pi}{2}$.

A full treatment of the effects on phase contrast of varying Υ and ψ for objects with varying Γ and φ in terms of phasors is given in Barer [1952a,b, 1953a,b].

3.2.4 Setting up phase contrast microscopy

Coherence requirements

Phase contrast clearly requires a high degree of coherence between the direct and diffracted waves; furthermore, Köhler illumination is essential (to allow manipulation of the illumination at the objective exit pupil and the condenser aperture stop). On the other hand, for good resolution and bright images, a large numerical aperture of the objective needs to be illuminated and the open area of the aperture stop cannot be too small.

Conjugate annuli

The best compromise for these conditions [Françon, 1954] is to illuminate with an annular condenser aperture stop and, conjugate with it, an annular phase ring in the objective exit pupil. Annular illumination allows a high degree of coherence with a relatively large aperture. Figure 3.3 shows the annular illumination, the

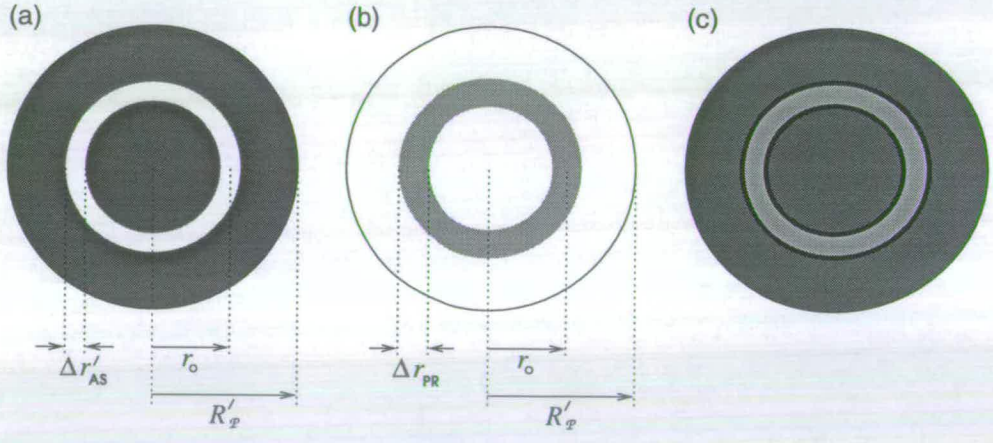

Figure 3.3: Conjugate annuli in phase contrast microscopy: images in the objective exit pupil, radius R'_p, of (a) the annular condenser aperture stop, radius r_o, width $\Delta r'_{AS}$, (b) the phase ring, radius r_o, width Δr_{PR} and (c) the combined image.

phase ring and the two combined, as seen at the objective exit pupil; this view can be obtained by removing the ocular and looking down the microscope tube.

The dimensions of a typical phase ring are chosen such that $\Delta r_{PR} \approx 1.25\Delta r'_{AS}$ and $2\pi r_o \Delta r_{PR} \approx 0.1\pi {R'_p}^2$ [Pluta, 1989, §5.2].

Phase objectives

Modern phase rings consist of a thin dielectric film – to add the phase shift – and a thin metallic film – for attenuation – mounted directly on top of one another on a flat glass plate. This plate will form a permanent part of the compound objective, meaning that special phase contrast objectives are required for this technique. Phase objectives can be readily identified, as the phase ring is clearly visible if the objective is viewed through its exit pupil; moreover, the objective will have "Ph" inscribed on its outer case, the international convention being that the lettering on phase objectives is green – further assisting identification.

Objectives of different numerical aperture will have different sized phase rings, indicated by the number after the "Ph". It is obviously important that the image of the aperture stop matches this, so different annular apertures are required for the condenser; these are likewise identified "Ph1", "Ph2" *etc.*, and must be carefully centred to match up with the phase ring, as shown in figure 3.3(c). This must always be checked when using phase contrast.

3.2.5 Phase contrast images of colloids

Figure 3.4 shows a series of images of a single colloidal sphere at varying degrees of defocus. These images have had their contrast digitally enhanced, to show the out-of-focus images more clearly. The major difference between these images and those of figure 3.1 is immediately clear: The focused image has the strongest contrast, with out-of-focus contrast reversals being very weak.

To explain the focused image we need to use the fact that the phase shift φ of light, wavelength λ_0, crossing the diameter $2R_p$ of a sphere of refractive index n_p in a liquid of refractive index n_m is given by

$$\varphi = \frac{2\pi}{\lambda_0}(n_m - n_p)\,2R_p. \tag{3.21}$$

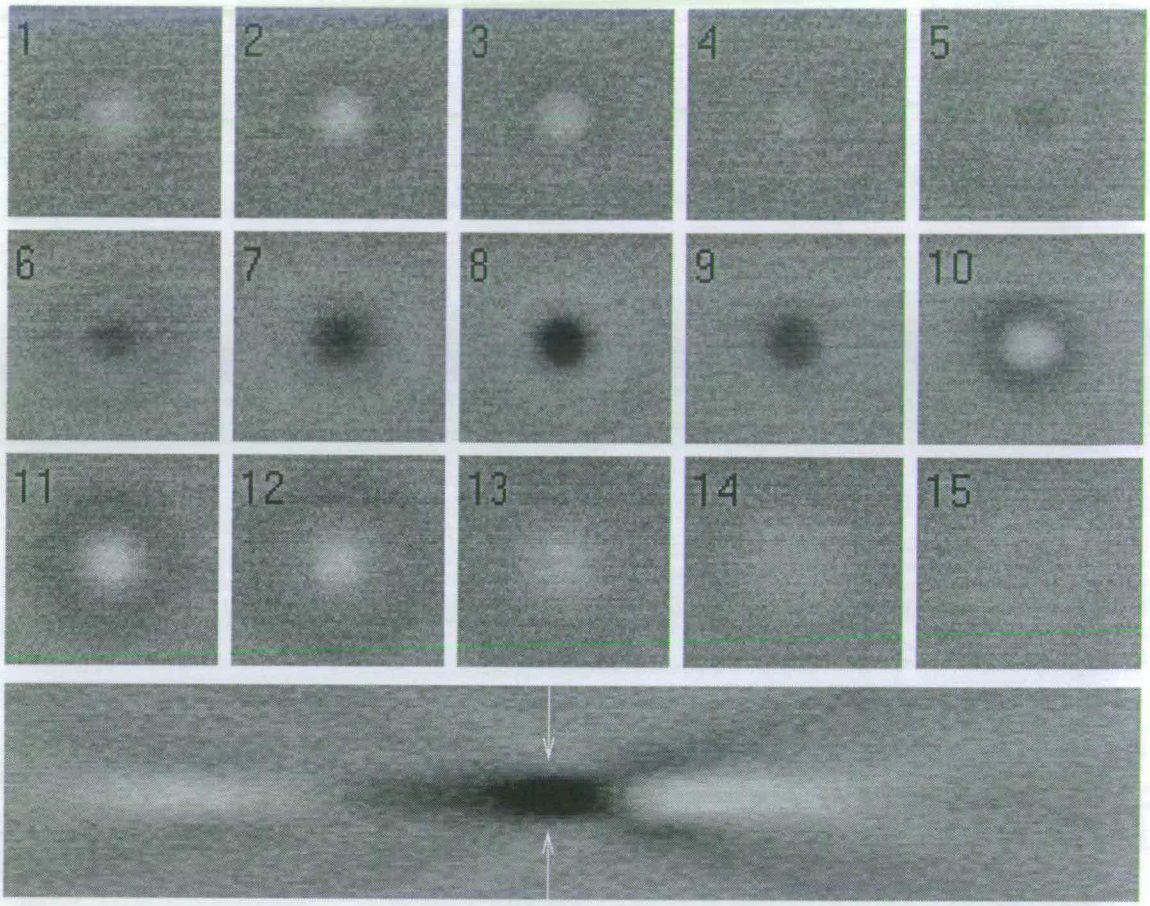

Figure 3.4: Phase contrast images ($\mathcal{A} = 1.4$, $\psi = +\frac{\pi}{2}$) of a single PMMA sphere, radius $R_p = 550 \pm 7$ nm, refractive index $n_p = 1.49$, in decalin, $n_m = 1.47$. The top 15 images (field of view 4.3 μm $\times$ 4.3 μm) form a series at varying degrees of defocus: 1.0 μm of forward axial (focusing) movement separate successive images, with 8 being in focus. The bottom image is a composite of 1 pixel-wide slices across the centre of 165 images like the above series, but with each separated by 0.11 μm; this gives a quasi-side-on view; image 8 of the upper series is at the line indicated by the arrows.

For the sphere in figure 3.4, this gives us $\varphi = -0.075\pi$ radians. Although Υ is not known for this objective, equations 3.17 and 3.18 show that the range $-0.075\pi < \varphi < 0$ would give unreversed positive contrast for $\Upsilon > 0.12$, which is very likely to be true. The fact that the contrast across the in-focus image of the sphere remains positive concurs with this prediction.

Figure 3.4 shows that out-of-focus images can show reversed contrast, but, as

long as all in-focus information is within the region of unreversed contrast, these need not cause confusion in digitally recorded images, as areas of reversed contrast can simply be set to the value of the background. Figure 3.5 demonstrates the

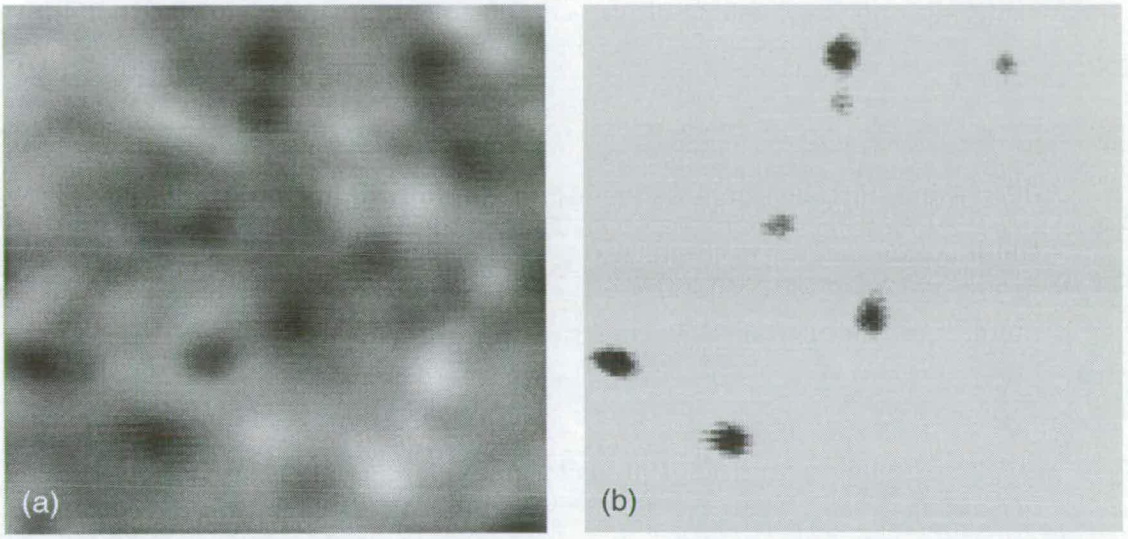

Figure 3.5: Phase contrast: (a) image of a low density suspension of 1 μm spheres, with grey scale values both above an below the background value, in this case 40; (b) the same image after processing by setting all brighter pixels to the background value and enhancing the contrast, the four in-focus spheres showing up very clearly.

effectiveness of this simple procedure for low density suspensions. Techniques such as this are the subject of §3.4.

Disadvantages of phase contrast

Figure 3.4 also shows one of the inherent adverse features of phase contrast, *viz.* the bright **halo**, which can just be made out around the in-focus sphere in image 8. This region of reversed contrast, and the related **shading-off** – loss of contrast – across the middle of the sphere (which is too weak to be detectable here), is due to the fact that some of the diffracted beam will pass through the phase ring. Zernike discusses this matter in his Nobel lecture [Zernike, 1964], making the point that the choice of a phase plate with circular symmetry means that the halo will be isotropic, at least.

The degree to which halo and shading off are problems depends on the properties of the phase ring – r_o, Δr_{PR}, $\Delta r'_{AS}$ and Υ, the object – φ and R_p, and the magnification – $\mathcal{M}$. The phase ring parameters are normally fixed, and modern research-grade microscopes have these chosen to minimize haloing and shading-off. As far as the microscopist is concerned, what needs to be known [Pluta, 1989, §5.3.1] is that

1. decreasing particle size broadens the halo, but diminishes the intensities of the halo and shading-off effect,
2. increasing the magnification has the opposite effects and
3. as long as it is within the region of unreversed contrast, increasing φ increases the halo width and intensity and shading-off intensity.

In practice, with colloidal suspensions, as can be seen from figure 3.4, these effects are not often a problem, the very small size of the particles being the main reason for this.

3.3 Normarski differential interference contrast microscopy

Differential interference contrast microscopy was first developed by Georges Normarski [1953, 1955]. Like phase contrast, this technique uses interference to generate intensity variations corresponding to phase differences. The particular advantage of DIC is that the optical sectioning is very good, which is to say that out-of-focus intensities drop off rapidly. For a fuller account than given here, see Chapter 7 of Pluta [1989] and Lang [1975].

3.3.1 The principle of differential interference contrast

In interference microscopy, two mutually coherent rays are typically used to form fringes. Any distortion or shifting of these fringes reveals phase differences due

the object. If the optical paths are set up so that a uniform object field gives only a single very broad fringe, *i.e.* an image intensity that varies only slightly across the image plane, phase changes will – generally – be shown by intensity changes. This is interference contrast.

Differential interference contrast (DIC hereafter) is achieved when both rays pass through the object, but with a lateral displacement e between them of less than the resolution ϱ of the optical system. For microscopy this means that $e \lesssim r_{\text{Airy}}$.

> The effect of DIC is to give intensity variations that are simple functions of the phase gradient along the line of the lateral displacement.

This generates images with a characteristic shadow-cast (see, *e.g.*, figure 3.9, where a single sphere appears lit from the top left of the image plane).

To arrive at expressions for image intensity and contrast, we must first consider the practical details of the DIC microscope.

3.3.2 The DIC microscope

The DIC microscope uses an arrangement of two polarizing filters and two birefringent "Wollaston" prisms[†] to split a single incident wavefront into two spatially-separated, non-interfering wavefronts passing through the object, then to recombine the two, such that the intensity of the final wave is a measure of the phase difference between the two paths taken through the object.

Figure 3.6 shows (a) the arrangement of these components, (b) the operation of the Wollaston prisms and (c) the orientation of the polarizing filters.

Two points should be noted concerning figure 3.6: First, diagrams (a) and (b) are not to scale. For clarity, the Wollaston prisms have been drawn much thicker

[†]Wollaston prisms – illustrated in figure 3.6(b) – consist of two right-angled wedges of a birefringent material such as quartz, cemented together so as to make a rectangular block. The optic axes of the two sections are cut to be perpendicular to one another in the composite prism.

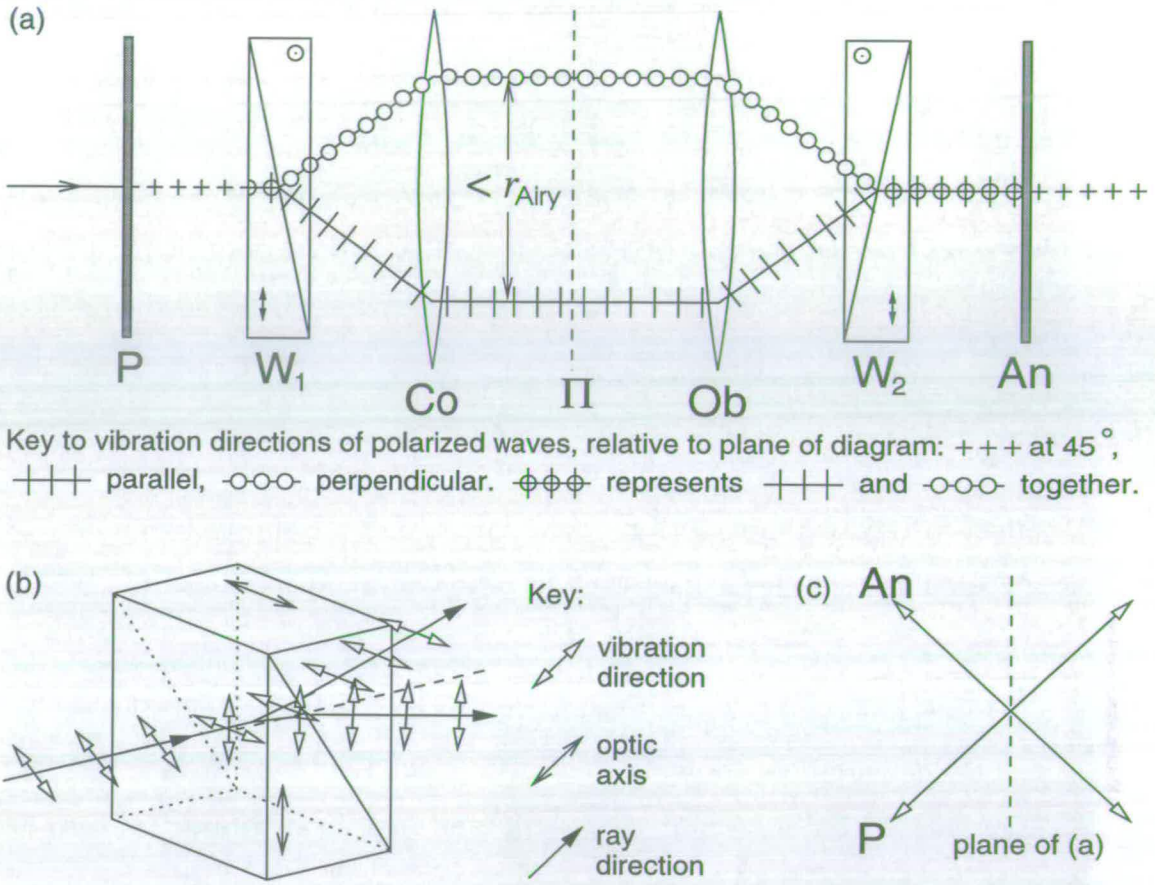

Figure 3.6: (a) The special components of the DIC microscope: a polarizer P, a Wollaston prism W_1 at the front focal plane of the condenser Co, another Wollaston prism W_2 at the back focal plane of the objective Ob and a second polarizing filter, the analyser A. (b) The operation of a Wollaston prism *viz.*, angular beam splitting (c). The vibration azimuths of P and A, as viewed along the optical axis.

in the axial direction than those used in microscopy, which are just thin plates. This has meant that the angular and lateral separations of the two rays shown are correspondingly exaggerated.

Secondly, in general, DIC microscopy does not require the polarizer and analyser to be crossed, as drawn. For pure phase objects, such as colloidal suspensions, however, the best contrast is achieved with this arrangement and this is the one considered in the analysis below.

The operation of the DIC microscope is as follows:

1. The polarizer P directs light linearly polarized at 45° to the optic axis of the front wedge of the first Wollaston prism W_1.

2. The front wedge of W_1 splits the light into two wavefronts, of equal intensity and polarized orthogonally to one another and at 45° to the vibration direction of the light incident on the prism. Being birefringent, the wedge has different refractive indices for the two vibration directions, so that the two waves will propagate at slightly differing velocities.

3. These two waves refract in opposite directions at the interface between the two wedges of W_1, because the fact that the optic axis of the back wedge is perpendicular to that of the front means that refractive indices for the two vibration directions swap over from what they were in the front wedge. When the two diverging waves emerge from the back surface of the prism, they will have a phase difference which depends upon the relative path lengths through the two halves of the prism. Rays originating from light incident on the mid-point of the Wollaston prism will be in phase, and those originating from either side will have increasing phase differences, of opposite sign on the two sides.

4. W_1 being sited such that the virtual point from which the two waves are diverging (see figure 3.8(a)) is at the front focal plane of the condenser, the effect of the condenser is bring the two wavefronts into parallel propagation, with a small lateral shift, somewhat less than the resolution of the microscope. Note that figure 3.6 greatly exaggerates both the angular and spatial separation of the two waves, for the sake of clarity.

5. Having passed through the object, the objective turns the lateral shift into an angular convergence of the wavefronts, the virtual centre of convergence being at the back focal plane of the objective.

6. The second Wollaston prism W_2, being situated at the objective back focal plane, brings the two wavefronts back into alignment. Each now propagates

just as the original light would have, in the absence of the prisms. W_2 also affects the phase relationship between the two wavefronts: if W_2 is perfectly laterally aligned with W_1, then the phase shifts due to the two prisms cancel out, right across the wavefronts, and only the phase differences introduced by the object remain. However, the final image may often be improved by laterally displacing W_2 and thereby introducing an additional phase difference δ, known as the bias, which is constant across the wavefront.

7. Finally, the second polarizing filter – the analyser An – resolves the two wavefronts along the same vibration direction, allowing them to interfere to form the intermediate image, which is observed in the normal way.

Under this scheme, images will appear as if two slightly displaced images have been superimposed. With a mid-grey background (the bias, incidentally, controls the background colour), one of these two images will appear dark and one bright. This gives the impression that the object has been lit from the side, the shear direction being the direction of the apparent illumination (see figure 3.9 for the appearance of a spherical object).

To determine an expression for image intensity and contrast for DIC, I will return to the phasor approach used previously for phase contrast.

3.3.3 Phasor representation

Figure 3.7 shows the DIC process, as represented by phasors. In each of the three diagrams the two waves which interfere behind the analyser are represented by the phasors $\vec{u_1}$ and $\vec{u_2}$.

Because the polarizer azimuth is at 45° to the optic axes of the Wollaston prisms (see figure 3.6(c)), the amplitudes of $\vec{u_1}$ and $\vec{u_2}$ will be equal. With unpolarized illumination of intensity I_{II}, the intensity behind P will be half this. Taking the quadratic relationship between intensity and amplitude into account, we get $|\vec{u_1}| = |\vec{u_2}| = \frac{1}{2}\sqrt{\frac{I_{II}}{2}}$, for a transparent object.

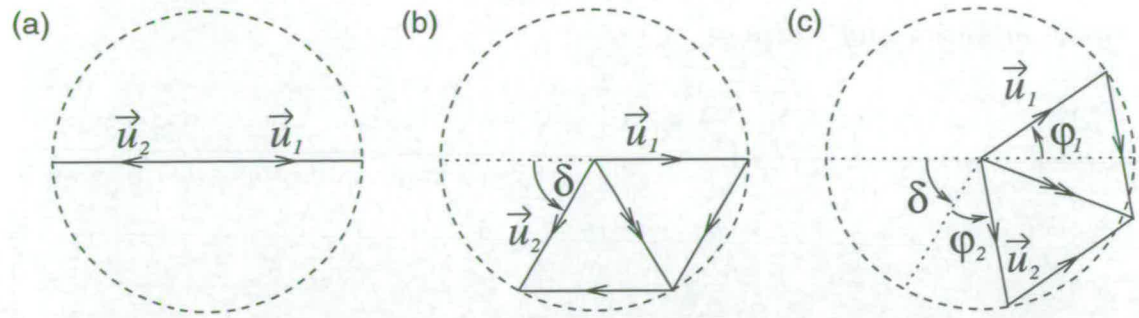

Figure 3.7: Phasors in DIC (a) Without object or bias phase shifts, (b) with a bias δ (c) with bias δ and phase shifts φ_1 and φ_2.

Background intensity

When neither an object nor a bias is present, as in figure 3.7(a), the effect, in terms of phasors, of P and An being crossed is to have $\vec{u_1}$ and $\vec{u_2}$ in antiphase. Being of equal amplitude, they will cancel out and the resultant intensity will be zero. So the background intensity for zero bias and crossed polars is zero, as one might expect.

The background intensity for crossed polars and nonzero bias can be determined with reference to figure 3.7(b), where the bias δ is added to one or other of the two waves. It is a matter of simple trigonometry to show that

$$I_0' = \frac{I_{II}}{4}(1 - \cos\delta) = \frac{I_{II}}{2}\sin^2\left(\frac{\delta}{2}\right). \tag{3.22}$$

For monochromatic illumination, equation 3.22 shows that any desired background intensity, up to half intensity of the illumination can be achieved by adjusting the lateral alignment of the two Wollaston prisms.

With white light illumination, the range of wavelengths present means that $I_0' = 0$ can only be achieved for $\delta = 0$. For increasing bias the Newton sequence of (reflected light) interference colours is seen[‡].

[‡]These colours are often referred to as Michel Lévy interference colours, after the mineralogists' colour chart that bears that name.

Image intensity and contrast

Figure 3.7(c) shows the situation with phase shifts φ_1 and φ_2 – due to the object – applied to $\vec{u_1}$ and $\vec{u_2}$ respectively. Once again, the application of simple trigonometry leads to an expression for intensity:

$$I' = \frac{I_{II}}{4}\left(1 - \cos\left(\delta + \varphi_2 - \varphi_1\right)\right) \tag{3.23}$$

$$= \frac{I_{II}}{2}\sin^2\left(\frac{\delta}{2} + \frac{\varphi_2 - \varphi_1}{2}\right). \tag{3.24}$$

With no bias, and small $\varphi_2 - \varphi_1$, DIC will therefore give $I' = I_{II}(\varphi_2 - \varphi_1)^2/8$. Thus small variations in refractive index along the direction of the lateral shift e will show up clearly on the dark background. What should be noted though, is that the sign of $\varphi_2 - \varphi_1$ is ambiguous under zero bias, meaning that objects will appear to be lit from two opposing directions, which can be rather confusing.

On the other hand, for $\delta = \frac{\pi}{2}$, we get

$$I' = \frac{I_{II}}{2}\left(1 + \sin\left(\varphi_2 - \varphi_1\right)\right). \tag{3.25}$$

In this case, we can use equation 3.1 to obtain an expression for contrast:

$$C' = \sin\left(\varphi_1 - \varphi_2\right). \tag{3.26}$$

So, for small $\varphi_2 - \varphi_1$, DIC gives contrast equal to the phase gradient along the lateral shift direction, with the contrast reversing for opposite signs of gradient. This is why one side of an object will appear dark and the other side bright.

With white illumination, $\delta = \frac{\pi}{2}$ can only be achieved for a single wavelength by a given bias. However, a path difference of 150 nm is close enough to $\frac{\lambda_0}{4}$ for most optical wavelengths to provide a grey-blue background with contrast behaviour approximating equation 3.26. This value of bias gives contrast that is suitable for a monochrome CCD camera and is also amenable to observation by eye.

With full colour observation, setting the bias so that the background is purple – corresponding to a path difference of 565 nm – clearly shows up small phase

differences as red or blue, depending on their sign (this behaviour is what gives this interference colour – first order purple – the description "sensitive tint").

In summary:

DIC gives images with a side-lit appearance, the strength of the side-lighting being controlled by the bias δ:

- With $\delta = 0$, crossed polars give a black background and lighting from two opposing directions.
- With $\delta = \pm\frac{\pi}{2}$, the background is grey and lighting is from a single direction. This gives the best contrast for monochrome images.

3.3.4 Normarski's modifications

To achieve the uniform background to DIC images, the lateral displacement between the two waves traversing the object, that is generated by the combination of W_1 and the condenser, must be perfectly cancelled out by the action of the objective and W_2.

As described above, this calls for W_1 and W_2 to be situated at the front and back focal planes of the condenser and objective respectively.

Figure 3.8(a) demonstrates why this is the case: The angular divergence which a Wollaston prism generates can be traced back to a plane within the Wollaston prism. This plane – traced by a dashed line in the diagram – is where interference fringes can be seen if a single Wollaston prism is placed between crossed polars[§]. For proper operation of the DIC microscope, this plane needs to coincide with the front focal plane of the condenser for W_1 and the back focal plane of the objective for W_2.

A problem arises, however, with high numerical aperture objectives: the back

[§]As in figure 3.6, the prisms in figure 3.8 are shown to be much thicker than they are in practice. This means that the small angle that the plane of the interference fringes is shown to be at, with respect to the plane of the prism, is even smaller in reality.

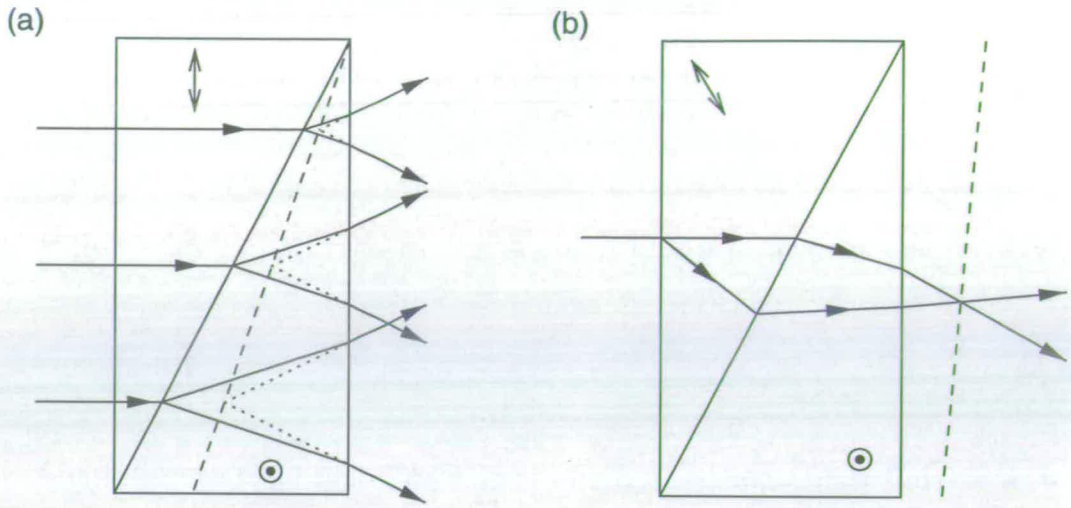

Figure 3.8: (a) A standard Wollaston prism, showing the plane of interference fringes (dashed line) (b) Normarski's modification of the Wollaston prism: the optic axis of one half is set at an angle to the plane of the front surface, moving the plane of the interference fringes outside the prism.

focal plane usually lies within the casing of the compound lens, making the siting of a Wollaston prism at that point impractical. Normarski's solution to this problem was to cut modified Wollaston prisms, with the optic axis in one half slightly tilted, as in figure 3.6(b). This has the effect of moving the plane of the interference fringes outside the prism, so that the prism itself can be sited outwith the confines of the objective housing.

3.3.5 Normarski DIC images of colloids

Figure 3.9 shows a series of images of a single colloidal sphere at varying degrees of defocus, analogous to the series of figures 3.1 and 3.4. Once again, contrast has been digitally enhanced, to show the out-of-focus images more clearly. As with phase contrast, and unlike bright field, the in-focus image has the strongest contrast.

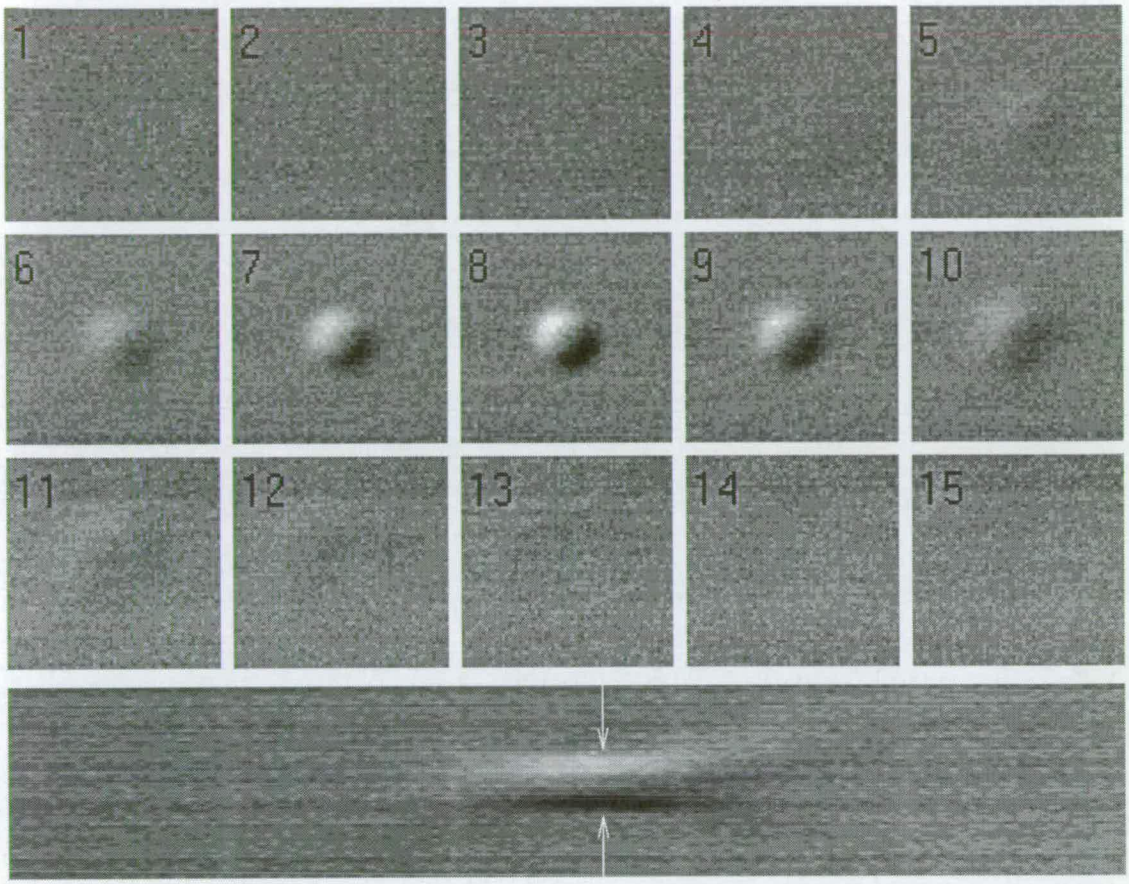

Figure 3.9: Normarski differential interference contrast images ($\mathcal{A} = 1.4$, $\mathcal{A}_C = 0.9$) of a single PMMA sphere, radius $R_p = 550 \pm 7$ nm, refractive index $n_p = 1.49$, in decalin, $n_m = 1.47$. The images (field of view $4.3\ \mu\text{m} \times 4.3\ \mu\text{m}$) form a series at varying degrees of defocus: $1.0\ \mu$m of forward axial (focusing) movement separate successive images, with 8 being in focus. The bottom image is a composite of 1 pixel-wide slices across the centre of 165 images like the above series, but with each separated by $0.11\ \mu$m; this gives a quasi-side-on view; image 8 of the upper series is at the line indicated by the arrows.

The azimuth effect

Because DIC images can only show phase variations along a particular direction, *viz.*, the direction of the lateral shear e, the contrast variations along lines across the image at different azimuths (about the optical axis) will be different, even for objects which are circularly symmetric about axes parallel to the optic axis. This is called the azimuth effect and it manifests itself in the characteristic side-lit

appearance of DIC images.

The images in figure 3.9 were recorded with $\delta = \frac{\pi}{2}$, giving a grey background and making the sphere appear to be lit from the upper left. The in-focus image is contained within a roughly elliptical shape, angled at 45° to the edges of the figure. The azimuth of its semi-major axis is the same as the shear azimuth. Likewise, the line joining the brightest point in the image with the darkest is along this azimuth.

With objects that have circular symmetry this effect is usually no problem, but features of an object perpendicular to the shear azimuth are poorly imaged by DIC. This disadvantage can be overcome by comparing DIC and phase contrast images of the same object. Alternatively, rotating the object about the optical axis of the microscope, where this is possible, will allow features at all azimuths to be observed clearly.

Modelling the DIC image of a transparent sphere

To calculate the ideal DIC image of a weak phase object when the bias $\delta = \frac{\pi}{2}$, so that the small φ approximation of equation 3.26 holds, all that is needed is to determine what shape a plane wavefront normally incident on the object becomes behind the object, take two of these shapes, shift one by e and subtract them from each other. The shape of the result will be the same as the intensity profile of the image.

Solving the wavefront problem for a transparent sphere is not easy, but the following simple model produces results very similar to those recorded experimentally.

Figure 3.10 shows a transparent sphere, radius R_p, refractive index n_p, in a liquid of refractive index n_m, illuminated by a collimated beam, represented by the plane wavefront Σ.

Arrow 1 shows a ray traversing the diameter of the sphere and arrow 2 is a ray which is not incident on the sphere. Arrow 3 represents no physical ray, but

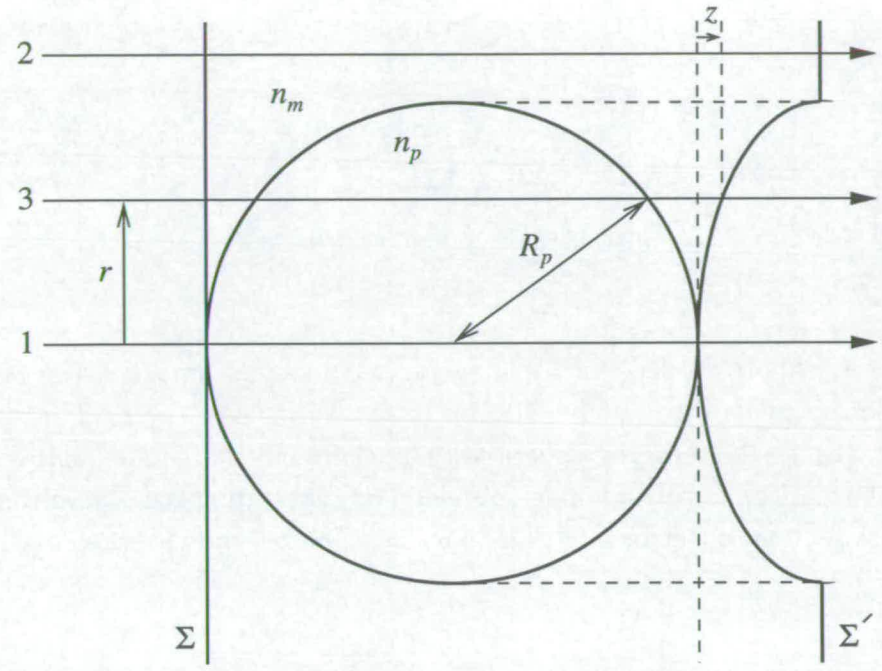

Figure 3.10: A transparent sphere illuminated by a plane wavefront Σ. A naïf consideration of optical path lengths along lines parallel to the incident direction suggests an elliptical wavefront Σ' behind the sphere.

simply a straight line parallel to rays 1 and 2 at a distance r from ray 1.

Ray 1 will undergo a phase shift of $\frac{4\pi}{\lambda_0} R_p n_p$ as it traverses the sphere. Ray 2 will travel a distance $2R_p + \frac{2R_p(n_p - n_m)}{n_m}$ for the same phase shift as ray 1. To achieve the same optical path length along arrow 3, a distance of $2R_p + z$ is needed, where

$$z = \frac{2(n_p - n_m)(R_p - \sqrt{R_p^2 - r^2})}{n_m}. \tag{3.27}$$

Given that $z(0) = 0$ and $z(R_p) = \frac{2R_p(n_p - n_m)}{n_m}$, using equation 3.27 as a putative equation for the shape of Σ' suggests itself.

This equation can be rearranged to give

$$\left(1 - \frac{z n_m}{2R_p(n_p - n_m)}\right)^2 + \frac{r^2}{R_p^2} = 1, \tag{3.28}$$

which, in cylindrical polar coordinates, is the equation of an ellipsoid of revolution (about the z axis).

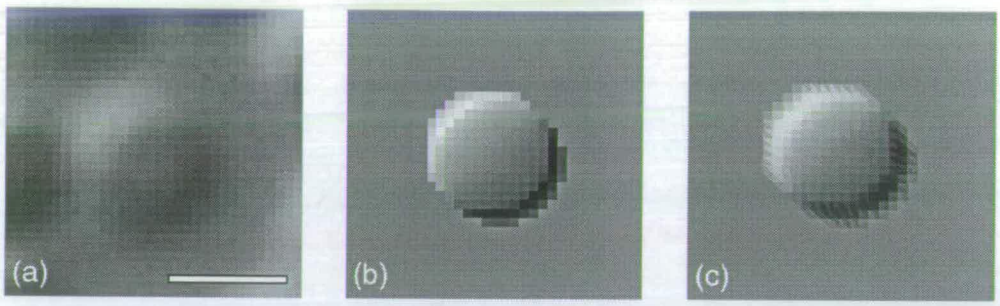

Figure 3.11: A simple model of DIC imaging (a) Recorded image ($\mathcal{A} = 1.4$) of colloidal spheres, radius $R_p = 460 \pm 10$ nm, refractive index $n_p = 1.49$, in decalin, $n_m = 1.47$; (b) single recorded sphere with background and noise removed and contrast enhanced; (c) calculated image obtained by subtracting two "wavefronts" of elliptical cross-section, offset by $e = \frac{2}{7}(R_p + r_{\text{Airy}})$. The bar in (a) represents 1 μm.

In figure 3.11, the difference between two such ellipsoids, one displaced by e perpendicular to z and using $R_p + r_{\text{Airy}}$ (to match the predicted image size), instead of R_p, has been plotted with a grey scale to represent z values, giving an image strikingly similar to the recorded DIC image of a sphere. For the recorded image $r_{\text{Airy}} \approx 0.61 \frac{\lambda_0}{\mathcal{A}} \approx 260$ nm. The ratio $\frac{e}{R_p + r_{\text{Airy}}} = \frac{2}{7}$ was chosen for the calculation as this gave $e \approx 206$ nm $\lesssim r_{\text{Airy}}$ for $R_p + r_{\text{Airy}} = 720$ nm.

Why this method should work so well is unclear, as the straight lines traversing the sphere above do not correspond to physical rays, except for $r = 0$ and $r > R_p$. Effectively, this method ignores the angle of incidence of the wavefront on the sphere. However, a comparison of this method with the application of Snell's Law, in the case of an isosceles triangular prism shows very close agreement, up to an angle of incidence of about 60°. This would correspond to roughly 87% of the diameter of the sphere, so perhaps the approximation is justified, for the rough calculation of images, at least.

Determining the lateral shear e

The "roughly elliptical shape" of DIC image of an object with circular cross-section we can see to be a "stretched disc" which results from two overlapping

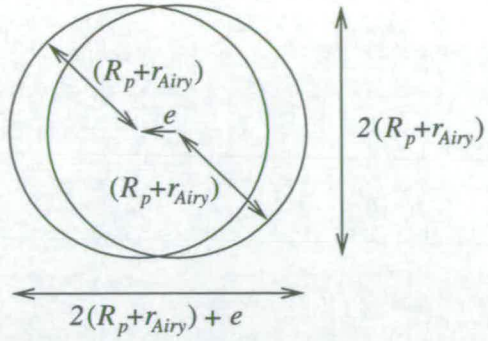

Figure 3.12: Determining the DIC lateral shear: the overlapping discs which form the image of an object with circular cross-section.

discs, each of radius $R_p + r_{\text{Airy}}$ and with the long axis of the resultant shape being parallel to the shear direction, as figure 3.12 shows. From this figure it is clear that the size of the DIC lateral shear e can be determined by measuring the difference between the length and the width of the "stretched disc".

In figure 3.11(a), the width $2(R_p + r_{\text{Airy}}) = 1340 \pm 130$ nm which agrees with the known particle radius (460 ± 10 nm) and $r_{\text{Airy}} \approx 260$ nm. The length $2(R_p + r_{\text{Airy}}) + e = 1540 \pm 130$ nm, so $e = 200 \pm 100$ nm $\lesssim r_{\text{Airy}}$, as expected.

The effect of condenser numerical aperture

DIC requires spatial coherence of illumination over a distance at least as large as the lateral shear e. As $e \lesssim r_{\text{Airy}}$, this coherence condition will always be met if the condenser numerical aperture is no bigger than the objective numerical aperture, *i.e.*, $\mathcal{A}_{\text{C}} \leq \mathcal{A}$.

For the best resolution, $\mathcal{A}_{\text{C}} \lesssim \mathcal{A}$ is best. Figure 3.13 illustrates the effects of reducing $\mathcal{A}_{\text{C}}$, *viz.*, an increased minimum distance of resolution and decreased optical sectioning. These effects can be seen particularly well in the sequences of decreasing $\mathcal{A}_{\text{C}}$ in (a) and (b), where the deterioration of the image is clear.

On the other hand, (c) shows how these same effects can produce a spurious improvement in image quality under certain circumstances: When trying to locate close-packed layers in a crystalline region, this may appear easier when $\mathcal{A}_{\text{C}}$ is

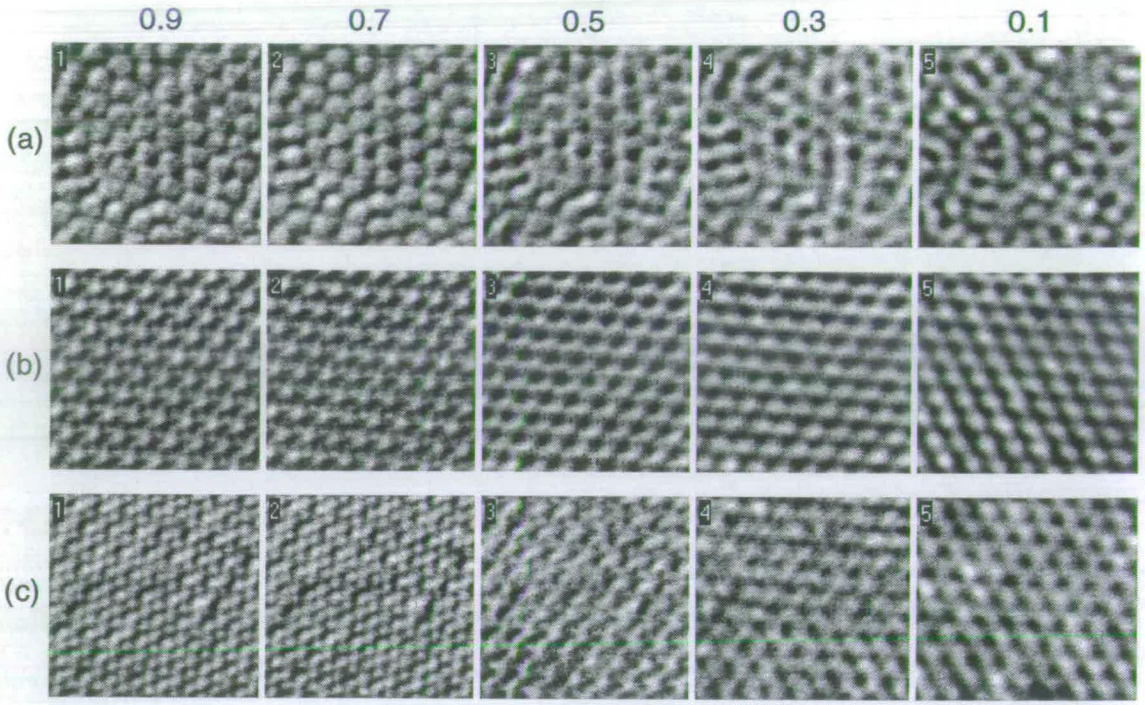

Figure 3.13: The effect of varying the condenser numerical aperture $\mathcal{A}_C$ on Normarski differential interference contrast images ($\mathcal{A} = 1.4$) of PMMA spheres, radius $R_p = 550 \pm 7$ nm, refractive index $n_p = 1.49$, in decalin, $n_m = 1.47$ at effective volume fraction $\phi^{\natural} = 0.526$. Each set of images shows the same object area (field of view 9 μm $\times$ 9 μm) at, from left to right, $\mathcal{A}_C = 0.9, 0.7, 0.5, 0.3$ and 0.1: (a) a partially ordered layer (b) a close packed plane of crystal (c) 0.5 μm below (b), between two crystal planes.

small, as a comparison of the right-hand images in (b) and (c) shows. However, the apparently more confusing high $\mathcal{A}_C$ image at the left-hand end of (c) actually gives a better indication of the axial position of the layers – by making it clear that the object plane is not at one!

The lesson to be learnt is that getting the apparently clearest image does not necessarily give a true representation of the object plane. For this reason,

$\mathcal{A}_C$ should be kept as large as possible.

3.4 Digital image processing

Images recorded by a CCD camera are stored as arrays of numbers. In the case of monochrome images, the value of the number of a pixel represents the intensity – the **grey level** – of the image at that pixel.

In order for images to be visually pleasing, differences between grey levels should not be discernible to the human eye. Although 50 grey levels are usually sufficient, in practice, 256 levels, corresponding to 8 bits, are used where images are to be subject to computer processing [Inoué, 1997, §12.2.2].

The purpose of digital image processing is to manipulate these 8-bit numbers in order to make it easier to extract the information contained in the image. The peculiar information to be gleaned from microscopical images of identical spherical colloidal particles of known size is that concerning individual particle positions. Techniques designed to highlight such information shall be the emphasis of this section.

3.4.1 Look-up table operations

When the analogue signal from the CCD microchip has been digitized it passes through a look-up table (LUT) where grey levels are assigned to the digital values. By changing the LUT, the brightness and contrast of an image may be increased and regions with particular intensity values highlighted or obscured.

A helpful tool in choosing suitable values for the LUT changes is the **grey-level histogram** of an image. Recorded images often use only part of the available grey-level range; precisely which part will be revealed by a histogram much more clearly than by the image itself. Figure 3.14 shows a number of examples of single-pixel operations, along with their effects on the grey-level histograms of the images.

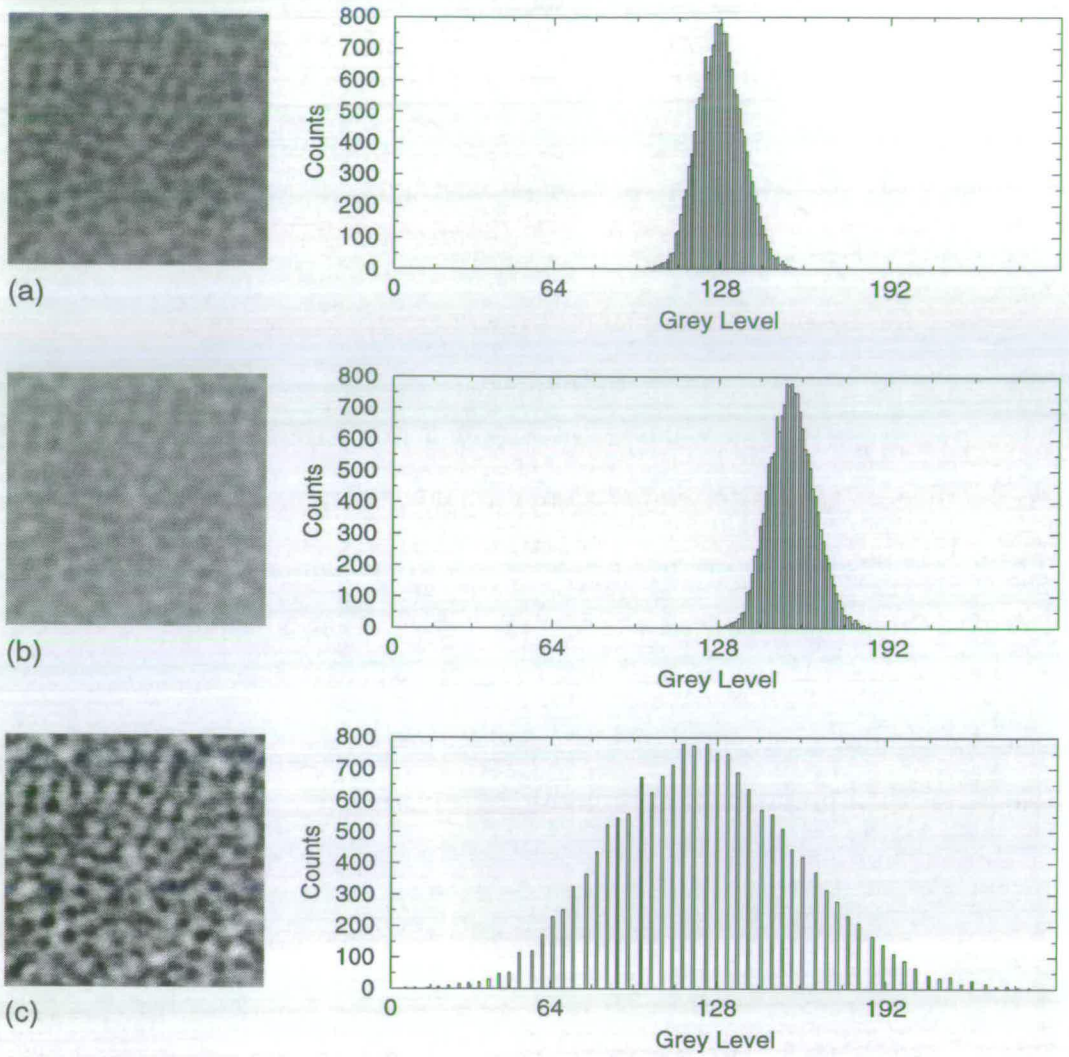

Figure 3.14: Brightness and contrast adjustments and their effects on grey-level histograms: (a) reference image (b) after a grey-level shift of 30 (c) after grey levels have been stretched from a range of 90–160 to one of 0–255.

Grey-level shifting

The simplest of all processes is to add a constant to all grey levels. This has the effect of **changing the brightness** of the image, a positive constant increasing it (*cf.* figures 3.14(a) and (b)). In order to avoid reducing still further the number of grey levels used by an image, it is important to ensure that the offset does not cause more than one pixel value to be set at the limit of the available range. Consideration of the grey-level histogram will help to avoid this **clipping**.

Grey-level stretching

To increase the **contrast** of an image, the range of grey levels employed needs to be increased, ideally to encompass all available levels. In such an operation, the amount by which a pixel value changes depends upon its grey level. A grey-level stretch of the LUT does this by redistributing the pixel values over a wider range of grey levels. While many automatic contrast-enhancing processes employed by standard image-processing software simply change the LUT so that the full grey-level range is employed (as in figure 3.14(c)), sometimes it may be preferable to set the range manually.

Thresholding, clipping and binarizing

It may be that it is known that those parts of an image with an intensity above or below a particular value are of particular interest, representing particle centres, perhaps. Or they may be of no interest, causing only confusion. In such cases, **thresholding** can be useful.

Thresholding involves setting all the pixels above or below a chosen threshold value to a chosen grey level, often the maximum or minimum grey level available (255 or 0 for an 8-bit image), as appropriate. The operation is sometimes referred to as **clipping** to the chosen grey level, as thresholding always reduces the grey-level range employed. In figure 3.15, (b) shows the effect of clipping the bright grey levels of (a) to an intermediate value.

Sometimes two thresholds are used, so that all the intensities between them are set to a some intermediate value, or else the outer ranges of intensity are set to extreme values. The limit of this latter scheme is when a single threshold is used as a "watershed", so that it divides all intensities into one of two grey levels, thereby reducing the image to being effectively binary. Where the two extreme values are actually converted into 1-bit numbers, this process is called **binarization**. With positive contrast, low grey levels correspond to particles, so binarization can be used in such a case to pick out the particle positions. In

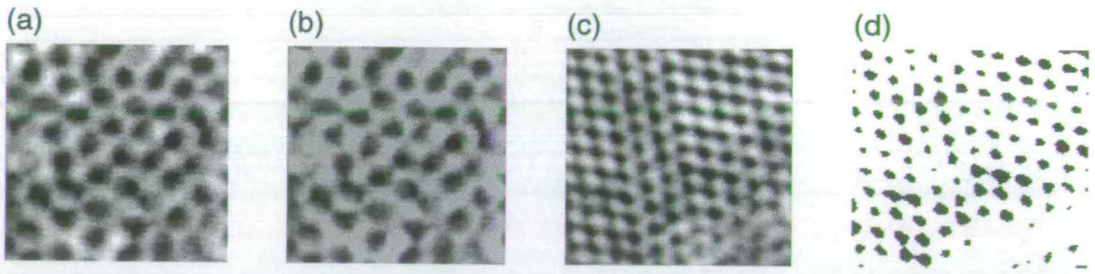

Figure 3.15: Clipping and binarizing: (a) is a phase contrast image, where the high grey levels correspond to out-of-focus information (b) shows the same image, after all grey levels more than one standard deviation above the average have been clipped to the value of that threshold; (c) shows part of a colloidal crystal and (d) shows the same image after binarizing to pick out the particle positions.

figure 3.15, (c) shows a positive phase contrast image of a colloidal crystal and (d) shows the result of binarizing (c) with a threshold set at its average grey-level value, so that the dark centres of the particles are rendered black in the binary image and the rest of the field of view is left white.

It is quite possible to have any number of thresholds up to the number of available grey levels and thereby reduce an image to as few bits as required. Conversely, multiplying all grey levels by a constant and storing the result as an image with more bits, before further processing will reduce the effects of the discrete nature of the grey levels in the final result, after conversion back to the original number of bits.

3.4.2 Multiple-image arithmetic

The intensity recorded at a particular pixel is, unfortunately, determined by factors other than that component of the image due to the object under investigation. By performing arithmetical operations on series of images it is possible to remove some of this unwanted information.

Averaging

One of the simplest ways to reduce noise is to take the average (pixel by pixel) of several recordings of the same image. Often, the image-grabbing hardware enables several frames to be stored and averaged before the result is sent to disk, but this can also be performed as a "post-production" process.

For suspensions of colloidal particles this (time-)averaging has the effect of "smearing out" the effects of particle motion. Particles in crystalline regions have the effects of their Brownian motion obscured and their lattice sites, about which they diffuse, are highlighted. Conversely, particles in fluid regions can be completely obscured if the averaged frames are recorded over times greater than their structural relaxation time. This can be a good way of distinguishing between ergodic and non-ergodic suspensions, or fluid and crystal regions of a single suspension.

Figure 3.16 shows a sequence of averages over increasing time intervals, em-

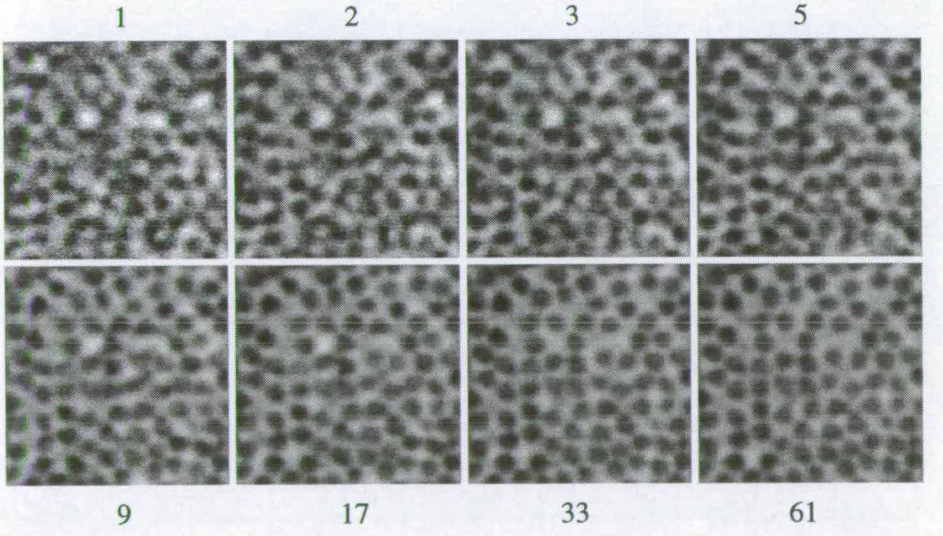

Figure 3.16: Averaging of images: a series of images of colloidal particles at the upper wall of their container was recorded every 2 seconds; the images in the figure represent (as indicated by the numbers) averages of increasing numbers of frames. Note how noisy the single frame image is and how those particles which have remained attached to one place over the full 2 minutes are increasingly enhanced through the series.

phasizing the way that fixed particles are highlighted.

Background subtraction

The effects of the non-uniform response of the CCD pixels and variations in background intensity can be reduced by subtracting an image which contains largely this information. This process is usually combined with a grey-level offset to some average value, to eliminate clipping.

A background image may be obtained simply by defocusing enough to ensure that no detail from the object can be discerned. It is important to ensure that, as far as possible, the condenser remains focused, so that the illumination remains representative. At high numerical apertures it may not be possible to defocus on the object sufficiently, while maintaining Köhler illumination, however, particularly for DIC imaging.

An alternative method is to average a series of many images recorded either at different positions within the suspension or over a time long enough for

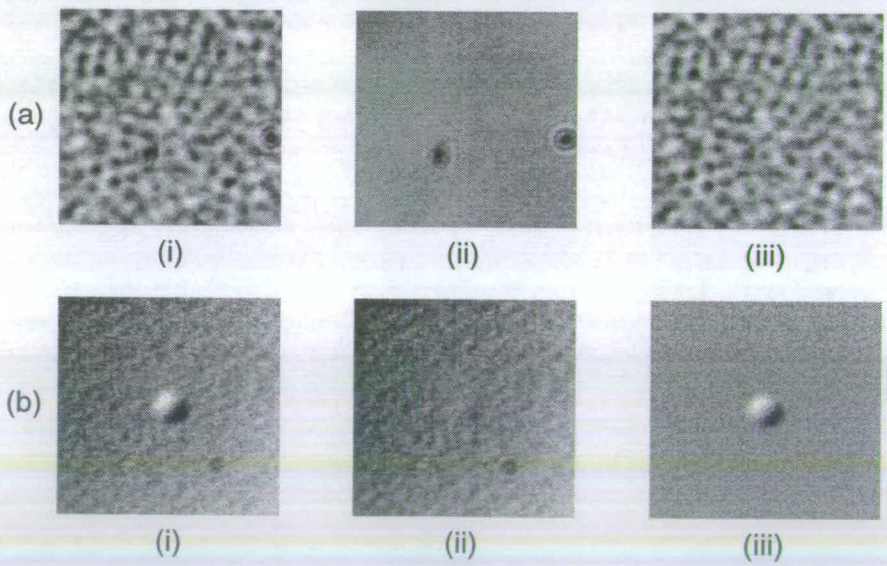

Figure 3.17: Background subtraction: (a) shows a phase contrast image (i), an image (ii) recorded 30 μm above this and the result (iii) of subtracted the latter from the former; (b) shows a DIC image of a single sphere (i), the average (ii) of a series of 183 images over an axial range of 20 μm and the result (iii) after subtraction.

the entire structure in the field of view to have changed. When this average is subtracted from individual images only the information peculiar to that image remains. Figure 3.17 shows background subtraction using both the defocus and the stack-average methods.

3.4.3 Multipixel operations

The processes described so far have treated the individual pixels of an image independently of one another, sometimes with reference to the grey levels of the image as a whole. In the methods described here, the grey levels of pixels in the neighbourhood of the given pixel to be altered shall be included in the determination of the change to be made.

Convolution

Many multipixel operations take the form of discrete convolutions of an image with a smaller array of numbers, called the convolution **kernel**.

Normally, the convolution $\mathcal{I}' = I' \circledast \mathcal{K}$, where I', $\mathcal{K}$ and $\mathcal{I}'$ represent the initial image, kernel and resultant image, respectively, involves performing the integral $\mathcal{I}'(x', y') = \int \int_{\infty}^{\infty} I'(x' - m_1, y' - m_2)\, \mathcal{K}(m_1, m_2)\, dm_1 dm_2$ (with m_1 and m_2 being dummy variables of integration).

In the case of a digital image, I' is a discrete array of numbers, so the convolution integral becomes a discrete sum of products:

$$\mathcal{I}'(x', y') = \sum_{m_1=\frac{1-\mathcal{K}_X}{2}}^{\frac{\mathcal{K}_X-1}{2}} \sum_{m_2=\frac{1-\mathcal{K}_Y}{2}}^{\frac{\mathcal{K}_Y-1}{2}} I'(x' - m_1, y' - m_2)\, \mathcal{K}(m_1, m_2), \qquad (3.29)$$

where $\mathcal{K}_X$ and $\mathcal{K}_Y$ are the numbers of pixels in the x and y dimensions of the kernel array¶.

Figure 3.18 shows the discrete convolution process diagrammatically: the ker-

¶The sum shown has the appropriate limits for a kernel with $\mathcal{K}_X$ and $\mathcal{K}_Y$ both odd, as is most commonly the case; for even values, the only change to the sum is that the limits become from $(1 - \frac{\mathcal{K}_X}{2})$ to $\frac{\mathcal{K}_X}{2}$ *etc.*.

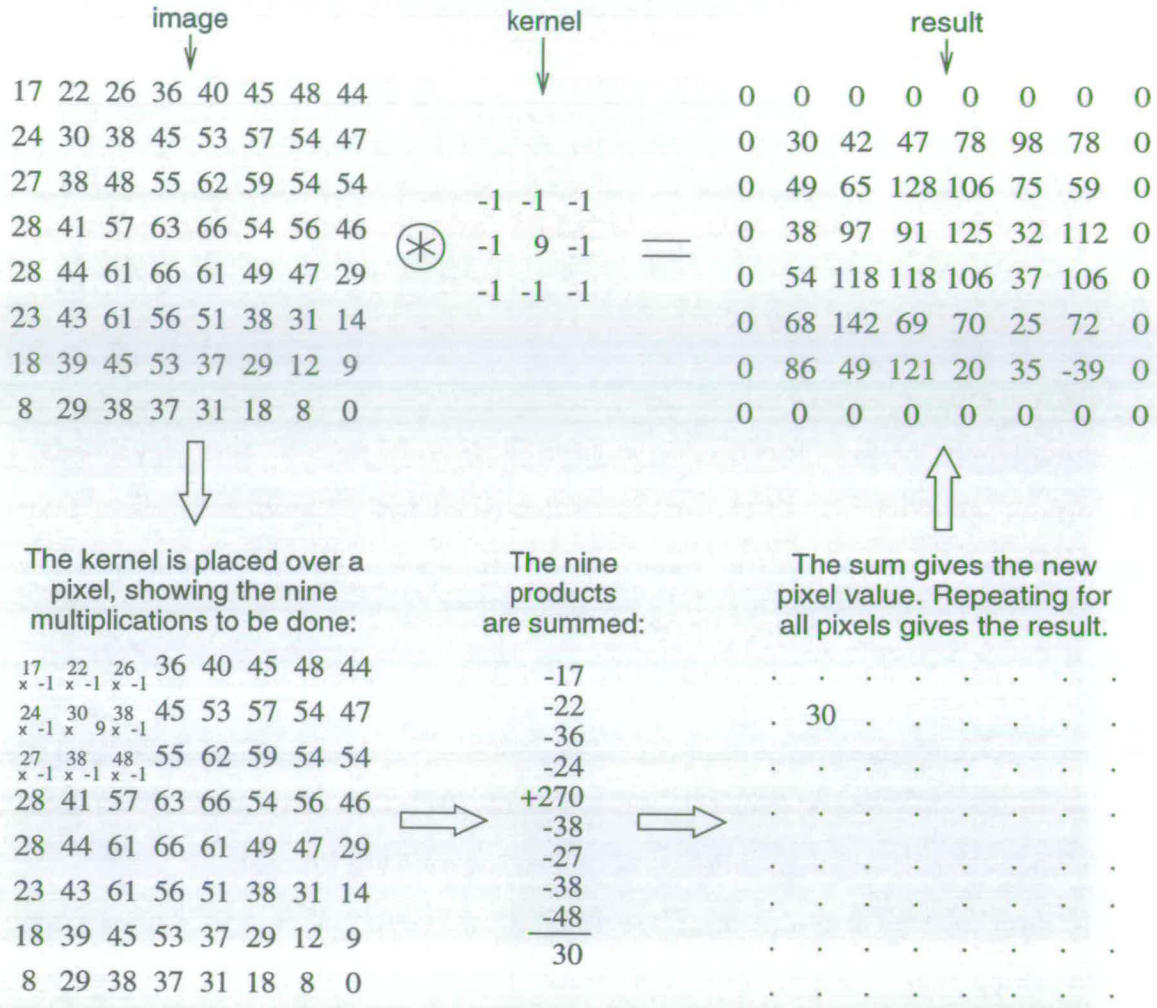

Figure 3.18: The shift-and-multiply process of convolution, as applied to digital images.

nel is placed over a target pixel and the kernel values are multiplied by the image values that they coincide with; the sum of these products gives the value for corresponding pixel in the output image. Then the kernel is shifted to the next target pixel and the process is repeated until all pixels in the image have been targeted.

Often a scaling is applied to the result, in order to ensure that all pixel values lie within the grey-level range in use. If the sum of the kernel pixel values is greater than unity, a general principle is to divide the result by that sum.

Figure 3.19 gives some examples of kernels and their effects. A kernel with

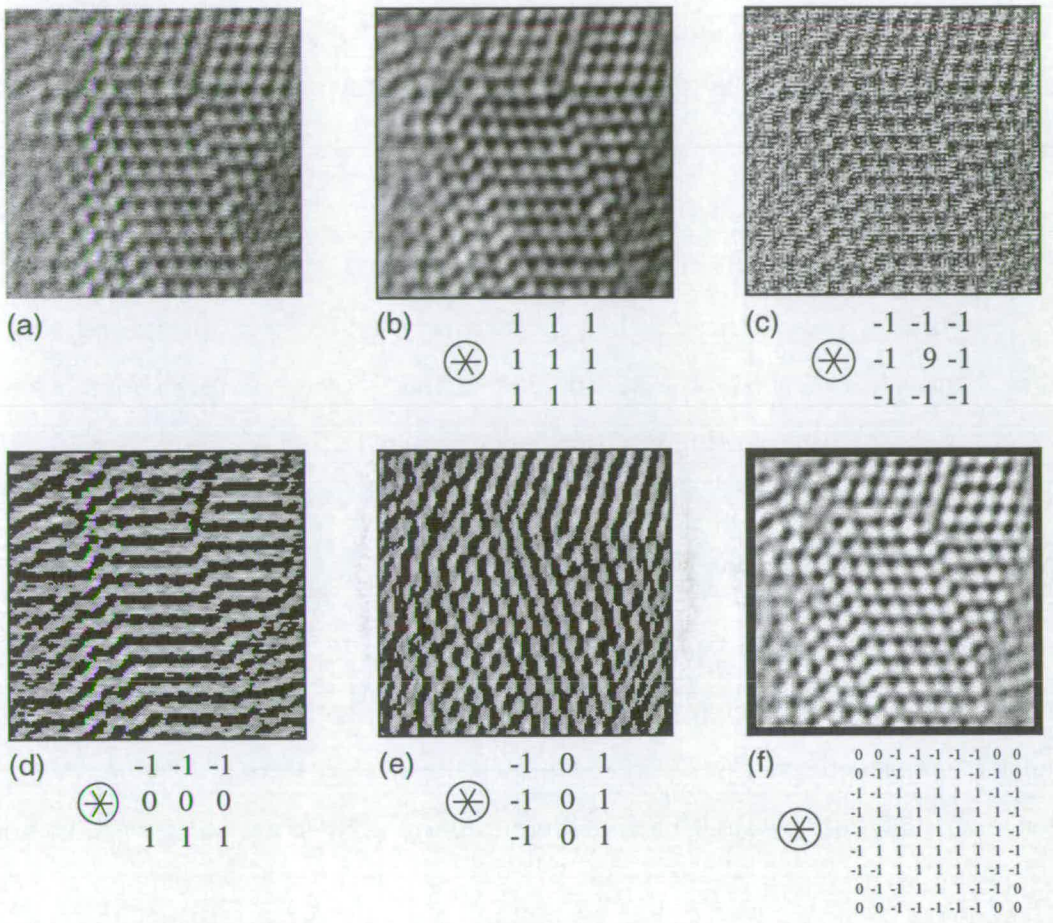

Figure 3.19: Some image convolutions and their kernels: (a) shows the original image; the other images show the results of convolving with the kernel shown below each one: (b) smoothing, (c) sharpening, (d) horizontal edge enhancement, (e) vertical edge enhancement, and (f) an example of a specialized convolution, used here to enhance the images of colloidal spheres.

all values equal performs an average over the area of the kernel, **smoothing** out high frequency noise, but also causing blurring. The size of the kernel (and shape, if some pixels are zero) will determine what size and type of detail is smoothed out.

For image **sharpening** a kernel is used which gives a result determined by the difference between a pixel and its neighbours. While enhancing fine detail, this also increases noise. One way to reduce noise without blurring is to **unsharp mask** by subtracting a smoothed image from its original.

Kernels which give results dependent on the rate of change of grey level across them are called derivative filters and are used for **edge detection**. Individual derivative filters will best enhance one particular orientation of edge, so, to detect edges in more than one azimuth, a sequence of convolutions is usually applied, each enhancing a different orientation.

Combinations of all these techniques can be used to form specialized kernels, which emphasize or obliterate particular features. Figure 3.19(f) shows a kernel which is good at highlighting circular features of a radius of about 7 pixels.

Morphometric operations

Where objects of interest have been defined by some process, usually in terms of a binary image, morphometric operations can be used to manipulate these objects, in order to characterize their shapes and positions. Here only operations designed for use on 1-bit images shall be considered; figure 3.20 shows some of those most frequently used.

Dilation and erosion involve adding or removing pixels at the edge of objects. Dilation works by setting all the eight neighbours of a given pixel to a value of 1, if less than a chosen number of them are at 0. Conversely, erosion sets a pixel to 0, if less than a chosen number of its eight neighbours are at a value of 1. By repeating one of these operations, it is possible to expand objects until only single pixels remain between them, allowing the space per object to be measured, or to reduce objects to single pixels, allowing their centres to be marked.

Other operations, such as **segmentation** allow overlapping objects to be separated, by first determining the distance of all object pixels (defined as being those at grey level 1) from their nearest background pixel (grey level 0). Any pixel which has a pair of opposing neighbours (*e.g.*, left and right, above and below, ...) with distance values both bigger than the distance value of the pixel in question is set to 0. As object centres lie at peaks in these distance values, the effect of setting all the relevant pixels to zero is to introduce 1 pixel-wide lines separating

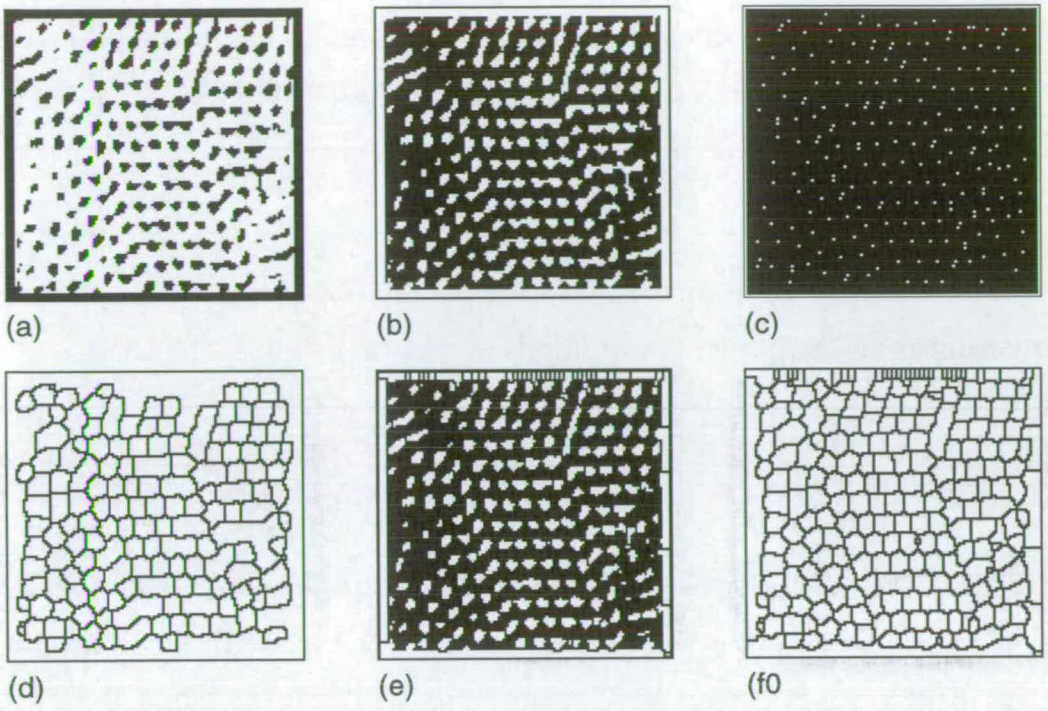

Figure 3.20: Morphometric operations on binary images: (a) is a binary image formed by thresholding figure 3.19(f) to pick out colloidal particles; in (b), the binary complement has been taken, so that the particles are now represented by bright pixels; (c) shows the effect of eroding the particles to single pixels, (d) the effect of dilating them until they nearly touch and (e) the result of segmenting; (f) shows how dilation after segmentation is a better method of picking out all particles than just dilating, on its own.

the objects. However, not all distance peaks genuinely represent object centres: the white boundary in figure 3.20(b), for instance, is divided into a number of "objects" in (e), so care is needed in interpreting these semented images. Many other operations are possible and are given in the standard textbooks, *e.g.*, Low [1991]; Gonzalez and Wood [1992].

3.4.4 Frequency space operations

Where particular spatial frequencies are a feature of an object, it can be quicker to deal with them in frequency space, especially where large convolution kernels would be required. Moreover, the convolution of the geometrical image with the

point spread function – which constitutes the diffraction-limited imaging process – can be "undone" – to recover the geometrical image – only in this domain.

Fourier filtering

The convolution theorem means that a simple multiplication of a Fourier-transformed image and a Fourier filter (of the same size) can replace convolution in real space, the inverse Fourier-transform of the product giving the desired convolved image.

By removing parts of the spatial frequency spectrum, noise can be removed or harmonic features enhanced. Figure 3.21 shows an image of a section of colloidal crystal and its Fourier transform, along with some Fourier filters and their effects.

Deconvolution

If the point spread-function appertaining to an image is known, then dividing the Fourier transform of the image by the Fourier transform of the PSF (known as the **optical transfer function**, OTF) can restore the geometrical image, when the quotient is inverse Fourier-transformed.

Though simple in principle, noise in images and PSFs and zeroes in the OTF both cause problems in the division process. A number of methods of surmounting these difficulaties have been published and while, research is still ongoing, many commercial image-processing software packages already offer some form of deconvolution (Inoué [1997] lists the main approaches in §12.7.7).

In the case of colloidal suspensions of identical spheres, the idea of deconvolution has a special appeal: images can be considered to be convolutions of "sphere spread-functions" with the particle coordinates, where the sphere spread-function (SSF) is just the point spread function convolved with the geometrical image of a sphere. So, using the Fourier transform of the SSF, instead of using the OTF, in the deconvolution process would, in principle, yield an image consisting of single intensity spikes at the particle coordinates.

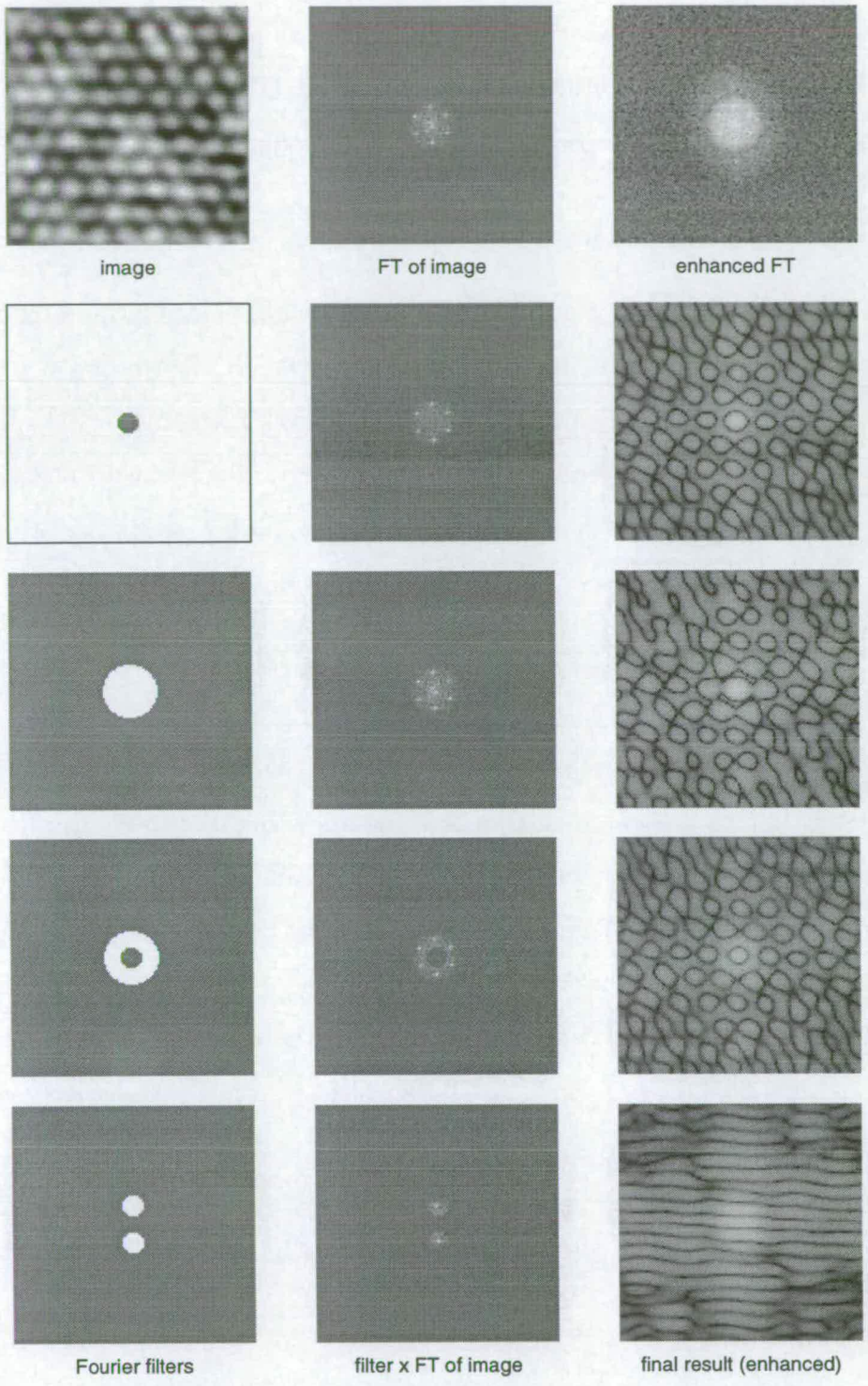

Figure 3.21: Fourier filtering: The top row shows an image of a colloidal crystal and its Fourier transform, along with a contrast enhanced FT, to show the detail at large spatial frequencies; the lower rows each show a Fourier filter, the product of the filter and the FT, and the result after inverse FT-ing (and enhancing the contrast).

This exercise suffers from the same difficulties as mentioned earlier, but some progress is being made [Renth, 1999] towards an effective scheme that would be of considerable use in the microscopical study of monodisperse colloidal suspensions.

Fourier-space operations in the microscope

As has been mentioned in a number of places already, Fourier transforms are at the heart of operation of the microscope. What is worth mentioning at this point is that, by direct observation of the objective back focal plane or exit pupil, we can see the Fourier transform of the image directly, which can provide a useful way of making a quick check of the frequency space information *e.g.*, the degree of polycrystallinity of a suspension. This information can then be used to inform the choice of Fourier filter*etc.*

* * *

The techniques presented in this chapter allow high contrast images of colloidal suspensions to be achieved, by means of a combination of imaging technique with "post-production" image processing, although there remains still opportunity for improvement. The key issues remaining to be considered, before full three-dimensional imaging can be achieved, are those concerned with the axial extent, or thickness of the suspension under observation; to which we now turn.

Chapter 4

The Microscopy of Thick Suspensions

The study of bulk behaviour in real space at an individual particle level is a realizable goal with optical microscopy, although the conditions for achieving it are stringent and special techniques are required to meet them.

The previous two chapters have described how colloidal suspensions can be imaged with a good degree of contrast. This chapter considers the particular challenges presented by objects of significant extent along the optical axis, *i.e.* thick objects, and presents methods developed to meet them.

These challenges present themselves at two levels: First, there is the need to achieve a genuinely three-dimensional suspension in the confined space between the objective and the condenser. Secondly, we need to find a way of converting series of recorded images, each representing a thin slice of the suspension, into three-dimensional information.

4.1 Achieving bulk conditions under the microscope

The basic challenge here is that the maximum space available, given the imaging requirements of colloid microscopy, is only just sufficient to meet the requirement

of the suspension to show true bulk behaviour.

4.1.1 Suspension requirements and optical limitations

For a suspension to be genuinely three-dimensional and hence show real bulk behaviour, the obvious requirement is that the shortest dimension of the suspension's container should be much greater than the particle size.

In the microscopical context, the shortest dimension is nearly always the one parallel to the optical axis. This, as before, shall be referred to as the z dimension.

The standard configuration in microscopy is to mount the object on a glass slide and cover it with a thin glass sheet, the cover slip. Colloidal suspensions can be mounted in this way, by placing a drop of the suspension on the slide, then placing a cover slip on top. This arrangement can provide a container of dimensions $X_\sqcup \times Y_\sqcup \times Z_\sqcup = 1.5$ cm $\times$ 1.5 cm$\times \approx 15$ μm. To maintain the confinement of the suspension, the edges of the cover slip should be sealed with a suitable adhesive.

Observation of colloidal suspensions mounted in this way show that behaviour is strongly influenced by the z confinement: for all but very low density suspensions ($\phi \lesssim 0.01$), particles are very quickly ordered into layers parallel to the glass surfaces. This agrees with the findings of, for example, Neser *et al.* [1997], whose experiments on confined suspensions showed that significant deviations from bulk behaviour were noticeable with suspensions up to 9 particle diameters thick.

It is possible, however, to mount thicker suspensions and still to be able to focus clearly on object planes at any axial position, but an upper limit to thickness is set by the imaging properties of the objective and condenser, *viz.*, their working distances, as well as the mechanical requirement to mount the suspension in a reasonably rigid container.

Objective and condenser working distances

Referring to figure 4.1, the working distance w_{Ob} of a microscope objective is

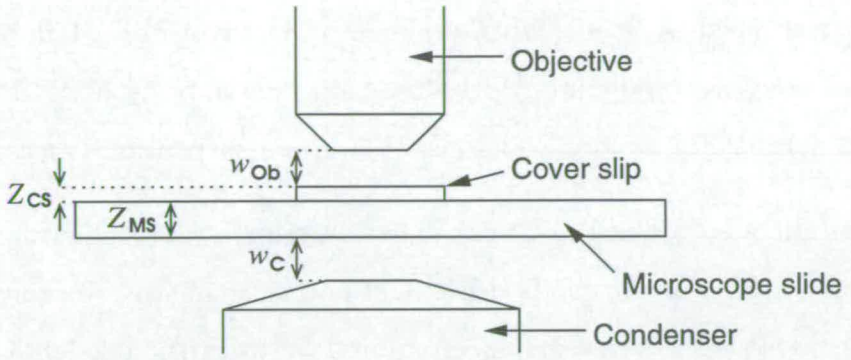

Figure 4.1: The definition of objective and condenser working distances, w_{Ob} and w_C.

defined as the free distance required between the front surface of the objective and the back surface of the cover slip to focus on a plane immediately in front of the cover slip. Objectives are corrected for a specific value of cover slip thickness Z_{CS}, the standard being $Z_{CS} = 170\ \mu$m.

By moving the objective closer to the cover slip, planes further from the glass are brought into focus. With dry objectives, the distance from object plane Π to the back surface of the cover slip must remain close to the value of Z_{CS} for which the objective is corrected, in order to benefit from the correction. A variation of no more than say $\pm\frac{Z_{CS}}{20} \approx 10\ \mu$m can be tolerated, inadequate for the suspension requirements.

With oil-immersion objectives, however, if the immersion oil, cover glass and suspension have very similar refractive indices, the objective can be brought right up to the glass with no loss of image quality. Moreover, the value of Z_{CS} can vary, so thinner glass can be used to increase still further the depth into the suspension that can be achieved for Π.

The general rule is that w_{Ob} decreases with $\mathcal{A}$, but there is no unique relationship between the two. Equations 2.16 and 2.17 show that to resolve detail on a length scale ϱ, using light of wavelength λ_0, we require

$$\mathcal{A} \approx \frac{\lambda_0}{\varrho}. \tag{4.1}$$

Given that optical wavelengths and colloidal length scales are very similar, this

means that we need $\mathcal{A} \gtrsim 1$. Oil immersion objectives with $\mathcal{A}$ in this range typically have $w_{\mathsf{Ob}} \approx 100$ μm. With Z_{CS} being possibly as little as 100 μm, focusing at depths of a hundred microns or so into a suspension is feasible.

For good images, we need to ensure that we can maintain Köhler illumination over this range; whether we can is dependent on the condenser working distance w_{C}. This is given by the free distance required between the condenser top lens back surface and the microscope slide front surface, in order to focus the illumination at a plane immediately behind the slide (see figure 4.1 again). For Köhler illumination, this plane must be coincident with the object plane Π, so for thick objects the condenser must be brought closer to the slide, when the objective is not focusing on the bottom of the suspension. Like objectives, condensers are corrected for a specific glass thickness, the standard being $Z_{\mathsf{MS}} = 1.1 \pm 0.1$ mm. A dry condenser might therefore be expected to tolerate a variation of ≈ 100 μm. Of course, an oil-immersion condenser will not suffer from this limitation.

Although thinner microscope slides are feasible and would allow thicker suspensions, their use is not really necessary, as a range of focus of the condenser within the object that is greater than the objective's range is superfluous. Moreover, thinner slides mean weaker suspension containers.

The net result of these considerations is that, with an oil-immersion objective of numerical aperture sufficient to resolve colloidal length scales, a suspension of thickness $Z_{\sqcup} \approx 100$ μm can be accommodated the space available, with the entire depth of the suspension accessible to imaging.

Experiments on suspensions of this thickness have shown that bulk behaviour can be genuinely achieved. The evidence for this can be found in the fact that suspensions show the same phase behaviour as in the bulk (in glass cells with $X_{\sqcup} \times Y_{\sqcup} \times Z_{\sqcup} = 1\text{ cm} \times 1\text{ cm} \times 5\text{ cm}$) and that structures have no preferred orientation, at least at distances of more than a few microns from the glass walls, or over time intervals of less than several weeks.

4.1.2 A method for mounting thick colloidal suspensions

The requirements for a mount for suitably thick colloidal suspensions may be summarized as follows:

- a parallel-sided container,
- glass thickness in front of the suspension ≈ 1.1 mm,
- glass thickness behind the suspension $\lesssim w_{\mathrm{Ob}} + 70$ μm and
- lateral dimensions $\gg$ particle size

These requirements can be met in a variety of ways; the method I have developed is therefore not the only possibility, but it works well and has the added advantages of quick and easy filling with colloid and readily obtainable and cheap components.

The basis of this method, illustrated in figure 4.2, is to contain the colloidal suspension within a rectangular section capillary tube. The tubes used have internal dimensions of 2 mm $\times$ 100 ± 10 μm, with walls of thickness 100 ± 10 μm. They are supplied in lengths of about 5 cm.

Tubes this narrow have the advantage that capillary action is sufficient to draw colloid into them, although this may take several minutes for $\phi \approx 0.5$. Once filled, the ends of the tube can be wiped clean, then sealed with epoxy resin.

For strength and condenser imaging reasons, these capillary tubes are mounted flat on microscope slides. So that observation may begin as soon as the tube has been filled and sealed, this mounting is done well before the tubes are filled, so that the mounting adhesive (the same epoxy resin as used for sealing will do) has time to set.

To make the ends of the tube accessible for filling once mounted on the glass slide, the ends are bent upwards. This is done, before the tube is mounted, by holding the ends in a blue Bunsen flame for a few seconds and removing as soon as they begin to bend under gravity.

One end needs to be bent enough so that it can reach into the container holding the colloid to be used and touch the surface of the suspension. In practice, the

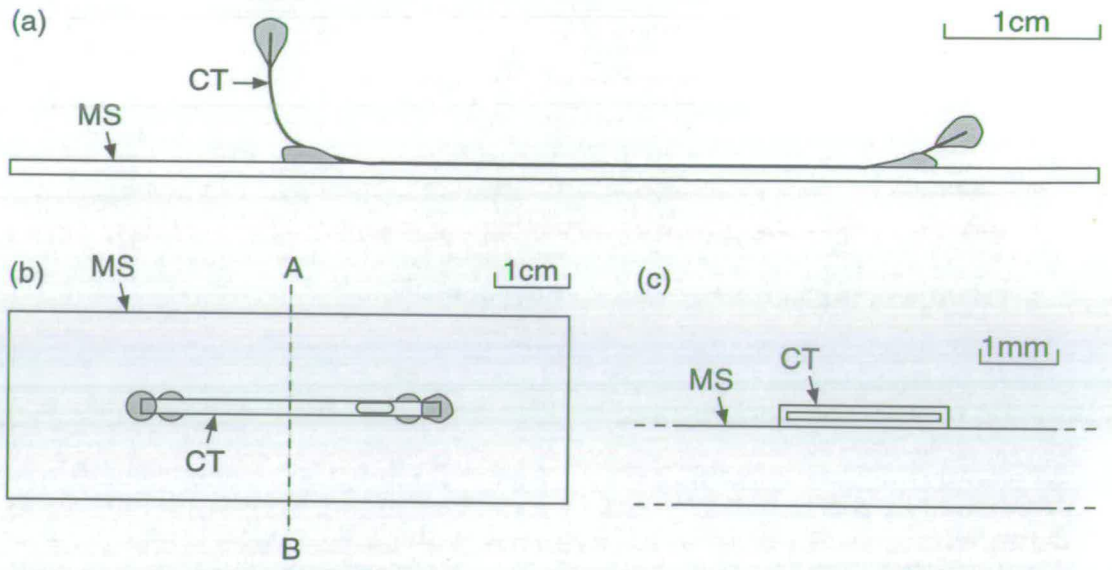

Figure 4.2: A method of mounting a thick colloidal suspension for microscopy, using a rectangular section capillary tube: (a) Side elevation of capillary tube (CT), with ends turned up and mounted on a microscope slide (MS). The grey blobs represent adhesive. (b) Plan of the same, at half the scale. Towards the right-hand end of the capillary a small bubble can be seen. (c) Magnified cross-section through the capillary and slide, along line AB of plan.

curve at this end needs to be about a centimetre long.

The other end only needs to be bent enough to prevent the colloid from leaking out once it reaches the end and to allow the sealing adhesive to encase the end properly. Half a centimetre is adequate for this curve.

One undesirable result of this method is that a small air bubble is always trapped at this "short" end of the tube. This can be minimized by curving the short end as little as possible. However, as long as the bubble is small – say only a few millimetres long, *i.e.* with volume less than a tenth of the suspension – and observation is more than a few millimetres away, then the bubble causes no problems.

When the curved tubes are mounted on their microscope slides, it is important to ensure that they sit as flat as possible on the slide. A small gap is almost inevitable, and it is very important to ensure that no spilt colloid is allowed

to enter it: the colloid will soon dry out to an opaque powder and render the mounting useless.

On the other hand, the immersion oil filling this gap once the mounting has first been prepared for observation will make it undetectable optically. Likewise any slight surface relief on the capillary walls – which are not manufactured to be optically flat – is rendered invisible by the index-matching oil.

Throughout this research, these mountings have been used with objectives of $w_{\mathrm{Ob}} \geq 80\,\mu$m quoted by the manufacturer. With the tube walls being $100 \pm 10\ \mu$m thick, it has indeed proved possible to image colloidal particles in contact with both top and bottom interior glass surfaces, $\approx 100\ \mu$m apart, the particles in question being clearly identifiable by their lack of Brownian motion. Whenever a new mounting is used, a check should always be made to see whether this can be done.

4.2 Acquiring three-dimensional information

A microscope image of a thick object is a combination of clearly focused detail from the object plane and gradually deteriorating detail from planes in the object on either side of this. The thickness of the object which is sufficiently clearly focused as to be indistinguishable from the diffraction-limited image is called the **depth of field**.

The best images have only a small proportion of poorly focused detail. One way to achieve this is by increasing the depth of field so as to have the entire thickness of the object in focus. Alternatively, we can decrease the depth of field to less than the typical length scale of axial intensity variations, giving a sharp image of a thin slice of the object. Whichever approach is used, the uncertainty in the axial position of any feature clearly focused cannot be less than the depth of field, a factor which must be taken into account when interpreting images.

Our approach in acquiring three-dimensional information shall therefore be to use the smallest possible depth of field and to employ the technique of **optical**

sectioning. This is simply the process of recording a series of images at axial positions separated by distances of the order of the depth of field or less. Such an axial series I will refer to as a **stack** of images. Where the object is undergoing structural changes over time, each stack recorded must be completed in a time significantly less than the structural relaxation time.

Practically, this requires us first to determine the depth of field so that we can choose an appropriate spacing for our stacks; secondly, we need to have a method of ensuring that the individual images of each stack are positioned accurately.

4.2.1 The determination of depth of field

Theoretical calculation

We know already that the geometrical image $\mathsf{O}'_{\bowtie}$ of a point object O is at the peak of a lateral intensity distribution; in the case of diffraction limited optics with circular apertures, this distribution is the Airy pattern (equation 2.7, figure 2.4).

It is also the case that $\mathsf{O}'_{\bowtie}$ is at the peak of intensity along the axial direction; this intensity variation is given by

$$I' = I'_0 \mathrm{sinc}^2 \left(\frac{\pi \mathcal{A}^2}{2\lambda_0 n' \mathcal{M}^2} z' \right), \tag{4.2}$$

where z' is the coordinate along the optic axis (in this case with its origin at the image plane Π'), I'_0 is the peak intensity, at $z' = 0$, $\mathrm{sinc}\, s = \frac{\sin s}{s}$, n' is the refractive index of the image space and $\mathcal{M}$ is the transverse magnification [Pluta, 1988, §3.7.1].

Small axial deviations from $\mathsf{O}'_{\bowtie}$ will only cause imperceptible reductions in intensity. At $z' = \pm \frac{\lambda_0 n' \mathcal{M}^2}{2\mathcal{A}^2}$ we have $I' \approx 0.8 I'_0$. This fraction represents the **Strehl limit** and is a common measure of the limit of perceptible intensity reductions. The range of z' over which the intensity drop is imperceptible is called the **depth of image** Z'_o.

Corresponding to the distance Z'_o in the image space is a distance Z_o in the

object space which is the axial range over which object points give intensities at the image plane which are imperceptibly different from the peak intensity. In other words, Z_o represents the axial range within the object which gives a well focused image at Π', *i.e.*, Z_o is the **depth of field.**

The relationship between Z_o and Z'_o is just given by the **longitudinal magnification** $\mathcal{M}_l = \frac{n'}{n}\mathcal{M}^2$, where n is the object space refractive index. Using the Strehl limit, we therefore have

$$Z_o = \frac{n\lambda_0}{\mathcal{A}^2}. \tag{4.3}$$

For $\lambda_0 = 550$ nm, an oil-immersion objective of $\mathcal{A} = 1.4$ will give $Z_o = 420$ nm, which should be suitable for optical sectioning of colloidal suspensions of particles at the larger end of the colloidal range.

Equation 4.3 assumes diffraction-limited optics and uses a criterion of the limit of clear focus which may be over-strict, so the effective depth of field $Z_o^\natural$ may be more than this. For this reason, it is as well to measure $Z_o^\natural$ experimentally.

Experimental measurement

The most direct way of doing this is to focus on a feature in the object, then record the limits of axial variation that are possible for the object to remain in clear focus. By measuring intensities in the stacks of images of which figures 3.4 and 3.9 show a subset, we find $Z_o^\natural = 1.20 \pm 0.06$ μm for phase contrast, whereas for DIC we find $Z_o^\natural = 1.90 \pm 0.06$ μm.

Figures 3.4 and 3.9 show single particles in isolation; examination of images of suspensions at high volume fraction suggests an effective depth of field that is much closer to the theoretical value, particularly for DIC: clearly focused images can be readily obtained of layers of particles in colloidal crystals, without any obvious influence from particles in adjacent layers (see, for example, figure 3.13(a) and (b)).

Measurements on stacks of images of suspensions at $\phi \approx 0.5$ give $Z_o^\natural \lesssim 0.9$ μm for phase contrast, which is an improvement. DIC gives even better results, with

$Z_o^b \lesssim 0.5\ \mu$m.

The reason for this density dependence of depth of field must be due to the influence of the out-of-focus information from nearby planes: what makes for a noticeably degraded image is not only the intensity decrease of the image of the feature we are interested in, but also the increase in intensity of images of features outwith the plane of this feature.

Where there is a large amount of out-of-focus information from nearby planes, as in high density suspensions, an image will degrade on defocusing much more rapidly than where there is relatively little out-of-focus information from nearby planes, as in low density suspensions, and the variation in intensity on defocusing is due solely to the object under examination.

High density suspensions would therefore seem to be particularly favourable for optical sectioning.

Depth of field and the three-dimensional point spread function

It is important to note that the depth of field is a diffraction effect: small depths of field, like small resolutions, are achieved by large numerical apertures. Of relevance to three-dimensional imaging is the fact that depth of field is always larger than resolution, so that a full three-dimensional point spread function does not have spherical symmetry and spherical particles will appear as prolate ellipsoids of revolution (rugby footballs) aligned along the optical axis.

4.2.2 The control of image position

There are two aspects to the control of image position: First, for optical sectioning it is obviously important to be able to set the axial position of the object planes accurately, so that the z-spacing of the pixels in the three-dimensional array formed by the image stack may be calibrated.

Secondly, as each image is of finite lateral extent, it is also important to be sure that any variation in the position of these lateral limits due to "stage drift"

is taken into account.

Axial control of object plane

The standard way of altering the axial position of the object plane is to use the microscope focusing controls. Indeed, to focus on an object is just to bring the object plane into coincidence with the plane of interest in the object.

Although focus knobs are often graduated, the best precision that can be achieved by hand is about ± 0.5 μm, which is insufficient for acquiring a series of images, each of which are to be separated by ≈ 0.5 μm. Moreover, with typical structural relaxation times $\mathcal{O}(10^2)$ s, it will be difficult to achieve stacks with more than one or two images in them in the time available.

One very precise method of focusing which can respond very rapidly is to use a piezoelectric translator attached between the objective and the microscope nosepiece, as in figure 4.3(a). By adjusting the voltage input to the translator, the objective can be positioned axially to a precision of ± 0.1 μm, over a range of about 100 μm. To achieve this accuracy a closed-loop system is needed to control the translator, *i.e.* one which actively monitors the actual position and maintains very close to its nominal value. This mode of operation is a standard option for commercially available systems*.

For movements of $\lesssim 1$ μm, the translator can respond in a few hundredths of a second; so, using computer control of the input voltage, a piezoelectric translator could enable a stack of several hundred images, covering a range of 100 μm or so, to be recorded within a few seconds. In practice, the time taken to acquire a stack depends on other factors, in particular the size of the individual images and the speed at which the computer hardware can grab and store them.

By way of example, using a typical image grabbing board, the MuTech MV-1000†, a stack of 100 images takes around 10 s to record, as long as the (8-bit

*The one used in this work was the P-862 produced by Physik Instrumente (PI) GmbH & Co., Polytec-Platz 5-7, 76337 Waldbronn, Germany.

†MuTech Corporation, 85 Rangeway Road, Billerica, Maryland 01862, USA

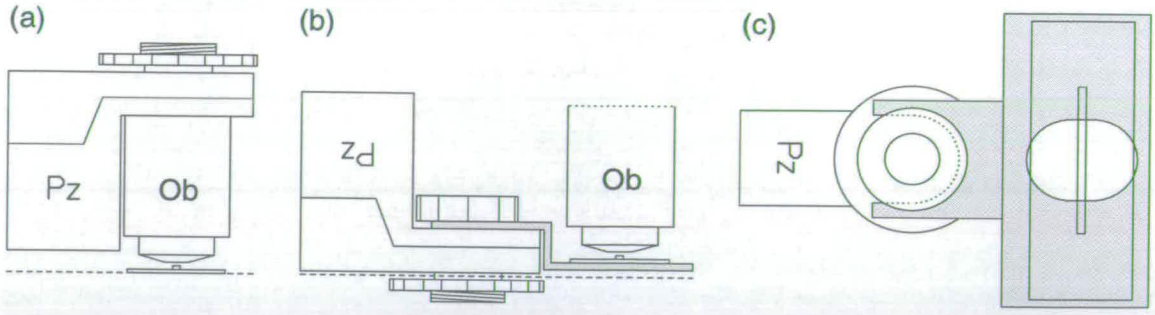

Figure 4.3: Controlling axial position with a piezoelectric translator: (a) the conventional configuration of translator Pz, with objective Ob fitted, suitable for bright field and phase contrast. The object (a capillary tube on a microscope slide) is shown in front of the objective, with the dashed line representing the microscope stage; the threaded attachment at the top of Pz is screwed into the microscope nosepiece (not shown here), being secured with the lockring shown (b) An alternative configuration, suitable also for DIC, where the inverted Pz is used to move the object, by means of a small platform (shown in grey) attached to it; in this configuration Pz is secured to the microscope stage by means of the lockring (c) a plan view of this alternative configuration, to show the positioning of the object on the platform and the aperture in the platform for illumination.

grey-scale) images are less than about 150×150 pixels^2 (which can adequately represent $(10\ \mu\text{m})^2$). Larger images increase the storage time at a rate of roughly $(80\ \text{pixels})^2\ \text{s}^{-1}$.

Faster hardware is available, but even these moderate speeds make it possible to acquire three-dimensional snapshots of reasonable extent in times significantly less than the relaxation time of dense colloidal suspensions.

To adjust the distance between the objective and the nosepiece is not suitable for Normarski DIC however, as the distance between the Wollaston prisms is critical for imaging. Following up the suggestion [Tanaka, 1997] to try moving the object instead, I have developed a method for acquiring image stacks that is both suitable for DIC and enjoys the benefits of piezoelectric positioning.

Figure 4.3(b) and (c) show this new method, whereby a small soldered brass platform is attached to an inverted piezoelectric translator which is itself attached to the microscope stage. The suspension mounting can be held in place on the

platform either by means of small rubber bands or by paper stickers. Comparison between translations achieved by the translator and those by the microscope focus controls show that the accuracy of the translator is as good as in its standard, upright configuration.

Problems with lateral alignment of images

It is important to ensure that the images in a given stack can be properly aligned laterally. If the object does not move laterally during the recording of a stack, then alignment poses no problem, but this will not necessarily be the case. As long as the object is properly secured, the main cause of lateral drift is thermal expansion/contraction.

Time-lapse series of images show that lateral drift is worst when images are recorded shortly after the microscope illumination has be switched on. Drifts of as much as 0.1 $\mu m\,s^{-1}$ have been recorded during the first few minutes. After an hour or two, drifts are only $\mathcal{O}(10^{-3})$ $\mu m\,s^{-1}$, and correlate closely with ambient temperature changes – $\mathcal{O}(10)$ K – in the laboratory. Ambient temperature control of ± 1 K is not difficult to achieve, so the problem of drift may be neglected, as long as the microscope has been on for some time.

Experiments have also shown that it is thermal expansion in the microscope that is the source of the large drift observed shortly after switching on the illumination: if a suspension mounting at ambient temperature is placed on the stage of an already warm microscope, noticeable drift occurs only over the first few tens of seconds, while the mounting warms up due to the illumination.

To reduce lateral drift to negligible amounts:

1. Turn on the microscope illumination, at the level to be used during experiment, at least two hours beforehand.
2. Maintain the ambient temperature constant to within ± 1 K for the duration of the experiment.

4.3 Displaying three-dimensional information

Once a stack of images has been recorded, the three-dimensional information can be extracted in a variety of ways. Displaying this information visually can be particularly helpful in revealing structures. In this section three methods of display are outlined, ranging from a simple selection of images to a sophisticated reconstruction of how a stack would appear viewed from some arbitrary direction.

4.3.1 Montages of selected images

The simplest method of displaying the three-dimensional information in a stack of images is simply to select a series of images at depths of interest within the object. Figures 3.1, 3.4 and 3.9 show montages of this kind.

This method is particularly suitable for obtaining a broad picture of variations over the thickness of an object, perhaps followed over a period of time, as in figure 4.4. On the other hand, the full three-dimensional nature of structures at an individual particle degree of resolution are not easy to visualize using this method.

4.3.2 Longitudinal sections through stacks

If the individual images of a stack measure $N^x_{\mathsf{pix}} \times N^y_{\mathsf{pix}}$, in terms of pixels, and there are $N_{\mathsf{im}} = N^z_{\mathsf{pix}}$ images in the stack, then the data represents an $N^x_{\mathsf{pix}} \times N^y_{\mathsf{pix}} \times N^z_{\mathsf{pix}}$ array. It is a straightforward matter to obtain axial slices of this array, measuring $N^x_{\mathsf{pix}} \times N^z_{\mathsf{pix}}$ or $N^y_{\mathsf{pix}} \times N^z_{\mathsf{pix}}$ pixels^2. The composite images at the bottom of figures 3.1, 3.4 and 3.9 are just such slices.

Usually the z-calibration $\mathcal{S}_z = 1/\Delta z_{\mathsf{pix}}$ (obtained from the axial spacing of the stack, as $\Delta z_{\mathsf{pix}} = \Delta z_{\mathsf{im}}$, the spacing of the images) will differ from the x- and y-calibrations, $\mathcal{S}_x$ and $\mathcal{S}_y$, of the recorded images (see page 34), so some adjustment of aspect ratio will be required for these sort of axial slices to display a proper image of a longitudinal section of the object. This sort of stretching is a standard

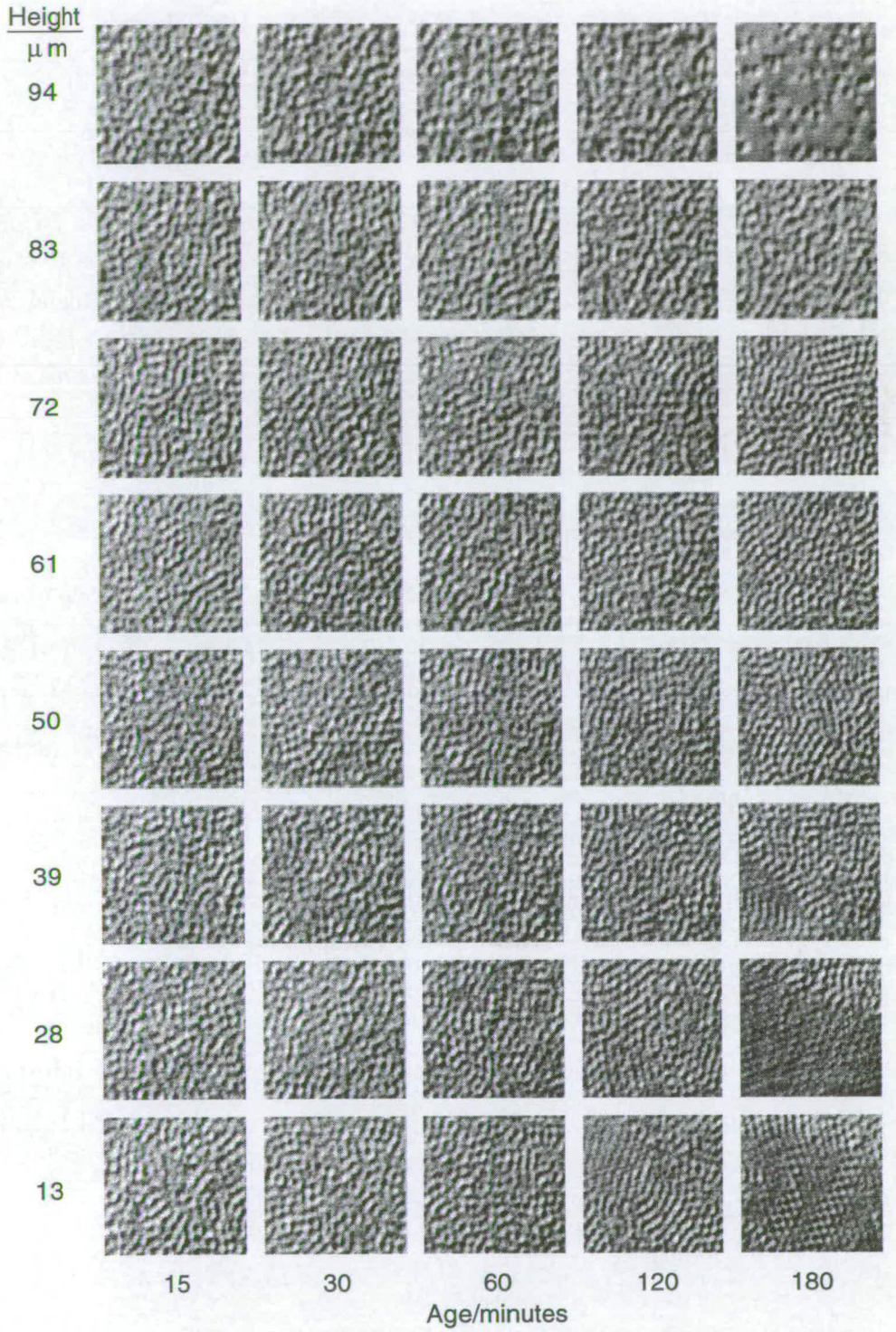

Figure 4.4: A series of montages of a dense colloidal suspension: each column is a montage of eight images recorded at different heights from the bottom of a 100 μm thick suspension of 1.1 μm diameter spheres at $\phi = 0.510$; the time after the suspension was sealed into its mounting is given beneath each montage.

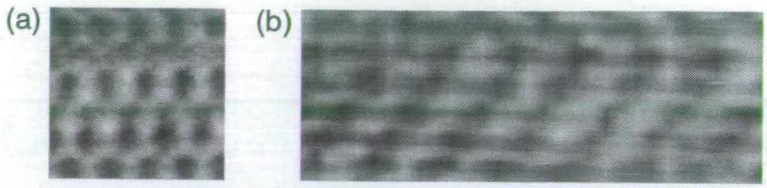

Figure 4.5: Longitudinal sections through stacks of images: (a) a single 76 pixel by 76 pixel image of a 31 plane stack through a colloidal crystal, showing a geometrical arrangement of particles typical of all planes in the stack (b) a longitudinal section through the middle of the stack, stretched in the z-direction (left to right across the figure) to make the magnification the same as in the y-direction (vertical in the figure).

procedure of digital image processing.

Figure 4.5(b) shows just such a longitudinal section through a stack of images of a colloidal crystal, one of which is shown in (a). The depth of field of images obtained in this manner, it is important to note, is given by the resolution in the x-y plane perpendicular to the plane of the section, and so is *less* than that of the recorded images.

Longitudinal sections are useful for revealing particle arrangements in three dimensions, but the longitudinal elongation of spherical particles – clearly evident in figure 4.5(b) – can make appearances deceptive and care must be taken in interpretation.

This approach is at its most useful when planes of particular interest are parallel to the three possible sections. Where it would be helpful to able to view the stack from other directions than along the x-, y- and z-axes, a more sophisticated approach to displaying the data is required.

4.3.3 Constructed views of entire stacks

With negative contrast, particles are represented by dark regions; so, if an $N^x_{\mathrm{pix}} \times N^y_{\mathrm{pix}}$ array is constructed from the darkest grey level values for each x- and y-coordinate, then an image with a depth of field as large as the z-extent of the

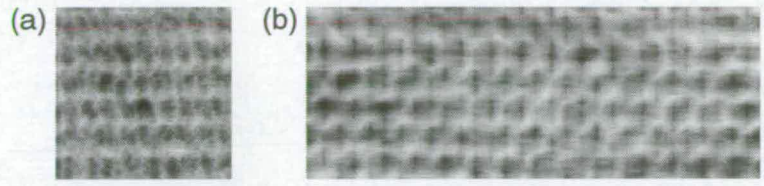

Figure 4.6: Views constructed from entire image stacks: (a) the view along the z-axis, through the entire stack of figure 4.5, (b) the view along the y-axis of the same stack.

stack is generated.

Figure 4.6(a) shows this construction for the stack displayed in figure 4.5. Note how the bright regions highlight the way that the particles must be arranged in planes perpendicular to this view.

We can also construct an image from the minimum grey level along lines parallel to the y-axis of the stack, to give an $(N^x_{\mathrm{pix}} \times N^z_{\mathrm{pix}})$ array which forms an longitudinal image of the stack, with a depth of field equal to the y-extent of the stack. This construction is shown in figure 4.6(b).

The principle of finding the darkest grey level value along lines parallel to a given direction can be applied to directions other than the three axes of the array. Figure 4.7 shows how this works in principle, using a two-dimensional equivalent for clarity: one-dimensional lines of pixels are arranged in a two-dimensional array and a new (one-dimensional) line of pixels is generated as the "view" of the array from an oblique angle.

MetaMorph®, the image-processing software[‡] used to construct the images in figure 4.6 by this method, allows views to be constructed at any integer number of degrees of rotation about either the x- or y-axis. Figures 4.6(a) and (b) represent angles of 0° and 90° to the y-axis respectively; examples at a range of other angles are given in §6.3, where the detailed interpretation of the images constructed in this way can be found. All that needs to be said here is that the

[‡]Universal Imaging Corporation, 502 Brandywine Parkway, West Chester, Pennsylvania 19380, USA

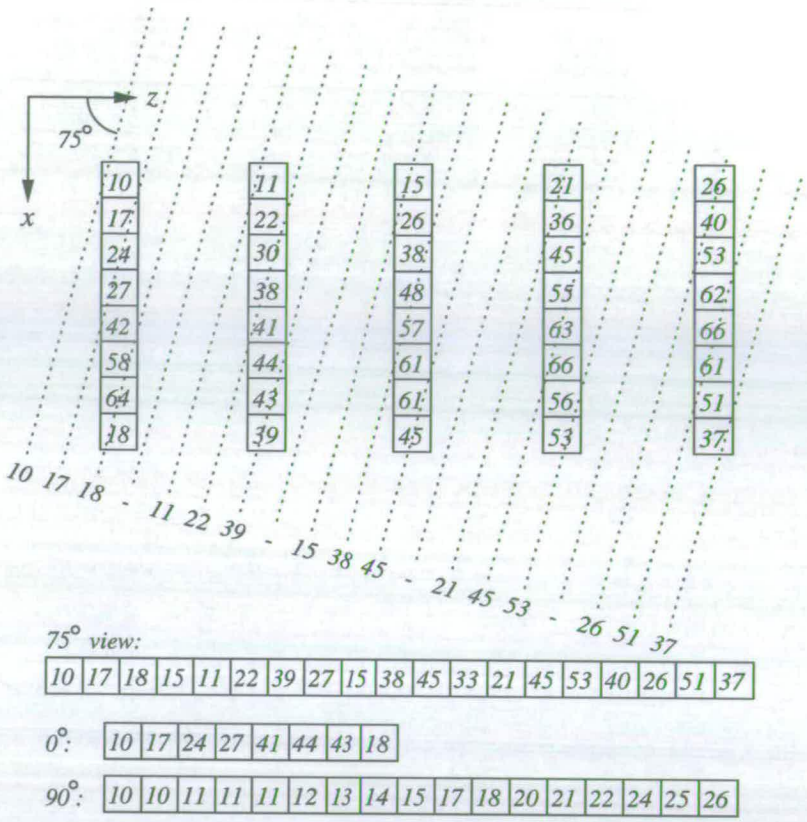

Figure 4.7: Construction method for oblique views of entire stacks: 1 – Five eight-pixel columns, the two-dimensional equivalent of five images in a stack, are spaced so that the array of pixels has the same aspect ratio as the object space it represents. 2 – The lowest pixel value along each of a set of lines, spaced the same as pixels in the columns, is recorded (here, dotted lines are used to show the construction the 75° view, with the recorded value indicated for each line). 3 – Where a line intersects with no pixel, gaps will exist in the line of pixel values recorded, so a linear (integer) interpolation is made to complete the construction (at the bottom of the figure, the final result for the 75° view is shown, along with the 0° view, along the z-axis, and the 90° view, along the x-axis.)

particular advantage of this method is that it effectively converts the stack of images into a solid body consisting of dark regions (the particles) embedded in a transparent medium, which we can tilt almost at will and thereby quickly arrive at an understanding of the arrangement of the particles in three dimensions.

* * *

Being now armed with the means to achieve high-resolution, fully three-dimensional images of colloidal suspensions thick enough to show bulk behaviour, the first part of this thesis is complete and we can now turn to the application of the principles and techniques set out here.

Part II

Applications of Colloid Microscopy

Chapter 5

Colloidal Hard Sphere Suspensions

5.1 The ideal hard sphere system

5.1.1 Monodisperse hard spheres

The hard sphere interaction

Ideal hard spheres are perfectly rigid bodies which exert no forces on one another, except when they come into contact. On touching, their rigidity means that arbitrarily large forces will prevent any deformation or overlap. This implies a very simple 'right-angled' pair potential for hard spheres (figure 5.1).

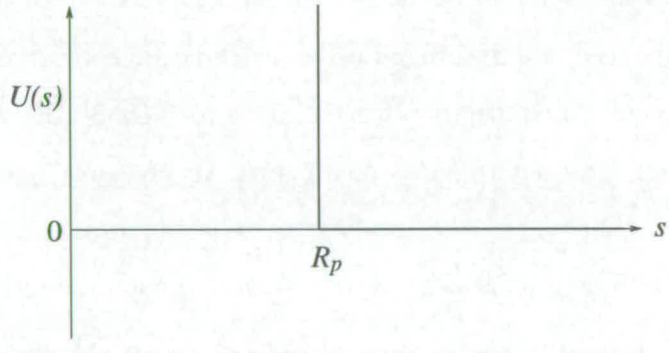

Figure 5.1: The pair potential $U(s)$ for hard spheres of radius R_p and separation s.

Monodispersity

Implicit in figure 5.1 is that the spheres in an assembly with such a pair potential all have the same radius R_p; such an assembly is said to be **monodisperse** in size.

5.1.2 Hard sphere phase behaviour

Two dimensionless parameters suffice to describe a monodisperse hard sphere assembly thermodynamically: reduced pressure $\tilde{P}$ and volume fraction ϕ. For an assembly of N_p hard spheres of radius R_p, confined to volume V, at temperature T and pressure P,

$$\phi = \frac{4\pi R_p^3 N_p}{3V} \tag{5.1}$$

$$\tilde{P} = \frac{PV}{N_p k_B T}. \tag{5.2}$$

As an assembly of identical spheres can never completely fill space, volume fraction is limited to the range $0 \leq \phi \leq \frac{\pi}{3\sqrt{2}} = \phi_{\mathsf{cp}} \approx 0.740$. In the low density limit, the hard sphere system approximates an ideal gas so reduced pressure is limited to $\tilde{P} \geq 1$.

Numerical calculations of the monodisperse equation of state [Wood and Jacobson, 1957] showed that, despite the simple non-attractive interaction between hard spheres, two different phases exist: one fluid-like with no long-range order, the other solid-like with a long-ranged order, with the symmetry of a close-packed crystal. Subsequent calculations [Hoover and Ree, 1968] showed that fluid at $\phi = 0.494$ and solid at $\phi = 0.545$ share the same pressure and entropy at any temperature, *i.e.*, they are in thermodynamic equilibrium, the difference in volume fraction implying that the phase transition must be first-order. Thus we can refer to freezing and melting volume fractions, $\phi_{\mathsf{F}} = 0.494$ and $\phi_{\mathsf{M}} = 0.545$, respectively. Figure 5.2 shows the equation of state schematically.

For $\phi < \phi_{\mathsf{F}}$, the fluid is the stable phase; the equation of state proposed by

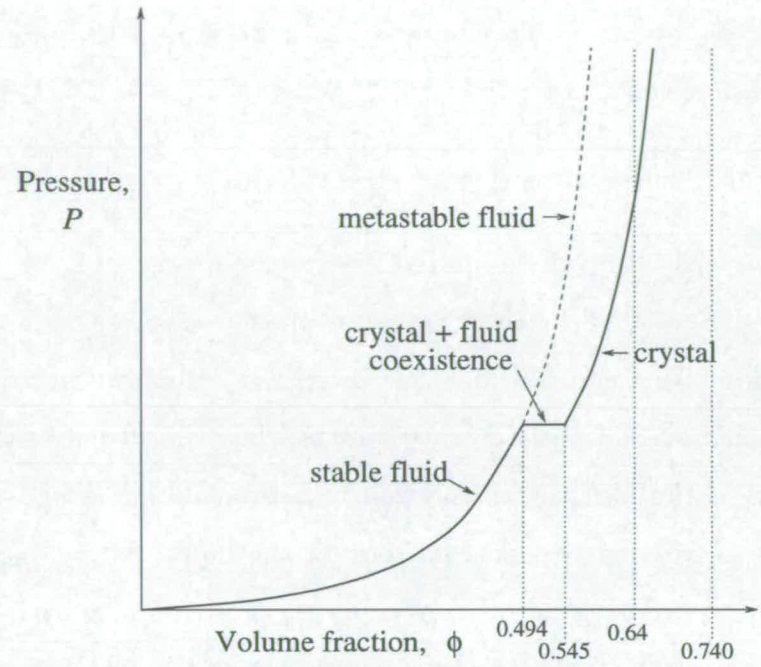

Figure 5.2: The hard sphere equation of state (solid curve). The dashed line shows the equation of state of the fluid for $\phi > 0.494$, in which region it is only metastable; this line approaches asymptotically to the line $\phi = 0.64$, the random close-packing limit.

Carnahan and Starling [1969],

$$\tilde{P} = \frac{1 + \phi + \phi^2 - \phi^3}{(1-\phi)^3} \tag{5.3}$$

holds well for the stable region of the fluid. Fluid may exist metastably up to $\phi = 0.64 = \phi_{\mathsf{rcp}}$, the random close-packing limit [Schaertl and Sillescu, 1994], however and above $\phi \approx 0.5$, the pressure exceeds that predicted by equation 5.3. A better expression [Woodcock, 1981] is

$$\tilde{P} = \frac{1.85}{0.64 - \phi}. \tag{5.4}$$

For $\phi_{\mathsf{M}} < \phi < \phi_{\mathsf{cp}}$ the stable phase is the solid; its equation of state [Hall, 1972] can be expressed by

$$\tilde{P} = \frac{2.22}{0.74 - \phi}. \tag{5.5}$$

For $\phi_F < \phi < \phi_M$ the assembly will separate in to fluid at $\phi = \phi_F$ and solid at $\phi = \phi_M$ with a fraction

$$\chi = \frac{\phi - \phi_F}{\phi_M - \phi_F} \tag{5.6}$$

being solid to satisfy the value required for the overall ϕ.

Hoover and Ree [1968] showed that the phase transition is entropy driven. Broadly speaking, one can consider this in terms of a competition between the large global entropy of the fluid state and the large local entropy of the solid phase: at high ϕ the particles in the fluid phase have increasingly less room to move around, decreasing the local entropy of the fluid. At $\phi > \phi_F$, the loss of global entropy on ordering into the solid phase, is outweighed by the increase in local entropy due to the fact that the spheres, though trapped within cages, have greater freedom of movement on a small scale (only at $\phi = \phi_{cp}$ do the spheres actually touch all their nearest neighbours).

Thus the monodisperse hard sphere system is one of great simplicity in its defining characteristics, yet has a phase behaviour which could make it a fruitful model of atomic systems. While much work has been done using computer simulations, the number of particles used is quite restricted, even on the most powerful computers. Numbers of particles exceeding these limits by several orders of magnitude are routinely achievable, however, by performing experiments using colloids.

5.2 Real nearly-hard sphere colloids

5.2.1 Limitations of assemblies of colloidal spheres

Sterically stabilized colloidal suspensions would seem to be good candidates for model hard sphere assemblies. Important differences between such systems and the ideal exist, specifically:

- no real system can have a perfectly hard interaction,

- no real system will be perfectly monodisperse.

Hardness of interaction

For hard spheres,

$$\frac{\phi_{\mathsf{M}} - \phi_{\mathsf{F}}}{\phi_{\mathsf{F}}} = 0.1 \tag{5.7}$$

is expected [Hansen and Schiff, 1973], but not for softer potentials. This ratio will therefore provide a useful measure of how close a candidate suspension approximates hard sphere behaviour.

Size polydispersity

For an assembly with a finite range of sizes of spherical particles, the distribution of particle size – the **size polydispersity** – is conveniently measured by the standard deviation ε_R of the distribution Pusey [1987].

Pusey showed that the hard sphere disorder-order transition should not be found in assemblies with $\varepsilon_R \gtrsim 6\%$ and ϕ_{M} and ϕ_{F} are known to vary with polydispersity [Bartlett, 1997; Bolhuis and Kofke, 1996, 1999; Fairhurst, 1999b], but, as long as crystallization is observed to occur, the monodisperse values are assumed [Fairhurst, 1999a] to hold.

5.2.2 Evidence for nearly-hard sphere behaviour in colloids

While both polystyrene [Papir and Krieger, 1970] and silica [de Kruif *et al.*, 1985] spheres have been used as good model hard spheres, the system of polymethylmethacrylate (PMMA) spherical latices, sterically-stabilized with chemically grafted coating of polyhydroxystearic acid (PHSA) "hairs" of length $\approx 0.1R_p$ or less, suspended in a nonpolar, refractive index-matching liquid, have also received a lot of attention.

Using decalin as a medium for a PMMA-PHSA suspension, with the addition of carbon disulphide to index match, Pusey and van Megen [1986] observed phase

behaviour very similar to that expected of hard spheres. By application of a lever rule (like equation 5.6) to phase separated samples showing fluid-crystal coexistence, they obtained values of $\phi_F = 0.407$ and $\phi_M = 0.442$, based upon literature values for the densities and a combination of electron microscopy, light scattering and crystallography for the particle sizing. Pusey and van Megen's value of $\frac{\phi_M - \phi_F}{\phi_F} = 0.085$ was close to the ideal [Hansen and Schiff, 1973], and they suggest rescaling to an effective volume fraction, $\phi^\natural$, using $\phi_F = 0.494$ as the datum.

Study of the analytical behaviour of the sedimentation velocities of PMMA-PHSA spheres in a mixture of decalin and tetralin over a range of volume fractions, using Pusey and van Megen's method of rescaling, gave Paulin and Ackerson [1990] a value of $\phi_M^\natural = 0.552$, and hence $\frac{\phi_M^\natural - \phi_F^\natural}{\phi_F^\natural} = 0.117$.

Later work by Underwood *et al.* [1994], using carbon disulphide for index matching gave even closer agreement with hard sphere predictions: their value of $\phi_M^\natural = 0.545 \pm 0.02$ was found to be independent of particle size R_p and refractive index of medium n_m. Furthermore, measurements of intrinsic viscosity were consistent with the ideal case and collective diffusion coefficient scaled linearly with R_p and sedimentation velocity with R_p^2 as expected for hard spheres.

Recent work [Phan *et al.*, 1998] using X-ray densitometry of equilibrium sediments to obtain the fluid equation of state as well as viscometry and coexistence region size measurements has only increased confidence in the ability of PMMA-PHSA suspensions in index-matching nonpolar solvents to provide model hard sphere assemblies. Such systems have been used exclusively in the current work.

5.2.3 The preparation of suspensions

In essence, three stages are required in preparing a colloidal suspension as a candidate hard sphere system. First, appropriate particles need to be synthesized; secondly, the particles need to be dispersed in a suitable medium; and thirdly, the desired concentration of particles in the medium needs to be achieved. This

subsection considers each of these stages in turn.

Particle Synthesis

This research has not involved the actual manufacture of colloidal particles, but reference to this stage of suspension preparation is included here for completeness. Details of the methods of synthesizing PMMA spherical latices, and the chemical grafting of the PHSA monolayer coating onto them, can be found in Antl *et al.* [1986] and Pathmamanoharan *et al.* [1989].

These methods have the useful side effect that size polydispersity decreases with mean particle size, so the relatively large particles that are needed for optical resolution are produced with polydispersities that lie within the range required for crystallization to occur. It is a matter of simple experiment to determine whether crystallization occurs, but for more accurate determination of ε_R light scattering techniques are used [Pusey and van Megen, 1984]. In this work, all the suspensions used were characterized, in terms of both size and polydispersity, by the synthesizers.

Solvent replacement

The stock suspensions produced by the above methods have dodecane as their medium. Although the refractive indices of dodecane, 1.42, and PMMA, 1.49, are similar, as required to reduce van der Waals attractions, they are not close enough ($\frac{\Delta n}{n} \approx 0.05$) for optical experiments, due to multiple Rayleigh scattering. So alternative media need to be found and the dodecane replaced.

Decahydronapthalene (commonly called decalin), with $n = 1.48$ (giving $\frac{\Delta n}{n} \approx 0.007$) matches PMMA closely and is a good solvent for PHSA; mixtures of decalin with tetralin (tetrahydronapthalene, $n = 1.54$) can be used to match the refractive indices even more closely. CHPB (cycloheptyl bromide, $n = 1.50$) is another good solvent for PHSA which closely matches refractive index with PMMA, but has the added advantage of matching the density of PMMA more closely ($\rho_{\text{PMMA}} =$

1.19 g cm^{-3} and $\rho_{\text{CHPB}} = 1.29$ g cm^{-3}, whereas $\rho_{\text{decalin}} = 0.89$ g cm^{-3} and $\rho_{\text{tetralin}} = 0.97$ g cm^{-3}).

The process of solvent replacement is examined in detail in Fairhurst [1999b], §4.1.1.; the stages are (1) centrifuge the suspension until it has separated into a dense, randomly packed sediment at $\phi \approx 0.64$ and pure solvent; (2) pour off the pure solvent; (3) add the alternative solvent, thereby diluting the previous solvent; (4) repeat the first three stages until the desired purity of solvent is achieved. Typically this involves 5 to 10 cycles (for precise calculation of the theoretical solvent purity see Fairhurst, *ibid.*). Confirmation of the purity can be achieved by comparing the measured refractive index with the expected value.

Volume fraction determination

Achieving the desired volume fraction could be done by adding/removing known masses of solvent, both microbalances and known solvent densities having high degrees of precision, were it not for a number of complicating factors: the core-shell structure of the PMMA-PHSA spheres, solvent penetration of the shell and possibly the core, and size polydispersity. Fairhurst [1999b], *loc. cit.*, explores these difficulties and their implications for measurement techniques; here the two techniques used in this research are outlined.

A rough measure of volume fraction can be obtained by centrifuging the suspension in a parallel sided container and adjusting the ratio of the heights of sediment and pure solvent. Using the theoretical value of the volume fraction of the sediment [Schaertl and Sillescu, 1994] for the known polydispersity and assuming that the sediment is genuinely random close packed and no crystalline regions exist, the effective $\phi^\natural$ that the particles occupy can be calculated.

If this centrifuging method is used to achieve $\phi_{\text{F}} < \phi^\natural < \phi_{\text{M}}$, the ratio χ of colloidal crystal (clearly distinguishable by optical Bragg scattering) to fluid can be measured. The crystals will sediment and, following Paulin and Ackerson [1990], the height of the crystal-fluid interface can be plotted against time and

extrapolated back to remove the effects of crystal compression and incomplete separation. As χ is a very sensitive measure of $\phi^\natural$, this is a very precise method.

All the samples used in this work had their effective volume fractions calibrated by the combination of these two methods alluded to above. Changes to desired values for particular experiments which lay outwith the coexistence region where then achieved by the addition/removal of carefully measured masses of solvent.

Over time, volume fractions tend to steadily increase, due to solvent evaporation. Keeping track of the mass of suspensions allows one to recalculate ϕ and replace solvent, when required. Evaporation is kept low by sealing suspension containers with air-tight stoppers and PTFE tape.

Chapter 6

The Structure of the Hard Sphere Solid

Predictions of the structure of the ordered, high density phase of the hard sphere system are well known and have been studied both by light scattering and microscopy. In this chapter, using this theoretical and experimental background as a starting point, a detailed microscopical study of the structure of the hard sphere solid is made.

This study is in two parts: First, an extensive set of optical micrographs is presented, showing a variety of defect structures, and a number of characteristic geometrical patterns. The *ab initio* interpretation of the latter in terms of diffraction theory is a formidable task. However, careful consideration of a computer model of the predicted structure, along with the imaging characteristics of the microscope used, allows a number of these patterns to be related, with a high degree of certainty, to particular crystal facets. One particular pattern is shown to provide a direct quantification of the degree of disorder in the solid, making for better statistics than achieved previously by another direct-imaging method.

Secondly, a series of views at various angles, constructed from a stack of micrographs, is used as a demonstration confirming the interpretations given to patterns in the first part of the study.

Such an interpreted collection of images can form the basis of future studies of defects and kinetic processes in colloidal crystals using optical microscopy.

6.1 Background

6.1.1 Predicted structure and crystallographic scheme

The isotropic nature of their interaction means that two-dimensional arrays of hard spheres will arrange themselves with hexagonal order at high density*. In three dimensions, a stacking up of such layers will be the expected arrangement. There will, however, be a degree of randomness associated with this stacking owing to the fact that there are two possible sites for stacking one layer on another.

Both the hexagonal order in two dimensions and the disorder in the third need to be taken into account in describing the structure of the solid.

Stacking probability α

Taking $\vec{a}$ and $\vec{b}$ as the lattice vectors in the hexagonal layers, the two possibilities lie at $(\frac{1}{3}\vec{a} + \frac{2}{3}\vec{b})$ and $(\frac{2}{3}\vec{a} + \frac{1}{3}\vec{b})$ relative to a given layer. Hence there are three possible lateral positions for hexagonal layers to occupy, the only constraint being that adjacent layers be in different positions.

Labelling the lateral position of a reference layer as A, we can label the lateral positions at the displacements given above as B and C respectively (see figure 6.1). An ordered stacking sequence such as ABCABC..., which cycles through the three lateral positions, is known as "face-centred cubic" (*fcc*) packing, whereas one alternating between any two, such as ACACAC..., is called "hexagonal close-packing" (*hcp*).

To quantify the degree of randomness in "randomly-stacked close-packing" (*rscp*) a stacking probability α that any pair of layers two apart have different

*It was Kepler [1611] who first suggested this arrangement for tiny ice spheres, to account for the six-fold symmetry of snowflakes.

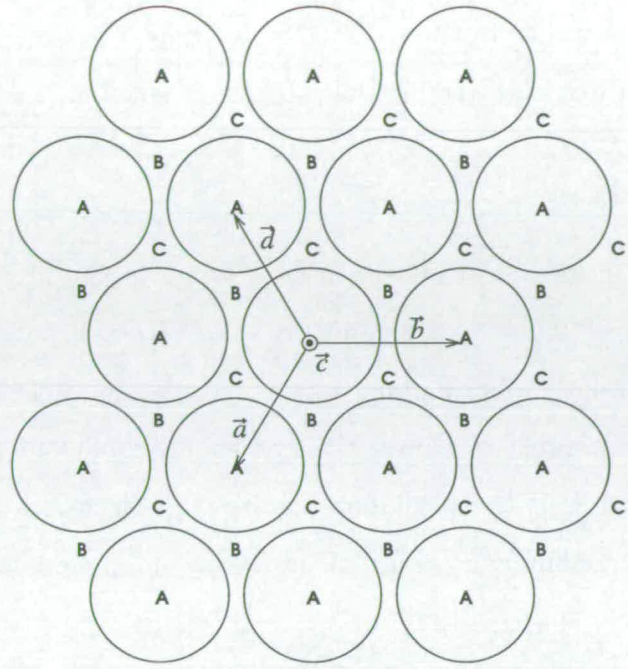

Figure 6.1: A diagram of the view "looking down" on a hexagonal layer of spheres in a crystal of volume fraction $\phi = 0.545$. The different sites for stacking of such layers are labelled A, B and C. Also shown are the lattice vectors $\vec{a}$, $\vec{b}$ and $\vec{c}$, along with the additional lattice vector used in the Miller-Bravais scheme, $\vec{d}$. Since *touching* spheres ($\phi = \phi_{\mathrm{cp}} = \frac{\pi}{3\sqrt{2}} \approx 0.740$) have $a = 2R_p$, for $\phi = \phi_{\mathrm{M}} = 0.545$, this diagram is drawn with $a = 2R_p \sqrt[3]{\frac{\phi_{\mathrm{cp}}}{\phi_{\mathrm{M}}}} \approx 2.22R_p$.

lateral positions is commonly used [Wilson, 1942]. For completely random stacking $\alpha = 0.5$, whereas $\alpha_{fcc} = 1$ and $\alpha_{hcp} = 0$.

The "reduced unit cell"

The stacking disorder means that each differently-stacked crystal will have its own unit cell. For the sake of generality in the labelling of directions within the *rscp* crystal, it makes sense to use a "reduced" unit cell as follows:

The conventional unit cell for *hcp* has $\vec{a}$ and $\vec{b}$ the same as the lattice vectors of the hexagonal layers (see figure 6.1) and $\vec{c}$ perpendicular to the layers and of magnitude equal to twice the spacing between adjacent hexagonal layers. A similar unit cell, but with $c = 3$ layer spacings can be used for *fcc*. There being

no regular repeat distance in the $\vec{c}$ direction for *rscp*, the sensible length scale to use for c in the reduced unit cell is the inter-layer spacing, *i.e.*, $c = \sqrt{\frac{2}{3}}a$.

Miller-Bravais indices

The hexagonal symmetry of the *rscp* crystal suggests the use of the augmented four-index system of Miller-Bravais indices $(hkil)$ to label lattice planes, as this makes symmetry-related planes easier to spot. Under this scheme h, k and l have their usual meaning and i measures the fractional displacement along the third close-packed direction of the hexagonal layers (the direction of $\vec{d}$ in figure 6.1). As $\vec{a}$, $\vec{b}$ and $\vec{d}$ are coplanar, h, k and i cannot be independent; in fact, it can be readily shown that $h + k + i = 0$.

The usefulness of the extra index i in crystals with hexagonal symmetry can be seen by considering the sets of lattice planes $(11\bar{2}0)$, $(1\bar{2}10)$ and $(\bar{2}110)$. The cyclic permutation of the first three indices shows immediately that these three sets constitute a crystallographic **form**, *i.e.* a complete set of symmetrically-equivalent sets of planes. While brackets are used to designate sets of planes, braces are used for crystallographic forms; thus we use $\{11\bar{2}0\}$ represent the form constituted by the three sets mentioned. Using standard Miller indices, it is much less obvious that the sets of planes (110), $(1\bar{2}0)$ and $(\bar{2}10)$ are all symmetrically equivalent and constitute the form $\{110\}$.

6.1.2 Results from earlier work

Light scattering results

The basic interlayer spacing for stacking at any α gives rise to a sharp Bragg reflection in the diffraction pattern. Randomness in the stacking $(0 < \alpha < 1)$ shows up in diffraction from a polycrystalline sample as bands of diffuse scattering underlying Bragg peaks.

Using the theory of these diffuse bands developed some time ago by Wilson [1942] and Hendricks and Teller [1942], Pusey *et al.* [1989] studied the stacking of

colloidal crystals in the sterically-stabilized PMMA hard sphere system. Having confirmed that the crystals were indeed made up of a more or less randomly-stacked sequence of hexagonal layers, they took measurements of the average α and found that crystals nucleating from a metastable fluid at $\phi = 0.535$ had $\alpha = 0.50$, *i.e.* totally randomly stacked, while crystals nucleating from a fluid at $\phi = 0.523$ showed a tendency towards *fcc*, with $\alpha = 0.58$.

A more complete study, by light diffraction, of the dependence of α on the parent metastable fluid density has been performed by Chui [1994].

Microscopical results

The structure of more-or-less randomly-stacked colloidal crystals of rhodamine-labelled silica spheres has been investigated by Verhaegh *et al.* [1995], using *fluorescence* confocal scanning laser microscopy (CSLM). In their work, individual hexagonal layers of particles were imaged one layer at a time, with the depth resolution in turbid samples provided by the confocal optics. This permitted the labelling of a sequence of a few hexagonal layers in terms of A, B or C, thus giving a direct measurement of the stacking probability, α.

6.2 Interpretation of single micrographs

Images of *rscp* polycrystalline solids can be expected to show a variety of patterns of particle arrangements, along with defects, and grain boundaries between regions with different patterns.

Figure 6.2 is a typical example of a micrograph of a hard sphere colloidal crystal. As expected, grain boundaries, vacancies and line defects are all visible. Two types of ordered arrangement are seen: hexagonal, as would be expected in any close-packed structure, and kinked lines, or zig-zags, which shall be shown below to be characteristic of random stacking.

In the following sections, these patterns and others shall be interpreted using

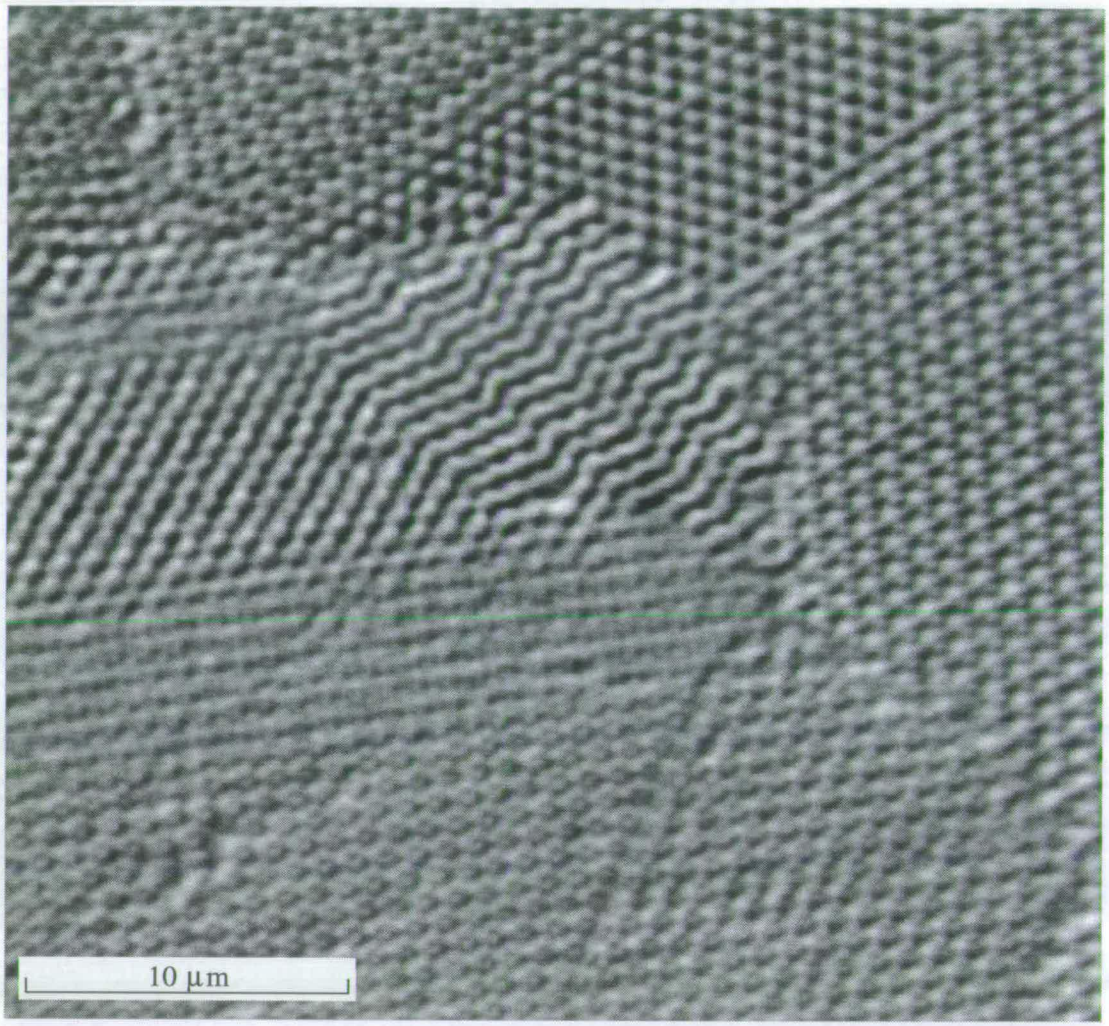

Figure 6.2: A Normarski DIC image, $Z_o = 420$ nm, of a suspension of $R_p = 460 \pm 32$ nm particles, age = 21 days.

a computer model, taking into account the finite-thickness slicing effect of the microscope depth of field.

6.2.1 Experimental details

All the micrographs presented here are of suspensions with volume fractions in the crystal-fluid coexistence range. Particle sizes and depth of field are given for each micrograph; sizes R_p were determined (for the most part by other workers) using static light scattering and depths of field Z_o are the theoretical values given

by equation 4.3, calculated for $\lambda_0 = 550$ nm and $n = 1.5$.

The suspensions were all sealed in rectangular capillaries (as in §4.1.2). The age given on each micrograph is the time elapsed since sealing, *i.e.* how long the suspension will have had to equilibrate from the metastable fluid.

Both phase contrast and Normarski DIC were used, with oil-immersion 100× objectives. Figure 6.4 was recorded using an Olympus BX 50 microscope ($\mathcal{A} = 1.25$); the microscope used for all the other micrographs was a Zeiss Axioskop FS ($\mathcal{A} = 1.40$).

6.2.2 Computer model

To assist with the interpretation, a computer-generated model of a small *rscp* crystal was built, using Molecular Simulations' Cerius^2 software, which is particularly versatile as a tool for the display and manipulation of user-defined crystal structures.

Having decided upon the stacking sequence ACACBAC so as to include both *fcc* and *hcp* stacking, as would be found in a *rscp* crystal, the first step in building the model was to define a hexagonal unit cell containing seven "atoms" at the fractional coordinates $(0,0,0)$, $(\frac{2}{3},\frac{1}{3},\frac{1}{7})$, $(0,0,\frac{2}{7})$, $(\frac{2}{3},\frac{1}{3},\frac{3}{7})$, $(\frac{1}{3},\frac{2}{3},\frac{4}{7})$, $(0,0,\frac{5}{7})$ and $(\frac{2}{3},\frac{1}{3},\frac{6}{7})$. Next, an array of $5 \times 5 \times 1$ unit cells was built into a small crystal of 175 particles, which could then be displayed in any desired orientation, specified either by azimuth and co-latitude or as parallel or perpendicular to a chosen crystal plane.

Figure 6.3 shows this model, with the boundaries of the unit cells picked out by dashed lines, and the radius of the "atoms" set at $a/2.22$, so that $\phi = \phi_{\mathsf{M}} = 0.545$, as in figure 6.1.

By faceting the crystal parallel to the plane of view thin slices of the model corresponding to the microscopical depth of field were made. In this manner a means of modelling the effect of the microscope's imaging of *rscp* crystallites in arbitrary orientations was arrived at.

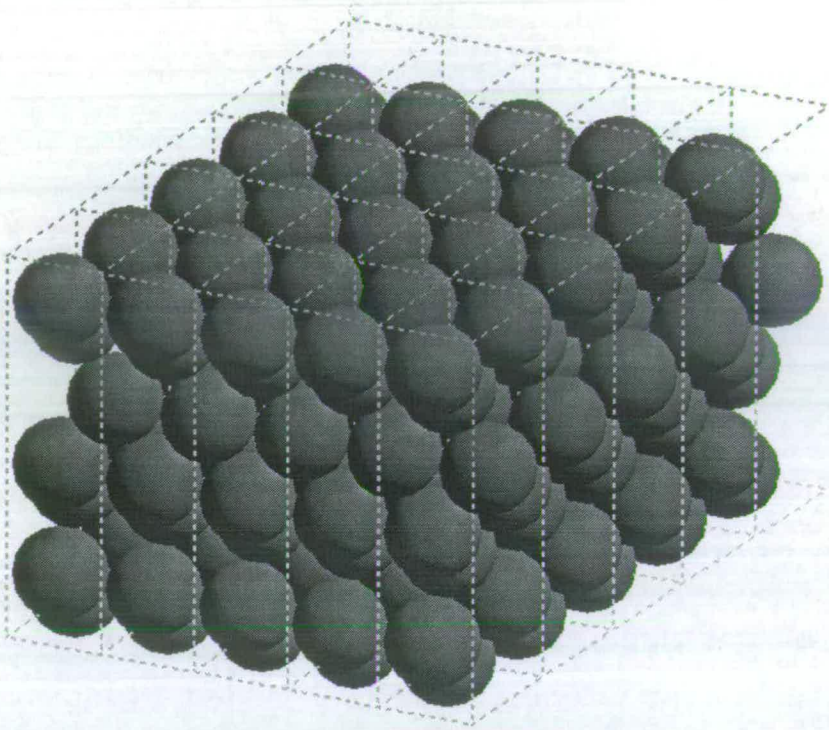

Figure 6.3: A computer visualization of seven hexagonally packed layers stacked in the sequence ACACBAC (from the bottom).

In the interpretations following, these conventions shall apply:

- For the sake of generality, the "reduced unit cell" scheme ($c = \sqrt{\frac{2}{3}}a$) shall be used, although the computer model was based on a seven-layer unit cell.
- Views of the model shall be labelled by the Miller-Bravais plane which is parallel to the plane of the figure.

6.2.3 Hexagonal patterns

Any crystal consisting of stacked hexagonal layers should reveal evidence of this hexagonal order if the crystal is oriented with the stacking direction along the optical axis of the microscope, *i.e.*, the (0001) view is taken.

Figure 6.2 shows a number of crystallites in this orientation. Despite differences in the contrast and distinguishability of the PMMA spheres in different parts of the image, hexagonal order on the same length scale is clear.

The differences in contrast and distinguishability can be explained with reference to the depth of field and the spacing of the particles: For $\phi = 0.545$ and $R_p = 460 \pm 32$ nm, the hexagonal layers are $\sqrt{2/3}a = 830$ nm apart. While a plane through the centres of the particles in a layer intersects only with the particles of that layer, planes more than $\sqrt{2/3}a - R_p = 370$ nm from the centres of the particles of one layer will also intersect with a second layer. With a depth of field $Z_o = 420$ nm, this means that focusing at more than 160 nm from the centre of a layer will image parts of two layers. For crystallites intersected at random one would therefore expect to see clear images of single layers only in about 40% of (0001) views. The left-hand images of figure 3.13(b) and (c) illustrate the difference between focusing directly on a hexagonal layer and at one particle radius below this.

On the other hand, scanning the plane of focus through such crystallites will allow individual planes to be imaged, which explains the shift of particle positions seen when this is done. Lateral positions A, B, or C can then be assigned to individual layers and the stacking probability α determined, after Verhaegh *et al.* [1995].

In terms of interpreting patterns however, the key point is that:

The hexagonal pattern represents the (0001) view of an *rscp* crystal.

6.2.4 Zig-zag patterns

In the upper centre of middle of figure 6.2 is a crystallite presenting a facet in which a more-or-less random sequence of "zig-zags" can clearly be seen. This pattern is often seen in hard-sphere colloidal crystals and has the property that, when the plane of focus is changed, particle positions do not appear to shift, indicating that, from this direction of view, particles are arranged directly behind

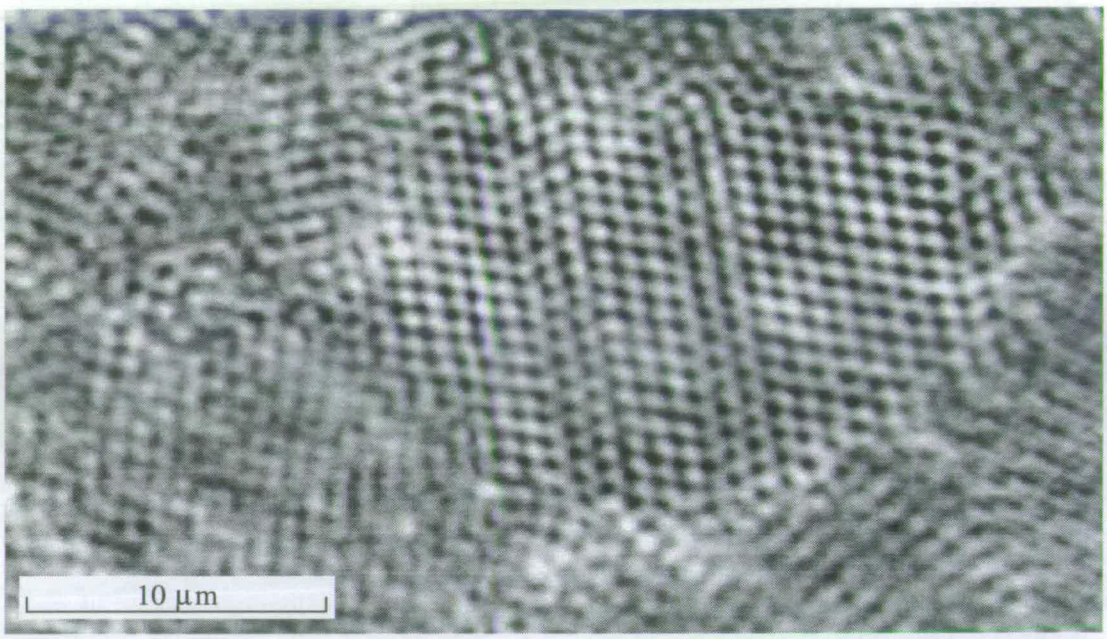

Figure 6.4: Zig-zag pattern (Phase contrast image, $Z_o = 530$ nm; $R_p = 460 \pm 32$ nm; age = 4 hours)

one another. Figure 6.4 shows a large crystallite with this pattern, this time in phase contrast.

The $(11\bar{2}0)$ view of the computer model, shown in figure 6.5(a), looks at the stacked hexagonal planes "sideways" (seen as horizontal lines) and shows a "zig-zag" pattern which can be traced down the image, with an angle that appears similar to that of the micrograph. Moreover, although this figure is a thin slice of the model, viewing the entire $5 \times 5 \times 1$ model shows no difference in the number of spheres seen, which can only mean that the other spheres must lie directly behind those seen.

Consideration of the model's parameters tells us that the spacings of the spheres in this view are given by: $\mathrm{SQ} = \mathrm{ST} = \frac{\sqrt{3}}{2}a$ and $\mathrm{RT} = \sqrt{\frac{2}{3}}a$. Therefore the angle that the zig-zags slant at an angle $\zeta = \angle\mathrm{RST} = \arccos\frac{1}{3} \approx 70.5°$ to the hexagonal layers.

Before comparing these values with measurements from the micrograph, we must consider the effect of the depth of field on the $\{11\bar{2}0\}$ view. Careful ex-

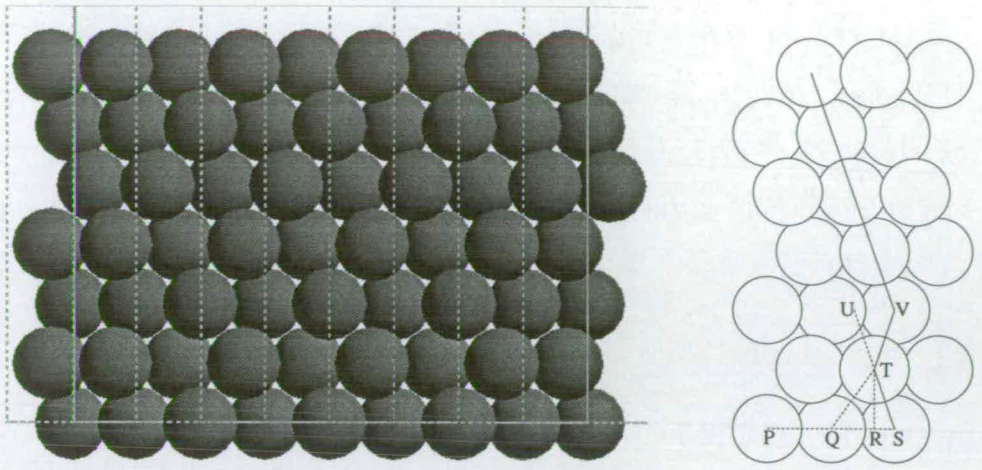

Figure 6.5: The zig-zag pattern seen in the $(11\bar{2}0)$ view (a) computer model (b) diagram highlighting the "zig-zag" feature.

amination of the thin slice in figure 6.5(a) reveals that the spheres shown are at two different levels. Consideration of the geometry of the (0001) layers leads to a value of $a/2$ for the distance between these two levels. The thickness of the slice was chosen to be just enough to show both levels. Any thinner slice shows zig-zags slanting at an angle $\aleph = \angle\mathrm{SQT} = \arccos\frac{1}{\sqrt{3}} \approx 55°$ and particles with a horizontal spacing of 2SQ, whereas any thicker slice shows no difference. The particle spacing perpendicular to this view is a. So, for $Z_o > a - 2R_p$, any $\{11\bar{2}0\}$ view will always show particles on two levels and, for $Z_o > a/2$, it will be impossible to distinguish these two levels.

For $\phi = 0.545$ and $R_p = 460 \pm 32$ nm, we have $a - 2R_p = 100$ nm and $a/2 = 510$ nm. As figure 6.4 has $Z_o = 530$ nm, the criteria for showing zig-zags slanting at the measured $70.5 \pm 0.5°$ are met. The predicted spacing of the hexagonal layers, $\sqrt{\frac{2}{3}}a = 830$ nm, also compares favourably with the measured value, 840 ± 13 nm.

However, the predicted spacing within the layers in the $\{11\bar{2}0\}$ view, $\frac{\sqrt{3}}{2}a = 880$ nm, is much larger than the measured value, 810 ± 16 nm. It is possible, though, for the particles to be more closely packed than in the model: for $\phi = 0.74$, we would expect $\frac{\sqrt{3}}{2}a = 800$ nm.

So, if the crystal were compressed parallel to the line of intersection between the {0001} and $(11\bar{2}0)$ planes, *i.e.* along the direction PQRS, until the particles were nearly at close-packing, the particle spacings would match the predicted values in all directions within the plane of the view. Moreover, no change in the angles of the zig-zags would be expected, so we can say with confidence that:

The zig-zag pattern represents a $\{11\bar{2}0\}$ view of an *rscp* crystal.

It is worth noting at this point that the each "zig" or "zag" is itself the trace of an hexagonal layer, of the form either $\{1\bar{1}01\}$ or $\{\bar{1}101\}$.

Given this identification, we now turn to the relationship of the zig-zags to the stacking sequence of an *rscp* crystal. Any instance of stacking we can consider to be either cycling forward through the three layer types, A, B and C, or backward. Thus *fcc* would be continuously "forward cycling" or continuously "backward cycling"; *hcp*, on the other hand, would be alternating between forward and backward cycling with every layer.

In figure 6.5, kinks occur at layers 2 and 3. Consideration of the stacking order shows that these kinks occur every time the stacking sequence changes its direction of cycling, the three segments of the zig-zag being AC, CA and ACBAC.

This means that:

Crystallites showing the zig-zag pattern can have their stacking probability α determined from a single image, without the need for axial scanning.

So, this method for the direct determination of the stacking probability α is able to achieve good statistics with much less effort than the method involving scanning through (0001) views.

Determining α from zig-zags

For a crystallite with κ kinks in $N_=$ hexagonal layers, it can be readily seen that

$$\alpha = 1 - \frac{\kappa}{N_= - 2}. \tag{6.1}$$

Thus the crystallite in figure 6.4, with $\kappa = 6$ and $N_{=} = 30$, has $\alpha = 0.79$.

The results (reported in Elliot *et al.* [1997]) of counting κ and $N_{=}$ in six crystallites showing zig-zags in a suspension with $\phi = 0.529 \pm 0.03$ are given in table 6.1. The mean value $\langle\alpha\rangle = 0.60 \pm 0.07$ is consistent with the data of Chui

$N_{=}$	26	40	28	36	35	51
κ	12	12	10	11	14	22
α	0.50	0.68	0.62	0.68	0.58	0.55

Table 6.1: Measurements of stacking probability α from the zig-zag patterns shown by the $\{11\bar{2}0\}$ view of *rscp* crystallites.

[1994], who obtained $\alpha = 0.550 \pm 0.005$ for fresh crystallites nucleating from a metastable fluid at $\phi = 0.532 \pm 0.003$. Continued observation of the sample over time suggested that there is a tendency for α to increase, *i.e.*, the structure was becoming more *fcc*-like. This is again consistent with the observations of Chui [1994].

Recently [Jackson and Bruce, 1999], simple theoretical considerations, fitted to simulation results, have suggested a relationship between α and the number of particles per hexagonal layer $N_{||}$ of the form

$$\alpha = \frac{1 + \tanh(N_{||}\Delta S)}{2}, \tag{6.2}$$

where ΔS is the entropy difference (per particle) between an *fcc* arrangement and an *hcp* one.

The measured crystallites showed no evidence of being significantly elongated or squashed, so the assumption $N_{||} \propto {N_{=}}^2$ seems reasonable. Figure 6.6 uses this assumption, in comparing the data of table 6.1 with the simulation result, plotted with Jackson and Bruce's value of $\Delta S = 44 \times 10^{-5} k_B$. From this we can see that the experimental data are both consistently below the simulated curve and show an altogether slower variation with $N_{=}$. These discrepancies need to be explored further, but the point to be made here is that only microscopical techniques, of

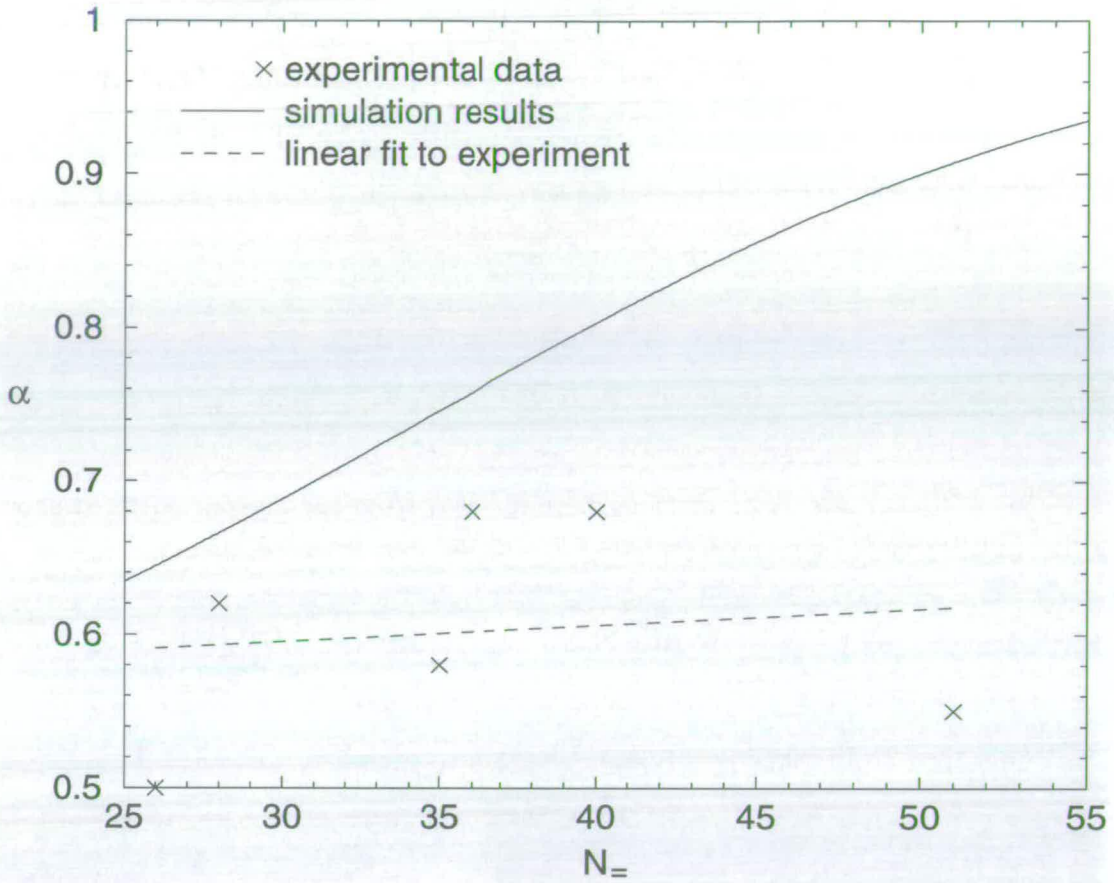

Figure 6.6: Experimental measurements of stacking probability compared with simulation results.

which the zig-zag technique is particularly user-friendly, could have allowed these comparisons to have been made.

Zig-zags and twinning

The change in the direction of cycling through layer types which gives rise to a kink may be considered as marking the boundary between *fcc* twins. This is most obvious where only a single kink is seen, as in figure 6.7. Under this scheme *hcp* is the limit of maximum twinning, but this is not usually the most helpful way to think of it.

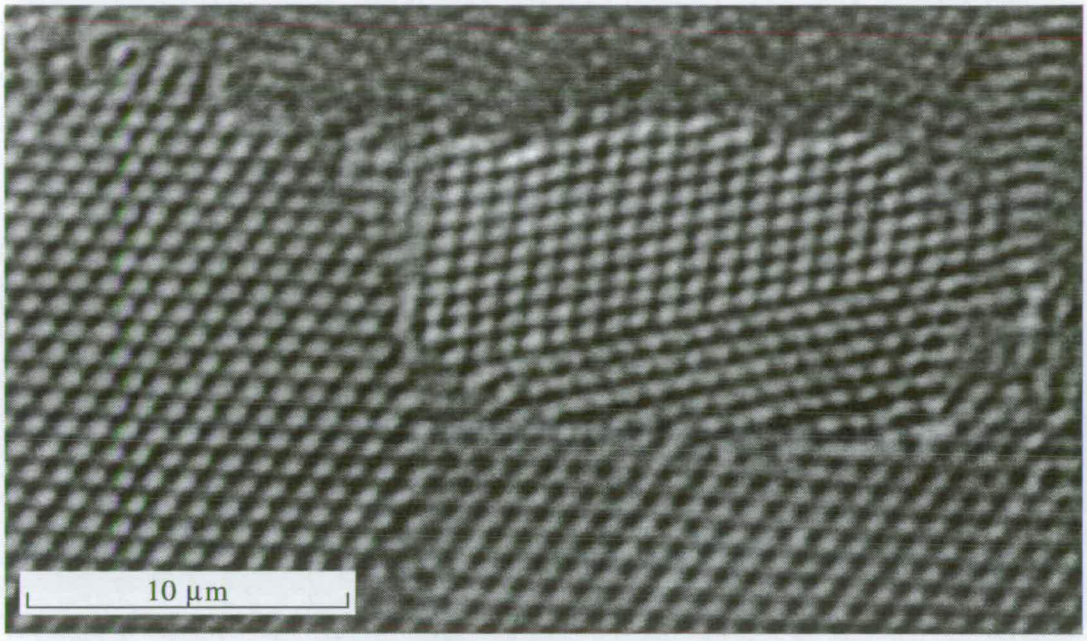

Figure 6.7: A zig-zag pattern with only one kink (DIC image, $Z_o = 420$ nm; $R_p = 460 \pm 32$ nm; DIC, age = 21 days)

6.2.5 Disjointed-line patterns

Figure 6.8 shows particles arranged in lines running across the micrograph; sometimes the particles in adjacent lines are aligned directly with one another, but sometimes they are so that the particles in one line are level with the gaps between particles in the other. This gives a somewhat disjointed effect overall. This effect is enhanced when the plane of focus is changed: the lines remain in place but the particles change their alignments.

Measurements of the micrograph show that, where the lines are "in register", the particles are arranged rectangularly. The particles' spacing along the lines was found to be 895 ± 19 nm, whereas the spacing of the lines themselves was 734 ± 12 nm.

The presence of such clear lines of particles suggests that this view, like the one revealing the zig-zag pattern, is "side-on" to the stacking direction, the trace of the hexagonal layers being responsible for the prominent lines. One such view is that parallel to the $\{10\bar{1}0\}$ crystal form. Figure 6.9 shows three successive slices

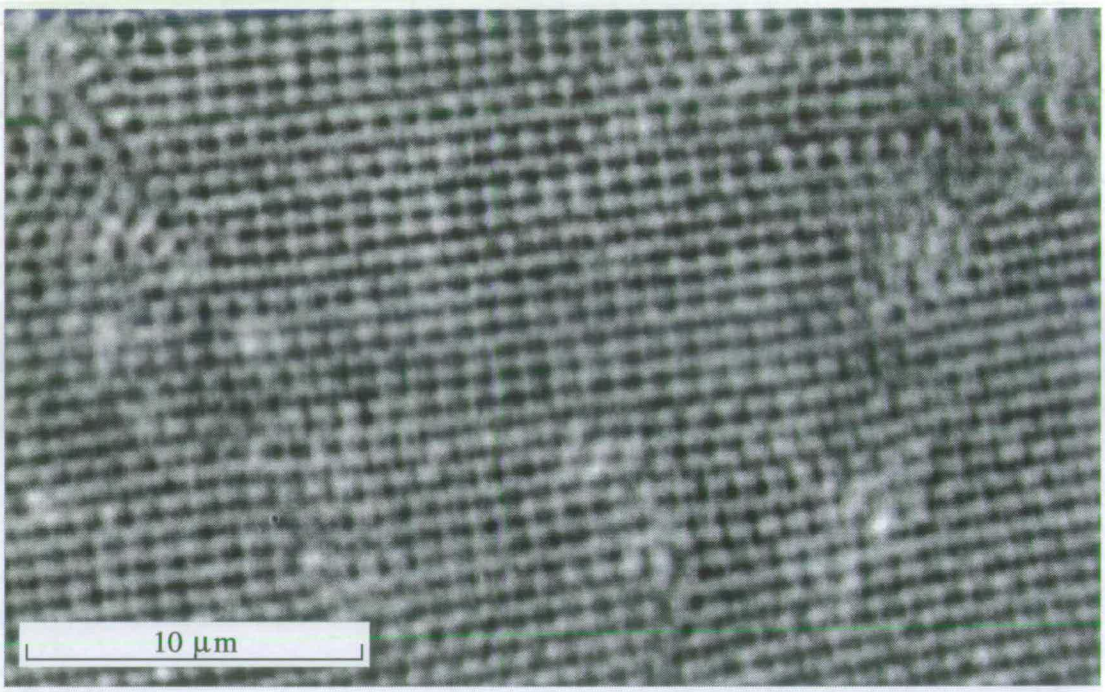

Figure 6.8: Disjointed lines (Phase contrast, $Z_o = 420$ nm; $R_p = 460 \pm 32$ nm; age = 59 days)

through the Cerius[2] model in this view, each slice containing all the spheres with centres lying in planes less than $\frac{\sqrt{3}}{2}a$ apart.

The middle image in figure 6.9 shows a rectangular arrangement of particles very clearly, with a single displaced line. The other two images also show this arrangement, although only a pair of lines are in register in each case. The spacing of the particles along the lines is a, whereas the lines are spaced by $c = \sqrt{\frac{2}{3}}a$.

These dimensions compare very favourably with the measured values, as long as the crystal is taken to be close-packed, so that $a = 2R_p$. In this case, and using $R_p = 460 \pm 32$ nm, the model gives $a = 920$ nm and $c = 750$ nm, whereas the micrograph has 895 ± 19 nm and 734 ± 12 nm. That the colloidal crystal should be at $\phi = 0.74$ rather than 0.545 is reasonable, given the time that the suspension has had to settle under gravity.

The thickness of the model slices in figure 6.9 was chosen to ensure that the traces of the hexagonal layers showed only a single line of spheres, yet that

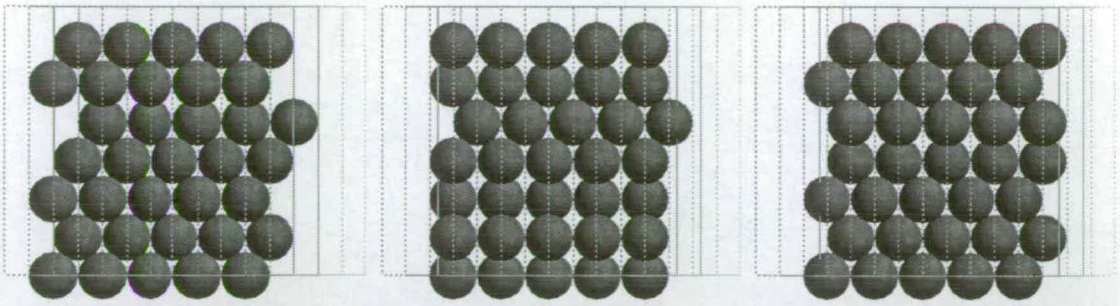

Figure 6.9: Disjointed-line patterns seen in $(10\bar{1}0)$ sections.

all three types of layer, A, B and C, would show a line. The particle spacing perpendicular to the $\{10\bar{1}0\}$ view is $\frac{\sqrt{3}}{2}a$, so the slices must be thinner than this. On the other hand the maximum displacement of one layer type to any other in this direction is two-thirds of this, setting a minimum thickness to the slices.

The equivalent depth of field of the model slices, for close-packed spheres of radius 460 ± 32 nm is therefore in the range 530 to 800 nm. Although the quoted value of Z_o is 420 nm, this is the theoretical value and, as has been seen previously, the experimental value for phase contrast may be as much as twice this, which would agree well with the model. The three different views of figure 6.9 would then represent the effect of changing the plane of focus. The way that the lines remain in place, but their alignments shift is just like the way that the micrograph pattern changes on refocus. It would seem that we can say with confidence that:

The disjointed-line pattern represents a $\{10\bar{1}0\}$ view of an *rscp* crystal.

While it is not possible to determine α from a single image in this view, it can be found by a comparison of two such views of the same crystallite, parallel but differing in the manner of figure 6.9, which would allow the stacking sequence to be determined.

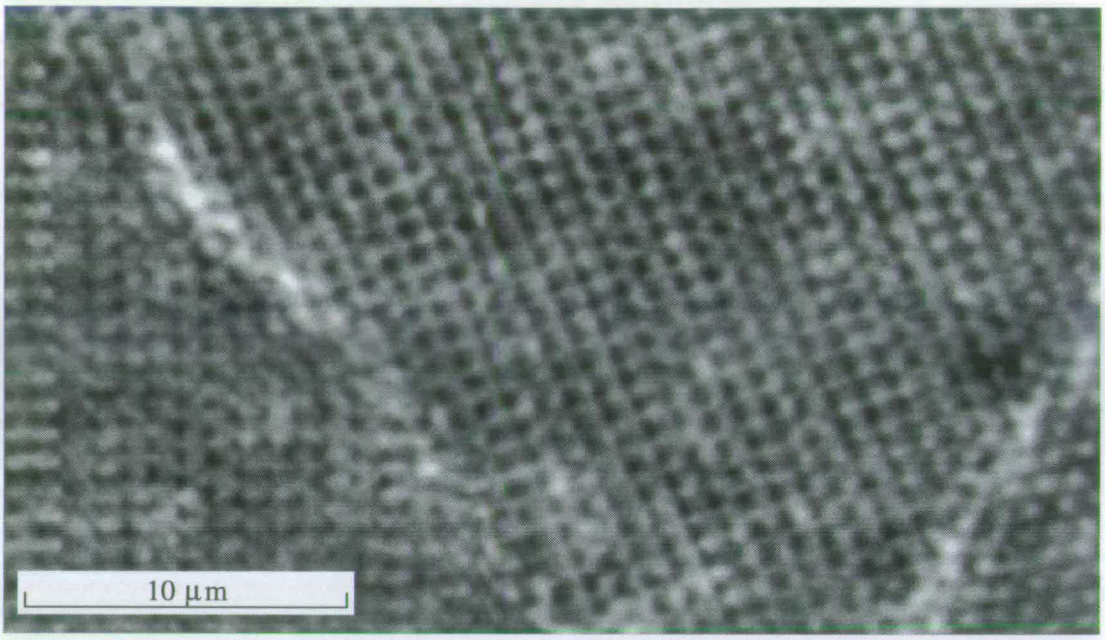

Figure 6.10: Square pattern (Phase contrast image, $Z_o = 420$ nm; $R_p = 460 \pm 32$ nm; age = 21 days)

Edge dislocations

Further confirmation that this pattern is evidence for a side-on view of the hexagonal layers comes from the presence of a number of edge dislocations in figure 6.8. These can been easily found by tracing along the lines of the pattern. The clearest example is just above the scale bar, towards its right-hand end.

6.2.6 Square patterns

The pattern shown in the majority of figure 6.10 is superficially similar to the disjointed lines of figure 6.8: lines of particles (here running almost vertically), sometimes with the particles in adjacent lines in register, sometimes not. However, measurement of the particle spacings shows that, where the lines are in register, the particles are an array that is very close to being square: the lines are spaced at 907 ± 13 nm intervals, whereas the particles are spaced at 895 ± 13 nm intervals along the lines. Both these dimensions are very close to the particle

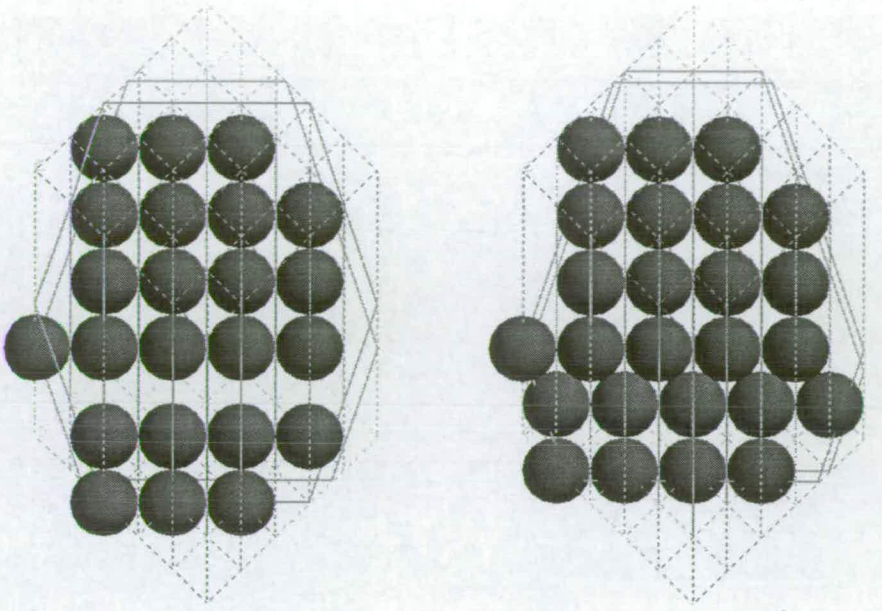

Figure 6.11: The square pattern seen in the $(3\bar{3}02)$ section.

diameter of 920 ± 64 nm.

Square order is characteristic of *fcc* stacking. The faces of the face-centred cubes which show this square order are represented by the $\{3\bar{3}02\}$ form in our reduced hexagonal crystallographic scheme[†]; under this scheme, the squares are of side a, so, if the squares in figure 6.10 are the same as these ones, it would appear that the crystal is close-packed, which would be reasonable, given the age of the suspension.

To display this view (figure 6.11), the computer model (figure 6.3) was modified to consist of only 6 hexagonal layers by removing the top one; this enabled the conversion of the Miller-Bravais indices to those appropriate to the model unit cell to be done in terms of integers. Two slices of the $(3\bar{3}02)$ view are shown, each of thickness $\frac{\sqrt{2}}{3}a$, equivalent to 430 nm $\approx Z_o$, for $\phi = 0.74$ and $R_p = 460 \pm 32$ nm. Both slices show two regions of primitive square order: the top four layers, in the (*fcc*) sequence ACBA, and the bottom two layers (AC); these two regions lie at

[†]In the more usual cubic system this is the $\{100\}$ form; in the standard hexagonal *fcc* scheme it is $\{1\bar{1}02\}$.

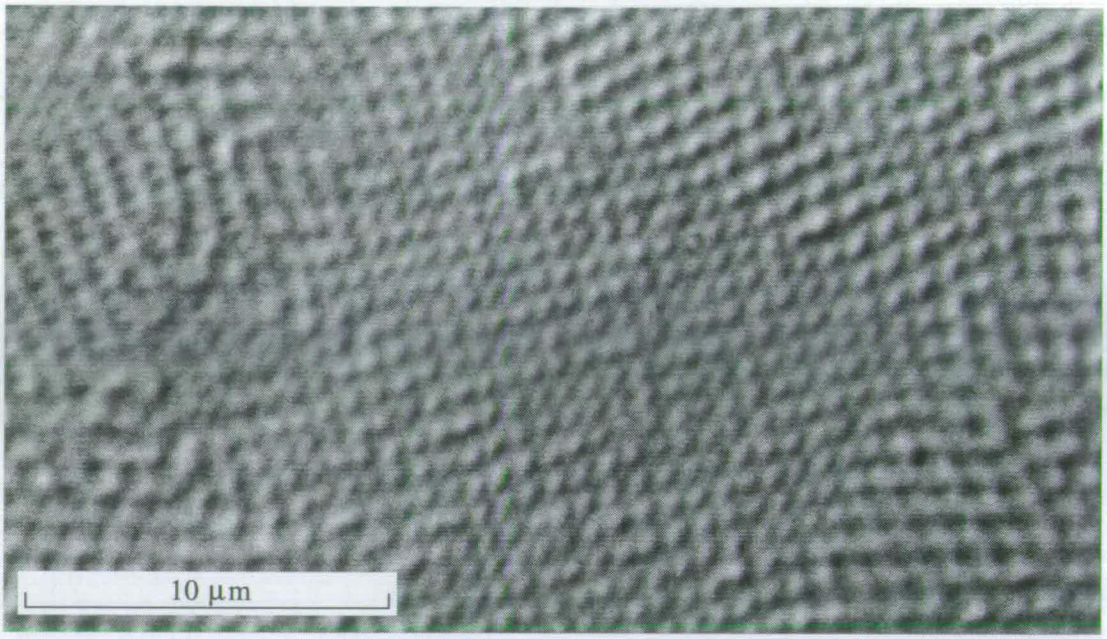

Figure 6.12: Small square pattern (DIC image, $Z_o = 420$ nm; $R_p = 540 \pm 27$ nm, age = 57 days)

different heights. The difference lies in the relative positions of the two regions.

Considering a view perpendicular to this plane, such as the $(11\bar{2}0)$ view, as in figure 6.5, where the traces of the square planes are shown by lines of particles slanting at $\aleph = \angle\mathrm{SQT} = \arccos\frac{1}{\sqrt{3}} \approx 55°$, shows the difference in the levels due to the zig-zag at hexagonal layers 2 and 3.

As the plane of focus is shifted in the $(3\bar{3}02)$ view, each square region alternates between two lateral positions, the particles in each lying in the gaps of the other. This alternation occurs for an axial shift of $\frac{a}{\sqrt{2}}$, but, as the planes of particles in each region are at different levels, the alternation of the regions between their two positions will occur at different positions of focus, giving two possible relative positions of the two regions, as in figure 6.11. The right-hand arrangement in figure 6.10 appears more frequently.

Sometimes, square order of a length scale rather less than the particle size is seen, as in figure 6.12. In the centre of this micrograph is a region where

what appear to be smaller particles than are seen in the rest of the field of view are arranged on lines at about 85° to one another (at about 17° and 103° from the rightward horizontal). The spacings of these particles are 740 ± 20 nm and 780 ± 20 nm along the two sets of lines. These distances correspond to roughly $\sqrt{2}R_p = 760 \pm 40$ nm.

This can be explained if the plane of focus is situated exactly half way between the two possible lateral positions of the square pattern of figure 6.11. This plane lies at $\frac{a}{2\sqrt{2}}$ from the "normal" square layers, a distance equivalent to 380 to 430 nm for $R_p = 540 \pm 27$ nm, depending upon how close-packed the crystal is. This distance is comparable with the depth of field, so, while neither of the adjacent square layers would be clearly imaged, parts of spheres from both would be. Given that the spheres in each layer are arranged in square of side a and that the spheres in one layer sit in the gaps between the spheres of the other, a spacing of $\frac{a}{\sqrt{2}}$ would be expected. For close-packing, this would be the $\sqrt{2}R_p$ value measured.

Figure 6.13 is another $\{3\bar{3}02\}$ view, this time the $(3\bar{3}0\bar{2})$ one. By displaying a thicker slice than previously and reducing the apparent particle size, square order at 45° to the normal pattern and with a spacing $\frac{a}{\sqrt{2}}$ can be seen in a band of 4 lines towards the bottom of the left-hand image. The right-hand image shows the particles at the proper size for $\phi = 0.74$, but viewed side-on to show the thickness of the slice. What is also apparent from this view is that this square order is due to particles in hexagonal layers 2 and 3 of the six layer model, *i.e.* the stacking sequence CA.

In the upper portion of the $(3\bar{3}0\bar{2})$ slice can be seen a more hexagonal arrangement of particles. Figure 6.12 shows a similar pattern at the upper-right edge of the "small square" region. As can be seen from the side on-view of the model, this pattern is due to the stacking sequence CABA of layers 3 to 6 of the model, which is the opposite *fcc* sequence to the region of the small squares, suggesting that the edges of the band in figure 6.12 represent stacking faults.

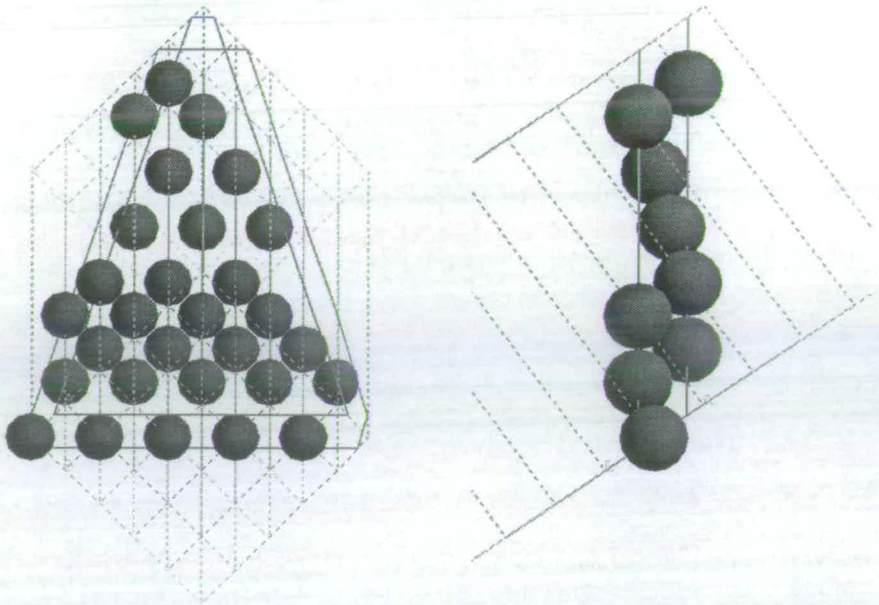

Figure 6.13: The square pattern seen in the $(3\bar{3}0\bar{2})$ section, with reduced particle size, and a view perpendicular to it, but with natural particle size.

So, whether of "normal" or "small" spacing, it would appear that:

Square order is found in $\{3\bar{3}02\}$ views of *rscp* crystals.

6.2.7 Other patterns

The patterns described above are not the only ones to be found in colloidal crystal. This section presents some others, which have not yet been as fully explained, but which are nonetheless worth reporting, albeit with rather tentative explanations.

Five-fold symmetry

Occurrence of five-fold symmetry is always of interest in crystallography. Figure 6.14(a) shows two particles (highlighted by dotted circles) which appear to be at five-fold centres of symmetry.

Examination of the appearance of the surrounding regions suggests that something akin to the zig-zag pattern could explain this image. Indeed, both particle

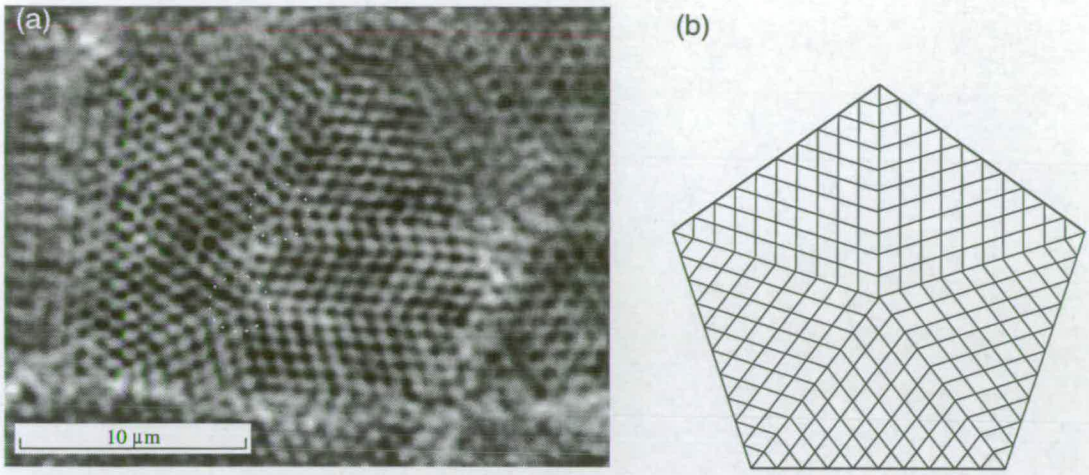

Figure 6.14: Five-fold symmetry? (a) Phase contrast image, $Z_o = 420$ nm; $R_p = 460 \pm 32$ nm; age = 21 days (b) Scheme for "pentagonal twinning".

spacings and the angles of their slanting lines are close to the zig-zag values. Remembering that the kinks of the zig-zag view can be considered as twin boundaries and that the angle between the (0001) hexagonal layers and the $\{1\bar{1}01\}$ slants (themselves traces of hexagonal layers) is $\zeta = \arccos\frac{1}{3} = 70.5° \approx 72°$, one could imagine that, with a small amount of distortion, a form of twinning whereby five-fold symmetry could be achieved.

Figure 6.14(b) shows a possible scheme: at twin boundaries of the zig-zag type, the (0001) planes of both twins are parallel to the boundary. However, the distinction between (0001) and $(1\bar{1}01)$ is arbitrary in an *fcc* region, so another twin boundary, at 70.5° to the first is possible. Repeating this rotation another three times would complete a pentagonal set of twins, if a small amount of distortion of the zig-zags were permitted. The sets of parallel lines in the figure represent the (0001)/$(1\bar{1}01)$ plane traces and show how this twinning scheme might work.

The situation in the micrograph is obviously more complicated than this and needs more careful explanation, but some form of multiple twinning would seem to be clear.

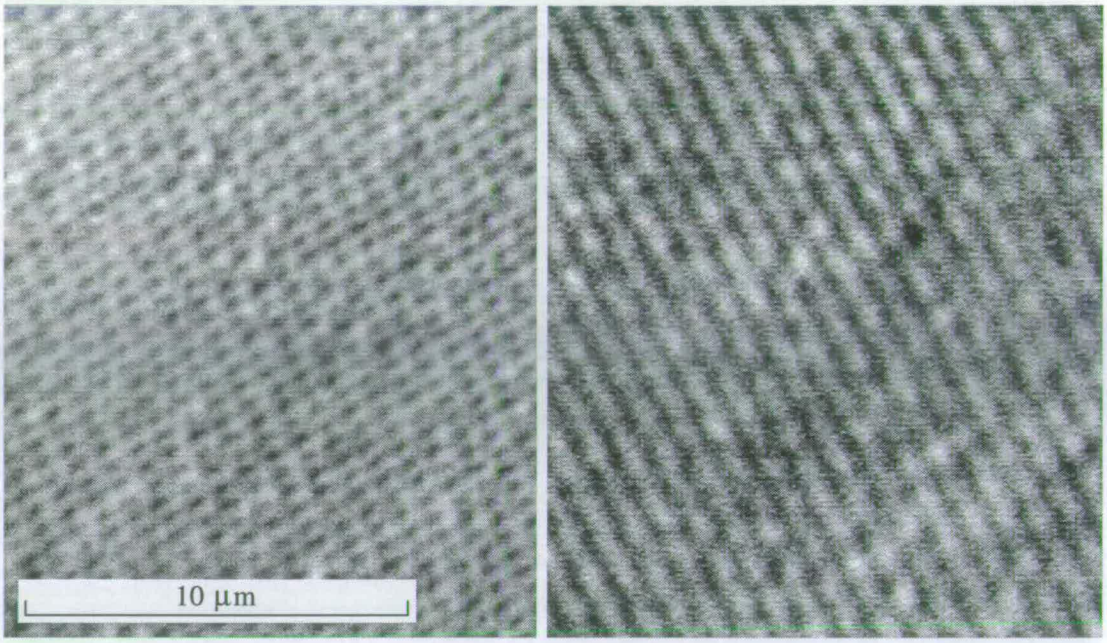

Figure 6.15: Linear patterns (DIC images; $R_p = 540 \pm 27$ nm; age = 57 days; (a) $\mathcal{A}_C = 0.9$ (b) $\mathcal{A}_C = 0.1$)

Lines

The peculiar symmetry of *rscp* crystals means that lines spaced comparably with the hexagonal layers are a common feature of micrographs of colloidal crystals, whereas order along the lines, with or without coordination between lines, can take many forms (as witnessed to above), if it is apparent at all.

Figure 6.15 shows an interesting variation on this theme. Both (a) and (b) show the same field of view, but the resolution of (b) is much decreased due to greater coherence of the illumination.

Common to the images is a length scale of 823 ± 40 nm, representing the spacing of lines running from top left to bottom right. For $R_p = 540 \pm 27$ nm, the layer spacing $\sqrt{\frac{2}{3}}a = 882 \pm 44$ nm for $\phi = 0.74$ and 795 ± 40 nm for $\phi = 0.545$, so this line spacing is consistent with the lines being traces of the hexagonal layers.

The interesting feature of figure 6.15 is the extra detail that DIC is able to bring to the lines (a phase contrast image of this field of view is very similar to

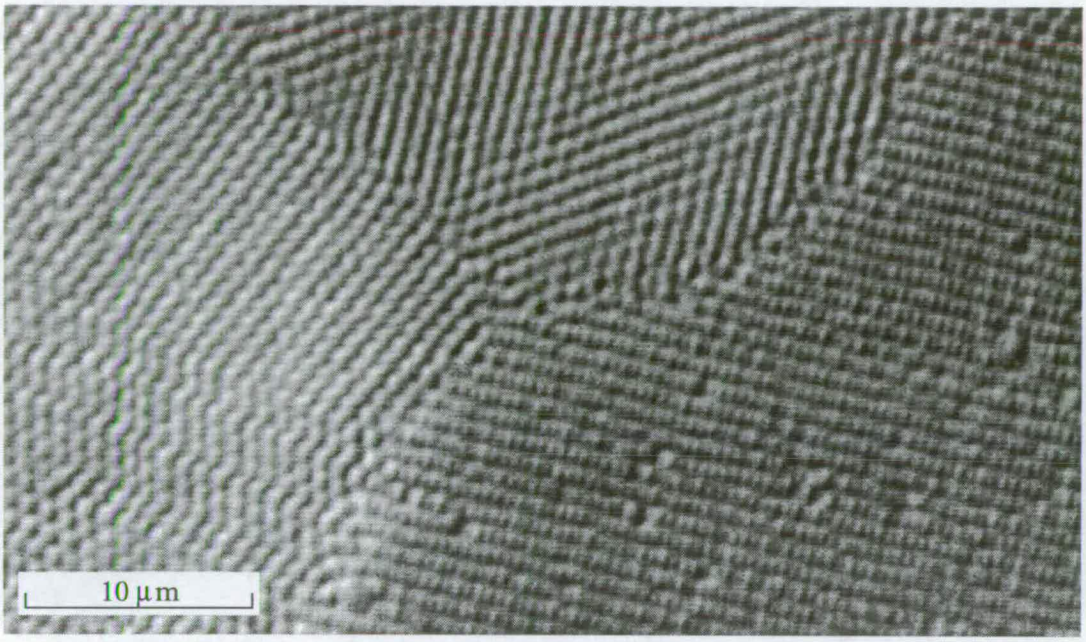

Figure 6.16: $R_p = 540 \pm 27$ nm, $Z_o = 420$ nm, DIC, age = 57 days

(b)). This detail is on a length-scale of 528 ± 10 nm, which is very close to $\frac{a}{2}$ if the crystal is close-packed, a contention the age of the suspension would support and the line spacing would allow. What is not apparent from this single micrograph is that a shift of focus causes the lines shift laterally, indicating that this view is not perpendicular to the c-axis, so a value for the line spacing of slightly greater than the layer spacing is understandable.

The question remains, then, of what might cause order on a length scale of $\frac{a}{2}$ within the layers. What seems most likely is that, due to the better optical sectioning of DIC (with a large condenser aperture), a slice between close packed lines is being seen and that this view may well be related to the disjointed lines of the $(10\bar{1}0)$ view, but further analysis is required.

Herringbone

Figure 6.16 shows parts of three crystallites: one showing the zig-zag pattern, another the lines of figure 6.15(a) and a third a sort of "herringbone" effect of

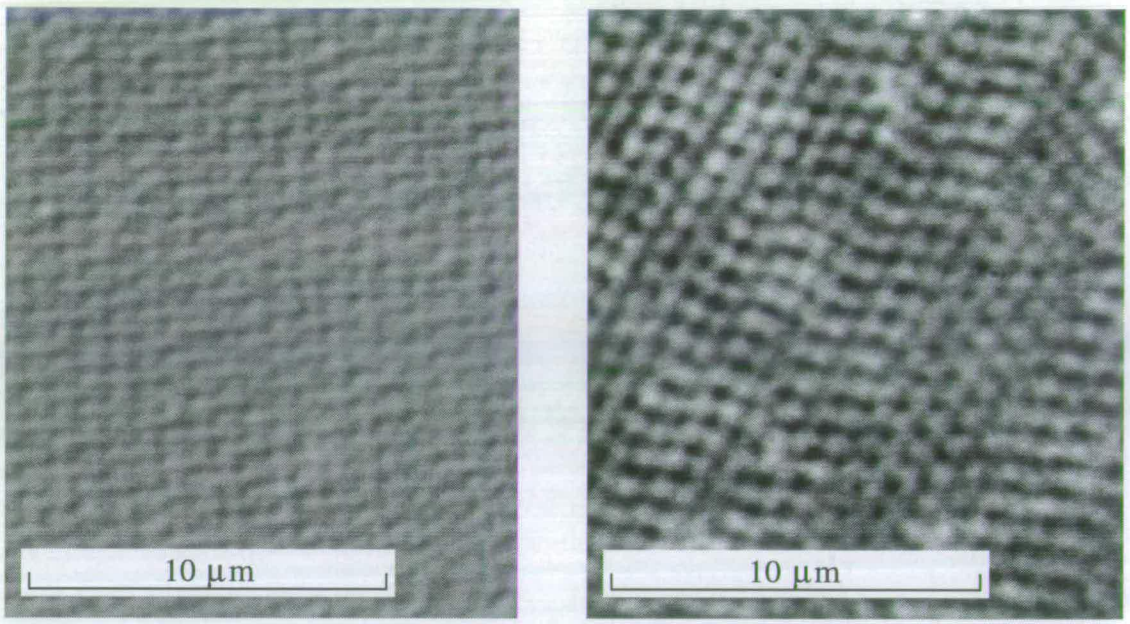

Figure 6.17: (a) "Basket weave", DIC image (b) Imperfect zig-zags, phase contrast image ($R_p = 460 \pm 32$ nm; $Z_o = 420$ nm; age = 59 days)

alternating bands of slanting lines. These lines are spaced at 811 ± 17 nm and those in adjacent bands slant at $56 \pm 0.5°$ to one another.

The way that particles appear to go in and out of focus across the herringbone pattern suggest that the section seen in this crystallite is at an angle to any one plane of particles. In the case of hexagonal patterns, it is not unusual to find crystallites where particles are clearly in focus only in bands across a crystallite. The regular spacing of such bands, which shift on focusing, supports the idea that it is a view tilted at a small angle to (0001) that is being imaged and suggests that the band spacing could be used to determine the angle of the tilt. However, in the case of this herringbone effect, while the lines within the bands shift on focusing, the bands themselves remain in place, so a more subtle explanation is needed.

Basket-weave

Figure 6.17(a) shows a "basket-weave" pattern only ever observed in DIC images.

The vertical "warp" is spaced by 764 ± 24 nm $\approx (0.83 \pm 0.03)a$ for $a = 2R_p$, as in close packing, so this could be due to the hexagonal layer spacing at $\sqrt{\frac{2}{3}}a \approx 0.816a$. The "weft", while appearing to run at right angles to this on a local scale, gives an effect of being angled $72.5 \pm 1.0°$ in the larger view, so some evidence for *fcc* stacking may possibly be here.

Imperfect zig-zags

Figure 6.17(b) shows a pattern in many ways similar to the zig-zags of the $\{11\bar{2}0\}$ view: the lines running from top right to bottom left are spaced by 740 ± 10 nm $\approx (0.80 \pm 0.01)a$ for $a = 2R_p$, and the zig-zag pattern tilts at $69.5 \pm 1.0°$ to these lines. However, the zig-zags are not as clearly imaged as in the "proper" pattern and sometimes the particles in adjacent lines appear to almost line up with one another.

* * *

The patterns presented in this section, some explained in detail and others requiring further analysis, have shown many of the features to be expected of sections through *rscp* polycrystalline solids. These single images of the hard sphere solid have thereby been able to confirm the structure expected from theory and reported previously from both light-scattering and microscopy. A full understanding of the patterns seen, along with an appreciation of how such parameters as the stacking probability can be determined from a given pattern is obviously fundamental to the application of microscopy for the study of how the structure of colloidal crystals varies with time, volume fraction, hardness of interaction *etc.* The work presented here therefore represents a springboard for the future.

6.3 Constructed views of an image stack

In this section, an image stack of a colloidal crystal is used as a three-dimensional data array and views of the array at a number of angles are constructed. These views are found to compare well with the images of a model crystal viewed from the same directions.

In the whole of this section, wherever x-, y- or z-directions are referred to, these shall be those of the experimental data set, *i.e.*, the z-direction is parallel to the optical axis of the microscope and forms the conventional right-handed mutually-perpendicular set with the x- and y-directions. In the micrograph shown in figure 6.18(a), which represents the top image of the stack, the x-direction is horizontal, from left to right; the y-direction is vertically upwards, as depicted in figure 6.18(c).

6.3.1 Experimental and analytical details

Experiment

A suspension of particles of radius $R_p = 460 \pm 32$ nm (as measured by static light scattering) in *cis*-decalin, at a volume fraction $\phi = 0.540 \approx \phi_{\mathsf{M}}$, so that most of the suspension would be crystalline, was sealed in a rectangular capillary of the type described in figure 4.1.2.

A week after sealing, the suspension was observed using an Olympus BX-50 microscope, fitted with an oil-immersion 100× oil-immersion objective ($\mathcal{A} = 1.25$). Initial examination confirmed that, as expected for $\phi \lesssim \phi_{\mathsf{M}}$, the polycrystalline solid occupied nearly the entire depth of the capillary. Under phase contrast, a region showing the "disjointed-lines" pattern identified above as being characteristic of the $\{10\bar{1}0\}$ view was found and an image stack measuring $N^x_{\mathsf{pix}} \times N^y_{\mathsf{pix}} \times N_{\mathsf{im}} = 76 \times 76 \times 32$, with $\Delta z_{\mathsf{im}} = 460$ nm $\approx R_p$, was recorded.

The field of view of each plane, the top one of which being shown in figure 6.18(a), is $(5.5 \pm 0.1\ \mu\mathrm{m})^2$. Six horizontal lines of dark particles can be seen, with

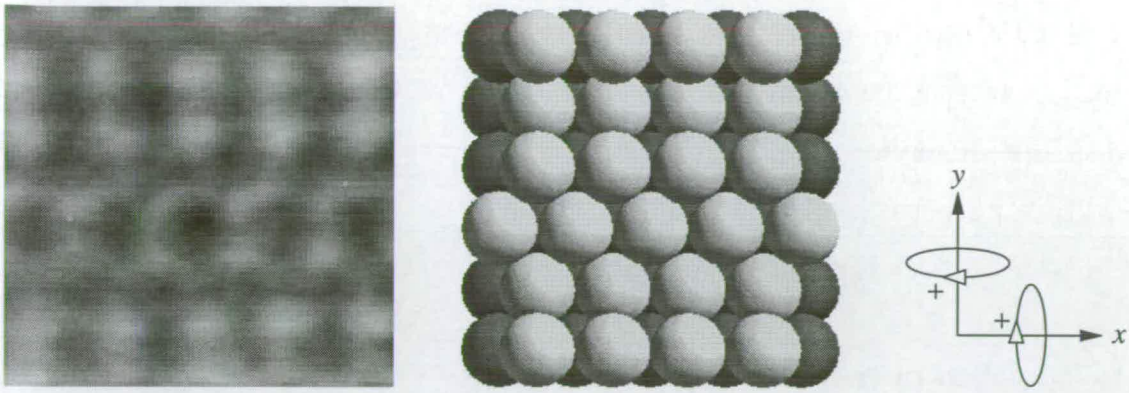

Figure 6.18: A section of colloidal crystal and its computer model: (a) the top image from a stack of 32 planes, showing 6 rows of (dark) particles in a "disjointed-line" pattern; (b) a computer model of 6 hexagonal layers, showing the $\{10\bar{1}0\}$ view, with the nearest spheres in each layer coloured a paler shade, to show that they are in the same arrangement as the particles in (a); (c) the direction conventions for the x- and y-axes and positive rotations about them, as used in this section.

the third line from the bottom being perhaps clearest, showing five spheres.

Measurements give the x-spacing of the particles to be 1130 ± 57 nm and the y-spacing to be 901 ± 45 nm. For $\phi = 0.545$, as expected for a suspension only a few days old, the $\{10\bar{1}0\}$ view would predict spacings of $a = 2.22R_p = 1021 \pm 72$ nm and $\sqrt{\frac{2}{3}}a = 834 \pm 58$ nm, respectively, so identifying the x-y plane in this way is consistent with the crystal being uncompressed.

Computer model

Given the close similarity between the disjointed-lines pattern of the planes in the stack and the $\{10\bar{1}0\}$ view of a *rscp* crystal, a computer model (using Cerius[2], as before) was constructed using six hexagonal layers in the stacking sequence ABCABA, chosen from the appearance of the stack side on (see the 90° image in figure 6.19). The original model of $20 \times 20 \times 1$ unit cells was faceted to give an x-width of 5 particles, to match figure 6.18(a) and a z-extent of 15 particles to agree with the side-on view.

Figure 6.18(b) shows the $\{10\bar{1}0\}$ view of this faceted model; the nearest spheres in each layer have been highlighted to make the comparison with the disjointed-lines pattern of (a) clearer.

By rotating this model, comparisons could be made with the angled views constructed from the experimental data.

Construction of views from experimental data

As described in §4.3.3, MetaMorph® image-processing software was used to construct views of the stack of micrographs at a variety of angles to the z axis.

6.3.2 Views obtained by rotations about the y-axis.

If the identification of the individual images in the stack with $\{10\bar{1}0\}$ sections is correct, then six-fold symmetry should be found about the y-axis. Figure 6.19 shows both MetaMorph® constructions and views of the Cerius^2 model at rotations at 30° intervals about this axis. The spheres in the model have been reduced slightly from their "natural" size (giving $\phi = 0.545$) so that their arrangement is easier to see. The views corresponding to 180° to 330°, are not included because they were found, as expected, to be simply mirror images of those shown.

The first point to be noted about figure 6.19 is that all the views show six horizontal lines (as do views constructed at any angle of rotation about the y-axis). If these correspond to six hexagonal layers, stacked parallel to the y-axis, one would always expect to be able to see the layering clearly in any view containing that axis, such as all these are.

Secondly, it is clear that the views can be divided into two sorts:

- at 60° intervals, starting from 0°, individual particles are hard to make out on the lines, whereas
- at 60° intervals, starting from 30°, the particles are clearer and seem to stack up along a slant.

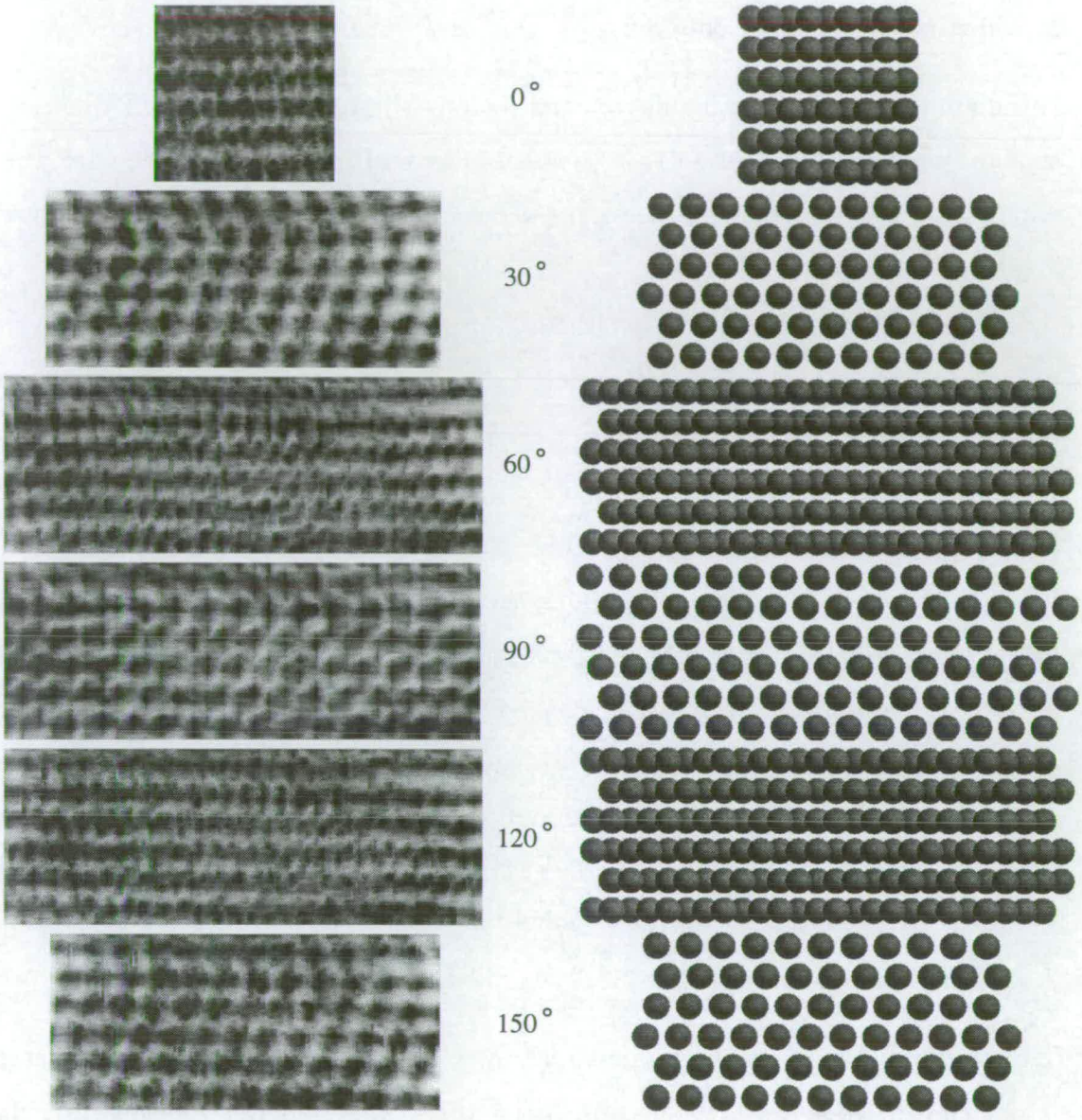

Figure 6.19: Views of an image stack constructed after rotation about the y-axis and the corresponding views of a computer model

That both sorts of views should repeat on 60° intervals is consistent with the hexagonal order of the six stacked layers suggested, but closer examination of the two gives even more evidence that the experimental data and putative model agree:

1. Lines of overlapping spheres

Although not easy to distinguish particles along the horizontal lines of the constructed views of the first sort, it is possible to find order compatible with the appearance of overlapping spheres, as shown in the model views at the same angles.

However, the first sort of view should correspond to $\{10\bar{1}0\}$ sections, where disjointed-line patterns might be expected. The individual images in the stack, as recorded, do show this pattern, but not even the 0° construction (which is parallel to the recorded images) does. The reason for this is that, while the individual images have a depth of field of $\lesssim 1\ \mu$m, in the reconstruction the depth of field is the thickness of the entire stack along the direction perpendicular to the plane of the view, so particles at any depth will appear. This explains the appearance of overlapping particles in both the constructed images and the computer model (remember that slicing was required to show the disjointed-line pattern in the model – figure 6.9, whereas the model here shows as many particles as the image stack).

2. Sloping lines of spheres

The most striking point about the appearance of the views at 30°, 90°, 150° *etc.* is not shown by figure 6.19, because the interval between the views is 30°. If a set of 360 views, at 1° intervals, had been given, what would be immediately clear is the way that only within a degree or so of the six angles corresponding to this sort of view do the particles become clearly distinct; for most rotations, the particles are not distinguishable even after the manner of the $\{10\bar{1}0\}$ views.

These angles, bisecting the $\{10\bar{1}0\}$ views and hence corresponding to $\{11\bar{2}0\}$ views, are perpendicular to the close-packed directions of the hexagonal layers, so the striking appearance of their views is due simply to the fact that most of the particles lie hidden directly behind others. Only at angles very close to these will this effect occur.

The sloping lines of particles also agree with the $\{11\bar{2}0\}$ identification of this view, where we would expect to find zig-zag patterns. Examination of the constructed view at 30° shows the bottom five layers to slope upwards to the right, at $71 \pm 2°$ to the horizontal, before a kink at the fifth layer to slope upwards to the left at $69 \pm 5°$. Both these angles are consistent with the expected value of $\zeta = \arccos \frac{1}{3} \approx 70.5°$.

By the nature of the $\{11\bar{2}0\}$ form, one would expect identical angles and slope directions at 120° intervals, but mirror images of the zig-zags at the angles bisecting these. The 150° view does indeed show the same pattern as the 30° one, and the 330° and 210° views are mirror images of them, but the 90° and 270° do not immediately appear to fit this scheme.

While mirror images of one another, and both showing a kink at the fifth layer, the more immediately obvious slope of the particles in the bottom five layers is upwards to the right, at $55 \pm 2° \approx \aleph$ to the horizontal, whereas we would expect a slope to the left at $\zeta \approx 70.5°$. Such a slope, at $69 \pm 2°$, can be found, however, although it is less clear. Similarly, it is possible to trace lines of particles sloping up to the left at $52 \pm 2°$ to the horizontal in the 30° and 150° views. The reason for the superficial difference in the appearance between the 90° and 270° views and the other four $\{11\bar{2}0\}$ views is probably due to the fact that the images of spheres are elongated along the z-direction, an effect which is most obvious in views containing that axis.

So, views constructed after rotation of the image stack about the y-axis would appear to confirm the identification of the stack as being of a region of *rscp* crystal with the stacking direction parallel to the y-axis and the individual planes representing $\{10\bar{1}0\}$ views. To complete the investigation, however, consideration of other views is required.

6.3.3 Views obtained by rotations about the x-axis.

The stacking sequence of the bottom five layers particles being *fcc* suggests that certain angles of rotation about the x-axis should present distinctive patterns.

If the sixth layer of particles is removed from both the image stack (*i.e.* cropping each image to $N^y_{\text{pix}} = 61$) and the computer model, only the *fcc* sequence will be seen.

Predictions from the computer model

Figure 6.20 shows the five layer Cerius^2 model: four angles of rotation about the x-axis are given, along with the 90° rotation about the y-axis. This last view helps to make clear the reasons for choosing the four given rotations about x-axis, the planes of the views of which are traced by dashed lines: the 19.5° and 54.7° views look directly along the sloping lines of the particles, whereas the 109.5° and 144.7° views are perpendicular to these.

The 19.5° view, for which the spheres have been displayed at $\frac{4}{7}$ of the size required for close-packing, shows a tight hexagonal order, with ten vertical lines of particles. With any larger size of sphere, overlapping obscures this order.

Even though displayed 25% larger, the particles are clearly separated in the 54.7° view, where hexagonal order is found too, but the hexagons are not regular: the spheres are aligned along horizontal lines and lines at ±55° to the horizontal, with 4 or 5 spheres, alternately, on the horizontal lines.

Any two of the four sets of hexagonal planes in an *fcc* crystal are at $\zeta = \arccos\frac{1}{3} \approx 70.5°$ to one another. A rotation of 109.5° achieves the same effect as would −70.5°, so, just as the original 0° view shows hexagonal layers side-on, so the distinctive feature of the 109.5° view is of horizontal lines caused in the same way.

Rotating by 144.7° from the $(10\bar{1}0)$ view gives the $(\bar{3}032)$ view, which, being of the $\{3\bar{3}02\}$ form, is parallel to one of the faces of the face-centred cubes. In this view particles are seen at two levels, each level being a primitive square lattice of

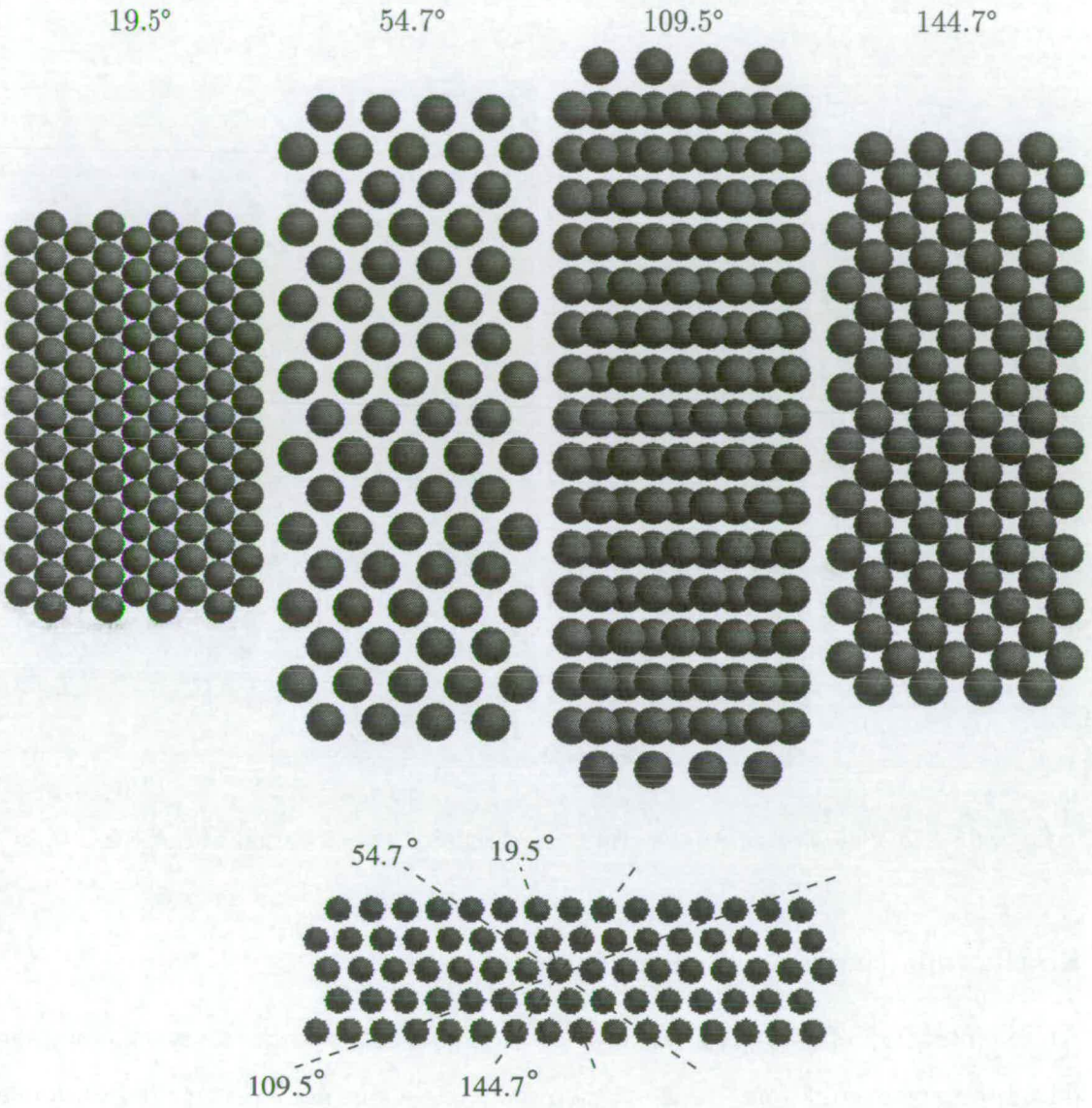

Figure 6.20: Four views of an *fcc* model obtained by rotation about the x-axis, with a 90° y-rotation view, as a key to show their planes.

twice the spacing of the pattern seen in the figure. The reason that the particles appear to touch in this view is because they have been displayed at $\frac{5}{7} \approx \frac{1}{\sqrt{2}}$ of the size required for close-packing.

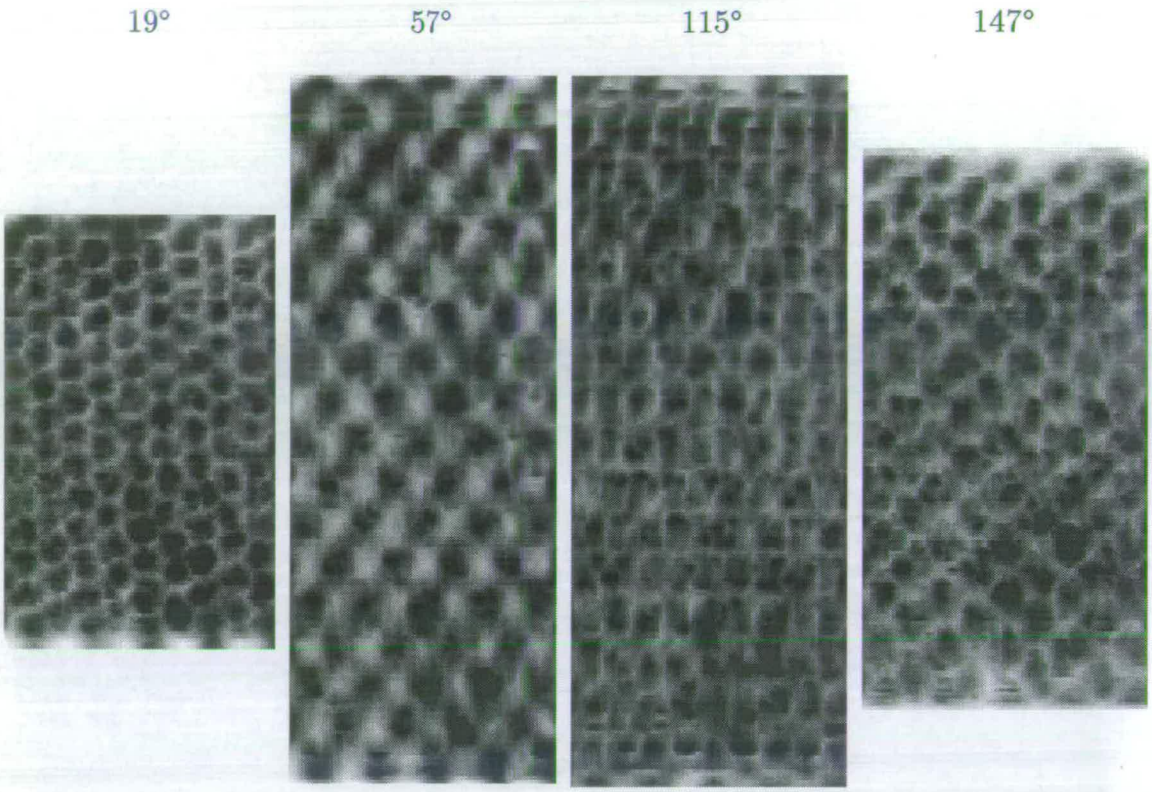

Figure 6.21: Views of an image stack constructed after rotation about the x-axis

Results from constructed views

An examination of the appearance of views constructed from the stack of image data, upon rotation about the x-axis showed a close, but not exact correspondence with the model views. The four views of figure 6.21 show patterns similar to the predicted ones. The angles chosen for these views were those that gave the clearest patterns. All four angles are close to those predicted.

The closest correspondence is in the case of the "small hexagon" pattern of the 19.5° model view and the 19° constructed view, where both show ten vertical lines of 12 or 13 particles. Given the overlapping of spheres that might be expected in this view, it is remarkable quite how well this order is shown. The 20° view was also constructed, MetaMorph® only allowing rotation by integer degree values, but the pattern was not quite as clear, indicating that the stacking of planes in the colloidal crystal may have been slightly displaced laterally from the ideal

positioning, although this is hard to understand, as the close agreement between predicted and constructed views under rotations about the y-axis eliminates the possibility that the z-scaling was incorrect, since this would lead to distortion of the hexagonal order in the x-z planes.

The 57° construction shows the same "squashed hexagon" pattern as the 54.7° model view: clearly separable particles arranged on horizontal lines and at $\pm(55 \pm 2°)$ to the horizontal, with 4 or 5 spheres, alternately, on the horizontal lines. The larger discrepancy between the angles of the two methods, compared to the "small hexagon" pattern views, can perhaps be explained by the fact that any extra displacement in the stacking sequence along the z-direction would become more apparent for views at smaller angles to that direction.

The 147° construction is consistent with the 57° one in that the two are perpendicular, as are the 54.7° and 144.7° model views. The constructed view shows a certain amount of distortion, in that the lines of the particles are not quite straight, but the angles between the lines measure $88 \pm 2°$ and the numbers of particles in the lines matches the model.

The least satisfactory comparison is between the model at 109.5° and the constructed view at 115°. Horizontal banding could only just be discerned in constructions at 109° and even the clearest pattern, the 115° one shown, was not very clear, but rotating the diagram by 90° can make it easier to detect by eye. The largest discrepancy in angle of the predicted and constructed views of the four patterns considered here can perhaps be explained, as before, by the fact that these angles are the closest to 90°.

To determine the precise nature of the reason for these angular discrepancies requires further thought, but the closeness of the agreement of the predicted views and those found by reconstruction suggests that only minor differences remain to be found between the ideal *rscp* structure of the computer model and the actual structure of the colloidal crystal.

* * *

While work remains to be done, the results presented in this chapter go some way towards proving the usefulness of direct imaging in unravelling the structure of colloidal crystal. Further analysis of other patterns may still be required and development of three-dimensional construction techniques to allow rotation to any azimuth and co-latitude may well be desirable but the methods established here provide a firm foundation for establishing any such work.

7.1 Experimental details

In all the experiments, the suspensions were prepared first in "bulk" containers, *viz.*, glass cells with $X_\sqcup \times Y_\sqcup \times Z_\sqcup = 1$ cm $\times$ 1 cm $\times$ 5 cm. These cells were then observed over a period long enough to allow the separation of those suspensions with volume fractions $\phi_\mathsf{F} < \phi < \phi_\mathsf{M}$ into crystal and fluid regions, so that both the volume fraction could be accurately determined (as Paulin and Ackerson [1990], see page 113 above) and some measure of an upper limit to the time required for crystals to nucleate could be gained, from the time for the first crystals to appear to the naked eye.

Before these suspensions were introduced into the capillary tubes used for the microscopical observation, they were thoroughly shear-melted by shaking until no solid regions could be found in the bulk containers by eye and then tumbled for at least 12 hours to remove all microscopic traces.

Two different suspension media were used: the "standard" mixture of decalin and tetralin and a mixture of decalin with cycloheptylbromide (CHPB), which provides a better density match for the PMMA-PHSA spheres (the case for using this medium shall be outlined in §7.3). For each medium, suspensions were prepared at three volume fractions: one in the middle of the coexistence region, one just above the freezing volume fraction and one just below it.

For all suspensions, the colloidal spheres had $R_p = 540 \pm 27$ nm and the mixture used as the medium was chosen to give a refractive index match close enough to allow crystallization to be observed by eye in the large glass cells, but not too close to give insufficient phase differences for good microscopical images; the image stacks, recorded in DIC, using a Zeiss Axioskop FS microscope with $\mathcal{A} = 1.40$, had $N^x_\mathsf{pix} = N^y_\mathsf{pix} = 128$ and $\Delta z_\mathsf{im} = 0.44$ μm.

Although the 14 μm square field of view gave access to only a narrow column within the suspension, observation of the wider field of view shown on the CCD video monitor, combined with previous experimental experience, including wide-ranging surveys of mature suspensions, confirms that these images are

Chapter 7

The Kinetics of Hard Sphere Nucleation

In this chapter six series of image stacks are presented, each series following the development of a different suspension over a period of time. The duration of the observation was chosen to be sufficient to demonstrate the occurrence or absence of crystal nucleation, depending upon what would be expected in each case from the observation of the behaviour of the suspensions in the bulk.

The results are presented in the form of montages of images, so that both time and depth variations can be followed together for a single suspension, and are supplemented by graphs showing the positions of crystalline regions, which are able to give better time-resolution, although they cannot show the appearance of the suspension.

The interpretation of results in this chapter concentrates on the key differences between the six series of images. As the intention here is to illustrate the potential of microscopical studies of nucleation, the emphasis is on presenting good results as the firstfruits of the microscopical techniques developed earlier in this work. For this reason, the full interpretation of what is presented here remains a challenge for future work.

representative of the behaviour throughout the central region of the capillary.

7.2 "Standard" suspensions

The mixture of decalin and tetralin used for these three suspensions had $n_m = 1.4915 \pm 0.0005$ (measured using an Abbe refractometer, with a filament lamp as illumination), with suspensions being prepared at $\phi = 0.525$, 0.502 and 0.490.

7.2.1 $\phi = 0.525$

In the large cell, this suspension first showed crystallites visible to the eye by Bragg reflections after about 80 minutes. The effective volume fraction was measured as $\phi^\natural = 0.525 \pm 0.001$.

Overview of entire observation period

Figure 7.1 shows how this suspension developed over the course of the three hours after it was introduced into the capillary tube used for microscopical observation. Over the course of this period the suspension separated, as expected, into an upper, fluid region and a lower, crystalline one. The effective volume fraction $\phi^\natural = 0.5251 \pm 0.0006$, implied by the observed final ratio of crystal to fluid, $\chi = 0.61 \pm 0.015$ (see equation 5.6) was in very close agreement with the bulk result.

That the suspension took only an hour or so to reach a state which required several days in the bulk may be explained by the fact that the crystallites in the capillary needed to sediment distances $\mathcal{O}(10^{-2})$ of those in the large cell, in order for separation into distinct regions to occur.

Images spanning the nucleation period

To show the appearance of the suspension during the course of its phase separation from the metastable fluid state in which it was introduced into the capillary, figure

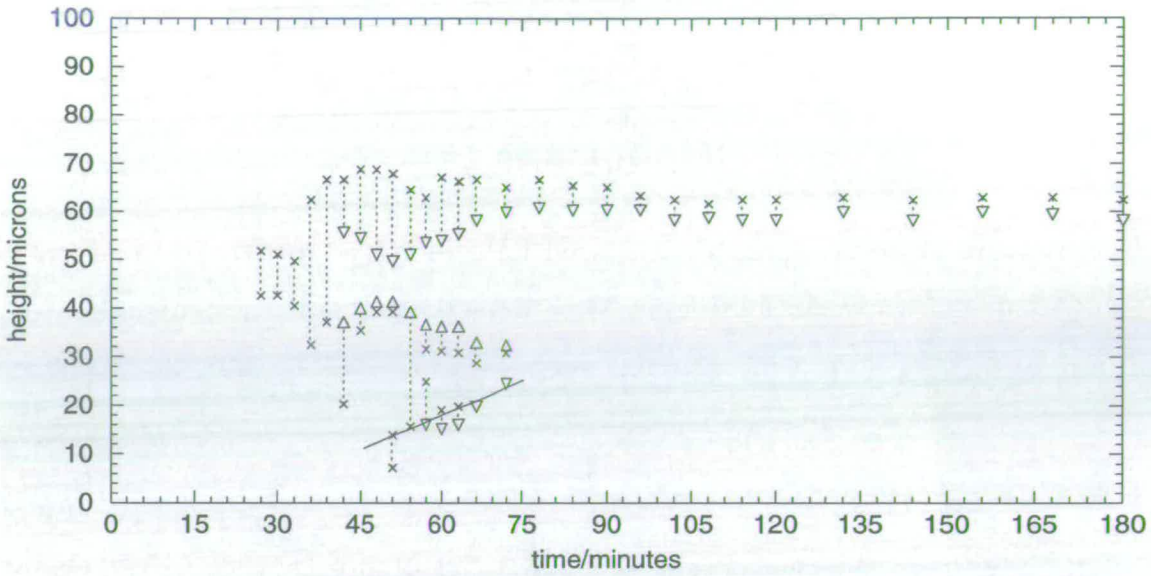

Figure 7.1: Graph of crystallization in capillary (interior vertical extent 100 μm), with $\phi = 0.525$. The limits of regions where crystallites can be found in the field of view are shown by "$\times$" symbols; "∇" and "Δ" represent the upper and lower bounds of a fully crystalline field of view. For clarity, dotted lines have been added to highlight partially crystalline sections of the image stack. The solid line, referred to on page 158, has a gradient of 8×10^{-9} m s^{-1}.

7.2 shows a selection of eight images from each of six of the stacks recorded. The images selected from each stack were from the same eight heights above the bottom of the tube, chosen to span the depth of the capillary and intersect with regions of interest identified by figure 7.1.

The stack at 7 minutes was the first recorded and shows only a very slight and gradual increase in particle density towards the bottom of the suspension. No regions of order can be found that are more than a few particles across.

The beginnings of a larger region of order may just about be detected in the image at 47.5 μm of the stack at 24 minutes, but after 30 minutes it is clear that crystallization is in progress, with at least two crystallites in view. This region is seen to grow in all three dimensions and eventually joins up with a region of crystal that has grown upwards from the bottom of the suspension. In the final stack, the sharp division of the suspension into polycrystalline and fluid regions

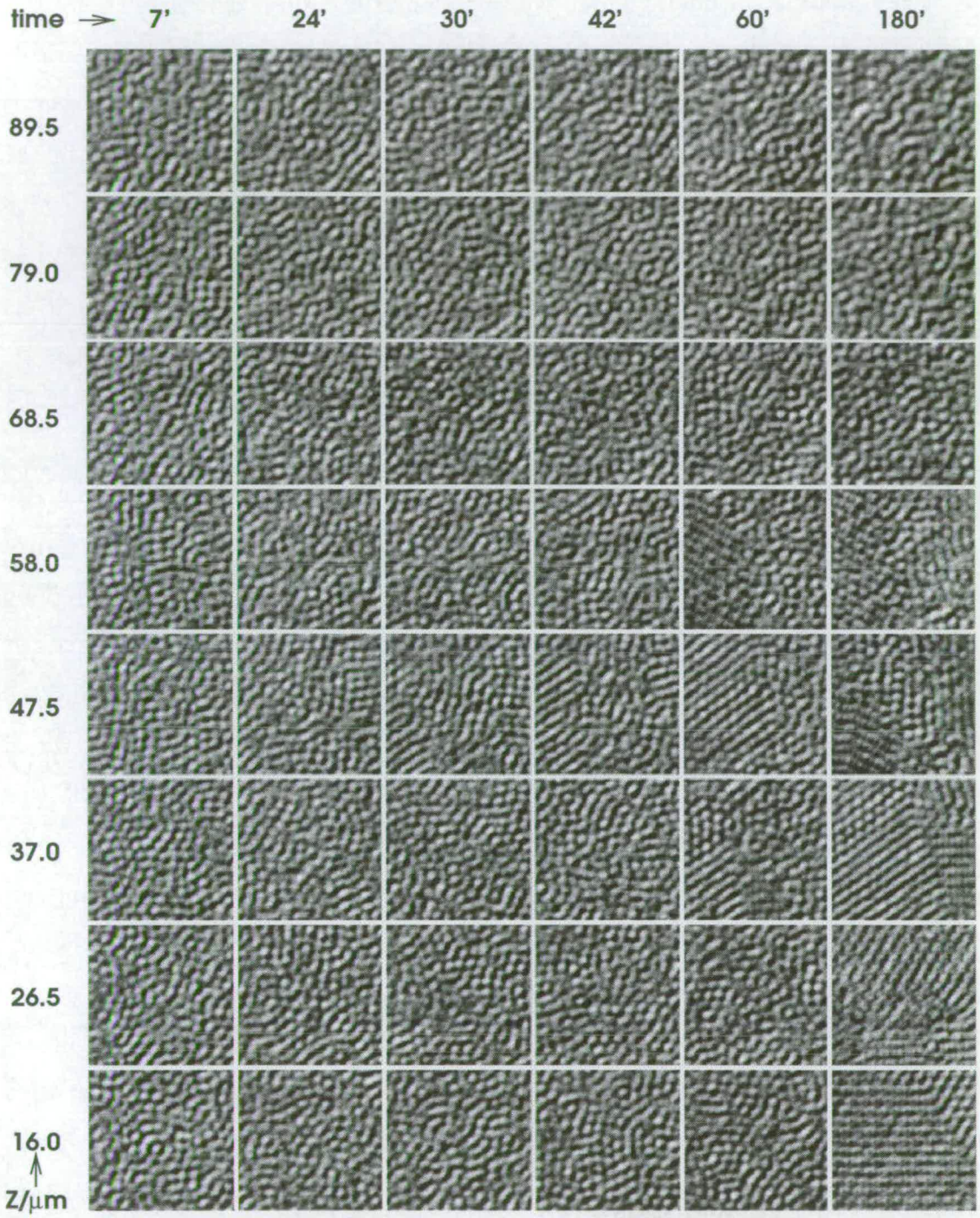

Figure 7.2: Images of phase separation at $\phi = 0.525$, showing the appearance of the suspension at heights $z = 16.0$, 26.5, 37.0, 47.5, 58.0, 68.5, 79.0 and 89.5 μm above the bottom of the 100 μm deep capillary tube, at times of 7, 24, 30, 42, 60 and 180 minutes after being left to settle.

is clear, as is the considerable density variation of the fluid region.

The later-appearing, lower crystalline region that appears to grow upwards is probably the result of sedimentation. In the bulk, a small region of crystals which appear to be columnar can be found growing up from the bottom of the cell, even with $\phi < \phi_F = 0.494$. Growth rates are typically $\mathcal{O}(10^{-9})$ m s^{-1}, which agrees with the graph in figure 7.1, where the solid line following the trend in upward growth of the lower crystalline region has a gradient of 8×10^{-9} m s^{-1}.

The sedimentation velocity of a single particle of radius R_p is given by

$$v_{sed} = \frac{2{R_p}^2(\rho_p - \rho_m)g}{9\eta_m}, \tag{7.1}$$

where ρ and η refer to density and viscosity and the subscripts p and m designate the particle and medium respectively. For this suspension, $\rho_p = 1.2 \times 10^3$ kg m^{-3} and $\rho_m = 9.0 \times 10^2$ kg m^{-3}. Using the *ad hoc* fitted expression suggested by Meeker *et al.* [1997], the viscosity of the medium in the presence of the particles is increased by a factor $(1 - \frac{\phi}{0.55})^{-1.76}$ over its natural value of 3.0×10^{-3} Pa s, so we have $v_{sed} \approx 3 \times 10^{-10}$m s^{-1}. Although collective diffusion of particles, which is somewhat quicker, is responsible for the growth of sedimentary crystals, this calculation shows that we are dealing with the right time-scale.

The middle crystalline region that appeared first, on the other hand, being initially unconnected with the bottom of the tube cannot be this sort of sedimentary crystal. Unfortunately, the first crystallites in this region appear to have grown into the field of view from outwith its limits, so the exact appearance of their earliest stages is not known from this experiment. It seems likely, however, that they had their origins in small ordered regions of the sort seen in the earlier stacks, but the answer to this question will have to await further experiments. What is clear is that this method is certainly amenable to answering such questions.

Discussion

Two main points of interest arise from the results of this experiment: The first is that the details of the phase separation of a suspension of this volume fraction, in

terms of both time-scale and spatial proportion, is in agreement with the findings in the bulk.

Secondly, the image stacks show that crystallization is able to occur within the bulk of the liquid, although sedimentation does have noticeable effects over the time-scale of the nucleation-and-growth process. While sedimentation is the likely explanation for some of the final polycrystalline region, other crystallites have formed independently of this mechanism.

7.2.2 $\phi = 0.490$

This suspension showed only a small region of sedimentary crystals at the bottom of the large cell when left to stand for several weeks. This region grew upwards at a rate of 7×10^{-9} m s^{-1}. The volume fraction $\phi = 0.490 \pm 0.02$ was calculated from the ratio of amorphous sediment to clear solvent after centrifuging (see §5.2.3).

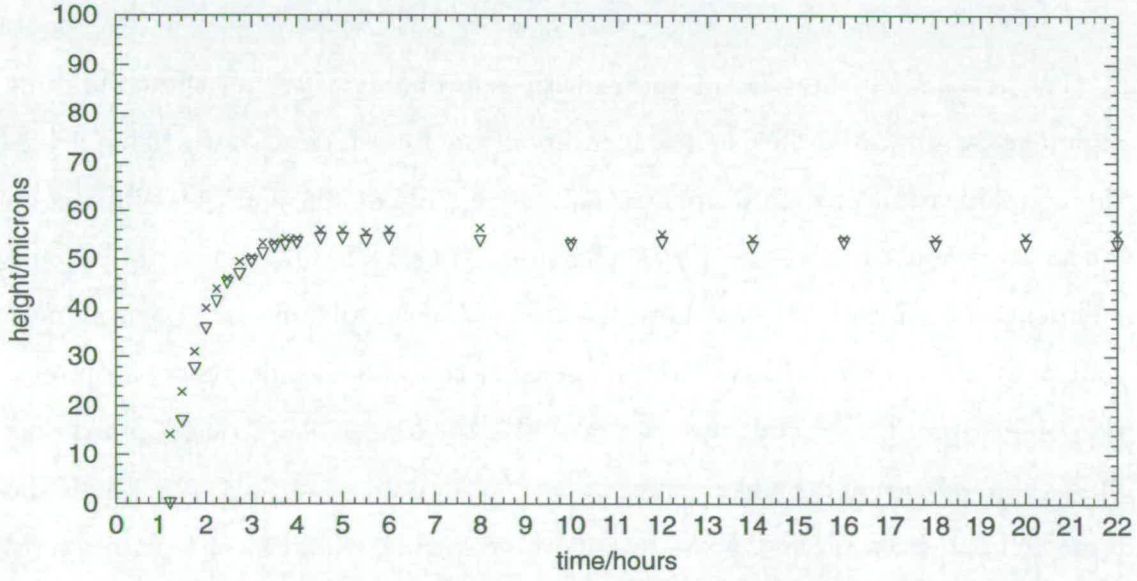

Figure 7.3: Graph of crystallization in capillary, with $\phi = 0.490$. The limits of regions where crystallites can be found in the field of view are shown by "$\times$" symbols; "∇" represents the upper bound of a fully crystalline field of view.

Figure 7.3 shows that the first signs of crystallization occur after an hour or so, with the crystalline region then growing upward from the bottom of the capillary

tube, initially at a rate of 6.5×10^{-9} m s^{-1}, but progressively more slowly until, after about 4 hours, no further growth of the sediment occurs.

The images in figure 7.4 illustrate various stages in this process: the stack at 15 minutes was the first to be recorded and shows no long range order and as yet little sedimentation; after 45 minutes, the top of the tube is becoming visibly less dense and the beginnings of order are perhaps just about to appear at the bottom; at 75 minutes, the bottom frame is showing long-range order more clearly; this becomes ever more apparent as the crystalline region grows upwards, as evidenced by the stacks at 105 and 135 minutes; the final ratio of crystal to fluid is shown in the stack at 240 minutes.

That the initial rate of upward growth of the crystalline region is very similar to the bulk rate would confirm the sedimentary explanation for the crystalline region in this suspension and that sedimentation should be a significant effect is clear from the appearance of the images close to the top of the tube.

The reason for the halt in the growth is probably that, as the crystalline region grows upwards, the osmotic pressure of the fluid region above which drives the crystallization process decreases, and there will come a point at which is no longer sufficient to drive the phase transition [Pusey, 1999]. When this occurs will depend upon the overall volume fraction of the sample, but one might expect that a significant proportion of the suspension container would be crystalline at this point (if all the crystal were at $\phi = 0.545$, the lowest likely value, an average fluid volume fraction even of as much as $\phi = 0.45$ would result in $\chi = 0.52$). If the large cell had been observed for the month or so that would have been required for the sedimentary crystals to reach a height of several centimetres, then this same stop to the sedimentation process would have been observed [Paulin and Ackerson, 1990].

By measuring the variation in particle density with depth over the fluid region a suspension at equilibrium, a measure of the significance of sedimentation, *viz.* the sedimentation length Z_{sed}, can be obtained (see §8.1). By counting the

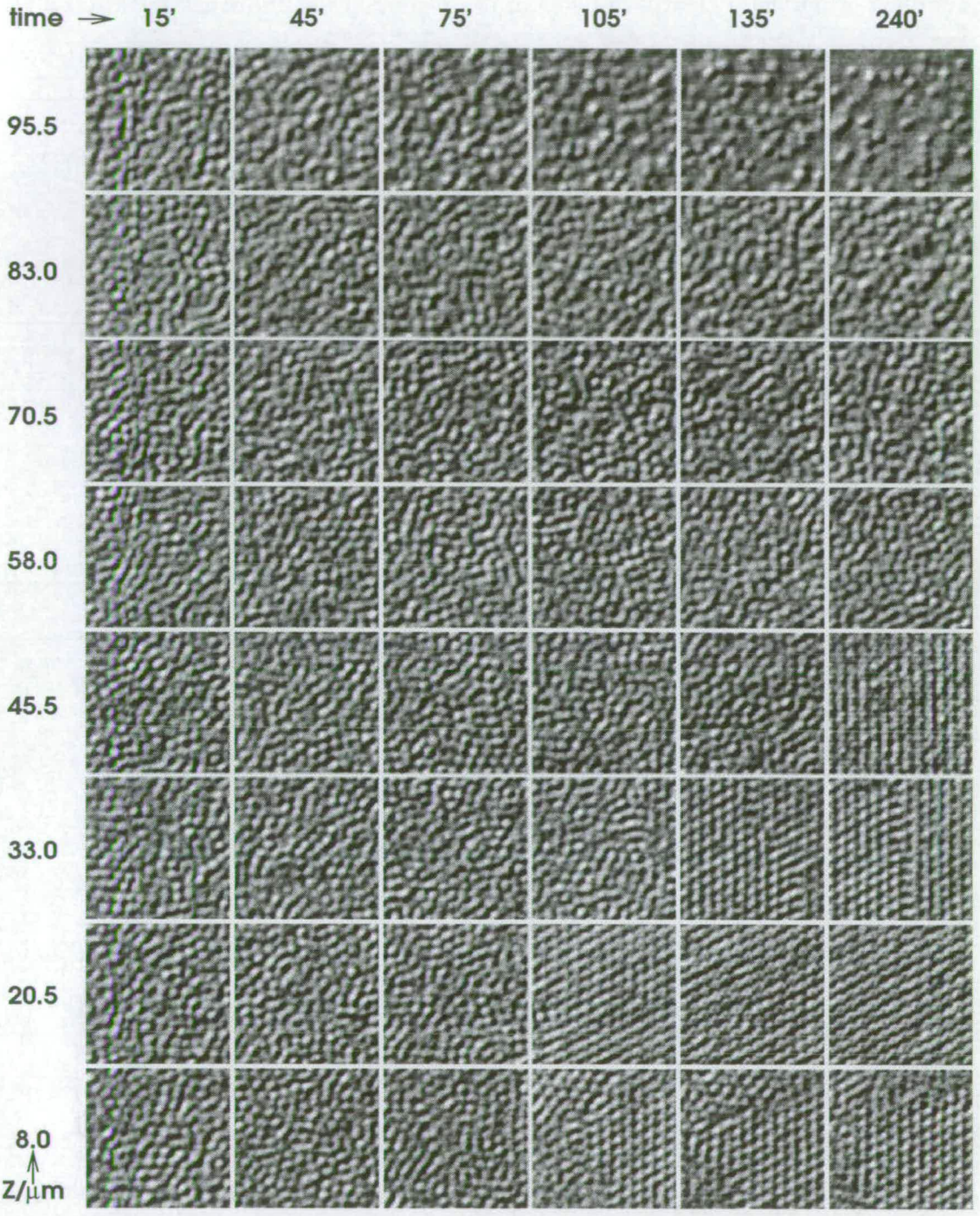

Figure 7.4: Images of sedimentary crystal growth at $\phi = 0.490$, showing the appearance of the suspension at heights $z = 8.0$, 20.5, 33.0, 45.5, 58.0, 70.5, 83.0 and 95.5 μm above the bottom of the 100 μm deep capillary tube, at times of 15, 45, 75, 105, 135 and 240 minutes after being left to settle.

numbers of particles clearly in focus in the top planes of the stack recorded after 22 hours, the results shown in figure 7.5 were obtained. In the most dilute region,

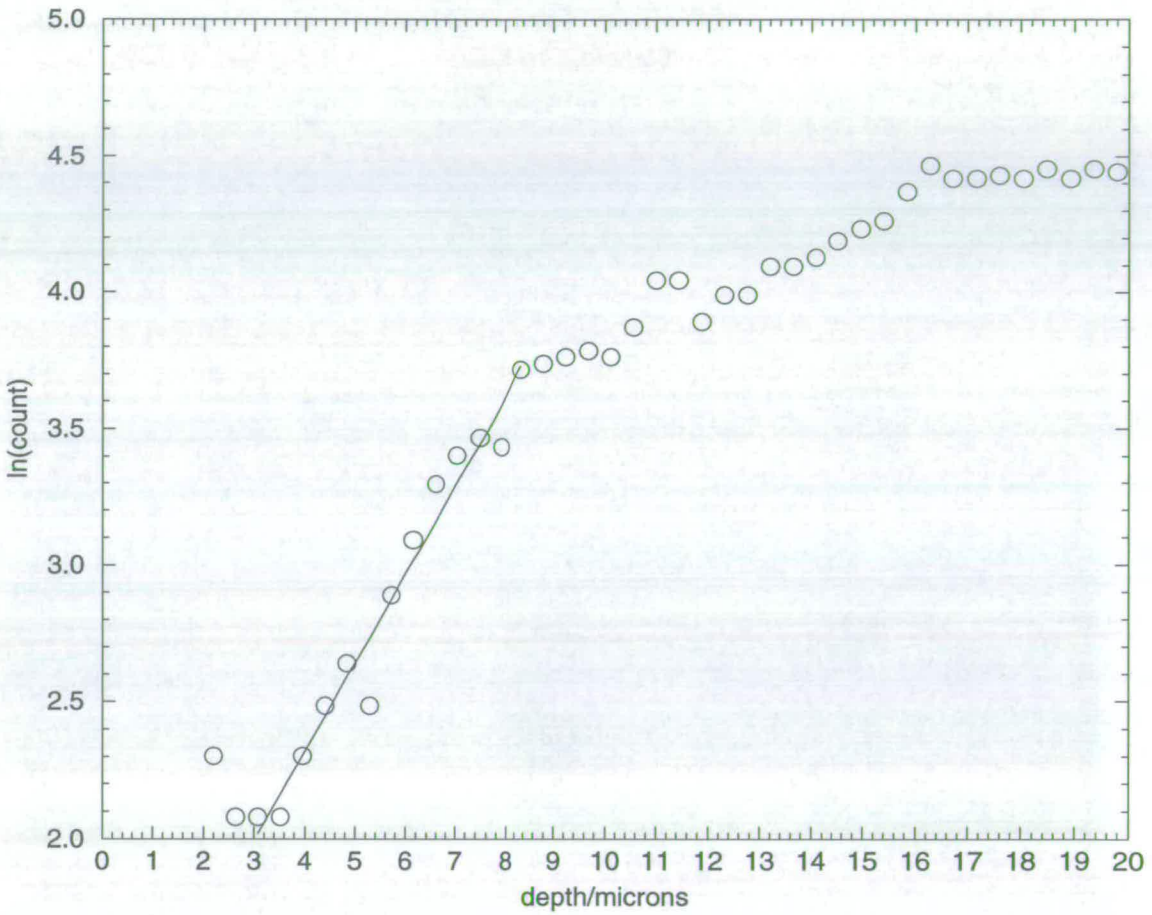

Figure 7.5: Sedimentation profile of $R_p = 540$ nm PMMA spheres in a decalin-tetralin mixture: the sedimentation length is found from the gradient of the dilute region.

toward the top of the liquid, the number density of particles increases close to exponentially with depth. The gradient of this region in figure 7.5, 3.09 ± 0.06 μm, is the sedimentation length. That it is not much larger than the particle diameter shows that sedimentation can be expected to be a significant effect.

Although this experiment does not teach us about the homogeneous nucleation of colloidal crystals, it does show that sedimentation is even more of a significant effect in these small capillary tubes.

7.2.3 $\phi = 0.502$

In the large cell, this sample first showed crystallites in the body of the suspension after 24 hours, although it took several days for them to begin to collect clearly at the bottom. Applying Paulin and Ackerson's method [1990] again, the effective volume fraction was determined to be 0.502 ± 0.002.

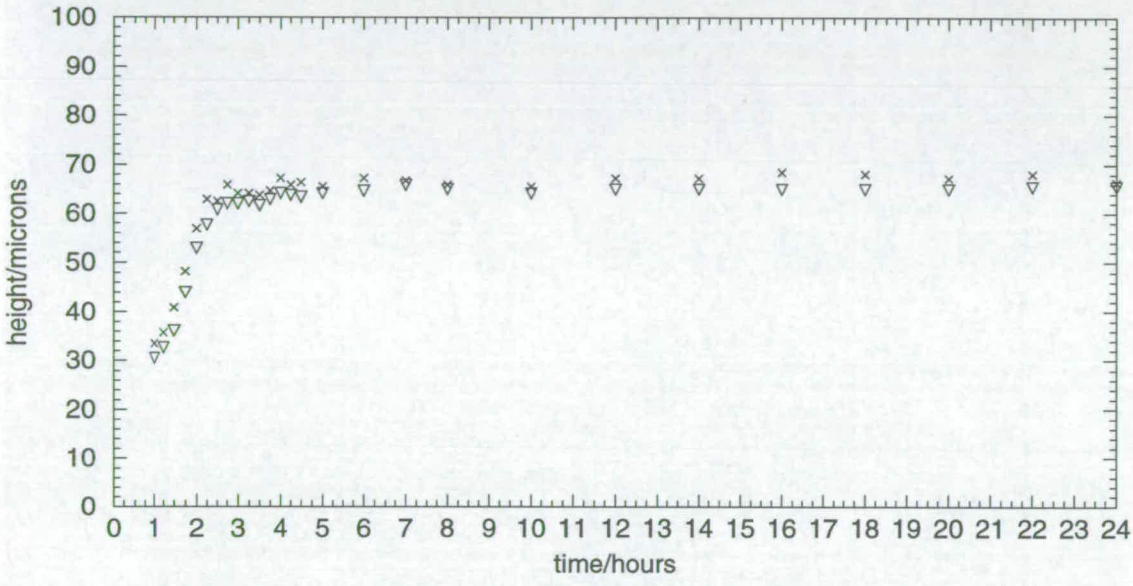

Figure 7.6: Graph of crystallization in capillary, with $\phi = 0.502$. The limits of regions where crystallites can be found in the field of view are shown by "$\times$" symbols; "∇" represents the upper bound of a fully crystalline field of view.

At first sight, the behaviour of this suspension in the capillary, as shown by figure 7.6, is closer to that of the suspension at $\phi = 0.490$ where only sedimentary crystals were seen, than that of the other suspension in the coexistence region, at $\phi = 0.525$. However, at least some tentative explanations may be found for this behaviour, by considering the constraints of the bulk nucleation process, given that sedimentation is occurring continuously.

Looking at the results in more detail, no crystallization is seen up to about an hour after the capillary was filled, as can be seen in the images at 20 and 45 minutes of figure 7.7, but after this point a crystalline region grows upwards from the bottom of the tube at about 8×10^{-9} m s^{-1}, stopping at a height of 65 μm

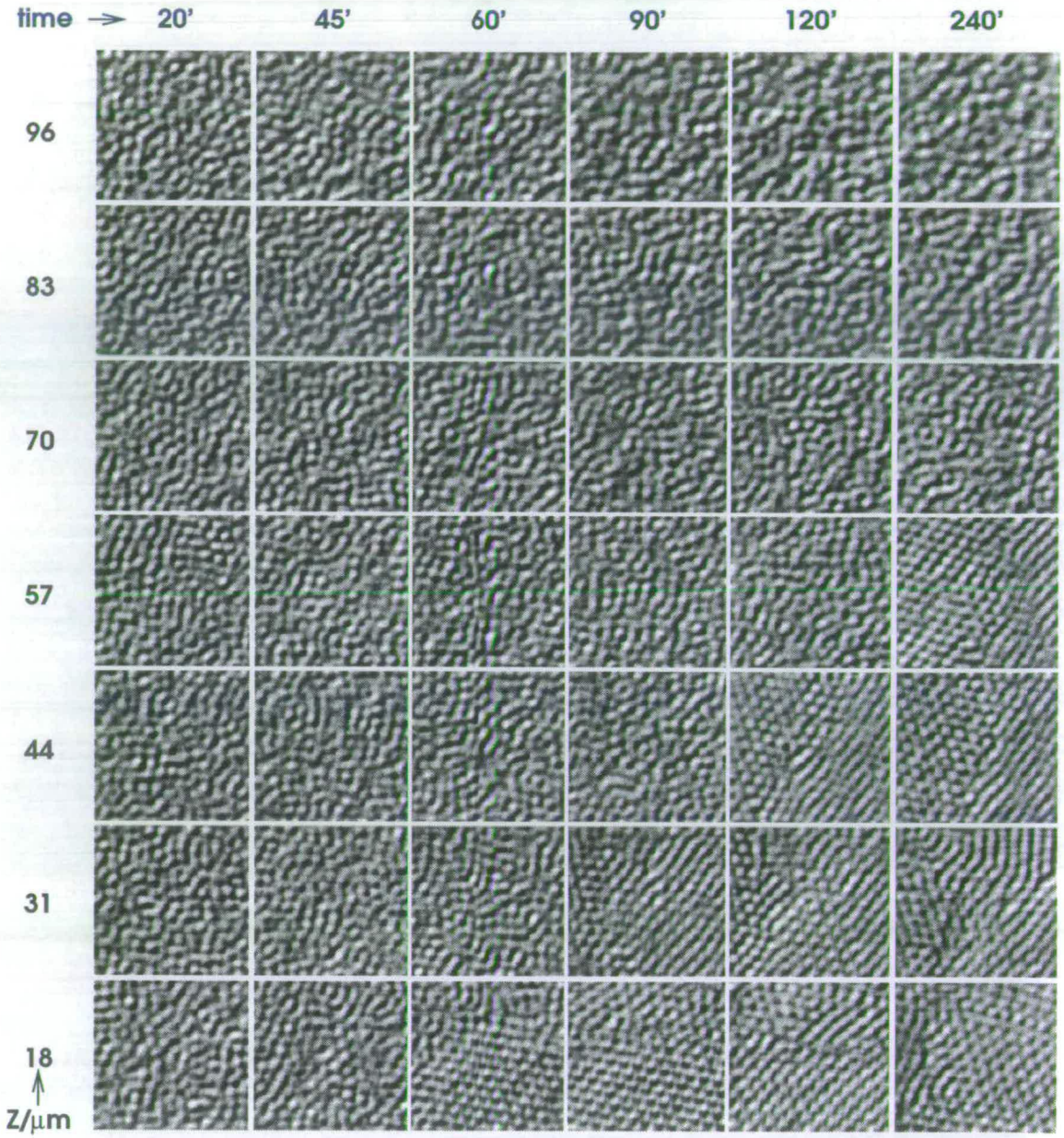

Figure 7.7: Images of phase separation at $\phi = 0.502$, showing the appearance of the suspension at heights $z = 18$, 31, 44, 57, 70, 83 and 96 μm above the bottom of the 100 μm deep capillary tube, at times of 20, 45, 60, 90, 120 and 240 minutes after being left to settle.

(see the remaining images of figure 7.7).

That sedimentation should be a significant effect is once again clear, both from the appearance of the images close to the top of the tube, which show a

marked decrease in particle density over the four-hour interval illustrated, and from the rate at which the crystalline region grew upwards, which is comparable with previous results for sedimentary crystals.

Two major differences exist between this crystallization sequence and that at $\phi = 0.490$: the rate of growth of the crystalline region comes to a much more abrupt halt and the height at which this occurs is noticeably greater.

The reason for this latter difference can be explained by the fact that the suspension is at a larger overall volume fraction, so that more crystal can grow before the fluid becomes too dilute to drive any further growth of sedimentary crystal.

The reason for the fairly abrupt stop to the growth of the crystalline region is probably related to the presence of some equilibrium coexistence crystal formation, that "fills in the gap" when the rate of growth of sedimentary crystal decreases. To address the question of why there is no other evidence for the appearance of bulk nucleated crystals, some reference to some aspects of the theory of hard-sphere nucleation is required.

Following van Duijneveldt and Lekkerkerker [1995], the free-energy ΔG required to form a nucleus of N_p particles is given by

$$\Delta G = A\gamma + N_p \Delta\mu, \tag{7.2}$$

where A is the surface area of the nucleus, γ the surface energy per unit area and $\Delta\mu$ the chemical potential difference.

For a spherical nucleus of radius R_ν, containing particles of radius R_p at volume fraction ϕ_ν, we have

$$A = 4\pi {R_\nu}^2 \tag{7.3}$$

and

$$N_p = \frac{\phi_\nu {R_\nu}^3}{{R_p}^3}. \tag{7.4}$$

So we get

$$\Delta G = 4\pi\gamma {R_\nu}^2 + \frac{\phi_\nu \Delta\mu {R_\nu}^3}{{R_p}^3}. \tag{7.5}$$

This rises from a minimum of zero at $R_\nu = 0$ to a maximum at $R_\nu = R_\nu^{crit}$ (for $\Delta\mu < 0$), given by

$$R_\nu^{crit} = -\frac{8\pi\gamma {R_p}^3}{3\phi_\nu \Delta\mu}. \tag{7.6}$$

By taking the nucleation process to occur at mechanical equilibrium, van Duijneveldt and Lekkerkerker [1995] suggest expressions of

$$\begin{aligned}\frac{\Delta\mu}{k_B T} = 3\Bigg(&\frac{\phi_{rcp}}{\phi_{rcp}-\phi_F} - \frac{\phi_{cp}}{\phi_{cp}-\phi_M} + \frac{\phi_{cp}}{\phi_{cp}-\phi_M+1.34\,(\phi_F-\phi)} - \frac{\phi_{rcp}}{\phi_{rcp}-\phi} \\ &+\ln\left(\frac{\phi_F\,(\phi_{cp}-\phi_M)\,(\phi_M+1.34\,(\phi-\phi_F))\,(\phi_{rcp}-\phi)}{(\phi_{rcp}-\phi_F)\,\phi_M\,(\phi_{cp}-\phi_M+1.34\,(\phi_F-\phi))\,\phi}\right)\Bigg)\end{aligned} \tag{7.7}$$

and

$$\gamma = \frac{0.65 k_B T}{4 {R_p}^2}. \tag{7.8}$$

Applying these relationships to the suspension in this experiment, we get a value of $R_\nu^{crit} = 14.5$ μm, representing $\mathcal{O}(10^4)$ particles. Given that a value of $R_\nu^{crit} = 3.1$ μm, representing $\mathcal{O}(10^1)$ particles, is obtained for a suspension at $\phi = 0.525$, which was seen to take at least half an hour to nucleate homogeneously, and that a 29 μm diameter nucleus would occupy nearly a third of the depth of the capillary tube, it is not surprising that the homogeneous nucleation of crystals should take much longer at this lower volume fraction and that the sedimentation process, taking only a few hours in the capillary, should take precedence. However, by the time that the sedimentation process has begun to slow down this mechanism can begin to surface.

7.3 Suspensions with a better density match

Because of the effects of sedimentation, a set of experiments was carried out using a medium with a much closer density to that of the spheres, *viz.* an 80 : 20 CHPB:decalin mixture (by mass), which had a refractive index $n_m = 1.493 \pm 0.001$. This mixture was calculated to have a density of $1.18 \pm 0.07 \times 10^3$ kg m^{-3}, which was very close to that of PMMA ($1.19 \pm 0.01 \times 10^3$ kg m^{-3}), but the ambiguity in the density-matching, shown by $\rho_p - \rho_m = 10 \pm 80$ kg m^{-3}, renders

this result unhelpful. For this reason, the sedimentation length was measured (for details, see §8.1) and found to be 28 ± 1 μm. This value is an order of magnitude larger than for the standard system and implies $\rho_p - \rho_m = 23 \pm 2$ kg m^{-3}.

This system has not yet been confirmed to provide a hard-sphere suspension, but initial results [Haw, 1996] suggest that suspensions with this ratio of CHPB to decalin should behave in very similar ways to the standard system. By measuring the proportion of crystal χ in coexistence samples and comparing it to expected values – which is a particularly sensitive way of comparing effective and theoretical volume fractions, my experiments suggest that in the few days after the medium has been changed a slight swelling (about 1.5% radius increase) of the particles occurs. This amount of swelling is consistent with measurements of form factors [Martelozzo, 1998]. Furthermore, rescaling the volume fractions to take account of this swelling maintains the hard-sphere result of $\frac{\phi_M^\natural - \phi_F^\natural}{\phi_F^\natural} \approx 0.1$ (equation 5.7). So, with the *caveat* that they are only provisional, the results presented in this section would seem to be worth at least airing.

The three volume fractions for these experiments were chosen to be close to those used for the standard system, for ease of comparison of the effects of sedimentation.

7.3.1 $\phi = 0.489$

In order isolate sedimentation effects, a suspension was prepared at effective volume fraction $\phi^\natural = 0.489 \pm 0.017$, determined from the proportion of amorphous sediment found after centrifuging for two days. Left to stand in a large cell, this suspension took several days before any sedimentary crystal could be seen and no crystallites were ever seen in the body of the suspension, during an observation period lasting four months. The steady rate of growth of the sediment observed over the first two months was 9.1×10^{-10} m s^{-1}, an order of magnitude less than that found for the previous experiments, as might have been expected from the ratio of the sedimentation lengths.

In the capillary, no evidence of any sort of crystallization was found, even over two days, so no plot of the crystal-fluid interface can be given, but figure 7.8 shows a selection of representative views. Given that sedimentary crystals first

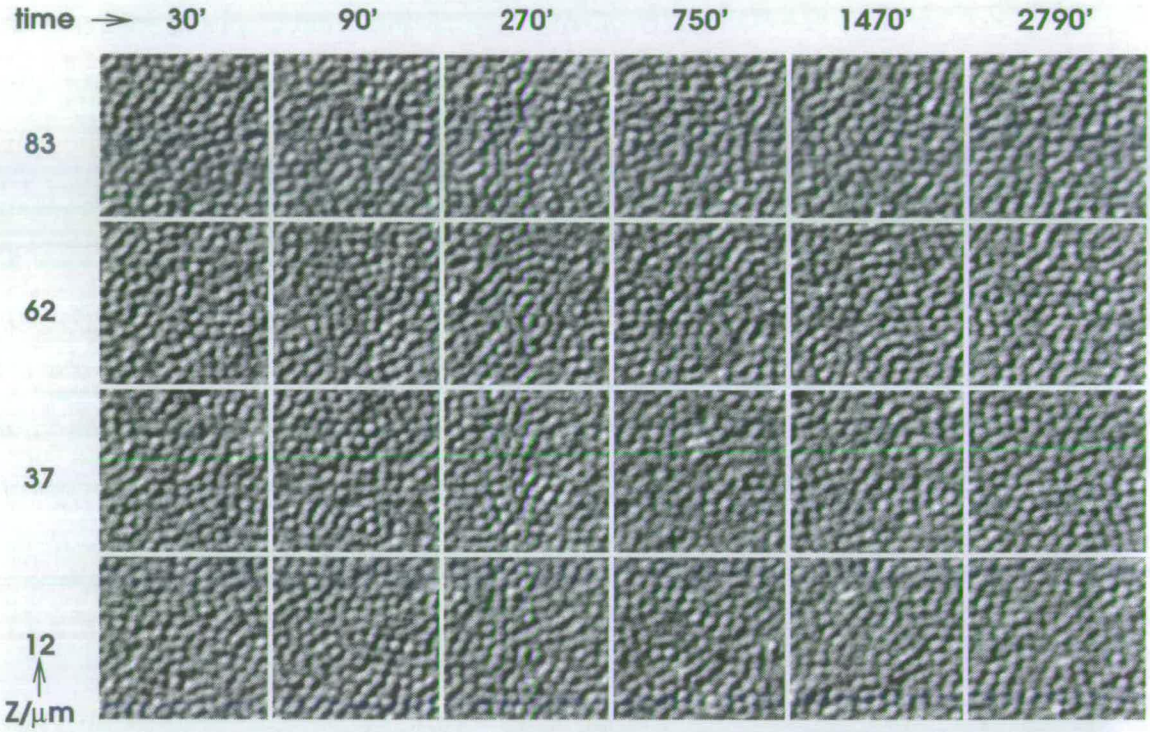

Figure 7.8: Images of a density-matched suspension at $\phi = 0.489$, showing the appearance of the suspension at heights $z = 12$, 37, 62 and 83 μm above the bottom of the 100 μm deep capillary tube, at times of 30, 90, 270, 750, 1470 and 2790 minutes after being left to settle.

appeared at this volume fraction previously after an hour or so, it might have been expected that some would have been found within a day or so. There may be some beginnings of ordering occurring in the latest stacks shown, but no clear evidence of sedimentation is found over the time period of this experiment, so we can perhaps ignore its effects over periods of a few hours in this system.

7.3.2 $\phi = 0.510$

A suspension at $\phi^{\natural} = 0.524$ was prepared, but nucleation was very rapid, with large regions of order being found within a few minutes of filling the capillary, so,

with the intention of increasing the time for nucleation to occur by increasing the critical nucleus size, another suspension, at $\phi^{\natural} = 0.510 \pm 0.002$, was prepared.

As can be seen from figure 7.9, this suspension shows some very interesting

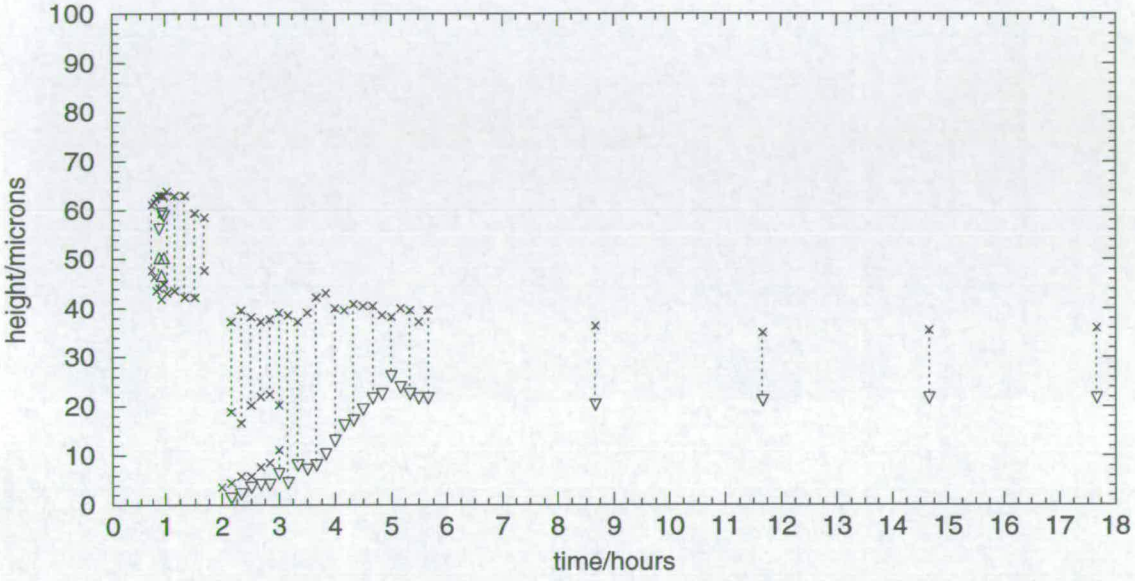

Figure 7.9: Density-matched crystallization in capillary, $\phi = 0.510$. The limits of regions where crystallites can be found in the field of view are shown by "$\times$" symbols; "∇" and "Δ" represent the upper and lower bounds of a fully crystalline field of view. For clarity, dotted lines have been added to highlight partially crystalline sections of some image stacks.

behaviour. Briefly, an ordered region appears in the middle of the tube after about 40 minutes, but after growing to fill the field of view it recedes completely over the next hour or so. Shortly after this another crystalline region appears, about a third of the way up the tube. This region appears unconnected with the previous one and with a region growing up from the bottom of the tube. These two new regions eventually join and, after about 6 hours after the start of the experiment, the suspension seems to have reached some sort of steady state, with roughly the bottom third of the tube being crystalline, which is consistent with a volume fraction of 0.51.

Figure 7.10 illustrates this behaviour. The three regions where crystallization was observed to originate are shown by the images at 48 and 59 μm of the stack

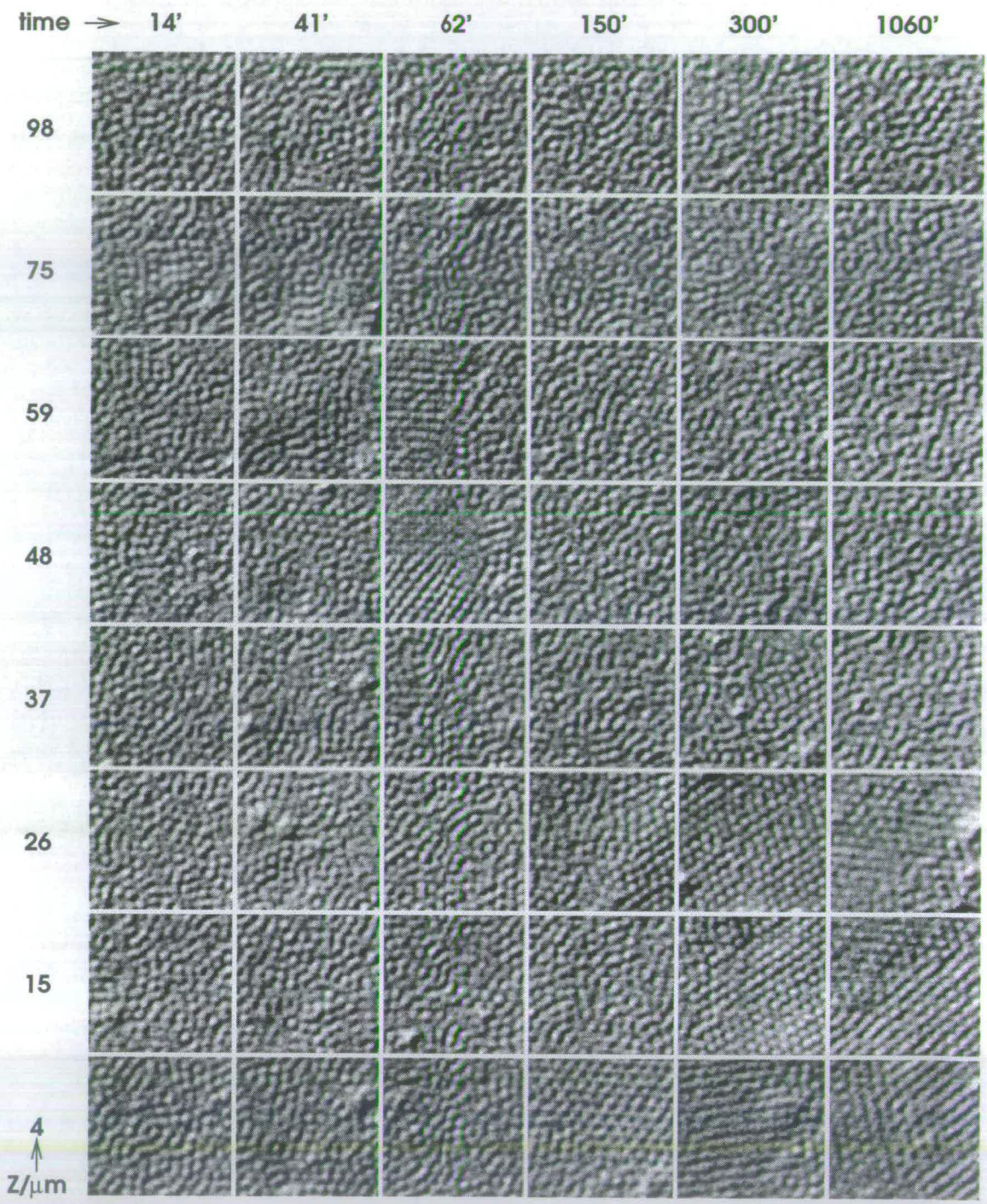

Figure 7.10: Images of a density-matched suspension at $\phi = 0.510$, showing the appearance of the suspension at heights $z = 4$, 15, 26, 37, 48, 59, 75 and 98 μm above the bottom of the 100 μm deep capillary tube, at times of 14, 41, 62, 150, 300 and 1060 minutes after being left to settle.

at 62 minutes, the image at 26 μm of the stack at 150 minutes and the image at 4 μm of that same stack.

First, we should note that the images very close to the top of the tube show very little evidence of any reduction in particle density and that the rate of upward growth of the bottom crystalline region – obtained from figure 7.9 – is $1.7 \pm 0.4 \times 10^{-9}$ m s^{-1}, so this region is unlikely to be due to sedimentation.

Secondly, we need to consider what has happened to the first crystalline region that appeared in the middle of the tube, grew to fill the field of view and then moved out of it. Five explanations seem worth considering: stage drift, diffusion, sedimentation, convection and melting.

Stage drift, *i.e.* the movement of the suspension mounting relative to the objective, can be ruled out, as movements $\mathcal{O}(10^0)$ μm are the maximum likely over the time-scale of the disappearance of the crystalline region, given that the microscope illumination had been turned on a long time previously (see §4.2.2). Not only is the field of view $\mathcal{O}(10^1)$ μm, but an ambient temperature change of several kelvin, such as would be expected for a magnitude of stage drift as large as this, is not likely in an air-conditioned laboratory.

Diffusion also seems very unlikely. This region was observed on the CCD video monitor to be at least 20 μm in diameter. The time for an object of radius R_p to diffuse its own radius is of the order of $\frac{{R_p}^3 \eta_m}{6\pi k_B T}$. Following Meeker *et al.* [1997] again, a viscosity $\eta_m = \mathcal{O}(10^{-1})$ Pa s, *i.e.* 10^2 times the value for the pure medium without any suspended particles, gives a time $t = \mathcal{O}(10^5)$ s, *i.e.*, several days would be expected.

That the crystallite does not disappear by sedimentation is clear, both from the fact that sedimentation does not have any noticeable effects over the time-scale of the whole experiment, let alone the much shorter time over which the crystallite disappears, and from the fact that the upper and lower bounds of this region, followed in figure 7.9, show no evidence for any general vertical drift.

Despite the way in which the crystalline region appears to disappear sideways,

convection would not appear to be the explanation, either. From past experience of similar experiments, the sort of large scale co-ordinated movement of particles, at least at the rates required here, has never been observed, except during the filling of capillary tubes and at the edges of drying out suspensions, neither of which are the case here. By way of confirmation, a recording of one image every second for half an hour, played back at high speed, showed no such drift in a suspension of similar age and volume fraction.

The most likely explanation would therefore seem to be that the crystalline region has melted, not having reached the critical radius. Treating this region as a sphere (its vertical and horizontal extents were comparable), its radius reached at least 10 μm. The theory of van Duijneveldt and Lekkerkerker [1995] suggests $R_\nu^{crit} = 6.8$ μm, but the surface tension of hard spheres is not well known and this theory assumes an isolated nucleus growing particle by particle from a dilute fluid, so that the expression used in this theory should give a value even this close to the lower limit implied by the melting explanation of this experimental result is in itself better than might have been hoped for.

If this region does represent an unstable nucleus, then its structure might be expected to show unusual features [van Duijneveldt and Frenkel, 1992; Shen and Oxtoby, 1996]. None were immediately apparent on examination of the relevant section of the image stack, but the data are of sufficient detail to merit further analysis, given the time. For the moment, all that can be said is that melting seems to be the most likely explanation for the disappearance of this crystalline region. What can be said with confidence, though, is that, whether this melting explanation is reliable or not, this experiment makes clear the potential for optical microscopy to make a significant contribution to colloid physics.

7.3.3 $\phi = 0.50$

In order to complete the comparison with the standard system, a density-matched suspension at just above the freezing concentration was prepared. In the large

cell, isolated crystals in the body of the suspension were first observed after four days, but no clear boundary between crystal and fluid could be discerned until a week later. The crystalline region at the bottom of the suspension, which appeared to contain only a very small layer of sedimentary crystal at the bottom, grew at a rate of 1.4×10^{-9} m s^{-1}, over the course of the two months that the suspension was allowed to stand. Since sedimentation did not seem to play a significant part in this growth, it seems likely that the extrapolation of the height of the crystalline region back to the start time would give a falsely low value for volume fraction. Indeed, the value of 0.496 ± 0.001 obtained by this method was towards the low end of the range 0.499 ± 0.010 suggested from measuring the sediment after centrifuging.

Figure 7.11 shows that nothing could be seen for the first five hours or so. After

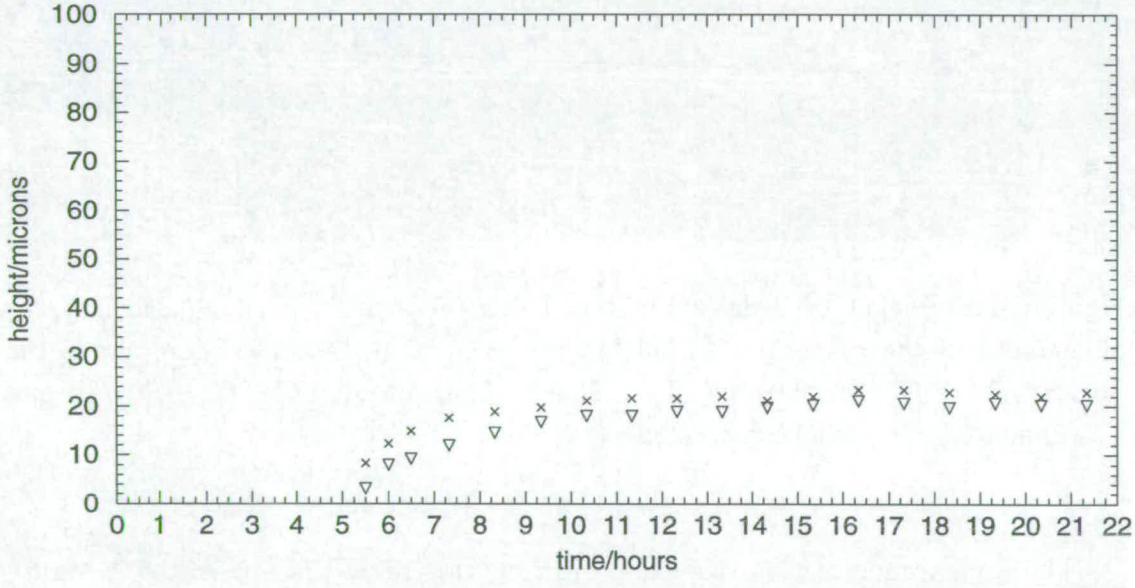

Figure 7.11: Density-matched crystallization in capillary, $\phi = 0.50$. The limits of regions where crystallites can be found in the field of view are shown by "$\times$" symbols; "∇" represents the upper bound of a fully crystalline field of view.

this, a crystalline region grows upwards from the bottom of the tube, initially at a rate of $7.1 \pm 1.2 \times 10^{-9}$ m s^{-1}, before halting at a level of 21 ± 2 μm. If this level represents the equilibrium proportion of crystal, then a value of $\phi^{\natural} = 0.505 \pm 0.001$

would be suggested.

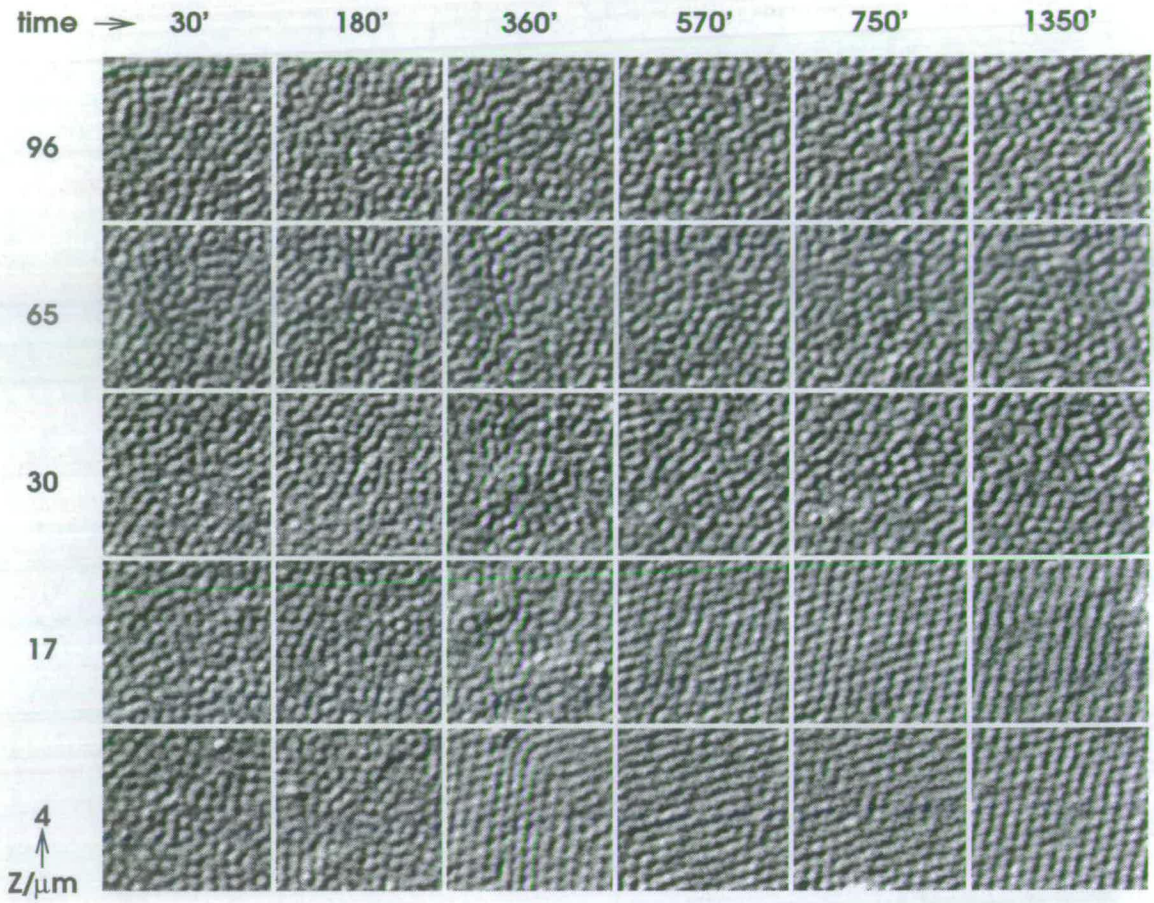

Figure 7.12: Images of a density-matched suspension at $\phi = 0.50$, showing the appearance of the suspension at heights $z = 4$, 17, 30, 65 and 96 μm above the bottom of the 100 μm deep capillary tube, at times of 30, 180, 360, 570, 750 and 1350 minutes after being left to settle.

The appearance of this suspension during this period is illustrated in figure 7.12, showing the way in which the crystalline region appears at the bottom, grows, then reaches a steady value, all while the topmost regions have yet to markedly decrease in density due to sedimentation.

Following van Duijneveldt and Lekkerkerker [1995] would suggest that the critical radius for a volume fraction of 0.505 would be about 10 μm, which could explain why only a single crystallite is seen in any image stack. That the volume fraction is more properly given by the value obtained from the capillary rather

than the bulk is likely, given that the speed at which the crystal growth occurs implies that the crystals are not sedimentary, whereas, the capillary being much shallower than the large cell, the equilibrium proportion of crystal to fluid is reached much quicker, *i.e.* within the duration of the experiment. If this conjecture holds, then the fact that the crystalline region nucleated at the bottom could well be just coincidental.

* * *

The results given in this chapter are obviously open to more detailed analysis. However, they satisfy the purpose of their inclusion, which is to give a taste of the sort of work which can be done using the experimental protocol established in the first part of this thesis. The following chapter adds to this demonstration, but those results have not been included here because they form a slightly disparate group, compared to the coherent set of this chapter.

Chapter 8

Additional Interesting Observations

This chapter contains several examples of the application of digital image processing techniques to colloidal optical micrographs. The first example is an updated version of a classic experiment, now automated for rapid data collection. The second example shows a system of how particle recognition can be achieved automatically in a particular, specific case. Thirdly, a possible method of measuring rates of diffusion is tentatively suggested. All three examples are included at this point by way of further demonstrating the potential of optical microscopy as a tool for colloid physicists, as well as suggesting avenues of future research. As such, they represent only preliminary results and await further development.

8.1 Sedimentation profiles

Being at the upper limit of the colloidal range, particles large enough to image will have a gravitational potential energy difference across their diameter close to their thermal energy, *i.e.*,

$$\frac{8}{3}\pi(\rho_p - \rho_m)gR_p{}^4 \approx k_B T, \tag{8.1}$$

where ρ_p and ρ_m are the densities of the particle and medium, respectively. The consequent particle-concentration variation with depth, or **sedimentation profile**, observed microscopically, was what lead Perrin [1908, 1910] to the discov-

ery of sedimentation equilibrium, for which he won the 1926 Nobel Prize for Physics and put "a definite end to the long struggle regarding the real existence of molecules"*.

For dilute suspensions, the equilibrium sedimentation profile is exponential in shape, with a characteristic **sedimentation length**

$$Z_{\text{sed}} = \frac{k_B T}{\frac{4}{3}\pi(\rho_p - \rho_m) g {R_p}^3}. \tag{8.2}$$

For sedimentation to have only a very slow effect on a suspension, we require $Z_{\text{sed}} \gg R_p$. Measurement of Z_{sed} for a particular combination of particle and medium will therefore be useful in determining how significant sedimentation effects might be, for instance, in crystallization.

Perrin carried out his measurements by directly counting particles, focusing by hand. With the automated system of acquiring image stacks, as described in §4.2, and an automated particle counting system, described here, sedimentation lengths can be measured in a few minutes.

Automated particle counting

Figure 8.1 shows a sedimentation profile for a suspension of PMMA-PHSA spheres in a mixture of CHPB and decalin (80 : 20 by mass), obtained from a stack of images spaced by 1 μm. The profile was the result of measuring the area of each image corresponding to in-focus particles, according to the following scheme (each stage is illustrated in figure 8.2):

(a) The stack was recorded in positive phase contrast, so that dark regions corresponded to particles. After recording, the stack average was calculated and a new stack was formed by subtracting this average and grey-level shifting by +128 for each image.

*Professor C.W. Osen, Royal Swedish Academy of Sciences, in the Presentation Speech – see Perrin [1965].

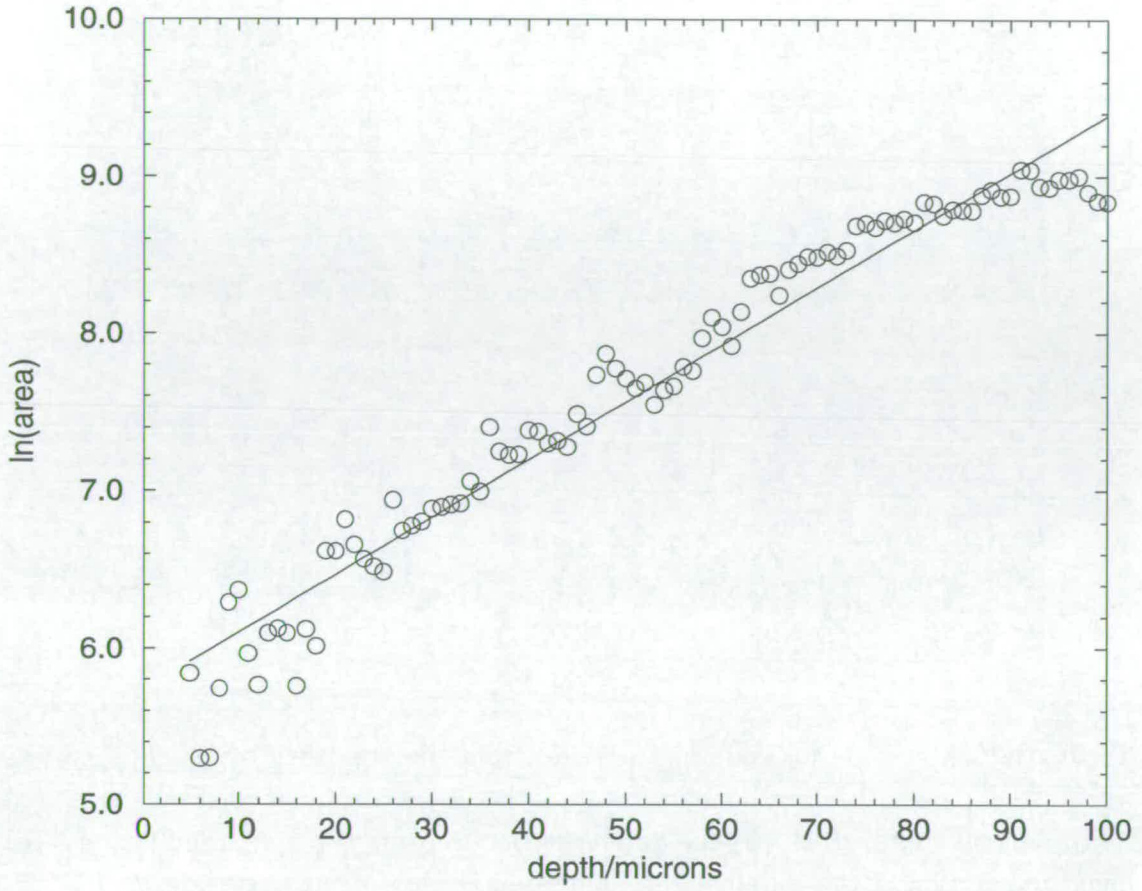

Figure 8.1: Sedimentation profile of a suspension of PMMA spheres ($R_p = 540 \pm 27$ nm) in a mixture of CHPB and decalin ($\phi \approx 0.05$). The straight line is a linear fit (correlation coefficient = 0.98); the reciprocal of the gradient, $Z_{\text{sed}} = 27.4 \pm 0.6$ μm.

(b) First, to remove noise, the images were convolved with 5×5 smoothing kernel (*cf.* figure 3.19(b), where a 3×3 kernel is illustrated).

(c) To remove long range contrast variations, a convolution with a 30×30 smoothing kernel was calculated.

(d) The difference between these two low passes, grey-level shifted by +128, gave a version of the original with contrast variations on length scales of 6 to 29 pixels enhanced (the in-focus particles were expected to be about 15 pixels in diameter).

(e) A threshold was set at grey level 125 (just below the average), and the high-

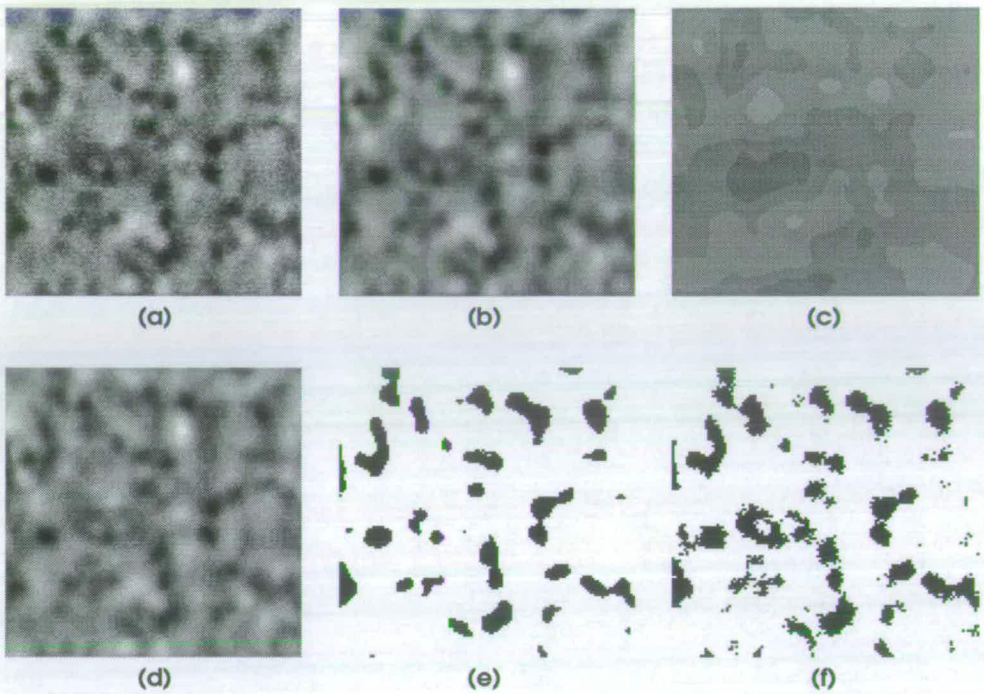

Figure 8.2: A scheme for counting particles from the area they occupy: (a) shows the basic image, (b) is the same image smoothed by a 5×5 convolution kernel, (c) *ditto*, but 30×30 kernel, (d) the difference between the two smoothed images, (e) binarized version of this difference, (f) binarized version of the basic image.

lighted (dark) area measured.

(f) If the same threshold were applied to the unsmoothed images a much less reliable estimate of area corresponding to particles would be achieved, owing to the noise and background intensity variations.

If the area highlighted is proportional to the number of particles, then a log-linear plot of area against vertical position should give a straight line and Z_{sed} should be obtainable from the gradient. By this method, figure 8.1 gave a value of 27.4 ± 0.6 μm, very close to that achieved by counting particles individually, *viz.*, 28.2 ± 0.6 μm. This close correlation was confirmed in a number of cases, so the thresholding-and-area-measuring method would appear to be justified. The advantage of this method is that the image processing and measuring can be entirely automated, without the need for sophisticated particle recognition systems.

8.2 A particle recognition scheme

If all in-focus objects have a common characteristic, digital processing can be used to identify the positions of such a characteristic, *i.e.*, we can achieve automatic particle recognition.

In practice, particularly in dense suspensions, where particles are very close, it is hard to achieve a general scheme for a given imaging system which requires no fitting beyond the expected particle size. Volume fraction and structure of the suspension, and brightness, contrast and noise of the image all affect the choice of parameters in a particle recognition scheme.

However, as an example of what can be achieved in one particular case, I include here a scheme for $R_p = 540$ μm spheres imaged by Normarski DIC:

Referring to figure 8.3, where the central image is the original image, as recorded, then (clockwise from the middle of the top row):

1. The raw image is smoothed (with a 3×3 kernel), to reduce noise.

2. The bright-to-dark intensity gradient from upper left to lower right across the DIC images of particles is picked out by convolving with the kernel labelled (a), which has a gradient of that sort, extending over a range comparable with the diameter of a particles.

3. To separate the regions corresponding to different particles, we convolve with sharpening kernel, (b).

4. By setting the threshold at a grey level of 128, binarizing divides the image into particles and background.

5. All bright pixels with fewer than 4 bright neighbours are eroded, repeatedly, until only single pixels remain.

6. As sometimes more than one pixel remains per particle, we convolve with a disc the size of the particles (kernel (c)).

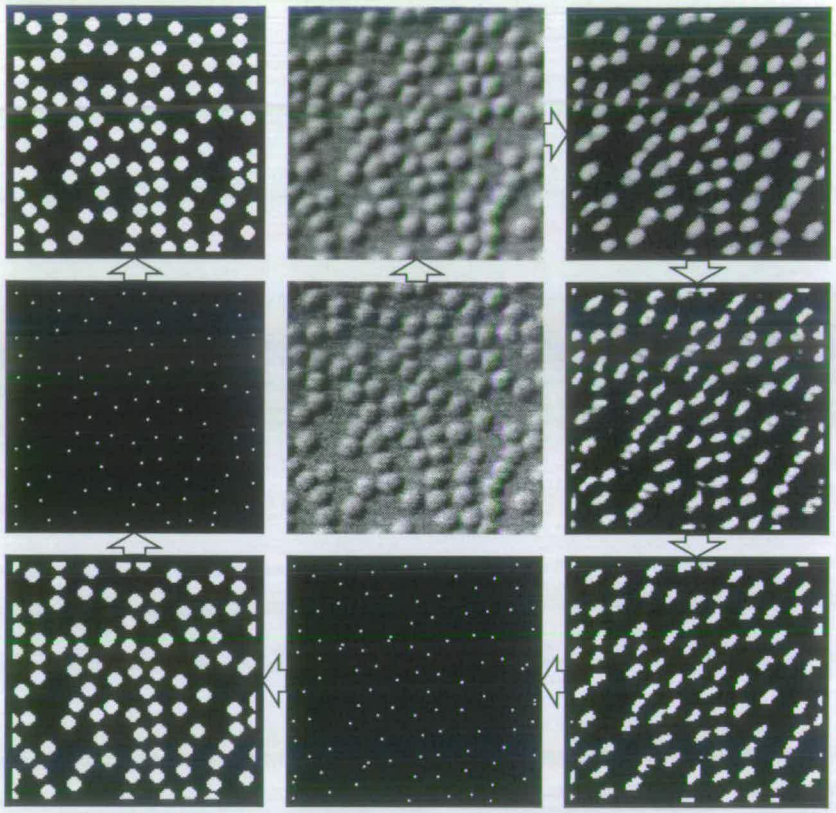

(a)

5	0	0	0	0	0
0	3	0	0	0	0
0	0	1	0	0	0
0	0	0	-1	0	0
0	0	0	0	-3	0
0	0	0	0	0	-5

(b)

-6	-9	-9	-9	-6
-9	8	14	8	-9
-9	14	40	14	-9
-9	8	14	8	-9
-6	-9	-9	-9	-6

(c)

0	0	0	0	0	0	0	0	0	0
0	0	0	1	1	1	0	0	0	
0	0	1	1	1	1	1	0	0	
0	1	1	1	1	1	1	1	0	
0	1	1	1	1	1	1	1	0	
0	1	1	1	1	1	1	1	0	
0	0	1	1	1	1	1	0	0	
0	0	0	1	1	1	0	0	0	
0	0	0	0	0	0	0	0	0	

Figure 8.3: A scheme for recognizing particles automatically: the central image is the recorded DIC image of $R_p = 540$ μm spheres; then, clockwise from the middle of the top row, this image is smoothed, convolved with the kernel (a), then with (b), binarized, eroded to single pixels, convolved with (c), eroded again, convolved with (c) again.

7. Those single pixels which had belonged to the same particle having now become large, but fairly round, single regions, we perform the erosion process again, to arrive at one pixel for each particle.

8. Finally, for the purpose of comparison with the original image we can convolve with the disc (c) again.

The positions of the single pixels in the penultimate image (middle row, left) are closely correlated with the positions of the particles (*cf.* the original image). If this is the information required from the stack, then a considerable reduction in data storage requirements can be achieved by following this scheme: a single

128×128 8-bit image requires at least 16 kilobytes, whereas the coordinate pairs for, say, 100 particle positions requires only 200 bytes. Even storing the final result as an image, either in single pixel form or after convolution with the particle-sized disc, will mean an eightfold saving, as these images are binary, *i.e.* 1-bit.

In the scheme given, grey-level values were scaled for each of the images shown, in order to bring the results of the convolutions to within the 0 to 255 range. The amount of scaling was chosen by inspection, for display purposes. Only when setting the threshold does a choice of a particular grey level make a qualitative difference to the final result. The threshold was chosen to lie at the midpoint of the range, in order to try to avoid being image-specific.

This scheme gives quite good results for colloidal fluids at volume fractions in the range $\phi \lesssim 0.5$, but is not as good for denser systems, ordered or disordered. Nevertheless, schemes such as this can be useful, as long as they are applied appropriately.

8.3 Measurements from time-average series

If a series of images of a colloidal suspension is recorded over a period of time and then a series of averages of increasing numbers of images is performed, as shown figure 3.16, then the effect of particle motion is to increasingly blur the (averaged) images.

How much blurring occurs will be a measure of how much movement has happened. Figure 8.4 shows results obtained by measuring the grey-level variance of six sets of averages. This measure was used because the effect of averaging is to reduce the range of grey levels used.

The six sets of averages were obtained from images recorded at 10, 20, 30, 40, 50 and 60 μm from the top of a suspension 100 μm deep, with $\phi = 0.515$. Sixty-one images were recorded for each set, at one second intervals; averages were of increasing numbers of images. Inspection of the recorded images showed that the five series closest to the top of the suspension were of colloidal fluid,

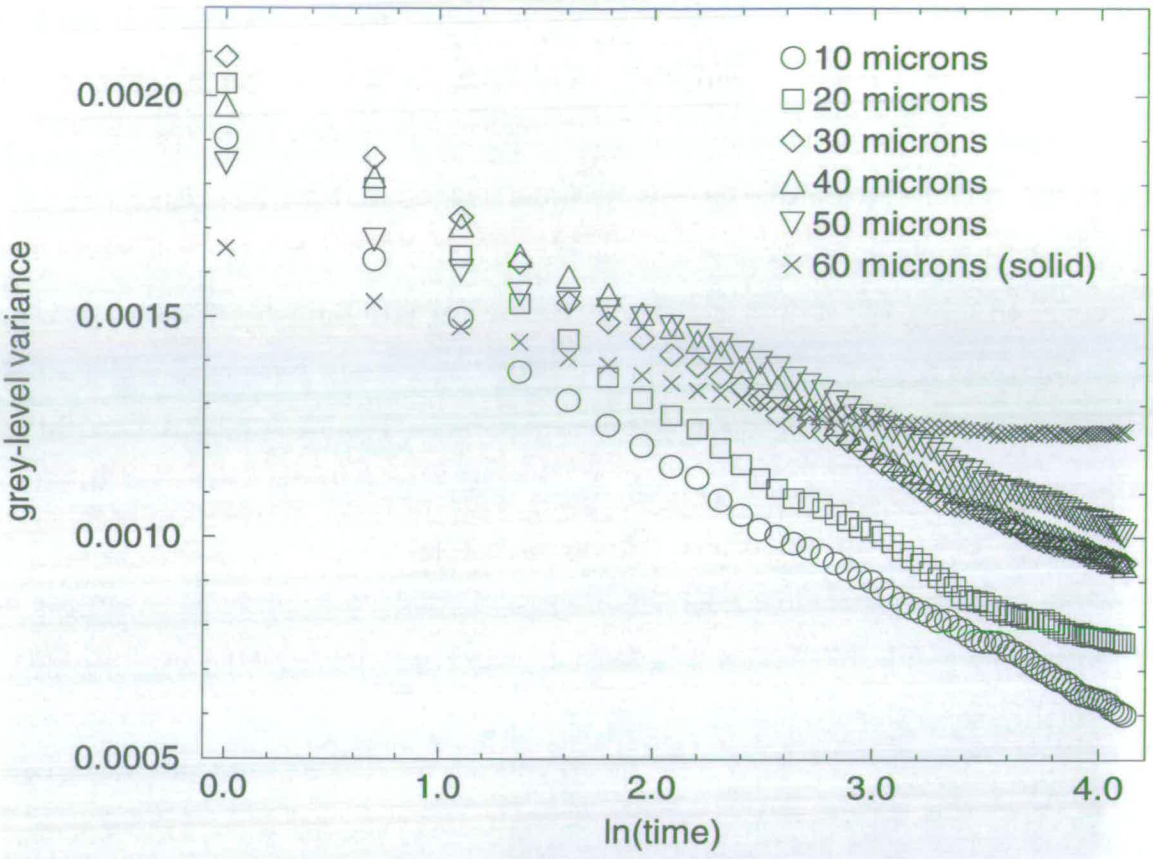

Figure 8.4: Diffusion coefficients from increasing time-averages?

whereas the deepest was of a crystalline region.

What is interesting about these results is the way that the contrast appears to decrease exponentially with time in the fluid regions, at rate that decreases with depth (it is also worth noting that the contrast of the crystalline region reaches a steady value). The volume fraction increase with depth may be the reason for the variation in the speed of blurring, so these measurements could possibly give some indication of diffusion coefficient, but the theory of how this would work has yet to be done.

Chapter 9

Conclusions

The aim of this thesis was to make the case for optical microscopy as a valuable tool for the colloid physicist, first by establishing a sound experimental protocol for optical microscopy suitable for colloidal suspensions, then by demonstrating some of the potential of such an approach.

Techniques of colloid microscopy

In establishing the experimental method reported here, many well-established techniques of the optical microscopy of phase objects were applied to the special case of colloidal suspensions and new techniques were developed in order to enable this application to include the full three-dimensional imaging of suspensions of sufficient thickness to show bulk behaviour.

Having reviewed the basic principles of the imaging process in light microscopy, under conditions suitable for resolving colloidal length scales, the effects of defocusing, in the case of the image of a single colloidal sphere, were used to demonstrate the deficiencies of standard, bright field microscopy, as well as the ability of both phase contrast and Normarski differential interference contrast to overcome these deficiencies, in their own peculiar ways. Expressions for the contrast of images of colloidal particles were developed and used to explain experimental results.

The effects of a wide range of digital image processing methods on images of colloidal suspensions were shown, too. In particular, methods for counting particles and for the display of three-dimensional data were demonstrated, along with an example of an approach to finding particle coordinates.

In solving the problems presented by the imaging of thick suspensions, new methods were presented for mounting such suspensions for microscopical observation, and for controlling the acquisition of three-dimensional image data.

These new methods, along with a number of observations concerning points of practice, aimed at obtaining the best possible data, combine with the illustrated application of established methods to provide an introductory set of tools for all aspects of the real-space, real-time study of the microscopical behaviour of colloidal suspensions in three dimensions.

Demonstrations of colloid microscopy

Aside from examples illustrating the application of individual tools in the set, some of the potential of the whole set was shown by a detailed study of the structure of the hard-sphere solid and an investigation of the nucleation process, with the determination of sedimentation length from density profiles as a supplementary example.

The structural study of the hard-sphere solid involved careful interpretation of the images obtained: by analysing image patterns, it was shown that, while unable to give as good optical sectioning as confocal microscopy, the quality of sectioning achievable was good enough, not only to confirm the expected random-stacked close-packed arrangement, but also to open the way for further investigation of local defects, the measurement of stacking probability being one particular illustration of this potential.

By means of a time-lapse series of image stacks, the earliest stages of nucleation were demonstrated to be accessible to study.

Both these studies illustrated well the advantages of direct imaging over recip-

rocal space methods: the direct route to structure determination and the ability to resolve fine detail spatially and temporally. This level of detail, impossible to achieve for atomic systems, has here been shown to be readily achievable for colloids, which can be used to model atomic behaviour with numbers of particles of several orders of magnitude larger than possible in computer simulations. So whether colloids are studied as model atoms, or in their own right, it can be seen that optical microscopy has a vital part to play, a part which it has been the purpose of this thesis to establish.

Suggestions for future work

Only some of the vast potential of optical microscopy, as applied to colloidal suspensions has been exploited here. Among the many avenues for further work, the following spring directly from what has been presented:

1. Further investigation of the polycrystalline nature of the solid structure, looking into ageing effects on stacking probability and the crystallite size distribution, deformations of crystallites and variations of stacking probability with volume fraction and crystallite size, is perhaps the most immediately obvious avenue for developing the work started here.

2. The full analysis of a number of patterns presented by images of the *rscp* solid also remains to be done. In particular, it would be good to establish how much information each can give about stacking probability. The use of three-dimensional display methods on image stacks would be worth pursuing in this context.

3. A deeper study of the nucleation process is required. Though particle tracking would yield the greatest detail, much could be obtained from following the development of the small regions of order as units. In particular, the structure of sub-critical nuclei would be worth examining further.

4. The key to a general scheme of particle recognition and hence coordinate extraction and tracking, would seem to lie in image deconvolution. A non-trivial exercise in digital image processing, success would provide a very powerful tool to complement those presented here.

There are many other possibilities which colloid microscopy opens up, but these suggestions, deriving from the work already done and presented here, serve as additional evidence for my original contention, *viz.*, that careful optical microscopy is an extremely useful tool for the colloid physicist.

Appendix A

Derivations

A.1 The Airy pattern – the bright field P.S.F.

This appendix derives the monochromatic light amplitude and intensity distributions for the image of an axial point object due to an aberration-free imaging system with a circularly symmetric exit pupil. The notation conforms to table 2.1, except where otherwise stated. We will follow the approach of Rayleigh [1896], who stated that we can associate all diffraction effects with the propagation of light between the exit pupil and the image, and treat the rest of the system geometrically.

The object

The object can be represented by a scaled Dirac delta function

$$u(r,\theta) = \Lambda\, \delta_{\perp}(r,\theta), \tag{A.1}$$

where Λ is the luminosity of the object, uniform over 2π steradians behind the object and the Dirac delta function $\delta_{\perp}$ may be defined by

$$\delta_{\perp}(r,\theta) = \delta_{\perp}(r) = \lim_{R\to 0} \frac{\mathrm{circ}\left(\frac{r}{R}\right)}{\pi R^2}, \tag{A.2}$$

the circle function $\mathrm{circ}(\frac{r}{R})$ being defined by

$$\mathrm{circ}\left(\frac{r}{R}\right) = \begin{cases} 1 & : \quad r \leq R \\ 0 & : \quad r > R \end{cases} \tag{A.3}$$

The geometrical output of the imaging system

For a distance from Π to $\Pi_{\mathcal{P}}$ of z, only a fraction

$$\frac{1}{4}\left[1 - \frac{z}{\sqrt{z^2 + {R_{\mathcal{P}}}^2}}\right] \tag{A.4}$$

of the light from the object will be accepted by the imaging system. where Λ is the luminosity of the object.

For an aberration-free imaging system, a point object will lead to spherical wavefronts at the exit pupil, converging on the geometrical image, *i.e.* wavefronts of the form

$$\frac{e^{\frac{2\pi i}{\lambda'}\sqrt{z'^2 + {r'_{\mathcal{P}}}^2}}}{\sqrt{z'^2 + {r'_{\mathcal{P}}}^2}}, \tag{A.5}$$

where z' is the distance $\Pi'_{\mathcal{P}}$ to Π' and λ' is the wavelength of the light behind the exit pupil $(\frac{\lambda}{n'})$.

The circularly symmetric exit pupil transmittance function $\tau'_{\mathcal{P}}$ is given by

$$\mathrm{circ}\left(\frac{r'_{\mathcal{P}}}{R'_{\mathcal{P}}}\right). \tag{A.6}$$

We get the light distribution at the exit pupil by multiplying together expressions A.4 (to get the brightness of the geometrical image right), A.5 (spherical wavefront) and A.6 (to set the lateral extent of the wavefront):

$$u'_{\mathcal{P}}(r'_{\mathcal{P}}, \theta'_{\mathcal{P}}) = \frac{\Lambda}{4}\left[1 - \frac{z}{\sqrt{z^2 + {R_{\mathcal{P}}}^2}}\right] \cdot \frac{e^{\frac{2\pi i}{\lambda'}\sqrt{z'^2 + {r'_{\mathcal{P}}}^2}}}{\sqrt{z'^2 + {r'_{\mathcal{P}}}^2}} \cdot \mathrm{circ}\left(\frac{r'_{\mathcal{P}}}{R'_{\mathcal{P}}}\right). \tag{A.7}$$

Dots have been used to separate the scaling, wavefront and pupil terms.

Equation A.7 represents the geometrical output of the imaging system. Now we just need to consider the diffraction of this light distribution between $\Pi'_{\mathcal{P}}$ and Π'.

The propagation of light from the exit pupil to the image plane

If λ' is small compared to z, $R_{\mathcal{P}}$, $R'_{\mathcal{P}}$ and z', then we can treat the light as a scalar and use the Rayleigh-Sommerfeld formulation of the Huygens-Fresnel principle. Expressed in polar coordinates, this tells us

$$u'(r',\theta') = \int_0^{2\pi}\int_0^{\infty} u'_{\mathcal{P}}(r'_{\mathcal{P}},\theta'_{\mathcal{P}}) \left[\frac{e^{-\frac{2\pi\imath}{\lambda'}d'}}{\imath\lambda' d'}\right] \frac{z'}{d'}\, r'_{\mathcal{P}}\, dr'_{\mathcal{P}}\, d\theta'_{\mathcal{P}}, \tag{A.8}$$

where s is the distance between the points $(r'_{\mathcal{P}},\theta'_{\mathcal{P}})$ and (r',θ'), so that

$$\begin{aligned} s &= \sqrt{z'^2 + (r'_{\mathcal{P}}\cos\theta'_{\mathcal{P}} - r'\cos\theta')^2 + (r'_{\mathcal{P}}\sin\theta'_{\mathcal{P}} - r'\sin\theta')^2} && \text{(A.9)}\\ &= \sqrt{z'^2 + {r'_{\mathcal{P}}}^2 + r'^2 - 2r'_{\mathcal{P}}r'\cos(\theta'_{\mathcal{P}} - \theta')} && \text{(A.10)}\\ &= z'\left(1 + \frac{{r'_{\mathcal{P}}}^2 + r'^2 - 2r'_{\mathcal{P}}r'\cos(\theta'_{\mathcal{P}} - \theta')}{z'^2}\right)^{\frac{1}{2}}. && \text{(A.11)} \end{aligned}$$

Equation A.8 shows us that the image amplitude distribution will be given by the sum over the exit pupil wavefront $u'_{\mathcal{P}}$ of an infinite number of spherical wavelets propagating towards Π', resolved along the optical axis. The term in square brackets represents the spherical wavelets and the $\frac{z'}{s}$ term the cosine of the angle between the wavelet normals and the optical axis (by symmetry, the components perpendicular to the axis will cancel).

Substituting for $u'_{\mathcal{P}}$, from equation A.7, into equation A.8:

$$u' = \frac{\Lambda}{4\imath\lambda'}\left[1 - \frac{z}{\sqrt{z^2 + {R_{\mathcal{P}}}^2}}\right]\int_0^{2\pi}\int_0^{\infty} \mathrm{circ}\left(\frac{r'_{\mathcal{P}}}{R'_{\mathcal{P}}}\right)\frac{e^{\frac{2\pi\imath}{\lambda'}\left(\sqrt{z'^2+{r'_{\mathcal{P}}}^2}-s\right)}}{s^2\sqrt{z'^2+{r'_{\mathcal{P}}}^2}} z'\, r'_{\mathcal{P}}\, dr'_{\mathcal{P}}\, d\theta'_{\mathcal{P}}. \tag{A.12}$$

Now, z' is large compared to $R'_{\mathcal{P}}$ and R' (*i.e.*, we have **Fresnel diffraction conditions**). Moreover, the integrand in equation A.12 is zero for $r'_{\mathcal{P}} > R'_{\mathcal{P}}$ and we have chosen R' to be such that no significant image information is found for $r' > R'$. This means that, expanding equation A.11, we can approximate

$$s \approx z' + \frac{{r'_{\mathcal{P}}}^2 + r'^2 - 2r'_{\mathcal{P}}r'\cos(\theta'_{\mathcal{P}} - \theta')}{2z'} \tag{A.13}$$

and

$$\sqrt{z'^2 + {r'_{\mathcal{P}}}^2} \approx z' + \frac{{r'_{\mathcal{P}}}^2}{2z'}. \tag{A.14}$$

While we apply these second-order approximations to the exponential in equation A.12, it is sufficient to apply the first order approximations $s \approx z'$ and $\sqrt{z'^2 + {r'_\mathcal{P}}^2} \approx z'$ elsewhere. This gives us

$$u' = \frac{\Lambda}{4\imath\lambda'}\left[1 - \frac{z}{\sqrt{z^2 + {R_\mathcal{P}}^2}}\right] \int_0^{2\pi}\int_0^{\infty} \mathrm{circ}\left(\frac{r'_\mathcal{P}}{R'_\mathcal{P}}\right) \frac{e^{\frac{2\pi\imath}{\lambda' z'}\left(r'_\mathcal{P} r' \cos\left(\theta'_\mathcal{P} - \theta'\right) - \frac{r'^2}{2}\right)}}{z'^2} r'_\mathcal{P}\, dr'_\mathcal{P}\, d\theta'_\mathcal{P}, \quad \text{(A.15)}$$

which we can rearrange to

$$u' = \frac{\Lambda}{4\imath\lambda' z'^2}\left[1 - \frac{z}{\sqrt{z^2 + {R_\mathcal{P}}^2}}\right] e^{-\frac{\pi\imath r'^2}{\lambda' z'}} \int_0^{\infty} r'_\mathcal{P}\, \mathrm{circ}\left(\frac{r'_\mathcal{P}}{R'_\mathcal{P}}\right) \int_0^{2\pi} e^{\frac{2\pi\imath r'_\mathcal{P} r'}{\lambda' z'}\cos\left(\theta'_\mathcal{P} - \theta'\right)} d\theta'_\mathcal{P}\, dr'_\mathcal{P}. \quad \text{(A.16)}$$

The quadratic phase term $e^{-\frac{\pi\imath r'^2}{\lambda' z'}}$ shows that the effect of our approximations has been to treat the spherical wavefronts as parabolic surfaces. This is the physical meaning of the Fresnel diffraction conditions.

Integrating with respect to θ, we get

$$u' = \frac{\Lambda}{4\imath\lambda' z'^2}\left[1 - \frac{z}{\sqrt{z^2 + {R_\mathcal{P}}^2}}\right] e^{-\frac{\pi\imath r'^2}{\lambda' z'}} \int_0^{\infty} r'_\mathcal{P}\, \mathrm{circ}\left(\frac{r'_\mathcal{P}}{R'_\mathcal{P}}\right) 2\pi J_0\left(\frac{-2\pi r'_\mathcal{P} r'}{\lambda' z'}\right) dr'_\mathcal{P}, \quad \text{(A.17)}$$

where J_0 denotes a zeroth order Bessel function of the first kind.

Applying the circ limits and rearranging gives

$$u' = \frac{\pi\Lambda}{2\imath\lambda' z'^2}\left[1 - \frac{z}{\sqrt{z^2 + {R_\mathcal{P}}^2}}\right] e^{-\frac{\pi\imath r'^2}{\lambda' z'}} \int_0^{R'_\mathcal{P}} r'_\mathcal{P}\, J_0\left(\frac{-2\pi r'_\mathcal{P} r'}{\lambda' z'}\right) dr'_\mathcal{P}. \quad \text{(A.18)}$$

Next, we change variables:

$$u' = \frac{\lambda'\Lambda}{8\pi\imath r'^2}\left[1 - \frac{z}{\sqrt{z^2 + {R_\mathcal{P}}^2}}\right] e^{-\frac{\pi\imath r'^2}{\lambda' z'}} \int_0^{-2\pi R'_\mathcal{P} r'/\lambda' z'} \frac{-2\pi r'_\mathcal{P} r'}{\lambda' z'} J_0\left(\frac{-2\pi r'_\mathcal{P} r'}{\lambda' z'}\right) d\left(\frac{-2\pi r'_\mathcal{P} r'}{\lambda' z'}\right). \quad \text{(A.19)}$$

Finally, integrating, using $\int_0^M m\, J_0(m)\, dm = M\, J_1(M) = -M\, J_1(-M)$, we end up with

$$u'(r',\theta') = u'(r') = \frac{\Lambda R'_{\mathcal{P}}}{4\imath r' z'}\left[1 - \frac{z}{\sqrt{z^2 + {R_{\mathcal{P}}}^2}}\right] e^{-\frac{\pi \imath {r'}^2}{\lambda' z'}} J_1\left(\frac{2\pi R'_{\mathcal{P}} r'}{\lambda' z'}\right), \quad \text{(A.20)}$$

where J_1 is a first order Bessel function of the first kind. This equation is our desired light amplitude distribution, the bright field **amplitude point spread function** of an axial point object, for an aberration-free imaging system with a circularly symmetric exit pupil.

Before we consider the intensity distribution, first note that the Fourier transform of a circ function is given by

$$\mathcal{F}\left\{\text{circ}\left(\frac{r'}{\lambda' z' R'_{\mathcal{P}}}\right)\right\} = \frac{R'_{\mathcal{P}} \lambda' z'}{r'} J_1\left(\frac{2\pi R'_{\mathcal{P}} r'}{\lambda' z'}\right). \quad \text{(A.21)}$$

Comparison with equation A.20 shows the important result that:

> The image $u'(r')$ of a point object O is just a scaled real-space Fourier transform of the pupil function $\tau'_{\mathcal{P}}$, centred on the geometrical image O′.

We should note secondly that, for off-axis point objects, the above arguments still work under Fresnel conditions, as can be shown by a simple change of coordinate origins.

Thirdly, we can make matters simpler if we normalize the Bessel function in equation A.20 to $2\frac{J_1(s)}{s} = \text{jinc}(s)$ to get an **alternative amplitude PSF**:

$$u'(r') = \frac{\pi \Lambda {R'_{\mathcal{P}}}^2}{4\imath \lambda' {z'}^2}\left[1 - \frac{z}{\sqrt{z^2 + {R_{\mathcal{P}}}^2}}\right] e^{-\frac{\pi \imath {r'}^2}{\lambda' z'}} \text{jinc}\left(\frac{2\pi R'_{\mathcal{P}} r'}{\lambda' z'}\right), \quad \text{(A.22)}$$

which has all the variation with r' contained in the jinc term alone; the other terms affect all values of r' (and θ') equally.

To determine the intensity, we use $I' = u'u'^*$, so that

$$I'(r') = \left(\frac{\pi \Lambda {R'_{\mathcal{P}}}^2}{4\lambda' {z'}^2}\right)^2 \left[1 - \frac{z}{\sqrt{z^2 + {R_{\mathcal{P}}}^2}}\right]^2 \text{jinc}^2\left(\frac{2\pi R'_{\mathcal{P}} r'}{\lambda' z'}\right). \quad \text{(A.23)}$$

This is our desired expression for the bright field **intensity point spread function** of an axial point object, for an aberration-free imaging system with a circularly symmetric exit pupil, *i.e.* the **Airy pattern**.

As before, all the variation over Π' is contained in the jinc^2 term, so we can often use

$$I'(r') = \text{jinc}^2\left(\frac{2\pi R'_p r'}{\lambda' z'}\right) \tag{A.24}$$

as our practical expression for the intensity point spread.

A.2 Phase contrast image intensity

This appendix uses the phasor representation of phase contrast to derive an expression for image intensity I'. Figure A.1 is an annotated copy of figure 3.2(c), showing the phasor scheme for phase contrast. This figure shall be used to determine I'.

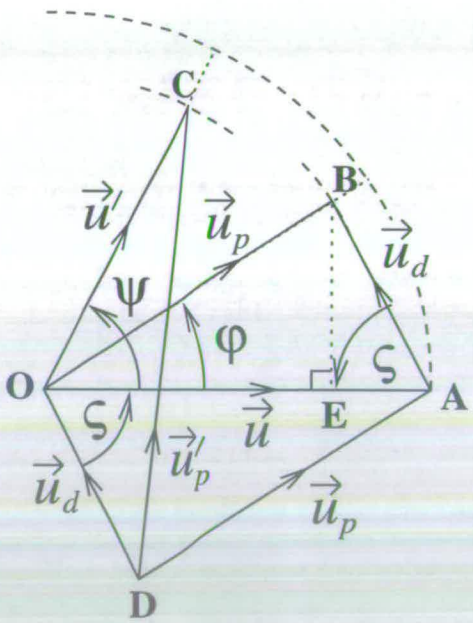

Figure A.1: Phasor representation of phase contrast

First, note that

$$\mathrm{OA} = |\vec{u}|\,, \tag{A.25}$$

$$\mathrm{OB} = |\vec{u}_p| = \Gamma\,|\vec{u}|\,, \tag{A.26}$$

$$\mathrm{OC} = |\vec{u}'| = \Upsilon\,|\vec{u}|\,, \tag{A.27}$$

$$\mathrm{OD} = \mathrm{AB}. \tag{A.28}$$

Now

$$I' = \left|\vec{u}'_p\right|^2 = \mathrm{DC}^2. \tag{A.29}$$

By the cosine rule,

$$\begin{aligned} \mathrm{DC}^2 &= \mathrm{OC}^2 + \mathrm{OD}^2 - 2\,\mathrm{OC}\,\mathrm{OD}\cos(\varsigma + \psi) \\ &= \mathrm{OC}^2 + \mathrm{OD}^2 - 2\,\mathrm{OC}\,(\mathrm{OD}\cos\varsigma\cos\psi - \mathrm{OD}\sin\varsigma\sin\psi)\,. \end{aligned} \tag{A.30}$$

Now, also by the cosine rule,

$$\mathrm{AB}^2 = \mathrm{OA}^2 + \mathrm{OB}^2 - 2\,\mathrm{OA}\,\mathrm{OB}\cos\varphi. \tag{A.31}$$

From equations A.25, A.26 and A.28, this gives us

$$\mathrm{OD}^2 = |\vec{u}|^2\left(1 + \Gamma^2 - 2\Gamma\cos\varphi\right). \tag{A.32}$$

By simple trigonometry,

$$\mathrm{AB}\cos\varsigma = \mathrm{EA} = \mathrm{OA} - \mathrm{OE} = \mathrm{OA} - \mathrm{OB}\cos\varphi. \tag{A.33}$$

From equations A.25, A.26 and A.28, this gives us

$$\mathrm{OD}\cos\varsigma = |\vec{u}|\,(1 - \Gamma\cos\varphi)\,. \tag{A.34}$$

By the sine rule,

$$\mathrm{AB}\sin\varsigma = \mathrm{OB}\sin\varphi \tag{A.35}$$

From equations A.26 and A.28, this gives us

$$\mathrm{OD}\sin\varsigma = |\vec{u}|\,\Gamma\sin\varphi. \tag{A.36}$$

So, using equations A.27, A.29, A.32, A.34 and A.36, equation A.30 becomes

$$I' = |\vec{u}|^2 \left(\Upsilon^2 + 1 + \Gamma^2 - 2\Gamma\cos\varphi - 2\Upsilon\left((1 - \Gamma\cos\varphi)\cos\psi - \Gamma\sin\varphi\sin\psi\right)\right) \tag{A.37}$$

Rearranging, and using $I_- = |\vec{u}|^2$ and the identity $\cos(P - Q) = \cos P \cos Q + \sin P \sin Q$, we arrive at our desired equation (3.13):

$$I' = I_- \left(1 + \Upsilon^2 + \Gamma^2 + 2\Upsilon\Gamma\cos(\psi - \varphi) - 2\Upsilon\cos\psi - 2\Gamma\cos\varphi\right). \tag{A.38}$$

Appendix B

List of Symbols and Abbreviations

B.1 Symbols

A	=	Area
$\mathcal{A}$, $\mathcal{A}'$	=	objective numerical aperture on object side, image side
$\mathcal{A}_\mathsf{C}$	=	condenser numerical aperture (on object side)
A_H	=	Hamaker constant
An	=	analyser (polarizing filter in image space)
A, B, C	=	the three lateral positions for stacking hexagonal layers
a, b, c, d	=	(Miller-Bravais) lattice constants
$\vec{a}$, $\vec{b}$, $\vec{c}$, $\vec{d}$	=	(Miller-Bravais) lattice vectors
C'	=	image contrast
C'_{+max}, C'_{-max}	=	maximum positive, negative phase contrast
Co	=	condenser
e	=	the lateral shear caused by a Wollaston prism
f, f'	=	focal length on object side, image side
f'_TL	=	image side (back) focal length of tube lens
F, F′	=	prinicpal focus on object side, image side
$\mathcal{F}\{\mathrm{f}(m)\}$	=	the Fourier Transform of the function f(m)
F_{vdW}	=	van der Waals force

g = acceleration of free fall

G = Gibbs free-energy

h, i, k, l = Miller-Bravais (crystallographic) indices

$(hkil)$ = the set of lattice planes for which $\frac{hx}{a} + \frac{ky}{b} + \frac{lz}{c}$ is an integer

$\{hkil\}$ = all the symmetrically equivalent sets of planes to $(hkil)$, *i.e.*, the crystallographic "form"

$\imath$ = $\sqrt{-1}$

I, I', I'_0 = intensity of object, image, image background

$I'_{\mathsf{coh}}, I'_{\mathsf{incoh}}, I'_{\mathsf{pcoh}}$ = *ditto* of image with coherent, incoherent and partially coherent illumination

$I_{\mathcal{P}}, I'_{\mathcal{P}}$ = *ditto* in plane of entrance pupil, exit pupil

I_-, I_{Il} = *ditto* in front of object, microscope substage

$\mathcal{I}'$ = *ditto* of image after convolution

j = dummy subscript

j_0, J_1 = zeroth, first order Bessel function of the first kind

k_B = the Boltzmann constant, 1.380658×10^{-23} JK^{-1}

$\mathcal{K}$ = convolution kernel

$\mathcal{K}_X, \mathcal{K}_Y$ = dimensions of *ditto* (in pixels)

m, m_1, m_2, M = dummy variables

$\mathsf{M}, \mathsf{M}_{\mathsf{Ob}}, \mathsf{M}_{\mathsf{Oc}}, \mathsf{M}_\mu$ = visual magnification, of objective, ocular, microscope

$\mathcal{M}, \mathcal{M}_\mu, \mathcal{M}_{\mathsf{PO}}$ = transverse magnification, of microscope, photo-ocular

$\mathcal{M}^x_\mu, \mathcal{M}^y_\mu$ = *ditto* of microscope along x-, y-direction

n, n', n_- = refractive index, of image space, in front of object

$n_p, n_m, n_{\mathsf{cs}}, n_{\mathsf{io}}$ = *ditto* of particle, medium, cover slip, immersion oil

N_p = number of particles

N_{im} = number of images in stack

N^x_{pix}, N^y_{pix}, N^z_{pix} = dimensions of an array of pixels

$N_=$, $N_{||}$ = number of hexagonal layers, of particles in each layer

O, O', $\mathsf{O}'_{\bowtie}$ = object, image, geometrical image

Ob, Oc = objective, ocular

p, p', p_{eye} = distance from lens to object, image, eye

P, $\tilde{P}$ = pressure, reduced pressure

P = polarizer (in front of microscope substage)

$\mathcal{P}$, $\mathcal{P}'$ = entrance, exit pupil of optical system

q, q' = distance from principal focus on object side to object, on image side to image

$\mathcal{Q}$ = tube lens factor

r, r', $r_{\mathcal{P}}$, $r'_{\mathcal{P}}$ = distance from optical axis in object space, image space, entrance pupil, exit pupil

r'_{Airy}, r_{Airy} = radius of Airy disc, conjugate in object space

r_{o} = radius of phase ring and image of annular aperture

Δr_{PR}, $\Delta r'_{\mathsf{AS}}$ = width of phase ring, image of annular aperture

R_p, R_ν = radius of particle, nucleus

R, R' = maximum radial extent of object, image

$R_{\mathcal{P}}$, $R'_{\mathcal{P}}$ = radius of entrance, exit pupil

s, $s_{\asymp}$ = separation (centre to centre), edge to edge

ΔS = entropy difference

$\mathcal{S}_x$, $\mathcal{S}_y$, $\mathcal{S}_x$ = scaling factors for digital images

t = time

T = absolute temperature

u, u', u'^* = light amplitude, in image, complex conjugate of *ditto*

$u_{\mathcal{P}}$, $u'_{\mathcal{P}}$, u_- = *ditto* at entrance, exit pupil, in front of object

$\vec{u}$, $\vec{u}_p$, $\vec{u}_d$, $\vec{u}'$, $\vec{u}'_p$ = phasor representing direct, perturbed, diffracted, attenuated direct, resultant wave

$\vec{u}_1$, $\vec{u}_2$ = phasors representing the two waves in DIC

U = interaction potential

v_{sed} = sedimentation velocity

V = volume

w_{Ob}, w_{C} = working distances of objective, condenser

w_{eye} = *ditto* of eye = distance of distinct vision

W_1, W_2 = Wollaston prism in front of condenser, behind objective

(x, y), (x', y') = cartesian coordinates in object, image plane

$(x_{\mathcal{P}}, y_{\mathcal{P}})$, $(x'_{\mathcal{P}}, y'_{\mathcal{P}})$ = *ditto* in plane of entrance, exit pupil

Δx_{pix}, Δy_{pix}, Δz_{pix} = pixel spacings

X, Y, Z; X', Y', Z'; = maximum linear extent of object; of image

$X_{\mathcal{P}}$, $Y_{\mathcal{P}}$; $X'_{\mathcal{P}}$, $Y'_{\mathcal{P}}$ = *ditto* of entrance pupil; of exit pupil

$X_{\sqcup}$, $Y_{\sqcup}$, $Z_{\sqcup}$ = dimensions of suspension container

y_{o}, y'_{o} = height of object, image

z, z' = axial coordinate in object, image space

Δz_{im} = spacing of images in a stack

Z_{CS}, Z_{MS} = thickness of cover slip, microscope slide

Z_{o}, $Z^{\natural}_{\mathsf{o}}$, Z'_{o} = depth of field, effective *ditto*, depth of image

Z_{sed} = sedimentation length

α = stacking probability

γ = surface free energy per unit area

Γ = amplitude attentuation factor of object

δ = DIC bias

$\delta_{\perp}$ = Dirac delta function

ϵ, ϵ_p, ϵ_m = relative permittivity, of particle, medium

ε_R = size polydispersity = standard deviation of the distribution of particle sizes

ζ = angle of zig-zags, $\arccos \frac{1}{3} \approx 70.5°$

η_m = viscosity of medium

θ, θ', $\theta_{\mathcal{P}}$, $\theta'_{\mathcal{P}}$ = azimuth in object space, image space, entrance pupil, exit pupil

κ = number of kinks in a zig-zag pattern

λ, λ', λ_0 = wavelength of light in object space, image space, *in vacuo*

Λ = luminosity

$\Delta\mu$ = chemical potential difference

ξ_2 = illumination degree of coherence of two points

Ξ = Airy optical unit, $\frac{2\pi R'_{\mathcal{P}} r'}{\lambda' z'}$

Ξ_1, Ξ_2 = *ditto* with shift of origin (see equation 2.13)

π = 3.1415...

Π, Π', $\Pi_{\mathcal{P}}$, $\Pi'_{\mathcal{P}}$ = object, image, entrance pupil, exit pupil planes

ρ, ρ_p, ρ_m = density, of particles, of medium

ϱ, ϱ_{coh}, ϱ_{incoh}, ϱ_{pcoh} = resolution limit, with coherent, incoherent, partially coherent illumination

σ, σ', σ_{C} = angular half-aperture of objective on object, image side, of condenser

ς = phase angle between diffracted and direct waves

Σ, Σ = wavefront in object, image space

τ, τ', $\tau_{\mathcal{P}}$, $\tau'_{\mathcal{P}}$, τ_{AS} = amplitude transmittance of object, image, entrance pupil, exit pupil, aperture stop

Υ = amplitude attentuation factor of phase ring

ϕ, $\phi^{\natural}$ = volume fraction, effective *ditto*

ϕ_{F}, ϕ_{M} = volume fraction at freezing (0.494), melting (0.545)

ϕ_{cp}, ϕ_{rcp} = *ditto* at close-packing ($\frac{\pi}{3\sqrt{2}} \approx 0.74$), random close-packing

ϕ_ν = *ditto* of crystal nucleus

φ, φ_1, φ_2 = phase shift due to object, for the two waves in DIC

χ = fraction of crystal coexisting with fluid

ψ	=	phase shift of phase ring
ω, ω'	=	angle subtended at eye by object, image
$\aleph$	=	"wrong" zig-zag angle, $\arccos \frac{1}{\sqrt{3}} \approx 54.7°$

B.2 Abbreviations

CHPB	=	cycloheptylbromide
CSLM	=	confocal scanning laser microscopy
DIC	=	differential interference contrast
fcc	=	face-centred cubic, *i.e.*, cubic close-packing
FT	=	Fourier Transform
hcp	=	hexagonally close-packed
LUT	=	look-up table
OTF	=	optical transfer function ($\mathcal{F}$(PSF))
PHSA	=	polyhydroxystearic acid
PMMA	=	polymethylmethacrylate
PSF	=	point spread-function
PTFE	=	polytetrafluoroethylene
SSF	=	sphere spread-function
rscp	=	randomly-stacked close-packed

List of Figures

2.1 The generic observation system 16
2.2 A aberration-free imaging system 18
2.3 The Airy pattern 22
2.4 Light distribution in the Airy pattern 24
2.5 The illumination of two point objects 26
2.6 The infinite tube-length compound microscope. 30
2.7 Transverse magnification 32
2.8 Visual magnification 33
2.9 Illumination of the infinite tube-length compound microscope. . . 36
2.10 Controlling angular aperture and area of illumination. 37
2.11 The effect on illumination of using an oil-immersion objective. . . 40

3.1 Bright-field imaging of a single colloidal sphere 43
3.2 Phasor representation of phase contrast 47
3.3 Phase contrast: conjugate annuli 50
3.4 Phase contrast imaging of a single colloidal sphere 52
3.5 Removal of contrast reversed regions 53
3.6 The DIC microscope 56
3.7 Phasors in DIC 59
3.8 Normarski's modification of the Wollaston prism 62
3.9 Normarski DIC imaging of a single colloidal sphere 63
3.10 Approximating the wavefront behind a transparent sphere 65
3.11 A simple model of DIC imaging 66

3.12 Determining the DIC lateral shear 67
3.13 The effect of condenser aperture on DIC imaging 68
3.14 Brightness, contrast and grey-level histograms 70
3.15 Clipping and binarizing 72
3.16 Averaging of images 73
3.17 Background subtraction 74
3.18 The shift-and-multiply process of convolution, as applied to digital images. 76
3.19 Some image convolutions and their kernels 77
3.20 Morphometric operations on binary images 79
3.21 Fourier filtering 81

4.1 Objective and condenser working distances 85
4.2 A rectangular-capillary microscope mount for colloidal suspensions 88
4.3 Controlling axial position with a piezoelectric translator. 94
4.4 A series of montages of a dense colloidal suspension 97
4.5 Longitudinal sections through stacks of images 98
4.6 Views constructed from entire image stacks 99
4.7 Construction method for oblique views of entire stacks 100

5.1 The pair potential for hard spheres 105
5.2 The hard sphere equation of state 107

6.1 Lattice parameters for hard sphere crystals 117
6.2 Micrograph showing typical *rscp* features 120
6.3 Computer model of *rscp* 122
6.4 Zig-zag pattern: micrograph 124
6.5 Zig-zag pattern: model 125
6.6 Experimental measurements of α compared with simulation . . . 128
6.7 A single kink as a twin boundary: micrograph 129
6.8 Disjointed-lines pattern: micrograph 130

6.9 Disjointed-line patterns: model 131
6.10 Square pattern: micrograph 132
6.11 Square pattern: model 133
6.12 Small square pattern: micrograph 134
6.13 Small square pattern: model 136
6.14 Five-fold symmetry? 137
6.15 Line patterns: micrographs 138
6.16 Herringbone pattern: micrograph 139
6.17 Basket-weave and imperfect zig-zags: micrographs 140
6.18 A section of colloidal crystal and its computer model. 143
6.19 Rotations about y-axis: constructed and model views 145
6.20 Rotations about x-axis: model views 149
6.21 Rotations about x-axis: constructed views 150

7.1 Graph of crystallization in capillary, $\phi = 0.525$ 156
7.2 Images of phase separation at $\phi = 0.525$ 157
7.3 Graph of crystallization in capillary, $\phi = 0.490$ 159
7.4 Images of sedimentary crystal growth at $\phi = 0.490$ 161
7.5 Sedimentation profile of PMMA spheres in a decalin-tetralin mixture 162
7.6 Graph of crystallization in capillary, $\phi = 0.502$ 163
7.7 Images of phase separation at $\phi = 0.502$ 164
7.8 Images of a density-matched suspension at $\phi = 0.489$ 168
7.9 Density-matched crystallization in capillary, $\phi = 0.510$ 169
7.10 Images of a density-matched suspension at $\phi = 0.510$ 170
7.11 Density-matched crystallization in capillary, $\phi = 0.50$ 173
7.12 Images of a density-matched suspension at $\phi = 0.50$ 174

8.1 Sedimentation profile of a PMMA-CHPB suspension 179
8.2 A scheme for counting particles 180
8.3 A scheme for recognizing particles 182

8.4 Diffusion coefficients from increasing time-averages? 184

A.1 Phasor representation of phase contrast 196

List of Tables

1.1 Examples of Colloids 3

2.1 Notation conventions 17
2.2 The first twelve extrema of the Airy pattern 25
2.3 Setting up Köhler illumination 39

6.1 Measurements of stacking probability from zig-zag patterns 127

Bibliography

E. Abbe, 'Beiträge zur Theorie des Mikroskops und der mikroskopischen Wahrnehmung', *Archiv für Mikroskopische Anatomie* **9** 413–468 (1873)

L. Antl, J. Goodwin, R. Hill, R. Ottewill, S. Owens, S. Papworth and J. Waters, 'The Preparation of Poly(Methyl Methacrylate) Latices in Nonaqueous Media', *Colloids and Surfaces* **17**(1) 67–78 (1986)

R. Barer, 'A Vector Theory of Phase Contrast and Interference Contrast. I. Positive Phase Contrast', *Journal of the Royal Microscopical Society* **72**(1) 10–30 (1952a)

R. Barer, 'A Vector Theory of Phase Contrast and Interference Contrast. II. Positive Phase Contrast, continued', *Journal of the Royal Microscopical Society* **72**(2) 81–98 (1952b)

R. Barer, 'A Vector Theory of Phase Contrast and Interference Contrast. III. Negative Phase Contrast', *Journal of the Royal Microscopical Society* **73**(1) 30–39 (1953a)

R. Barer, 'A Vector Theory of Phase Contrast and Interference Contrast. IV. B-Type Phase Contrast', *Journal of the Royal Microscopical Society* **73**(4) 206–215 (1953b)

P. Bartlett, 'A geometrically-based mean-field theory of polydisperse hard-sphere mixtures', *Journal of Chemical Physics* **107**(1) 188–196 (1997)

P. Bartlett, R. Ottewill and P. Pusey, 'Superlattice Formation in Binary Mixtures of Hard-Sphere Colloids', *Physical Review Letters* **68**(25) 3801–3804 (1992)

A. van Blaaderen, 'Imaging Individual Particles in Concentrated Colloidal Dispersions by Confocal Scanning Light Microscopy', *Advanced Materials* **5**(1) 52–54 (1993)

A. van Blaaderen and P. Wiltzius, 'Real-Space Structure of Colloidal Hard-Sphere Glasses', *Science* **270**(5239) 1177–1179 (1995)

P. Bolhuis and D. Kofke, 'Monte Carlo study of freezing of polydisperse hard spheres', *Physical Review E* **54**(1) 634–643 (1996)

P. Bolhuis and D. Kofke, 'Freezing of polydisperse hard spheres', *Physical Review E* **59**(1) 618–622 (1999)

J. Bongers and H. Versmold, 'Microscopic investigations of the single particle dynamics in colloidal crystals', *Journal of Chemical Physics* **104**(4) 1519–1523 (1996)

J. C. Brown, P. N. Pusey, J. Goodwin and R. Ottewill, 'Light scattering study of dynamic and time-averaged correlations in dispersions of charged particles', *Journal of Physics A* **8**(5) 664–682 (1975)

M. Carbajal-Tinoco, F. Castro-Román and J. Arauz-Lara, 'Static properties of confined colloidal suspensions', *Physical review E* **53**(4) 3745–3749 (1996)

N. F. Carnahan and K. E. Starling, 'Equation of State for Nonattracting Rigid Spheres', *Journal of Chemical Physics* **51** 635–636 (1969)

T.-T. Chui, *M.Phil.*, Master's thesis, The University of Edinburgh (1994)

N. A. Clark, J. H. Lunacek and G. B. Benedek, 'A Study of Brownian Motion Using Light-Scattering', *American Journal of Physics* **38**(5) 575–585 (1970)

J. C. Crocker, 'Measurement of the hydrodynamic corrections to the Brownian motion of two colloidal spheres', *Journal of Chemical Physics* **106**(7) 2837–2840 (1997)

J. C. Crocker and D. G. Grier, 'When Like Charges Attract: The Effects of Geometrical Confinement on Long-Range Colloidal Interactions', *Physical Review Letters* **77**(9) 1897–1900 (1996)

H. Cummins, N. Knable and Y. Yeh, 'Observation of Diffusion Broadening of Rayleigh Scattered Light', *Physical Review Letters* **12**(6) 150–153 (1964)

B. Derjaguin and L. Landau, 'Theory of the stability of strongly charged lyophobic sols and the adhesion of strongly charged particles in solutions of electrolytes', *Acta Physicochimica URSS* **14** 633–662 (1941)

A. Dinsmore, P. Warren, W. Poon and A. Yodh, 'Fluid-solid transitions on walls in binary hard-sphere mixtures', *Europhysics Letters* **40**(3) 337–342 (1997)

P. Duffieux, *L'intégrale de Fourier et ses applications à l'optique* (Faculté des Sciences, Besançon, 1946)

P. Duffieux, *The Fourier Transform and Its Application to Optics*, 2nd ed. (John Wiley and Sons, New York, 1983)

J. S. van Duijneveldt and D. Frenkel, 'Computer simulation study of free energy barriers in crystal nucleation', *Journal of Chemical Physics* **96**(6) 4655–4668 (1992)

J. S. van Duijneveldt and H. N. W. Lekkerkerker, 'Crystallization in Colloidal Suspensions', in *Science and Technology of Crystal Growth* (eds. J. van der Eerden and O. Bruinsma), pp. 279–290 (Kluwer Academic Publishers, 1995)

A. Einstein, 'Über die von der molekular kinetischen Theorie der Wärme geforderte Bewegung von in ruhenden Flüssigkeiten suspendierten Teilchen', *Annalen der Physik* **17** 549–560 (1905)

A. Einstein, 'Zur Theorie der Brownschen Bewegung', *Annalen der Physik* **19** 371–381 (1906)

M. S. Elliot, B. T. F. Bristol and W. C. K. Poon, 'Direct measurement of stacking disorder in hard-sphere colloidal crystals', *Physica A* **235** 216–223 (1997)

D. J. Fairhurst (1999a), private communication

D. J. Fairhurst, *Polydispersity in Colloidal Phase Transitions*, Ph.D. thesis, The University of Edinburgh (1999b)

M. Françon, *Le Microscopie à contraste de phase et le microscope interférentiel* (CNRS, Paris, 1954)

R. C. Gonzalez and R. E. Wood, *Digital Image Processing* (Addison-Wesley, Reading, Mass., 1992)

J. W. Goodman, *Introduction to Fourier Optics*, 2nd ed. (McGraw-Hill, Singapore, 1996)

T. Graham, 'Liquid Diffusion Applied to Analysis', *Philosophical Transactions of the Royal Society of London* **151** 163 (1861)

D. G. Grier and C. A. Murray, 'The microscopic dynamics of freezing in supercooled colloidal fluids', *Journal of Chemical Physics* **100**(12) 9088–9095 (1994)

K. R. Hall, 'Another hard sphere equation of state', *Journal of Chemical Physics* **57** 2252–2254 (1972)

H. Hamaker, 'London-van der Waals attraction between spherical particles', *Physica* **4** 1058–1072 (1937)

J. Hansen and D. Schiff, 'Influence of interatomic repulsion on the structure of liquids at melting', *Molecular Physics* **25**(6) 1281–1290 (1973)

J. Harland, S. Henderson, S. Underwood and W. van Megen, 'Observation of Accelerated Nucleation in Dense Colloidal Fluids of Hard Sphere Particles', *Physical Review Letters* **75**(19) 3572–3575 (1995)

J. Harland and W. van Megen, 'Crystallization kinetics of suspensions of hard colloidal spheres', *Physical Review E* **55**(3) 3054–3067 (1997)

H. Haselmann, 'Who was August Köhler?', *Proceedings of the Royal Microscopical Society* **18** 170–172 (1983)

M. D. Haw, 'Density-matching experiments with PMMA particles', (1996), unpublished

Y. He, B. Ackerson, W. van Megen, S. Underwood and K. Schätzel, 'Dynamics of crystallization in hard-sphere suspensions', *Physical Review E* **54**(5) 5286–5297 (1996)

S. Henderson, T. Mortensen, S. Underwood and W. van Megen, 'Effect of particle size distribution on crystallisation and the glass transition of hard sphere colloids', *Physica A* **233**(1-2) 102–116 (1996)

S. Hendricks and E. Teller, 'X-Ray Interference in Partially Ordered Layer Lattices', *Journal of Chemical Physics* **10**(3) 147–167 (1942)

W. G. Hoover and F. H. Ree, 'Melting Transition and Communal Entropy for Hard Spheres', *Journal of Chemical Physics* **49**(8) 3609–3617 (1968)

S. Inoué, *Video Microscopy: The Fundamentals*, 2nd ed. (Plenum Press, New York, 1997)

A. N. Jackson and A. D. Bruce (1999), private communication

J. Kepler, *Strena, Seu, de Nive Sexangula* (G. Tampach, Frankfurt am Main, Germany, 1611)

C. de Kruif, E. Israel, A. Vrij and W. Russel, 'Hard-Sphere Colloidal Dispersions - Viscosity as a Function of Shear Rate and Volume Fraction', *Journal of Chemical Physics* **83**(9) 4717–4725 (1985)

W. Lang, 'Normarski Differential Interference Microscopy', *Zeiss Informations Reprint* (S 41-210.2-5-e) (1975)

P. Langevin, 'Sur la théorie du mouvement brownien', *Comptes Rendus Hebdomadaires des Séances de l'Académie des Sciences* **146** 530–533 (1908)

J. Liu, D. Weitz and B. Ackerson, 'Coherent crystallography of shear-aligned crystals of hard-sphere colloids', *Physical Review E* **48**(2) 1106–1114 (1993)

A. Low, *Introductory Computer Vision and Image Processing* (McGraw-Hill, London, 1991)

A. H. Marcus and S. A. Rice, 'Observations of First-Order Liquid-to-Hexatic and Hexatic-to-Solid Phase Transitions in a Confined Colloid Suspension', *Physical Review Letters* **77**(12) 2577–2580 (1996)

A. H. Marcus and S. A. Rice, 'Phase transitions in a confined quasi-two-dimensional colloid suspension', *Physical Review E* **55**(1 PtB) 637–656 (1997)

V. Martelozzo (1998), private communication

S. Meeker, W. Poon and P. Pusey, 'Concentration dependence of the low-shear viscosity of suspensions of hard-sphere colloids', *Physical Review E* **55**(5 PtB) 5718–5722 (1997)

W. van Megen and S. Underwood, 'Change in crystallization mechanism at the glass transition of colloidal spheres', *Nature* **362**(6421) 616–618 (1993)

W. van Megen and S. Underwood, 'The glass transition in colloidal hard spheres', *Journal of Physics: Condensed Matter* **6**(S23) (1994)

S. Neser, C. Bechinger, P. Leiderer and T. Palberg, 'Finite-Size Effects on the Closest Packing of Hard Spheres', *Physical Review Letters* **79**(12) 2348–2351 (1997)

G. Normarski, 'Dispositif interférentiel á polarisation pour l'étude des objects transparents ou opaques appartenant à la classe des objects de phase', French Patent (1953)

G. Normarski, 'Microinterféromètre différential à ondes polarisées', *Le Journal de Physique et le Radium* **16** 9S–11SS (1955)

Y. S. Papir and I. M. Krieger, 'Rheological Studies on Dispersions of Uniform Colloidal Spheres: II. Dispersions in Nonaqueous Media', *Journal of Colloid and Interface Science* **34**(1) 126–130 (1970)

C. Pathmamanoharan, C. Slob and H. Lekkerkerker, 'Preparation Of Polymethylmethacrylate Lattices In Non-Polar Media', *Colloid and Polymer Science* **267**(5) 448–450 (1989)

S. Paulin and B. Ackerson, 'Observation of a Phase Transition in the Sedimentation Velocity of Hard Spheres', *Physical Review Letters* **64**(22) 2663–2666 (1990)

J. B. Perrin, 'Grandeur des molécules et charge de l'électron', *Comptes Rendus Hebdomadaires des Séances de l'Académie des Sciences* **147** 594–596 (1908)

J. B. Perrin, *Brownian Motion and Molecular Reality* (Taylor and Francis, London, 1910)

J. B. Perrin, 'Discontinuous structure of matter', in *Nobel Lectures - Physics*, vol. 1922–1941, pp. 138–164 (Elsevier, Amsterdam, 1965)

S. Phan, W. Russel, J. Zhu and P. Chaikin, 'Effects of polydispersity on hard sphere crystals', *Journal of Chemical Physics* **108**(23) 9789–9795 (1998)

P. Pieranski, 'Colloidal Crystals', *Contemporary Physics* **24** 25–73 (1983)

M. Pluta, *Advanced Light Microscopy*, vol. 1 (Elsevier, Amsterdam, 1988)

M. Pluta, *Advanced Light Microscopy*, vol. 2 (Elsevier, Amsterdam, 1989)

W. C. Poon, A. D. Pirie and P. N. Pusey, 'Gelation in Colloid-Polymer Mixtures', *Faraday Discussions* (101) 65–76 (1995)

P. Pusey, W. Poon, S. Ilett and B. P., 'Phase behaviour and structure of colloidal suspensions', *Journal of Physics: Condensed Matter* **6** A29–A36 (1994)

P. N. Pusey, 'The dynamics of interacting Brownian particles', *Journal of Physics A* **8**(9) 1433–1440 (1975)

P. N. Pusey, 'The effect of polydispersity on the crystallization of hard spherical colloids', *Journal de Physique* **48** 709–712 (1987)

P. N. Pusey, 'Colloidal Suspensions', in *Liquids, Freezing and Glass Transition* (eds. J. P. Hansen, D. Levesque and J. Zinn-Justin), pp. 763–942 (Elsevier, Amsterdam, 1991), Les Houches, Session LI, 1989, Course 10

P. N. Pusey (1999), private communication

P. N. Pusey and W. van Megen, 'Detection of small polydispersities by photon correlation spectroscopy', *Journal of Chemical Physics* **80**(8) 3513–3520 (1984)

P. N. Pusey and W. van Megen, 'Phase behaviour of concentrated suspensions of nearly hard colloidal spheres', *Nature* **320** 340–342 (1986)

P. N. Pusey, W. van Megen, P. Bartlett, B. A. Ackerson, J. G. Rarity and S. M. Underwood, 'Structure of Crystals of Hard Colloidal Spheres', *Physical Review Letters* **63**(25) 2753–2756 (1989)

Lord Rayleigh, 'On the theory of optical images, with special references to the microscope.', *The London, Edinburgh and Dublin Philosophical Magazine and Journal of Science* **42**(255) 167 (1896)

F. Renth (1999), private communication

W. Russel, D. Saville and W. Schowalter, *Colloidal Dispersions* (Cambridge University Press, Cambridge, 1989)

W. Schaertl and H. Sillescu, 'Dynamics of Colloidal Hard Spheres in Thin Aqueous Suspension Layers - Particle Tracking by Digital Image Processing and Brownian Dynamics Computer Simulations', *Journal of Colloid and Interface Science* **155**(2) 313–318 (1993)

W. Schaertl and H. Sillescu, 'Brownian Dynamics of Polydisperse Colloidal Hard Spheres: Equilibrium Structures and Random Close Packings', *Journal of Statistical Physics* **77**(5-6) 1007–1025 (1994)

P. Segrè, S. Meeker, P. Pusey and W. Poon, 'Viscosity and Structural Relaxation in Suspensions of Hard-Sphere Colloids', *Physical Review Letters* **75**(5) 958–961 (1995a)

P. Segrè, W. van Megen, P. Pusey, K. Schätzel and W. Peters, '2-color Dynamic Light Scattering', *Journal of Modern Optics* **42**(9) 1929–1952 (1995b)

Y. C. Shen and D. W. Oxtoby, 'bcc Symmetry in the Crystal-Melt Interface of Lennard-Jones Fluids Examined through Density Functional Theory', *Physical Review Letters* **77**(17) 3585–3588 (1996)

M. von Smoluchowski, 'Przyczynek do teoryi endosmozy elektrycznej i niektórych zjawisk pokrewnych – Contribution à la théorie de l'endosmose électrique et de quelques phenomènes corrélatifs', *Bulletin International de l'Académie des Sciences de Cracovie* **8** 182–200 (1903)

M. von Smoluchowski, 'Versuch einer mathematischen Theorie der Koagulationkinetik kolloider Lösungen', *Zeitschrift für Physikalische Chemie* **92** 129–168 (1918)

D. Tabor, *Gases, liquids and solids and other states of matter*, 3rd ed. (Cambridge University Press, Cambridge, 1991)

H. Tanaka (1997), private communication

S. Underwood, J. Taylor and W. van Megen, 'Sterically Stabilized Colloidal Particles as Model Hard Spheres', *Langmuir* **10**(10) 3550–3554 (1994)

N. A. Verhaegh and A. van Blaaderen, 'Dispersions of Rhodamine-Labeled Silica Spheres: Synthesis, Characterization, and Fluorescence Confocal Scanning Laser Microscopy', *Langmuir* **10**(5) 1427–1438 (1994)

N. A. M. Verhaegh, J. S. van Duijneveldt, A. van Blaaderen and H. N. W. Lekkerkerker, 'Direct observation of stacking disorder in a colloidal crystal', *Journal of Chemical Physics* **102**(3) 1416–1421 (1995)

E. Verwey and J. Overbeek, *Theory of the Stability of Lyophobic Colloids* (Elsevier, Amsterdam, 1948)

A. J. C. Wilson, 'Imperfections in the structure of cobalt II. Mathematical treatment of proposed structure', *Proceedings of the Royal Society of London* **180** 277–285 (1942)

W. W. Wood and J. D. Jacobson, 'Preliminary Results from a Recalculation of the Monte Carlo Equation of State of Hard Spheres', *Journal of Chemical Physics* **27** 1207 (1957)

L. Woodcock, 'Glass Transition in the Hard-Sphere Model and Kauzmann's Paradox', *Annals of the New York Academy of Sciences* **371** 274–298 (1981)

M. Würth, J. Schwarz, F. Culis, P. Leiderer and T. Palberg, 'Growth kinetics of body centered cubic colloidal crystals', *Physical Review E* **52**(6 PtB) 6415–6423 (1995)

F. Zernike, 'Diffraction theory of the knife-edge test and its improved form, the phase-contrast method', *Royal Astronomical Society Monthly Notices* **94** 377–384 (1934)

F. Zernike, 'Das Phasenkontrastverfahren bei der mikroskopischen Beobachtung', *Zeitschrift für technische Physik* **16** 454–457 (1935), also in Phys. Z. 36:848-851 (1935)

F. Zernike, 'Phase-contrast, a new method for the microscopic observation of transparent objects. Part I', *Physica* **9** 686–698 (1942a)

F. Zernike, 'Phase-contrast, a new method for the microscopic observation of transparent objects. Part II', *Physica* **9** 974–986 (1942b)

F. Zernike, 'How I discovered phase contrast', in *Nobel Lectures - Physics*, vol. 1942–1962, pp. 239–246 (Elsevier, Amsterdam, 1964)

J. Zhu, M. Li, R. Rogers, W. Meyer, R. Ottewill, STS-73 Space Shuttle Crew, W. Russell and P. Chaikin, 'Crystallization of hard-sphere colloids in microgravity', *Nature* **387**(6636) 883–885 (1997)